Improved Efficiency of Miscible CO_2 Floods and Enhanced Prospects for CO_2 Flooding Heterogeneous Reservoirs

Final Report
April 17, 1994–May 31, 1997

Work Performed Under Contract No. DE-FG22-94BC14977
Prepared for the
U.S. Department of Energy

by

Reid B. Grigg
David S. Schechter

New Mexico Petroleum Recovery Research Center
New Mexico Institute of Mining and Technology
Socorro, New Mexico 87801

August 1997

PRRC Report 97-22

TABLE OF CONTENTS

LIST OF TABLES

LIST OF FIGURES

ABSTRACT

The overall goal of this project was to improve the efficiency of miscible CO_2 floods and enhance the prospects for flooding heterogeneous reservoirs. This objective was accomplished through experimental and modeling research in three task areas: 1) foams for selective mobility control in heterogeneous reservoirs, 2) reduction of the amount of CO_2 required in CO_2 floods, and 3) low IFT processes and the possibility of CO_2 flooding in fractured reservoirs. This report provides results from the three-year project for each of the three task areas.

In the first task, we investigated a desirable characteristic of CO_2-foam called selective mobility reduction (SMR) that improves displacement efficiency by reducing the effects of reservoir heterogeneity. Research on the SMR of foam focused on three subjects: 1) to verify SMR in different rock permeabilities that are in capillary contact; 2) to test additional surfactants for the SMR property; and 3) to develop a modeling approach to assess the oil recovery efficiency of SMR in CO_2-foam on a reservoir scale. The experimental results from the composite cores suggest that rock heterogeneity has a significant effect on two phase (CO_2/brine) flow behavior in porous media, and that foam can favorably control CO_2 mobility. The numerical modeling results suggest that foam with SMR can substantially increase sweep efficiency and therefore improve oil recovery. Foam screening indicates that interfacial tension (IFT) improvement correlates well with the extent of SMR for the system tested.

The second task examined increasing the efficiency of CO_2 by decreasing the mass of CO_2 required to produce a barrel of oil. Methods used were minimizing the flood pressure, using foam to increase the sweep efficiency, or both. A number of phase behavior tests were performed to determine the effect of pressure, temperature, and reservoir fluid composition on recovery efficiency. Coreflood tests were performed to examine how interstitial flow rate and foam quality (volume fraction of gas) affect foam formation. The foam tests were used to develop descriptions of the mechanisms associated with the displacement of oil by CO_2-foam injection These mechanisms provide input parameters for reservoir simulation. The programming and testing of two reservoir simulators and testing on a reservoir scale for the foam option were completed. The behavior seen in our simulations closely matched behavior seen in a field CO_2 foam pilot. The horizontal option was developed, tested, reported, and verified during this project.

In the third task the development of methods to measure and predict interfacial tension (IFT) at reservoir conditions progressed well. Under conditions near miscibility the IFT approaches zero and systematic errors of traditional methods become unacceptable at low IFT. A new method for determination of low IFT was developed based on a static force balance on the lower half of the pendant drop. The measurements of surface and interfacial tension determined with this new method indicate it is more accurate than the traditionally used methods for the low IFT region (IFT < 1 mN/m). A second area of major achievement is the development of a new mathematical model based on Darcy's law and film flow theory to describe free-fall gravity drainage with equilibrium fluids. The new model shows better accuracy for the 20 sets of experimental data examined than existing models. A simple methodology was developed that allows the user to calculate IFT of any crude oil/gas system.

EXECUTIVE SUMMARY

In Task 1, we progressed well in our studies of selective mobility reduction (SMR), the property of CO_2-foam by which mobility is reduced by a greater fraction in higher than in lower permeability cores. This property promises to improve displacement efficiency in CO_2 floods by reducing the effects of reservoir heterogeneity. We verified SMR in both series and parallel heterogeneous composite cores. The uneven distribution of fluid in heterogeneous composite cores was verified and, more importantly, we verified the positive effect of CO_2-foam in compensating for the effects of heterogeneity in the cores. A potential method for quick screening of surfactants to assess their potential as SMR agents was developed using IFT at reservoir pressure. The favorable effects of CO_2-foam and the augmented positive effect of SMR-CO_2 foams on reservoir scale were implemented using a simple reservoir model.

In Task 2, we developed a phase behavior data bank that concentrates on the effects of pressure, temperature, and fluid compositions on the development of efficient CO_2 displacements under reservoir conditions. This information can be used directly to understand phase behavior in reservoir fluid - CO_2 displacements and can also be used to determine IFT and solubility parameters under dynamic reservoir conditions. All these data are being used to predict miscibility and recovery in CO_2 displacement under reservoir conditions. Coreflood tests were used to identify and quantify a number of variables in foam flooding; effects of flow rate, gas foam quality (gas volume fraction), and surfactant concentration. During the first year foam and horizontal well features were developed. During the second year the foam feature was refined and tested for verification. The foam model in the initial test displayed phenomena similar to those seen in the East Vacuum CO_2-Foam Pilot Test. The foam feature has been installed in two types of reservoir simulators and is ready for field tests. The horizontal feature was tested using a Society of Petroleum Engineers (SPE) test problem and was within the range of fourteen other versions. In the final year a reservoir model was developed and the foam option was tested on pilot test results.

In Task 3, we investigated multiphase flow behavior in fractured reservoirs. Understanding the relationship of fluid flow and reservoir heterogeneity in fractured reservoirs is the key factor in developing a strategy of improving oil recovery in these reservoirs. We improved the apparatus for measuring IFT at reservoir conditions. The traditional method for determining IFT using the pendant drop technique works well except at low IFT. A new method for calculation of low IFT was developed and shown to work at low IFT. The new method is based on a static force balance on the lower half of the pendant drop. Another area of major achievement was the development of a new mathematical model based on Darcy's law and film flow theory to describe free-fall gravity drainage with equilibrium fluids. The ability to measure and predict IFT under reservoir conditions and to describe gravity drainage are necessary developments toward the goal of improving oil recovery in fractured systems that previously have not been seriously considered for CO_2 flooding.

INTRODUCTION

Background

Because of the importance of CO_2 flooding to future oil recovery potential in New Mexico and west Texas, the New Mexico Petroleum Recovery Research Center (PRRC) maintains a vigorous experimental program in this area of research. This research has been supported by the Department of Energy (DOE), the State of New Mexico, and a consortium of oil companies. Based on encouraging results obtained in a project entitled "Improvement of CO_2 Flood Performance," the DOE awarded a grant to the PRRC in 1989 to transfer promising research on CO_2-foam to a field demonstration site that was a successful forerunner of DOE's Class I, II, and III projects. As part of the field demonstration test, the PRRC provided laboratory and research support for the design of the project entitled "Field Verification of CO_2-Foam," and continued to perform experimental work related to mechanisms involved in CO_2 flooding. This project is a continuation of the prior work in those and new, related areas.

New concepts that were investigated provide a more favorable response from the use of foam for achieving mobility control in CO_2 floods, the possibility of obtaining good oil recovery efficiency while still using less CO_2 than is commonly practiced in field operation, and the possibility of CO_2 flooding vertically fractured reservoirs. Each of these areas have potential for increasing oil production and reducing costs in fields presently under CO_2 flood that are viewed as candidates for future CO_2 flooding. Also, the results of this research should expand viable candidate fields to include lower pressure and much more heterogeneous or fractured reservoirs.

With large quantities of oil unrecoverable in fractured reservoirs, new concepts are being considered for such reservoirs that have the potential of recovering huge volumes of the remaining oil. These new concepts demonstrate the need for research into improvements for CO_2 flooding in heterogeneous reservoirs so that domestic oil recovery from these reservoirs can be maximized and premature abandonment of potentially productive wells prior to implementation of IOR can be avoided.

Program Objectives

The objectives of this work consisted of experimental and modeling research aimed at improving the effectiveness of CO_2 flooding in heterogeneous reservoirs. New concepts were investigated that can be applied by field operators within the next two to five years. We conducted experimental research in three closely related areas: 1) exploration of the applicability of selective mobility reduction, 2) potential higher economic viability of floods at reduced CO_2 injection pressures, and 3) exploitation of gravitational forces during low-IFT CO_2 flooding in tight, vertically fractured reservoirs.

Report Content

This report describes work performed during the project. Separate discussions and supporting material are provided for each of the three task areas.

TASK 1 : CO_2 FOAMS FOR SELECTIVE MOBILITY REDUCTION

Introduction

In the oil recovery process, CO_2 foam is an effective mobility reducing agent for CO_2 flooding. Recent research indicates that some CO_2 foams show an exciting additional characteristic— selective mobility reduction (SMR).[1-8] In laboratory experiments, SMR in foams reduces the mobility of CO_2 by a greater fraction in higher permeability cores than in those of lower permeability. With this property, foam can flow at the same velocity in high and low permeability regions in reservoir formations and preserve the uniformity of the flood front while propagating through rocks with non-uniform permeability. Presumably, this property could reduce the effect of both vertical and horizontal rock heterogeneity in reservoir formations. As a consequence, the use of CO_2-foam showing SMR would delay CO_2 breakthrough and produce higher displacement efficiency in heterogeneous reservoirs.

The objective of this study was to identify surfactants that induce SMR, and to understand the phenomena and develop methods to predict which foaming agents can be expected to exhibit SMR behavior. The following tasks were pursued over the past three years to develop a better understanding of SMR:

Preliminary work: Core flooding experiments were conducted to explore the occurrence of SMR in various domains of surfactant type and concentration, flow rates, foam quality, and rock type.
Capillary contact experiments (series flow system): The first type of porous media, comprising two well-defined permeability regions in capillary contact that were arranged in series, was used to test surfactant capability to generate foam with SMR.
Capillary-contact experiments (parallel flow system): The second type of porous media, comprising two sections coaxially arranged parallel to the flow direction, was used to verify SMR behavior of foam and its capability as a diverting agent.
Numerical simulation: A simple numerical model was developed to simulate SMR in corefloods and to analyze its effect on oil recovery.
Establishment of correlation: Foam properties in a bulk phase and in porous media were correlated by means of two assessment methods.

Preliminary Laboratory Work

Preliminary work was conducted to explore the occurrence of SMR in coreflooding with two different experimental setups. The first series of experiments (Series A) was designed to measure the mobility of fluid in small cores (measuring 1.0 inch in length and 0.5 inch in diameter) with different permeabilities, arranged in series along the flow path of a system. In this design, the mobilities of flowing fluid were measured simultaneously during a single experiment, a procedure that substantially reduced the time required to obtain experimental results. The second set of experiments (Series B) was designed to investigate the effect of core sample size and geometry on

the experimental results. A larger core (measuring 2.75 in. long and 1.40 in. in diameter) was used in this second series of experiments.

Test Series A

To screen surfactants for occurrence of SMR in foam flooding process, a standard high-pressure mobility experiment was modified to expedite measurement of the mobility of CO_2-foam through rock samples with different permeabilities. Two coreholders were assembled in series in the flow path of the CO_2-foam in such a way that the mobilities of foams in two cores of different permeability could be measured simultaneously during a single experiment. The validity of this design was examined by interchanging the positions of two cores in the flow system during the mobility measurement. Additional mobility measurements were performed to examine the effect of surfactant type, concentration, rock type and flow rate on SMR of CO_2-foam. The results and discussion of these tests are presented below.

The first modification was made to increase the speed and efficiency of the tests. This change consisted of the insertion of a second coreholder and rock sample in series with the foam generator and first core in the system, to transport the mixture of dense CO_2 and brine or surfactant solution. Consequently, the flow of the two fluids were the same in the steady state for the two cores, and the mobilities could be observed by recording the pressure drops across each.

The second change was replacing the needle valve that had been used to control the flow rate. For this purpose, we added an additional, backwards-running Ruska pump downstream in the system. Although the individual flow rate of the CO_2 and the brine (or surfactant solution) was controlled by separate injection pumps, the additional pump made it possible to maintain constant the total volumetric flow rate of CO_2-foam or CO_2-brine during the experiment. Thus, the same flow rate of CO_2 mixtures through each core at steady state was assured and the mobilities in high and low permeability rock samples were determined simultaneously. The schematic of this apparatus is shown in Fig. 1. Because the CO_2-aqueous mixture was corrosive, the rear portion of the floating piston contained distilled water to protect the inside barrel of the pump.

Two surfactants, Chaser™ CD1045 and CD1050, were used in the Series A tests. They were supplied by Chevron Chemical Company as 46.7 wt% active and 70 wt% active aqueous solutions, respectively. In different tests, two surfactant concentrations, 500 ppm (near or below the critical micelle concentration of each surfactant) and 1000 ppm (above each surfactant's CMC) were used to generate the foam. These concentrations were calculated on an active basis. Simultaneous injection of CO_2 and brine or CO_2 and surfactant was maintained at a volumetric ratio of 4:1 (or quality of 80%) while the total flow rates varied from 7.5 cc/hr to 15 cc/hr (corresponding to Darcy velocities of 4.7 ft/day to 9.4 ft/day). All experiments were conducted at 101°F and 2100 psig.

Core samples used in this preliminary work were cut from two types of quarried rocks, Berea sandstone and Baker dolomite, and from one "preserved state" carbonate reservoir rock. The core plug used as a foam generator was 0.5 in. in diameter and 0.5 in. in length, while the other core

samples were 0.5 in. in diameter and 1.0 in. in length. The permeability of Berea sandstone varies from 130 md to 900 md, whereas the permeability of Baker dolomite varies from 30 md to 110 md. The reservoir rock used here was supplied by the Phillips Petroleum Company as a piece of core slab retrieved from an observation well in the East Vacuum Grayburg San Andres Unit Field. This core slab was wrapped and sealed at the well site and contained the original reservoir fluids. Using the PRRC scanning minipermeameter, we measured 286 permeabilities on one flat surface of this core slab, with a 0.05 in. square grid. From this measured permeability map, we found the permeabilities to vary from 0.1 md to 900 md on a small area of surface (15 $in.^2$). The permeabilities are not uniformly distributed and are mostly below 70 md. By carefully locating the high and low permeability regions on this core slab, we were able to cut several core plugs with average permeabilities ranging from 50 to 500 md for the tests.

Four experiments were conducted to examine the effect of core position on mobility measurements in the new two-core system. The first two experiments were conducted with the high permeability core positioned ahead of the low permeability core, whereas the other two experiments were conducted with the cores the other way around. Baker dolomite and fired Berea sandstone were used in these tests with surfactant CD1050. In Fig. 2, the mobility values are plotted with respect to the core permeabilities. From the results, it is evident that whether the high or low permeability core is placed first in the flow stream is not significant. A line connecting the data points of different permeability indicates the relationship between mobility of fluid and the rock permeability. For an ordinary fluid flowing through different permeability rock samples, the mobilities are proportional to the rock's permeabilities, and the slope of the line should be 1.0. On the other hand, for a foam showing an ideal SMR (where the mobility of foam is roughly the same at high and low permeability), the slope of the line connecting the mobility data points will be zero. Any slope of the line falling between zero and one indicates the occurrence of SMR to some degree; a lesser value suggests a more favorable SMR. Based on this deduction, we introduced a regression method to analyze the slope of the line and used it to qualitatively describe SMR. These slopes can be determined from data shown in Figs 2–7. In order to avoid congestion on the figures, making it difficult to distinguish the individual results, all of the straight line approximations have been omitted, except for the unity slope line through the “no surfactant” points.

Assuming Newtonian fluids, the slope values of data sets in Fig. 2 for CO_2-brine should be one, if the total mobility of a two-phase mixture without surfactant is proportional to the rock permeability. In fact, the slope values of CO_2-brine were calculated to be 1.13 and 1.03, respectively, for the two different core positions (as identified at the bottom of the plot). As the surfactant concentration increased, the slope of the mobility line decreased to 0.70, 0.77 (at 500 ppm) and 0.77, 0.81 (at 1000 ppm) for the two core positions. These lower-than-one values for the slope indicated that the foam showed SMR. Although noticeable difference in slope values were found when core positions were changed, the difference was not significant in the interpretation of SMR. Therefore, for consistency, the remaining mobility measurements were conducted with the higher permeability core placed ahead of the lower permeability core in the flow system.

When the mobility measurements were taken with quarried rocks, SMR was observed in

most cases in using both surfactants CD1045 and CD1050. In the tests with the carbonate reservoir rocks, however, favorable SMR was not observed for either of these surfactants. This difference may have resulted from hydrocarbon residue remaining in the cores that interfered with foam formation, or may have been the result of unusually large changes in and erosion of the EVGSAU core during the test. In addition, it was found that the extent of SMR varied consistently among the other tests. Of the several factors examined, the surfactant type and flow rate were found to be the two most significant parameters, while the rock type and surfactant concentration (so long as this was above the CMC) affected the SMR to a lesser extent.

A typical set of results showing the dependence of mobility on rock permeability is plotted in Fig. 3. The two groups of rocks represented in this plot are Baker dolomite (ranging from 30 md to 110 md) and Berea sandstone (ranging from 130 md to 900 md). At a total flow velocity of 4.7 ft/day and regardless of rock type, the mobilities of CO_2-brine (depicted as solid squares) fall more or less on a line of unit slope when they are plotted against the sample permeabilities. In fact, the slope of this line as obtained from the regression shows a value of 0.95. As surfactant CD1050 concentration is increased from 0 to 500 ppm, the mobility of foam (shown as open diamonds) is significantly reduced. The slope of the line connecting these data points is reduced to 0.60, indicating that SMR occurs within the whole range of permeability. As the surfactant concentration is increased further, the mobility of foam is somewhat further reduced. However, the slope increases slightly—suggesting that additional surfactant does not improve SMR in this case.

Similar results are also plotted in Figs. 4 to 6, in which mobility dependence is examined with different surfactants and with different flow rates. In addition to these plots, the slope values determined with the regression method are also tabulated in Table 1. Factors considered in this table include the flow rate, rock type, and surfactant type and concentration. By comparing the listed values, the slopes for most of CO_2-brine cases (0 ppm) are in the neighborhood of one. On the other hand, the slopes of most of the foam cases are significantly less than one. As described previously, the slope value can be used as an indicator to show the extent of SMR among different cases. Therefore, surfactant CD1045 exhibits a slightly more favorable SMR in Berea sandstone than in Baker dolomite, because the slopes in samples of Berea sandstone cores are less than those in the samples of Baker dolomite. Likewise, surfactant CD1050 exhibits a less favorable SMR in the Berea sandstone than in the Baker dolomite. In most cases, the increase of surfactant concentration improves the SMR when using surfactant CD1045, but fails to improve the SMR when surfactant CD1050 is used. Moreover, the results also reveal that a better SMR is exhibited at low flow velocity of CO_2-foam (4.7 ft/day) than at high flow velocity (9.4 ft/day) in all cases. This implies that SMR of foam may be improved when foam has traveled far away from the injection wells in the formation.

Unlike the results found in the quarried rocks, however, a favorable SMR was not observed in the tests using dolomite reservoir rocks retrieved from an observation well in the EVGSAU. The relationship between mobilities and rock permeabilities is displayed in Fig. 7. The mobilities of CO_2-brine fall approximately onto a unit slope line. The lines connecting mobilities of CO_2 foam for each surfactant, however, have slopes greater than one. Such a foam exhibits an unfavorable SMR, in which mobility is much higher in the higher permeability core than it is in the lower

permeability. This unfavorable result indicates that existence of hydrocarbon in core samples can have a significant effect on foam properties, and therefore, on the SMR behavior of foam.

Test Series B

This work was carried out in a somewhat different experimental circumstance. Fired Berea cores of 3.7 cm diameter and 7 cm length were used. These were somewhat larger than those used in Test Series A. The permeabilities of the cores were 140, 490, and 985 md. Again, constant displacement pumps served as sources of dense CO_2 and surfactant-brine, and a smaller section of core was used as a foam generator in which to mix the fluids. In this case, though, a commercial high-pressure back-pressure regulator (TEMCO BPR-50) was used to maintain the system pressure and to regulate the output fluids uniformly. The arrangement of experimental apparatus used in the Series B experiments is shown in Fig. 8. Two sets of steady-state experiments were conducted, investigating the effects of several parameters including rock permeability, flow rate, foam quality, surfactant type, and surfactant concentration. In the first set of experiments, a constant CO_2-to-surfactant solution flow rate ratio of 4:1 (foam quality of 80%) was used. In the second set, the ratio was broadened so that a wider range of foam quality (from 50% to 98.5%) was examined.

The results of this first set of experiments are described[25] completely elsewhere. Two major conclusions are presented here. First, it is clear from these tests that varying degrees of SMR were consistently observed in Berea rock, with CD1045, CD1050 and Enordet X2001. SMR was not found, however, with another, Chaser™CD1040. Because these experiments were purposely performed with larger core samples, using a back-pressure regulator for pressure control at the downstream end of the core, it was possible to make meaningful measurements prior to attainment of steady state, and to dispel any idea that the SMR observed in the Series A experiments might be an artifact of the small size of the core or the manner in which the experiments were conducted. By varying the flow ratio, we were also able to run tests over a much wider range of quality than has previously been performed.

Secondly, these tests provided an opportunity to explore and resolve an apparent difference between experiments carried out at PRRC and foam experiments conducted at the University of California at Berkeley.[9] In that work, not only was the quality of the foam higher — generally above 90% — but the flow of CO_2 or other gases and that of the aqueous liquid were regulated and varied separately. Thus the pressure drops across the core sample were measured predominately as a function of the flow rate of one of the components, while the flow of the other fluid was held constant. Under these circumstances, described in a recent paper by Kovscek *et al.*,[9] the measured pressure drops seemed mostly dependent on the liquid flow rate. At constant gas flow rates, the pressure increased almost linearly as the flow of liquid was increased. On the other hand, at constant liquid flow rates, the pressure increased only slightly with increasing gas flow rate. In Kovscek's tests, although the same pressure drop and flow data were taken, measurement of foam mobility was not the primary emphasis, and it was in fact not calculated.

When we employed procedures like those described by Kovscek *et al.*,[9] our results in a high

quality region were generally quite similar to theirs. Similar curves of pressure drop versus increasing CO_2 and surfactant rates, along with the foam mobility results in these series B tests, proved that the SMR as observed in series A is valid. Concerns about the influence of the small core size or the manner in which the experiments were conducted in Series A test proved unnecessary.

Capillary Contact Experiments

In earlier experiments, the occurrence of SMR with some surfactants was observed in individual cores of relatively uniform permeabilities. For verification of SMR in a heterogeneous media where both high and low permeability regions are present and in capillary contact, as they are in different portions of a heterogeneous reservoir, core systems containing well-defined high and low permeability regions must be used. The composite core samples discussed in the following sections provide artificial heterogeneity in a system in which the permeability varies spatially—either parallel or perpendicular to the flow path. Using such a flow system, we measured the ratio of mobilities of foams between the two sections as if they were flowing in different portions of a heterogeneous reservoir. The results from these tests provided experimental confirmation of the major conjecture upon which the reservoir use of foam is based—the idea that the favorable mobility variation seen in isolated homogeneous cores occurs also in the reservoir, in different sections of a naturally heterogeneous reservoir rock. Two types of such flow systems—series and parallel—were constructed and used.

The first type of two-region experiments consisted of composite core with two short pieces of core samples (each measuring 3 in. long and 0.5 in. in diameter) that were stacked together in capillary contact and arranged in series along the flow direction. The second type of two-region experiments consisted of composite core with varying permeabilities in regions parallel to the flow direction. A 1.5 in. diameter Berea core had an axially located 0.5 in. hole filled with fine unconsolidated sand. The steady-state pressure drop along the two sections was the same since they were parallel, and, again, the mobilities were measured by observing separate flow rates from the two regions.

Series Flow System

The series assembly used two cores of 0.5 in. diameter, each approximately three in. long. The coreholder that contained them was fitted with five equally-spaced pressure taps, arranged so that the middle tap was near the junction between the cores. The two abutting end-faces of the cores were carefully cut perpendicular to their axes and were ground flat prior to mounting them end-to-end. In such an assembly, the unavoidable space between the two core faces was filled with a fine sand and five pressure taps were mounted along the coreholder, defining four segments of the composite rock. The experiment yielded records of four pressure differences between each pair of successive pressure taps. A sketch of such a composite core is presented in Fig. 9.

A schematic of the high-pressure mobility measurement system is also presented in Fig. 9. In this flow system, the fluids flowing into the foam generator and the composite core are injected by two pumps (a RUSKA positive displacement pump for the CO_2 and an ISCO piston pump for brine or surfactant solution). Near-constant system pressure is maintained by leading the output fluids into a backwards-running ISCO pump, which takes in the output at the total rates of the other two pumps. When the experimental conditions reach steady state, pressure drops in each segment of core are recorded as a function of time. The mobility of injected fluid, defined as the ratio of Darcy or superficial velocity of the fluid to the average pressure gradient along each segment of core, is calculated and compared for different injection schemes.

As a standard procedure, the foam generator and core sample were first preflushed with synthetic brine for at least 50 pore volumes before starting the brine permeability measurements. The heterogeneity of the series composite core was determined by measuring the brine permeabilities for four different sections along the core. Following the permeability measurements, dense CO_2 and brine were simultaneously injected into the core sample. The mobility of this two-phase mixture was measured for each core section and used as a reference for later comparison. After the baseline was established, a sequence of foam experiments was started by displacing 50 pore volumes of surfactant solution to satisfy the adsorption requirement, then coinjecting CO_2 and surfactant solution into the core until steady state was reached. Foam mobility was measured and the core was then postflused with another 50 pore volumes of brine. During the coinjection of CO_2 and brine or CO_2 and surfactant solution, the ratio of the volumetric flow rate of CO_2 to aqueous phase was maintained at 4:1. The total injection rate, however, was varied from 5.0 cc/hr to 15 cc/hr, which corresponded to Darcy velocities of 3.1 ft/day to 9.4 ft/day.

All the mobility measurements were conducted at 77°F and 2000 psig. The two composite cores used in the experiments had permeabilities ranging from 525 md to 128 md (composite core #1) and 819 md to 106 md (composite core #2). During the foam experiments, 0.1 wt% surfactant solutions were used in the core #1 experiments while 0.05 wt% surfactant solutions were used in the core #2 experiments.

Results and Discussion

Surfactants used in foam mobility tests are described in Table 2. Detailed mobility data and sequence of experiments are summarized in Tables 3 and 4; however, the mobility data of the last section of core in all the foam experiments are not available. The missing data are due to the limited range of the fourth differential pressure transducer. When the mobility data in the first three sections are compared, it is clear that the mobility of CO_2/brine is effectively reduced by adding surfactant. The foam mobilities are significantly lower than the total mobility of CO_2/brine. The extent of this mobility reduction varies with surfactant, surfactant concentration, and flow condition. In general, the mobility of foam is lower when foam is generated at a higher surfactant concentration or when foam is displaced at a lower injection rate.

When mobility dependence on rock permeability is examined, SMR is also found to depend on the surfactant type, concentration and flow rate. Typical results of mobility dependence on rock

permeability of a series composite core are presented in Fig. 10. On this log-log scale plot, the mobility of CO_2/brine or CO_2-foam is plotted against the sectional permeability. Also included in this plot are values determined by regression based on each set of data points. The numerical value, representing the slope of each line of each set of data, is used to indicate how favorable the mobility dependence of fluid is to the permeability of porous media. A slope of one indicates that the mobility of the fluid is proportional to the rock permeability (as described in Darcy's law). A value of less than one shows a favorable dependence of selective mobility reduction that will lead to a more uniform displacement front when the fluid is flowing through heterogeneous porous media. It is observed that the slope of CO_2/brine data is greater than one, indicating that unfavorable mobility dependence occurs when CO_2 and brine are flowing in a heterogeneous porous media. Nevertheless, the results in the same graph also show that using foam can correct such a problem by not only reducing the mobility of CO_2 but also changing the mobility dependence in a favorable direction (*i.e.*, when surfactant is added to the brine and generates the foam, the slope of foam mobility versus rock permeability data becomes less than that of CO_2/brine, and preferably less than one).

The extent of SMR depends on the type of surfactant. As shown in Table 5 and Fig. 10, the slopes of seven surfactants at a 0.1 wt% concentration vary considerably. Also shown in Table 5 are similar results, presented in Fig. 11 as well, where the slope values of seven surfactants at a lower concentration (0.05 wt%) vary from 1.09 to 0.55. Other relevant data are summarized in Table 5 in which the slope values are found to depend on the surfactant, concentration and flow rate condition. In general, the value of the slope decreases when surfactant is added into brine as a foaming agent. This suggests that foam is useful in correcting the nonuniform flow of CO_2 and brine in a porous system consisting of differing permeabilities. At lower velocities, the value of the slope becomes smaller, indicating that more favorable SMR occurs at a lower displacement rate. This characteristic would be beneficial for foam application in the field, especially assuming that radial flow applies in the reservoir. In that case, the desired SMR will become more evident as foam travels away from the injection wellbore, where the flow velocity of foam becomes slower.

Parallel Flow System

The parallel system involves cores in which high and low permeabilities are parallel to the flow direction. Early in our work, we designed a test in which a core would be cut from rock containing two regions, in such a way that the plane separating the regions included the diameter of the core. End-to-end flows through the two sections would be kept separate, in order to measure the two mobilities. Our search for samples from which such parallel heterogeneity cores can be cut has not produced any candidate cores from reservoirs. Alternatively, we constructed composite cores with two coaxial porous systems in different permeabilities. Figure 12 shows a schematic diagram of the axial sectional area of a composite core of two regions of permeabilities. The composite core, 1.40 in. (3.56 cm) in diameter, consists of a fired Berea core with a 0.625 in. (1.59 cm) central hole drilled from end to end. This central region is filled with relatively uniform (either sieved or elutriated) silica sand particles. Two series of tests were conducted in two different composite cores

that had permeabilities of 0.5 darcy and 5.2 darcy in the central sandpacks and permeabilities of 1.40 darcy and 1.37 darcy in the annular Berea core regions. These were designated as Core I and Core II, respectively.

Fluid inputs of aqueous brine and high-pressure CO_2 entered these parallel core systems from floating-piston cylinders, driven by distilled water from positive displacement injection pumps (see Fig.13 for system schematic). The input faces of the parallel composite cores were exposed to incoming flow that consisted of CO_2 alone, brine alone, CO_2/brine mixture without surfactant, or a foam mixture of CO_2 with a brine containing either 500 ppm or 2500 ppm of one of three surfactants (CD1045, CD1050, and Enordet X2001). The output flows from the two regions were separated by a circular barrier of the same diameter as the central zone of the composite. Each of the two output regions had their own exit plumbing, each leading into a TEMCO BPR-50 back pressure regulator (BPR) in which the dome pressure was maintained at 2100 psi. The two low-pressure liquid outputs from the BPRs (brine or surfactant-brine) flowed into receiving flasks placed on digital scales, while the two outputs of atmospheric pressure CO_2 flowed through a wet-test meter and a dry-gas volumeter.

A series of steady-state flow tests were performed on these composite cores to measure overall permeability to brine alone, total mobility during simultaneous flow of CO_2 and brine mixtures, and mobility of CO_2-foam. In all the tests, the mobility λ, was defined in terms of the measured flow rate Q, the pressure drop Δp, the length L, and cross-sectional area A as follows:

$$\lambda = \frac{QL}{A\Delta p} \tag{1}$$

In cases where no surfactant was used, this value was equal to the ratio of permeability to viscosity, or for different phases, the sum of the ratios of effective permeabilities to the viscosities of the corresponding fluids. For foam, where it is difficult to agree on the definition of viscosity, we simply calculated mobility from the equation (also directly usable in field calculations), so the results would be easily understood.

Results and Discussion

In parallel flow tests where capillary contact was present between the two permeability regions of the composite cores, the mobility measurements were striking both with and without surfactant in the CO_2/brine flow. During the simultaneous flow of CO_2 and brine with no surfactant, capillary contact caused an equalizing flow of brine from the higher to the lower permeability region; as a result, the high permeability zone water saturation became depleted (richer in CO_2), while the low permeability zone increased in water saturation. Figure 14 shows the flowing behavior of CO_2/brine in the first composite core (Core I). In this plot the total flowing quality of CO_2 in the system rises rapidly and reaches a plateau at 80% gas quality at about three total injection pore volumes. The flowing quality of CO_2 in the high permeability region (central section) increases swiftly and reaches 85% gas quality after about two pore volumes of total injection. However, the

flowing quality of CO_2 in the low permeability region (annulus section) increases slowly and reaches an average gas flowing quality of 60% after about five pore volumes of total injection. The separation of the flowing quality of CO_2 in these two regions increases the mobility ratio in the two zones significantly more than the permeability ratio. Thus, the rate of CO_2 flow through the high permeability region is even greater than might be expected.

A similar but more significant evidence of such behavior is shown in Fig. 15 where the higher permeability region in the second parallel composite core (Core II) is in the annulus section, while the lower permeability region is in the central section. In this case, the brine in the high permeability region (annulus section, having greater cross-sectional area) laterally flows to the lower permeability region (central section). Thus, the central region has a higher water saturation than the annulus of Core (I) with a gas quality less than 60%. As a result, the separation of flowing quality of CO_2 in two regions becomes larger than in the previous examples.

The behavior of such a two-phase flow in a heterogeneous porous system was supported by computational modeling results. The DOE reservoir simulator MASTER,[10] recently modified at the PRRC,[11] was used to verify this experimental observation. By using hypothetical petrophysical data, we simulated the displacement and steady-state flow of CO_2 and surfactant-free brine at the experimental conditions. The computational results qualitatively agree with what has been observed in the laboratory measurements. Figure 16 presents the computational effluent profiles in terms of flowing quality of CO_2 as a function of pore volume of total fluid injected into the Core I system. These effluent profiles are similar to the experimental results. A higher quality of gas is flowing through the center portion of the system (a high permeability region) compared to that flowing through the annular portion (a low permeability region). A lower water saturation region in the higher permeability layer in such a parallel flow system apparently is caused by the redistribution of saturation as a result of capillary equilibrium when two different permeability regions are in capillary contact. As a matter of fact, the average water saturation derived from the model calculation is 0.44 in the high permeability region, whereas the average water saturation in the low permeability region is 0.48. This slight saturation contrast becomes more noticeable in the second parallel system using Core II, where the low permeability region is in the center.

The effluent profiles for the flow of CO_2 and surfactant-free brine in the second parallel core system are presented in Fig. 17. In this plot, the flowing quality of gas in the center portion (low permeability region) is much lower than that in the annulus region (high permeability region). The water saturation in the low permeability region increases to 0.54, whereas saturation in the high permeability region decreases to 0.46. These computational results indicate that the saturation contrasts are a result of the heterogeneity of the porous media. As a consequence, the displacement efficiency in an actual reservoir formation could be less than predicted, where nonuniform displacement can be induced simply by the heterogeneity of the reservoir. Our foam experiments show that foam can be an effective displacement agent to minimize the saturation contrast, and therefore decrease the mobility contrast between different permeability regions.

When surfactant was present in the brine, the qualities of flowing CO_2 in two different permeability regions became more uniform. As shown in Fig. 18, the curves representing the flowing qualities of CO_2 in two sections become closer to each other than those observed without foam (see Fig. 15**)**. This indicates that more CO_2 is diverted into the lower permeability section which in turn results in a higher quality of foam in the low permeability region. A similar trend is also observed when foam flows with higher surfactant concentration (2500 ppm). As shown in Fig. 19, the qualities of flowing CO_2 are also similar to each other in both regions. This suggests that CO_2 flow rates through high permeability sections are substantially reduced when a foaming agent is used.

To further investigate whether SMR exists in parallel composite core systems, we plotted the mobility of displacement fluids as a function of core permeability on a log-log scale. A typical example is presented in Fig. 20 where the mobilities of CO_2/brine and CO_2-foam are plotted as functions of permeabilities in the regions of the two composite core samples. Since these core systems are not like the separate core samples tested before, the fluids behave slightly differently when they flow through different permeability regions that are in capillary contact. The mobility curves of CO_2/brine and CO_2-foam increase with increasing permeability in both composite cores. However, the mobility value of CO_2/brine in the high permeability region of Core II is much higher than that in the low permeability region of Core I when both permeabilities are at a comparable level (1.3 d). This difference becomes greater with increasing flow rate. When the surfactant is present in the brine and foam is formed, the separation of mobilities between the two regions of each composite core system is reduced. The decrease of separation demonstrates the effect of using foam to minimize the total mobility contrast between different permeability zones. Moreover, the mobility data in the same graph show a favorable dependence on the rock permeability when foam is present in the composite cores. A line drawn through the data points with the presence of surfactant has a slope much less than that in the cases where CO_2 and brine flow together. As described earlier, the slope of this line can be used to indicate the extent of SMR, or how favorable the mobility dependence on permeability is in the displacement process. In some cases, we found that the SMR behavior was more evident when the surfactant concentration and the flow rate were low.[8] But at all tested flow rates (Darcy flow velocities varied from 0.44 ft/day to 8.7 ft/day), SMR existed in the parallel composite core systems when surfactants were present in the aqueous phase.

Modeling Work to Assess the Usefulness of SMR

Our laboratory measurements identified several surfactants that generate foam exhibiting SMR at reservoir conditions. SMR offers the promise of reducing the variability of flow rates as gas flows through a reservoir with large permeability contrasts between layers. Presumably, CO_2-foam systems could reduce the effect of both vertical and horizontal rock heterogeneity, and as a consequence, delay the breakthrough of CO_2 and lead to a higher displacement efficiency throughout heterogeneous reservoirs. In order to assess the efficiency of SMR for CO_2 injection, we adopted the calculation technique described by Lake[12] and extended it to analyze the features of SMR for displacement through parallel layers of a formation.

Other assumptions considered in this modeling were: 1) one-dimensional displacement takes place in a parallel layered reservoir; 2) no communication occurs in the vertical flow direction; 3) the displacement of oil by the displacing fluid is piston-like and the dissipative effects of dispersion and diffusion are ignored; 4) the mobility of the displacing fluid depends on the permeability. Based on these assumptions, equations were derived to calculate successive displacing front positions in each layer, and subsequently to estimate oil recovery as a function of time and injected fluid volume. The equations and details of their derivation are described by Tsau.[6]

As we demonstrated earlier in the experimental results, SMR can be represented by the slope of the line that, on a log-log graph, shows the variation of mobility with permeability. We can take the mobility of foam as proportional to the permeability raised to a specific exponent—the slope of that line—and use it in the numerical calculation. If a foam showed no SMR, and acted like an ordinary fluid, this exponent would be one. If the SMR were perfect (so that there was no variation of mobility with permeability) the exponent would be zero. Systems have been found in which the mobility actually decreases over a permeability range at higher permeabilities.[1-3,5] Over the range where that extreme case is observed, the SMR exponent would be negative. For our purpose here, the exponent considered in the modeling lies between zero and one. In order to cover a greater range, in the event more extensive data were available, a database could be implemented to examine the variation of mobility with permeability in the modeling.

To demonstrate the effect of SMR on oil recovery, we considered a hypothetical five-layer horizontal reservoir in which each layer has the same porosity, thickness, and oil saturation. The permeability, however, varies in decreasing order from 500 md in the top layer to 300 md, 100 md, and 50 md in the middle layers, and 20 md in the bottom layer. The mobility dependence of displacing fluid on permeability, as represented by the SMR exponent, varies from 1.0 to 0.1. Four types of displacement fluid with different characteristics are presented in Fig. 21. The ordinary fluid shown on this graph is simulated to be like the CO_2/brine mixture. The fluid with SMR exponent of one is simulated to be like an ordinary mobility reducing agent. Two other fluids with differing SMR values are simulated to be SMR enhanced foams. The one with the exponent of 0.75 represents foam with mild SMR. The other with the exponent of 0.1 represents foam with more favorable SMR.

The oil recovery efficiency resulting from displacement of these fluids is presented as a function of pore volumes of injected fluid in Fig. 22. In this reservoir model, arrow symbols indicate the breakthrough time for all cases at the fastest layer. It is clear that the breakthrough time of the displacing fluid at the fastest layer is delayed and the vertical sweep efficiency of the model is improved if the mobility of the injected fluid is reduced. At one pore volume of injected fluid (Fig. 22), the oil recovery of the ordinary displacing fluid is about 63%. The recovery is increased to 72% when the mobility of displacing fluid is reduced, but shows no SMR (exponent of 1.0). The oil recovery is improved further to 78% when a mild SMR fluid (exponent of 0.75) is used, and to 96% when a nearly complete SMR fluid (exponent of 0.1) is applied as a displacing agent. The benefit of using SMR-enhanced foam becomes more obvious when considering the pore volume of fluid required to achieve the same degree of recovery. Figure 22, for example, shows that the pore volume

of fluid required to achieve 90% oil recovery can be reduced from 3.0 PV (no foam) to 2.3 PV (foam without SMR), to 1.6 PV (SMR foam with exponent of 0.75), or to 0.9 PV (SMR foam with exponent of 0.1). The modeling results suggest that the occurrence of SMR in the displacing fluid can cause substantial increases in the rate at which oil is swept from reservoirs by a miscible phase like CO_2. The value of the increase depends on the amplitude of the SMR and on the extent of the permeability contrasts encountered in the reservoir.

Because the model described here does not account for several features of an actual CO_2-foam flooding process, the number presented above are primarily used to show the order of magnitude of the effect of SMR on the oil recovery. In an actual reservoir in which shape, well placement, horizontal and vertical permeability variations, and fluid properties must be accounted for, a much more detailed and sophisticated reservoir simulation must be used. A correlation that accounts for the effects of CO_2-foam with SMR in the simulators would provide variable mobility for the foam phase, in which foam mobility is determined in each CO_2-foam containing cell as a simple power of the cell permeability. As more experimental results become available, this correlation could be improved as suggested above. We will endeavor to develop such a modification in simulators that will be used in CO_2 flood prediction, so that operators can assess the value of SMR foam in their own application.

Foam Durability Test

Because of the great potential of using foam to improve oil recovery in CO_2 floods, the need to identify surfactants that induce SMR is important to the success of foam application. As tremendous amount of surfactants are available commercially, it is indispensable to find a feasible means to identify surfactants as good foamers. In the course of our CO_2 foam study, a high pressure foam durability test apparatus was constructed[1] and screening tests were successfully conducted to select surfactants for field foam application.[2] These tests determined the foaming ability of each surfactant, exhibited the stability of the foam, and provided other valuable information of surfactant properties, such as the interfacial tension (IFT) between a surfactant and dense CO_2, and the critical micelle concentration of a surfactant. By assessing some of the properties of surfactants and foams with the test apparatus, as well as analyzing data obtained from the core flooding experiments, we were able to establish possible correlation among data to be used for future surfactant screening study.

A schematic of the foam durability test apparatus is shown in Fig. 23. This foam-durability apparatus consists of a CO_2 source tank, a visual cell made out of a transparent sapphire tube, a buffer solution cylinder, and a Ruska pump. The major part of this system, the CO_2 tank and the sapphire tube high pressure cell, is contained in a temperature-controlled water bath. The buffer solution cylinder and the Ruska pump are installed outside the water bath, and their temperatures are maintained at the same temperature as the water bath through another temperature control system.

First, the sapphire visual cell is filled with the solution to be tested. Once the system is brought to the desired pressure by means of the Ruska pump, the dense CO_2 is introduced through a needle at the lower end of the cell. The CO_2 is drawn upward inside the cell when the Ruska pump

is running backwards. Because of the density difference between dense CO_2 and tested solution, CO_2 bubbles are formed and collected at the upper end of the cell. Depending on the effectiveness of the surfactant, these bubbles will then either form a layer of foam-like dispersion at the top of the sapphire tube or coalesce into a clear layer of dense CO_2. After a standard volume of CO_2 (1.75 cc) has been introduced into the sapphire tube, the pump is stopped and the duration of formed foam is measured.

Seven surfactants used in foam mobility tests were tested with this apparatus. Different batches of surfactant solution (each at 1 wt% active component) were prepared by dissolving the surfactant as received from the suppliers into a brine system consisting of 5.6 wt% NaCl and 1.4 wt% $CaCl_2$. Different concentrations of the surfactant solution were subsequently prepared by diluting the batch solution with the 7 wt% brine. All screening tests were conducted at 77 °F and 2000 psig.

By measuring the time needed to form a bubble at the needle in the sapphire tube and the number of bubbles formed within a certain period of time, the average volume and radius of each bubble were calculated. Once the average radius of dense CO_2 bubble was known, the interfacial tension between surfactant solution and dense CO_2 was calculated, provided that the radius of the needle from which the bubble emerged, the density of the surfactant solution and the density of the CO_2 were known. Examples of how the IFTs were calculated were published previously. [1]

Results and Discussion

The results of calculated IFTs are plotted as a function of surfactant concentration and presented in Fig. 24. On this graph, the IFT decreases with the surfactant concentration and levels off at a region where the IFT no longer decreases as the surfactant concentration increases. This concentration, at which the interfacial properties between surfactant and CO_2 show no significant change, is called the critical micelle concentration (CMC) and can be graphically determined (as indicated by the arrow bar). It is apparent that the IFT curves and CMC values vary with surfactant formula. The CMC values for surfactants are: Alipa^{R} CD128, 0.04; Chaser^{TM} CD1040, 0.06; Chaser^{TM} CD1045, 0.07; Chaser^{TM} CD1050, 0.07; Witcolate^{TM} 1259, 0.15; Witcolate^{TM} 1276, 0.01, Dowfax^{TM} 8390, 0.35.

Other results obtained with the foam durability apparatus were the foaming ability of surfactant and durability of foam at high pressure conditions. The foaming ability of a surfactant is defined as the ease with which a bubble is formed at the needle when the surfactant solution is initially contacted with the CO_2. The durability of foam is defined as the subsequent persistence of the foam bubbles after a standard volume of CO_2 has been introduced. A cathetometer is used to measure the foam height and the height of the CO_2 so that the percentage of foam inside the sapphire tube can be calculated and the persistence of foam can be assessed.

For the same surfactant, it was found that the foam formed more easily as the surfactant concentration increased. In other words, the foaming ability of surfactant increased as the interfacial tension between CO_2 and surfactant solution decreased. Furthermore, the longest-lasting foams were

not necessarily found at the best foaming conditions. The typical results of static decay of the CO_2-foam using surfactant CD1050 are presented in Fig. 25. This graph shows that there is an optimum concentration (in this case, 0.075 wt%) at which the foam has the best stability or the longest durability. The persistence of foam decreases at concentration either above or below this optimum concentration. This trend was observed with surfactant CD128, with an optimum concentration of 0.05 wt% (see Fig. 26**)**. In both cases, the optimum concentration was close to the surfactant's CMC (*i.e.*, 0.07 and 0.04 wt% for CD1050 and CD128, respectively). The bubbles formed by surfactants Dowfax 8390, Witcolate 1259, and CD1040 coalesced in less than a minute, whereas most of the bubbles formed by surfactant CD1045 and Witcolate™ 1276 lasted longer than 90 minutes. Therefore, the optimum concentration to generate the longest-lasting foams were not identified for surfactant Dowfax™ 8390, Chaser™ CD1040, Witcolate™ 1259, Witcolate™ 1276, and Chaser™ CD1045. Nevertheless, the effectiveness of surfactant to stabilize the foam was determined by this method. Surfactant Chaser™CD1045 generated the most stable foams, followed by surfactants Witcolate™1276, Chaser™CD1050, Alipa®CD128, Chaser™CD1040, Witcolate™1259, and Dowfax™ 8390.

Correlation of Surfactant and Foam Properties

When results from the foam durability tests are compared with those of the mobility tests, the stability of foam in the bulk phase can be correlated with the resistance factor (R_f) of flowing foam in the porous media. The resistance factor, defined as the ratio of total mobility of CO_2/brine to the foam mobility, increases with the foam life. As foam stability increases, R_f also increases. As shown in Fig. 27, at 0.10 wt% surfactant concentration, a noticeable resistance factor of 6 or more is found in cases where the foam life lasts less than a minute. This suggests that mobility reduction with a less stable foam can be achieved by breaking and reforming mechanisms during the foam flow.[7,13] When foams become more stable, more resistance to flow results in a higher mobility reduction. Based on these observations, it is believed that the effectiveness of foam in reducing the mobility of CO_2 is likely due to the capability of surfactant to stabilize the bubble film or lamellae in the porous media. Furthermore, the R_f also increases as the reduction factor of the interfacial tension (designated as RIFT in Fig. 27) between CO_2/brine and CO_2/surfactant increases. Since the RIFT is favorable for foam generation, more lamellae can be generated in the flow path of porous media that will increase the resistance of flow during the foam displacement.

Other factors that cause a more stable foam to generate (such as higher surfactant concentration and lower displacement rate) also give a more favorable SMR. As indicated in Table 5, the slope values determined by the regression method are smaller (in other words, SMR is more favorable) at a higher concentration of surfactant or at a lower displacement rate. When these slope values (SMR indices) were correlated with RIFT of different surfactants (Fig. 28), we found that SMR value generally decreased with the increase of RIFT value. This indicated that more favorable SMR occurred when the interfacial tension between CO_2 and aqueous phases was reduced more. Based on this correlation and the one shown in Fig. 27, we believe that RIFT can be a useful indicator for screening surfactants in foam application.

Despite our reservations on the cause of SMR, we expect that in most cases the use of a proper CO_2-foam could minimize the mobility contrast between high and low permeability zones in reservoir flow, thus markedly increasing the efficiency of oil displacement. This project, as well as earlier experimental research, makes it clear that the SMR property of CO_2 foam exists, is observed in parallel-core and series-core tests with capillary contact, and can be presumed to function similarly in actual field situations. It should therefore be very useful in oil recovery from reservoirs containing crude oil of suitable composition.

Conclusions

1. After examining the experimental setup for measurement of mobility of two cores in separate coreholders, we found that the position of the cores did not produce a significant effect on the interpretation of SMR in mobility measurements.

2. Measuring CO_2-foam mobility in separate cores showed that selective mobility reduction was affected significantly by the surfactant type and the flow velocity of foam. Rock type and surfactant concentration also affected the SMR of foam, but to a lesser extent.

3. SMR was found to be more favorable in Baker dolomite rocks than in Berea sandstone, when surfactant CD1050 was used as a foamer. When surfactant CD1045 was used as a foamer, however, SMR was found to be more favorable in Berea sandstone than in Baker dolomite rocks.

4. Extensive mobility measurements on larger Berea cores were taken, with results similar to those obtained with smaller cores.

5. Experiments with composite core samples of known heterogeneity were a better alternative to using separate cores to investigate SMR and to examine the effect of heterogeneity on foam flow behavior. Experiments with composite core samples provided information that could not be acquired from separate, individual cores of relatively uniform permeability.

6. SMR, in which the CO_2-foam reduces the mobility to a greater extent in high permeability zones than in low, occurred over a wide range of Darcy flow rates (from 0.44 ft/day to 9.4 ft/day) and permeabilities of core samples (from 30 md to 900 md). In many cases, it was observed that low surfactant concentrations were more effective in causing SMR than high concentrations.

7. SMR was still observed in experiments with parallel or series flow through higher and lower permeability zones of a composite core, in which the zones were in capillary contact.

8. In the same composite core, the presence of surfactant in brine injected with the CO_2 was observed to have a strong beneficial effect on the saturation differences that would otherwise develop. This effect decreased the total mobility contrast between different permeability zones.

9. CO_2-foam floods, augmented by SMR, are promising for improved oil recovery. They cause flow and displacement to be more uniform, thus increasing displacement efficiency.

10. Oil recovery efficiency depends on the extent of SMR and the permeability contrasts that are normally encountered in the reservoir.

11. SMR effect on oil recovery can be demonstrated with a simple simulation scheme that can be incorporated into existing reservoir simulators.

12. The stability of foam in the bulk phase can be correlated with the performance of foam flowing in porous media. When comparing different surfactants, a greater stability of foam gives more mobility reduction in foam displacement.

13. The R_f increases as the RIFT between CO_2 and the aqueous phase increases.

14. An optimum concentration exists at which the stablest foam in the bulk phase is formed. This optimum concentration is close to the CMC of each surfactant solution.

15. Factors that favor reducing the mobility of CO_2/brine also lead to a more favorable SMR when foam flows in a composite core consisting of differing permeabilities.

TASK 2: REDUCTION OF THE AMOUNT OF CO_2 REQUIRED IN CO_2 FLOODING

Introduction

A multitude of successful gas injection projects throughout the world[14] have demonstrated that high pressure CO_2 injected into oil reservoirs improves oil recovery. It was recently stated that "One of the most significant opportunities for expanding CO_2 could be the application of CO_2 flooding in reservoirs in which near miscible conditions exist."[15] There is considerable economic and operational incentive to operate a gas injection project at the lowest possible pressure. Incentives include purchasing smaller gas volumes and decreased gas compression costs. Also, the possibility of operating a gas project below the minimum miscibility pressure (MMP) means the reservoirs that might otherwise be excluded could be considered as candidates for gas injection. Some laboratory tests,[16-19] simulation studies,[20] and field tests [21,22] have indicated that floods at or below the MMP may be as efficient, if not more so, than at pressures well above the MMP. The unit cost of producing oil by CO_2 injection would decrease if the amount of CO_2 required per unit of oil produced is decreased. This can be achieved by decreasing the mass of CO_2 required to fill a unit reservoir volume by reduction in reservoir pressure or by increasing the sweep efficiency of the CO_2. Sweep efficiency can be increased using mobility control agents and/or horizontal wells.

Reduction in Operating Pressure for CO_2 Flooding

At a constant temperature the density of CO_2 decreases with decreasing pressure, thus increasing the reservoir fill volume with the same mass. The slope of density versus pressure (density change) is commonly at the maximum near the MMP. The change of density can be substantial over a few hundred psi[23,24] (see Fig 29). A number of MMPs are also indicated on the appropriate isothermal curve in Fig. 29.[16,25-29] Not taken into account in Fig. 29 is the effect of extracted oil components on the density of CO_2. Figure 30 shows an example of the effect extraction of a small percent of hydrocarbon will have on the density of CO_2.[30] Here, the addition of a small amount of hydrocarbons decreased the pressure required to reach a specified density for the CO_2-rich phase. Thus the MMP shifted from that predicted by a temperature correlation for the MMP of CO_2.[25,31] Figure 31 compares the final results of two slim tube tests series (tests used to determine MMP's) at 100°F and 110°F, respectively. The MMPs differ by over 600 psi, as shown by points S and F in Fig. 29. If the two oils were of similar composition, only a 100 psi shift in pressure due to temperature would have been observed. The prediction of MMP is generally much better when a simple oil composition factor is included in the model.[32-34] When predictive models that consider oil composition are used, the MMP of the two fluids in Fig. 31 are predicted to differ by 700-800 psi, which is much closer to the experimental values.

Another parameter used to predict MMPs that takes into account the composition of each fluid is the Hildebrand solubility parameter,[35] δ, originating from regular solution theory for mixtures of nonpolar liquids such as hydrocarbons. Recently, δ has been described[36] for pure CO_2 and a

number of hydrocarbons. The δ increases with density for both CO_2 and crude oils. Since multi-contact miscibility is closely related to the abundance of oil components soluble in CO_2, δ can be used with some degree of accuracy in determining if miscibility will occur and at what rate. The δ of a crude oil is influenced by composition, molecular weight, and temperature. At a given temperature a good approximation of δi s a linear function of molecular weight or API gravity. For CO_2, density is directly related to pressure and temperature. Thus, while pressure has little effect on the oil δ, pressure has a profound effect on the CO_2 δ. By raising the pressure on a system, δ for CO_2 increases while δ for the oil remains essentially constant. Thus the MMP is related to the point where the CO_2 δ and the oil δ are close enough to develop miscibility. As the CO_2 δ increases, more hydrocarbon components are evaporated into the CO_2-rich phase, thus raising the CO_2-rich phase δ.

A final quantity that can be used to understand the development of miscibility and more importantly, fluid displacement, is interfacial tension (IFT). This is a major focus of Task 3, but here it suffices to say that (theoretically) good displacement can occur before complete miscibility, as the IFT is lowered sufficiently to overcome capillary forces.[37,38]

Capillary forces imply that a porous structure is involved. A complete understanding of miscibility development must include the incorporation of each of the above concepts in a porous medium. Slim tube studies are the simplest porous medium configuration, and have been an industry standard for determining MMP for a number of years.[39] Slim tube[26,40] and micromodel studies[27] have demonstrated that on a microscopic scale the most efficient recovery conditions (mass of oil produced per mass of CO_2 injected) are reservoir pressures at or just below the MMP. Slim tube and micromodel systems are more homogeneous than reservoir rock, do not contain water saturation, and are composed of glass or unconsolidated sand. Tests or simulations using reservoir rock[16-22] do not necessarily duplicate the results of slim tube and micromodel tests. At least some rock studies indicate that the MMP is not a magic value and at times there is very little difference below and above the MMP in oil recovery. As an example, Shyeh-Yung[16] saw very little difference when comparing recovery in a core test at pressures below and above the MMP. In a more recent study Grigg *et al.* [28] observed the opposite behavior. Some of the results from these two studies are compared in Fig. 32. The reduction in recovery below the MMP was as dramatic in core floods as it was in slim tube tests in Grigg's study[28] while Shyeh-Yung[16] observed only a gradual change. The second study[28] indicated that dropping below the MMP can be as critical in a reservoir—if not more so— as it is in a simple series of slim tube tests. The differences between these results have several possible explanations that include (though these are not all-inclusive) the following: reservoir fluid, rock type, experimental procedure, and data interpretation. Thus, it requires additional examination to answer the question of how low the pressure can be relative to the MMP with no loss in the efficiency of CO_2 .

The phase behavior experiments described in Task 2 helped explain a number of concepts in increasing CO_2 efficiency. The slim tube tests identify the approximate MMP. The compositional, density and viscosity information obtained from Continuous Phase Equilibrium (CPE) tests are used in determining reservoir condition IFT and δ, and provide required CO_2 flood input data for reservoir simulation. Pressure-volume-temperature (PVT) and swelling test data are required for reservoir simulation and should be valuable in IFT and δ developments.

Improvement in Mobility Control

The specific property of SMR in CO_2-foams was studied in Task 1. In Task 2, CO_2-foam was also considered, but as a general mobility reduction agent for CO_2. This is especially critical in regions where the microscopic displacement of oil by CO_2 is sufficient, but due to viscosity and/or density differences of the oil and CO_2-rich phases, the macroscopic displacement is adversely affected. In one visual micromodel study (Fig. 33), we showed that as the pressure is reduced below the MMP, recovery with foam in the system is much better than without foam.[27] Because of favorable laboratory tests[3,27,41] and a successful CO_2-foam field pilot test,[42,43] considerable effort has been expended in developing CO_2-foam models that can be used in reservoir simulation. Many core tests have been performed to delineate the parameters required in reservoir foam predictions. These tests include foam quality (volume percent of gas injected), flow rates, and surfactant concentration. The foam model has been tested in two reservoir simulators: MASTER (Miscible Applied Simulation Techniques for Energy Recovery), a multi-component pseudo-miscible reservoir simulator obtained from the Department of Energy and UTCOMP, provided by the University of Texas at Austin.

Horizontal wells, properly placed, can be used to inject and produce fluids with increased sweep efficiency. In the first annual report on this project,[40] a horizontal well subroutine was described. This has been tested further and is in place so we can compare results using foam and other methods of improved sweep efficiency in reservoir models.

This report describes details on phase behavior, slim tube, coreflood tests and reservoir models that have been developed and tested. Each test has been designed to improve our understanding of CO_2 flood processes and is intended to improve the efficiency of CO_2 flooding.

Experiments—Phase Behavior

A number of tests can be performed, each helping to explain displacement mechanisms. Several of these tests have been performed during this project. We ran a number of tests on an oil from a Spraberry reservoir. This reservoir is of interest both as a candidate for CO_2 flooding and as a fractured reservoir. This oil was also selected because its reservoir temperature of 138°F is too high (above 120°F) to allow three hydrocarbon-CO_2 phases at high CO_2 concentrations. Other oils that were tested because of previous work carried out in this laboratory were Maljamar,[44] Wasson,[45] and Sulimar Queen.[46]

The tests described here can be used for a number of purposes. These include understanding flooding mechanisms, pressure effects, and mobility control. The results can also be used to tune equations of state that are then used to predict results as the systems change due to dynamic compositional changes occurring in real systems. These results are then used to model and understand behavior on a reservoir scale.

Conventional PVT Study

Several types of phase behavior tests are used to develop our understanding of fluids in a reservoir. The first is the conventional pressure-volume-temperature (PVT) study. This is a standard test on a reservoir fluid at reservoir conditions. A separator oil or a weathered oil sample is recombined with solution gas to reproduce the original or present oil reservoir composition. Standard tests (formation volume, viscosity, compressibility, compositional) are performed to define standard reservoir fluid and produced fluid parameters. These parameters are required for reservoir simulation and as a base for understanding all phase behavior and fluid simulations. A conventional PVT was performed on Sulimar Queen oil and has been reported in a previously published study.[46]

Slim Tube Tests

The MMP of a solvent/oil mixture is usually determined experimentally from displacement tests using a slim tube apparatus. This experiment attempts to isolate the effect of phase behavior on displacement efficiency in a flow setting that minimizes the effect of viscous instability inherent in the displacement of oil by low viscosity CO_2. The center piece of the apparatus is a high pressure, sand-packed, coiled tube with an internal diameter (ID) of 0.25 to 0.50 in. and a length of 30 to 140 ft.[47,48] The tube is saturated with an oil at the desired temperature and pressure. Then, the solvent is injected to displace the oil at a rate ranging from 2 to 40 ft/hr. The MMP is determined from the displacement recovery vs. pressure profile.

A variety of MMP criteria by which the MMP can be determined from displacement tests data have been proposed in the literature. The MMP criteria are usually based on the measurement of the fraction of oil recovered in slim tube displacement at a given pressure, and rarely based on the analysis of phase diagrams. Many authors have define the MMP as the pressure at which a certain recovery value (80-100%) is achieved after 1.2 pore volume of CO_2 has been injected.[8,33-35] Instead of using a certain recovery value as a criterion, Johnson and Pollin[49] use a sharp break point in the slope of the recovery vs. pressure curve as the MMP criteria. Despite the enormous amount of work in this area and the similarities among the described MMP criteria, there is no standard method or unique criterion for the determination of the MMP. Nevertheless, slim tube tests are used as the standard tool in most displacement studies. With some slight modifications a slim tube apparatus may also be used to study the phase behavior of the transition zone of the displacement process.[50]

The slim tube tests performed in this project used tubes 40 ft long with a 0.25 in. inside diameter (ID) and a pore volume of 117.9. The indicated test pressure is the pressure at the inlet of each slim tube test. The inlet pressure was controlled by changing the pressure of the back pressure regulator at the outlet side of the slim tube. The injection rate of the CO_2 high-pressure gas was 30 cm^3/hr. Slim tube results were used for comparison with results obtained from the extraction experiments. Four series of slim tube displacement tests were performed to determine the MMP of CO_2 with the oils tested in the extraction experiments. The tests were conducted at the same temperature and pressure ranges as in the extraction experiments.

The setup apparatus had two back pressure regulators (BPRs), one at the outlet of the CO_2 accumulator and the other at the slim tube outlet (see Fig. 34 for the apparatus schematic). Unlike most conventional slim tube experiments, where the displacement pressures refer to the pressure at the slim tube outlet, the displacement pressure in this study refers to the pressure at the slim tube inlet. This procedure is considered more effective since the system pressure inlet is more representative of the pressure at the injection front. This is because the pressure drops between the inlet pressure and the solvent front are considerably less (always less than 5 psi) than those between the solvent front and the slim tube outlet (sometimes more than 100 psi). The displaced fluids were collected and volume, weight and composition were determined for each sample. A wet test meter was used to measure the gas production.

All slim tube tests performed on Spraberry and Sulimar Queen crude oils are not reported in this section. They were done in conjunction with extraction tests that will be discussed in a later section.

Spraberry

Figure 35 shows a series of slim tube test results with percent recovery indicated after 1.187 and 1.527 PV of CO_2 injected into the slim tube in each case. The tests are differentiated by the pressure of each test. These tests were run on Spraberry separator oil at 138°F (reservoir temperature). Note that above 1550 psig, there is little increase in recovery with increasing pressure, especially when comparing tests at 1.187 PV of CO_2 injection, while below 1550 psig there is a significant pressure effect on recovery. Approximately 1550 psig is the MMP. Complete data sets from each run can be obtained from the PRRC upon request.[53] The measured MMP might be lower than the bubblepoint pressure in some parts of the reservoir. The bubblepoint pressure is believed to be as high as 1900 psig in parts of the reservoir. Thus the MMP should be considered to be the higher of either 1550 psig or the bubblepoint pressure. Each test was conducted for 420 minutes with volume of oil produced and grams of CO_2 injected recorded every 20 minutes, and pressure drop across the core every 6 minutes.

MMP tests were performed on Spraberry oil that had been weathered at 138°F because gravity drainage tests were being conducted on this oil and required an estimation of miscibility. Tests were performed at 1700, 1900, and 2000 psig and, as shown in Fig. 36, the systems were not near miscibility. The weathering removed essentially all the components of molecular weight less than decane. The change in MMP due to weathering, calculated using compositional correlations,[32,33] predicted increases from 2050–2175 psig to 4250–4500 psig. These values compares to a measured value of 1550 psig for the unweathered sample at 138°F.[40] Even though the predictions are high by 500–600 psi for the unweathered sample, the predicted values show an approximate effect on the MMP for the weathered sample that was void of all hydrocarbons with molecular weights below decane. These three tests provide information to explain the effect of composition on the development of multi-contact miscibility.

Maljamar

Slim tube tests on Maljamar oil were performed at 1400 and 1600 psig at 140°F. At both pressures, the recovery was lower than for Spraberry oil at similar pressures. The temperature was only two degrees higher. The API gravities of the two oils are quite similar. The big difference was that the Maljamar oil was not a separator oil that had been maintained under pressure; rather, it was a weathered sample from which some of the intermediate components had evaporated. In developing multicontact miscibility, the intermediate components (especially hexanes through decanes) lost due to evaporation upon weathering are critical.

Other slim tube tests[26] and micromodel studies[27] have shown that when plotting recovery versus grams of CO_2 injected or the recovery efficiency (mass of oil produced per mass of CO_2 injected), the combination of high recovery and mass of CO_2 required to produce a given volume of oil is best near the MMP. Figure 37 compares results of Maljamar separator oil displaced by dense CO_2 gas at 90°F for several micromodel tests[27] versus pressure: the most efficient displacement was at 1000 psia, which is essentially the MMP in the system. At higher pressures, the final recovery was about the same, but the mass of CO_2 required to fill the pore volume was greater because of the higher CO_2 density.

Continuous Phase Equilibrium Tests

The PRRC's continuous phase equilibrium (CPE) apparatus was used to obtain compositions, densities, and viscosities for samples of Spraberry and Wasson recombined reservoir oil. In these tests high-pressure CO_2 is injected continuously at a constant flow rate into a constant volume cell filled initially with the selected oil. The pressure in each test is maintained at a constant value. The constant pressure is maintained by controlling the production rate and alternating the production from the top and bottom of the constant volume cell. As fluid is removed alternately from the top and bottom of the cell densities and viscosities are recorded, at pressure and temperature for each stream. The mass and composition of each stream are measured throughout the tests. For additional details of this process, refer to earlier articles.[45,51]

Spraberry

Tests on Spraberry oil were done at 138°F and at 1425, 1850, 2100 and 2450 psig. Pressures from well above the MMP (estimated at 1550 psig) to below the MMP were recorded. Figures 38 and 39 show the results of density and viscosity versus experimental time for both the upper and lower production for two tests. The first few hours of each test comprised injection of reservoir fluid. During this time calibration of the instruments was completed and a steady state was obtained. Upon initiation of CO_2 injection two observations were recorded: the viscosity instantaneously started dropping and the density of the system increased slightly. The viscosity decrease was the most apparent. Another phenomenon easily observed in Figs. 38 and 39 is phase separation when the system becomes saturated with CO_2. Phase separation is sensitive to both the density and viscosity, with each showing significant differences from one phase to another. Density is the more accurate indicator on the time of occurrence for phase separation. This is because the viscosimeter

is extremely sensitive to two-phase flow and to particles such as asphaltenes that might deposit on the quartz crystal. Deposition often occurs near the time of phase split, so erroneous values appear just before and just after phase split in the viscosity readings. These erroneous values are obvious because they are several orders of magnitude off the true values. They are removed before presentation. The density measurements do not cause any significant problems in the readouts near the time of phase split and thus are considered the most accurate indicator of phase split.

Figures 40 and 41 show compositional shifts in the upper and lower phases during CPE tests. In each of these figures, CO_2 is excluded, thus normalizing the hydrocarbon fraction of the oil. In both cases the compositions produced from the bottom of the cell changed much less than those produced from the top of the cell. As expected, the more significant changes occur in the top production after the phase split. The CO_2-rich upper phase had less liquid hydrocarbon dissolved in it than did the lower phase, but we noted that there was still a significant amount of hydrocarbons being extracted by the CO_2-rich phase. Analysis of the amounts of hydrocarbons extracted by the CO_2-rich phase is used to explain the development of miscibility.

Wasson

The PRRC's continuous phase equilibrium (CPE) apparatus was used to obtain composition, density, and viscosity for a west Texas recombined crude oil (Wasson) during the injection of high pressure CO_2, which was continuously injected at constant pressure and flow rate. The system was maintained at constant pressure during CO_2 injection by controlling the production rate. Fluid properties were monitored continuously at outlets at both the top and bottom of the CPE apparatus. Compositions, densities, and viscosities of the produced fluids were determined at system pressure and temperature.

The Wasson tests were run using both pure and impure CO_2 at 105°F and pressure ranging from 1200 to 2500 psig. The MMP of the system is about 1350 psig for pure CO_2. Impurities added to the injection gas were methane, ethane, and propane. The solubility of the injected CO_2 in the oil-rich phase was found to have little dependence on pressure, while the solubility of hydrocarbons in the CO_2-rich phase increased with increasing pressure. Impurities in the injected CO_2 did not significantly affect trends in composition, density, and viscosity of each phase. More detail can be found in paper SPE 28974, "Dynamic Phase Composition, Density, and Viscosity Measurements During CO_2 Displacement of Reservoir Oil."[51] All experimental data is available upon request from the PRRC.[52]

CO_2 Swelling Tests

The swelling tests consisted of injecting an oil into a high pressure windowed cell and incrementally adding CO_2 under reservoir conditions. For each incremental addition of CO_2 the saturation pressure of the system, compressibility above the saturation pressure, and multi-phase volumes below the saturation pressure were determined.

Spraberry

Two sets of Spraberry swelling tests were conducted with oil recombined to two different bubblepoint pressures. CO_2 gas was injected into a PVT cell that contained live Spraberry oil at 138°F. The first live oil was prepared by combining separator gas and oil to approximate a reservoir oil with a bubblepoint pressure of 1900 psig. Figure 42 compares the composition of the separator oil used in the slim tube tests with the live oil used in the swelling tests. Figure 43 is a summary of the constant composition volume expansion tests. Seven tests were done with the added CO_2 content ranging from zero to 73 mole percent. The constant volume contour lines were calculated using the measured phase volumes versus pressure data taken at each CO_2 concentration. Experimental phase volumes, compositions, and densities can be obtained from the PRRC in PRRC Report 95-21.[53]

The Spraberry recombined reservoir oil swelling test was performed with separator oil recombined with separator gas to a reservoir bubblepoint of about 822 psig at reservoir temperature. This was about 1000 psig under the system examined earlier and closer to the present reservoir bubblepoint pressure. A series of pressures taken after each incremental addition of CO_2 with associated system volume, volume relative to the bubblepoint pressure volume, volume relative to the original oil, vapor phase volume below the saturation pressure, and vapor volume as a percent of total volume, are listed in Table 6 . These values were determined for nine incremental additions of CO_2 and the original oil. Figure 44 shows the bubblepoint (0% vapor volume contour) and dew points (100 % vapor volume contour) along the saturation curve. Plotted in Fig. 44 are the constant vapor (CO_2-rich phase) volume % contour curves. The contour curves are an aid in determining the critical point that was found to be 69 mole % CO_2 and 3900 psig. This is within 50 psi of that determined for the higher solution gas Spraberry oil and about 5 mole % more CO_2. The higher CO_2 concentration should not be surprising since the lower solution gas oil would require more CO_2 to reach the same gas-oil ratio.

As expected, the temperature was too high to allow a three-phase region in this system. There is no distinct transitional region as found in the lower temperature systems, where there is a transition between a low density vapor and high density liquid in the upper phase. Figure 45 shows a more gradual change in this system.

At lower CO_2 concentrations the saturation pressure can be determined using a pressure-volume curve. In the cases at 0.0 and 31.3 mole percent CO_2, the saturation or bubblepoint can be determined from the distinct change in slope (compressibility) that occurs in the system when vapor begins to form. At higher CO_2 concentrations, the upper vapor phase has high density and low compressibility. Thus, a pressure-volume curve cannot be used to determine the saturation pressure. In this case the saturation pressure was a dew point, and, as shown in Fig. 46, there is no apparent slope change at a dew point. Between about 1500 and 2500 psig the compressibility of the upper phase goes from being vapor-like to liquid-like. In this system the CO_2 is at temperatures well above the critical temperature, so it is not surprising that the CO_2-rich phase behaves as a supercritical fluid.

A plot of pressure vs the vapor phase as percent of total volume, shown in Fig. 46, is another method of showing a very distinct difference between bubblepoint and dew point behavior. It can

be seen that the composition at 67.7 mole percent CO_2 is nearing the critical point. This type of representation can be used to determine constant volume percent contour lines. Since most of the fluid properties change more gradually in the higher pressure system, an estimate of the MMP is not obvious in high temperature phase diagrams.

Sulimar Queen

A swelling test was performed at 70°F on the Sulimar Queen separator oil. The separator oil was a dead oil, so the oil bubblepoint was atmospheric pressure at 70°F. Test pressures, system volume, volume relative to the bubblepoint pressure volume, volume relative to the original oil, vapor phase volume below the saturation pressure, vapor volume as a percent of total volume, and the volume of the second liquid in and above the three phase region after each incremental addition of CO_2 are shown in Table 8. This was done for nine incremental additions of CO_2. Figure 47 shows the bubblepoint and dew points along the saturation curves. In this system there is a three-phase region that is common in many low temperature (<120°F) reservoir oil/CO_2 systems.[26,54] The upper pressure boundary of the three-phase region in a bubblepoint pressure curve for the upper liquid phase and the lower pressure boundary is a dew point curve for vapor phase. Tthe total system volume can decrease by half under a pressure increase of about 10%, although the lower liquid volume changes very little. The large change in volume (density) is in the upper phase(s) with the solvent properties changing significantly over a small pressure range. Thus, the system at lower pressures goes from a relatively immiscible system to one in which multi-contact miscibility develops quickly. In systems with a three-phase region, it is conservative to call the MMP the maximum pressure of the three-phase region (for Sulimar Queen oil, this is about 850 psig.) In fact, multicontact miscibility can and does occur in the three-phase region, so the lowest pressure for multicontact miscibility would be the lowest pressure where the three-phase region is found. For the Sulimar Queen oil, that is at approximately 780 psig. An expanded view of the three phase region is shown in Fig. 48 and extrapolated above 90% CO_2. Figure 49 examines the two-phase liquid-liquid regions above the three-phase region. The phase volume constant contour lines were used to identify the critical point composition and pressure. In the Sulimar Queen system the critical point on the saturation curve was also the low CO_2 concentration apex for the three-phase region. This information will be used in future tests to calibrate the phase behavior model developed earlier to simulate the phase behavior for this system.

With the information obtained from these two tests, other factors can be determined, such as an estimate of the swelling of the system oil and CO_2 content. For example: if the pressure of the lower GOR Spraberry system is 1835 psig, the maximum solubility of CO_2 in the oil, without going two-phase, is 42.3 mole %. The oil would swell 17.4 %. Compare this to the bubblepoint volume at 822 psig with no added CO_2. Here, the amount of swelling would be 21.2 % over what it would be at zero % CO_2 and 1835 psig. These values can be determined from the relative volumes listed in Tables 6 and 7 and the plots found in Figs. 44 and 47. All this information is used to calibrate the phase behavior model developed earlier to simulate the phase behavior for these system.

Conclusions for Phase Behavior Work

1. The CO_2 MMP with Spraberry separator oil is 1550 psig. This will also be appropriate for Spraberry reservoir oil unless the bubblepoint pressure is above 1550 psig. To prevent the formation of a large immiscible methane bank, gas should be injected above the bubblepoint pressure.
2. It is critical to prevent weathering before tests such as MMP determinations.
3. A detailed Px phase diagram was completed for the CO_2-Spraberry recombined reservoir (live) crude system. This system has a saturation curve that includes bubblepoint pressure, dew point pressures, and estimated critical point. Also shown are the constant volume contour lines estimated from measured phase volume data.
4. Continuous-phase equilibrium tests on Wasson oil with both pure and impure CO_2 and below and above the MMP using recombined reservoir crude found pressure affected the solubility of oil in CO_2 much more than CO_2 in oil.
5. The PVT study on a low temperature medium grade oil has been completed.
6. Several types of CO_2- phase behavior studies have been completed for two oils: one at a low reservoir temperature (70°F) and one at a moderate reservoir temperature (138°F.). Two continuous equilibrium tests, two swelling-phase behavior tests, and three slim tube tests were completed.
7. Results are used to analyze the effects of pressure, temperature, and oil composition on the fluid behavior under reservoir conditions during gas injection.

Experiments—Extraction and Slim Tube Tests

Introduction

Extraction of hydrocarbons by CO_2 is the principal mechanism in the development of mult-contact miscibility. Laboratory tests indicated production approaching 50% could be achieved by extraction (see the low permeability reservoir core tested in Task 3).[55] Thus, the question arises of whether production in the field could result from extraction of hydrocarbons. A number of experimental studies in the literature concern the capacity of CO_2 to extract hydrocarbons from crude oils.[32,33,51,56-59] Each researcher worked with different experimental methods, variables and parameters of interest, and CO_2-oil systems. We have investigated the extraction behavior of CO_2 using a semi-batch extraction system in which CO_2 was continuously bubbled through a vessel of oil while the upper phase of the CO_2-oil mixture was continuously produced. The objective was to determine how pressure, temperature and oil composition affect the CO_2 extraction capacity. In addition, a series of slim tube displacement tests were performed to compare with results obtained from the extraction experiments.

The phase relationship of a wide variety of simple systems containing carbon dioxide and hydrocarbons have been investigated and reported.[60-65] The phase behavior of a complex CO_2-hydrocarbon mixtures was examined by Menzie.[56] He charged a constant temperature windowed

cell with an oil sample and injected high-pressure CO_2, then agitated the cell until equilibrium was reached. The vapor phase was removed and condensed in a separator at atmospheric pressure. The remaining oil in the cell was recharged with CO_2 and then the cell was agitated until a new equilibrium was reached. The vapor phase was then again removed and condensed. After repeating this procedure five times, Menzie found the multiple contact process could recover about half the original oil charged into the cell. Alsinbili[57] investigated the effect of oil gravity and injection pressure on oil recovery by CO_2 injection and found the recovery increased with increasing oil gravity and with higher the pressure.

Several authors have measured the phase behavior and fluid properties of CO_2-oil mixtures in conjunction with their work in equation of state tuning,[66-68] for simulation work[34,51,58,69,70] or with displacement tests.[26,71,72] Their experiments were performed to explain and predict the behavior of test systems. Other authors have measured the phase behavior and fluid properties of other CO_2-oil mixtures to describe the behavior of CO_2-oil mixture[73,74] or to develop correlations predicting the performance of CO_2 displacements.[33,59] The phase behavior and fluid properties were measured using either a standard PVT apparatus or a continuous multicontact equilibrium apparatus. The PVT tests were performed as single contact or multicontact tests similar to those performed by Menzie.[56]

Carbon dioxide is not first-contact miscible with most reservoir fluids at reservoir conditions. However, it is multicontact-miscible with reservoir fluids at attainable pressures in many reservoirs. Generally, investigators agree that the development of CO_2/oil miscibility is the result of extraction of some hydrocarbons from the oil by dense CO_2. Hutchinson and Brown[75] and Rathmel *et al*.[76] argued that CO_2 can extract hydrocarbons present in the oil and generate composition paths that avoid two-phase regions in displacements with ternary systems. Gardner *et al.*,[58] Orr *et al.,*[44] and Sigmund *et al.*[77] used such mechanisms to quantitatively predict oil recovery for CO_2-crude oil displacement in slim tubes. Holm and Josendal[32] believed that extraction and dispersion mechanisms take place along a miscible displacement path. During flooding CO_2 extracts a fraction of hydrocarbons from the reservoir oils. After multiple contacts, the displacement front has vaporized enough hydrocarbons to develop a composition that is miscible with the oil. At this point the extraction process stops until the developed miscible front breaks down by the dispersion mechanisms. When miscibility is lost, the extraction mechanism again occurs to reestablish miscibility. Thus, the miscible bank is formed, dispersed and reformed throughout the displacement path. Bahralolom and Orr[78] conducted a series of flow visualization experiments of CO_2 miscible displacement and found that the efficiency of the displacements is more sensitive to the efficiency of extraction of hydrocarbons by CO_2-rich phase than it is to the solubility of CO_2 in the crude oil.

In summary, considerable research on understanding the development of CO_2/oil miscibility mechanism has been done. Most authors agree that the development of CO_2/oil miscibility is the result of extraction of some hydrocarbons from the oil by dense CO_2. In dynamic miscible floods, oil recovery increases with pressure until a pressure is reached at above which further increase does not significantly improve oil recovery. At and above this optimum pressure the injected solvent is miscible with the reservoir oil. The lowest pressure that allows the injected solvent to achieve dynamic miscibility with the reservoir oil is commonly referred to as the minimum miscibility

pressure (MMP) of the solvent/oil mixture. The MMP is an important parameter in the evaluation of gas flooding prospects. It is needed to determine whether a reservoir could be miscibly flooded and whether it is economically justified to flood the reservoir.

CO_2-Oil Extraction Experiment Description

Two different sets of experiments were performed. One was a slim tube test used to compare extraction results with a conventional method. The other was a series of CO_2-oil extraction experiments in which hydrocarbons were extracted from crude oils using high pressure CO_2. Two series of CO_2-oil extraction experiments were performed: the first to examine the effect of pressure, temperature and crude oil composition on CO_2-oil extraction performance and the second to study the performance of a CO_2-oil extraction system in an extended extraction time. Each was performed using an extraction apparatus in which CO_2 was continuously injected into a column of oil with an upper CO_2-rich phase with hydrocarbons extracted from the oil. The performances of the extraction systems were evaluated from the measured extraction efficiency, upper phase density and produced oil composition.

Extraction Apparatus

The extraction apparatus consisted of an extraction vessel, a CO_2 injection system, a recycling pump and a fluid condenser. The schematic diagram of the extraction apparatus used in this study is presented in Fig. 50. Excluding the recycling pump and the condenser, the apparatus was enclosed in a temperature-controlled air bath. The extraction vessel was a 5000 psig, 1.15 liter (6.7 cm ID and 50 cm length), constant-volume variable-composition blind mixing cell set to operate with continuous injection and production. The inlet port, at the bottom of the vertical standing vessel, was equipped with a 9-mm thick disc-shaped sintered-steel frit used to disperse the injected CO_2.

The CO_2 injection system consisted of a sliding piston accumulator and a 375-cm^3 constant rate metering pump. The extraction vessel and CO_2 accumulator pressures were each controlled by a separate diaphragm back pressure regulator (BPR). A wet test meter measured the produced gas rate. The system pressures were measured using 0-2000, ±1 psia pressure transducers. The density of the exit stream was measured using a high pressure high temperature ±0.001 g/cm^3 densitometer.

Experimental Procedure for CO_2-Oil Extraction

Two oil samples were used: a stock tank oil from the Sulimar Queen field and a separator oil from the Spraberry field. Each test was run at a constant temperature of either 95°F or 138°F. The extraction pressure for each temperature varied between 1000 and 1900 psig. At each extraction pressure, the mass and volume of produced oils, volume of produced gas, volume of the injected CO_2 and the density of the exit stream were recorded. The matrix of the experiments is presented in Table 8. The second series of experiments was performed to investigate the behavior of CO_2 extraction over an extended period. A Sulimar Queen oil sample was extracted at 1200 psig and 95 °F for a total of 103 hours. All test were run at a constant CO_2 mass flow rate of 38 g/hr.

The extraction experiment procedure consisted of three main components: oil loading, CO_2 loading and CO_2 injection. Each procedure step was the same for the variable pressure and extended extraction experiments, except for CO_2 injection, which continued for a much longer time.

Oil Loading: Similar to the method of Grigg *et al.*[28] who produced coreflood transition zones externally, the volume of oil loaded into the extraction vessel was 500 cm^3. This allowed room for CO_2 swelling of the oil without filling the vessel. The stock tank oil sample was loaded by pouring 500-cm^3 oil samples through the top opening of the extraction vessel. The samples were weighed using a laboratory balance before use. The separator oil was loaded into the extraction vessel partially loaded with CO_2 at room temperature.

CO_2 Loading: To obtain the desired CO_2 pressure in the accumulator, CO_2 was loaded below room temperature by simultaneously cooling (icing) the accumulator and allowing CO_2 to flow from the CO_2 tank, then warming the accumulator to system temperature. To obtain 2000 psig CO_2 in the accumulator at 95°F, the accumulator was cooled for about one hour. To achieve the same CO_2 pressure at 138°F, the accumulator was cooled for around 30 minutes. To avoid contamination, the accumulator was evacuated before filling with CO_2.

CO_2 Injection: CO_2 was injected into the extraction vessel to pressure the system to the desire test pressure, then to mix with and extract hydrocarbons from the oil continuously at a constant pressure. Usually it took about four hours to equilibrate the system. To achieve equilibrium of the mixture faster, fluid from the upper phase of the mixture was recycled through the inlet port of the extraction vessel using a recycling pump. The mixture was considered at equilibrium when the vessel pressure remained constant for at least five minutes after CO_2 injection was stopped.

The phases of the produced fluids were separated in the condenser at atmospheric conditions. The gas leaving the condenser was routed through a wet test meter for produced-gas volume measurement. The CO_2 injection and upper phase fluids production continued until the volume of the liquids collected at the vials had reached about 3 cm^3. The extraction process was then terminated by stopping the CO_2 injection and the vials were removed from the condenser for oil production determination and compositional analysis. After increasing the back pressure to the next desired extraction pressure, the experiment was continued by injecting CO_2 into the vessel. As in the previous experiment stages, CO_2 was injected first to increase the vessel pressure and later to extract hydrocarbons from the oil left in the vessel.

For one set of experiments, i.e., one oil sample for a given temperature, the above procedure was performed for at least six extraction pressures. The extraction at the first pressure used fresh oil sample and the sixth test used oil sample with about 3 volume % depletion (3 cm^3 production in each of the previous five extraction tests). Early tests indicated that oil depletion of up to around 10 volume % did not affect the extraction performance significantly. Therefore, it was assumed that the behavior of CO_2 extraction using an oil sample with depletion level of up to 10 volume % would be similar to using fresh oil. After the completion of each run the system was depressurized and the amount of the remaining oil was determined.

To investigate the behavior of CO_2 extraction over an extended period, the Sulimar Queen sample was extracted at constant pressure of 1200 psig and 95 °F for a total of 103 hours, during which time about 7800 grams of CO_2 was injected. The extraction rate during the course of the extended extraction experiment decreased with time. The interval of oil sampling was adjusted so that in each interval the amount of oil condensed was sufficient for oil compositional analysis. Thus, the sampling interval ranged from fifteen minutes at first to as long as four hours just before terminating the test.

Discussion of Results

Effect of Pressure, Temperature and Oil Composition

To investigate the effect of extraction pressure, temperature and oil composition on the extractive capacity of CO_2, four variable pressure extraction experiments were carried out using the two oils, each at two temperatures (95°F or 138°F) and at variable pressures between 1000 and 1900 psig. Each test was done at a constant mass flow rate of 38 g/hr. As an example, at 138°F and 2000 psig the density of CO_2 was 0.562 g/cc and the volumetric injection rate was about 68 cc/hour. To investigate the effect of pressure, continuous CO_2 injections and CO_2-oil upper phase productions were performed for at least six different pressures. In most of the experiments the extraction pressures were increased for each test, going from lower to higher pressures. To examine pressure-hysteresis, the extraction pressures for some test runs were changed from higher to lower pressures.

In this study, CO_2 extraction capacity is the parameter used to evaluate the performance of CO_2-oil extraction in terms of the capability of CO_2 to extract hydrocarbons from crude oils. It is defined as the ratio of the mass of produced oil to the mass of CO_2 injected to produce that oil. The extraction performances of four CO_2-oil extraction systems obtained from the experiments conducted in this study are presented in Table 9.

The extraction capacities of CO_2 at different CO_2-oil extraction systems were also plotted as a function of extraction pressure. Throughout the remainder of this report these plots are designated as extraction profiles. These plots are shown in Figs. 51–54. For comparison, the final percent production of the original oil in the slim tube is plotted with the extraction capacity, both versus pressure. Details and complete data sets for each of the tests are described by Siagian.[79]

From Figs. 51–54 one can see that all runs have similar CO_2 extraction capacity vs pressure profile. In each run, the CO_2 extraction capacity increases with increasing extraction pressure with a drastic increase in extraction capacity over a relatively small pressure range that we call the critical pressure range. This drastic increase in extraction capacity corresponded well with the slim tube break point, or MMP. Table 10 presents the slim tube MMPs and the critical pressure ranges of the four extraction experiment runs.

While this extraction experiment cannot be used to determine a definite value of CO_2-oil MMP, the critical pressure ranges can be used as a CO_2-oil MMP estimate. The extraction

experiment can be performed in about two days, while slim tube displacement tests usually take two weeks. Thus the former test is a good tool to estimate MMP or, if preferred, to screen the displacement pressures that will be obtained in slim tube tests. The fact that slim tube CO_2 MMPs are always within the range of pressures where efficient CO_2-oil extraction starts suggests that extraction is the process responsible in the development of CO_2-oil miscibility. Extraction experiment findings support the generally accepted CO_2-oil miscibility development mechanism, i.e., vaporizing gas drives.

Table 10 demonstrates that the widths of critical pressure range for low-temperature extraction systems are narrower than those for high-temperature extraction systems. This is not surprising because CO_2 density, which is believed to be an essential factor in the CO_2 -oil extraction, also behaves similarly. At pressures near to the CO_2 critical pressure, CO_2 density increases drastically over a small increase in pressure. At higher temperatures the CO_2 density increases more gradually with increasing pressure. In Table 10 and Figs. 51–54 it is shown that the maximum extraction capacities obtained in these experiments are about the same for three series at about 0.1 gram of oil per gram of CO_2 injected and about half that for Sulimar Queen samples at 138°F. This test was conducted before we started using the recycling pump, so this effect could be the result of the experiment running in a non-equilibrium state.

Oil composition was delineated in terms of the mole fraction of the component carbon number as determined from gas chromatographic analysis. The compositions of the original oil used in these experiments are presented in Table 11 and Fig. 55. It can be seen from Table 11 and Fig. 55 that the two oils have similar composition, particularly in the C_5-C_{10} fractions. However, Spraberry oil had 9.5 mole % solution gas. Table 11 also shows that the two oils also had a similar API gravity. The solution gas did not appear to have a significant effect on the MMP. This finding is in agreement with Holm and Josendal[80] who stated that CO_2-oil MMP does not depend on the C_2-C_4 fraction of the oil. The compositions of the produced oils and extraction residue collected from each test were determined from gas chromatographic (GC) analysis. Figure 56 is an example of the analysis of the produced oils from a series of tests.

The C_{37+} fraction was excluded from the composition distribution because the accuracy of GC analysis in determining C_{37+} fraction is low. It is worth noting that in GC analysis all errors that occur in the C_1 through C_{36} fractions are lumped together and added into the C_{37^+} fraction. Figure 56 shows that the compositions of the produced oils are similar. There are fewer light ends in the produced oils than in the original oil sample because they were vaporized by the produced CO_2. This result is confirmed by the analysis of the residual oil that showed the light ends had been produced (see Fig. 57). Figure 57 indicates the type of hydrocarbons stripped the most by CO_2. As this figure shows, mostly light ends up to around C_{20} were extracted. It also shows that a large portion of C_5 was extracted by CO_2. The low C_5 concentration in the produced oils suggests that this component was not captured by the separator condenser, but carried with the CO_2 gas.

The densities of the upper or produced phase of the CO_2-oil mixture were measured during the course of each extraction run with a Mettler-Paar densitometer. An example of the density

measurements as a function of vessel pressure for one set of extraction runs is presented in Fig. 58. For discussion purposes, the slim tube MMP and the extraction capacity of the corresponding extraction runs are also presented in this figure. The extraction started when the upper phase density was approximately 0.4 g/cm^3. For the 95°F extractions, maximum extractions occurred when the upper phase densities were around 0.8 g/cm^3. For the 138°F extractions, it took place when the upper phase densities were slightly lower, i.e., around 0.7 g/cm^3. This is probably because oils have lower densities at elevated temperatures. Therefore, as shown by Lange,[36] they have lower solubility parameters and require a lower CO_2 density.

Extended Extraction Experiment

To examine the behavior of CO_2-oil extraction in an extended period of time, a 750-cm^3 (617 grams) Sulimar Queen oil sample was extracted for a total of 103 hours at constant pressure and temperature of 1200 psig and 95°F, respectively. Oil and gas production and the upper phase densities of the CO_2-oil mixture were monitored and recorded during the course of the experiment. A total of 91 produced oil samples were taken. Some of the sample were analyzed using simulated distillation by gas chromatography to determine composition.

This experiment showed that from the 750 cm^3 original oil in place about 525 cm^3 (~400 grams) oil was extracted by CO_2. This result means that this type of extraction process could result in oil recovery of 70% by volume or 64% by weight. The total amount of CO_2 that was injected to extract that amount of oil was 7857 grams, which means that, on average, 20 grams of CO_2 is required to extract each gram of oil produced.

Figure 59 presents the extraction capacity of CO_2 as a function the amount of oil left in the extraction vessel expressed as weight percentage of oil with respect to the weight of original oil in place. Figure 59 shows that, as expected, the extraction capacity of CO_2, (grams of produced oil per gram of CO_2 injected) decreased with decreasing percent of oil left in the vessel. This occurred because the amount of oil left in the vessel as hydrocarbon extraction by CO_2 proceeded obviously decreased and the injected CO_2 interacted with less and less oil. In addition, the injected CO_2 was not only spent for oil extraction processes but also was used to compensate for pressure losses due to decreasing amount of oil in the vessel. The CO_2 extraction capacity of this experiment decreased from about 0.3 gram oils per gram injected CO_2 early in the run to only about 0.006 g oil/g CO_2 by the end of the test. Figure 60 shows the extent to which the light and intermediate hydrocarbons were extracted.

Conclusions For Extraction and Related Slim Tube Tests

The CO_2 extraction capacity, defined as the weight of oil extracted per weight unit of CO_2 injected, increases with increasing pressure. In each CO_2-oil system investigated, there is a relatively small pressure range over which a sharp increase in the extraction capacity occurs. Above this range, an additional increase of pressure does not significantly increase the extraction capacity.

1. The effect of pressure on the density of CO_2-oil upper phase in a multiphase system is similar to its effect on the extraction capacity. The density increases with increasing pressure; over

a narrow pressure range the density drastically increases, above which an additional increase of pressure does not significantly increase the density.

2. In CO_2-oil extraction experiments, the pressure range over which a sharp increase in both extraction capacity and upper phase density occurs is similar to the slim tube MMP. At lower temperatures the pressure range over which a sharp increase in upper phase density occurs is as distinct as the sharp increase of extraction capacity.
3. Extraction experiments provide a good estimate for the MMP and are a good screening tool if confirmation of MMP in slim tube tests is desired.
4. CO_2 extraction capacity is a strong function of extraction temperature. It decreases with an increase of temperature. The pressure at which CO_2 starts to efficiently extract hydrocarbon from an oil increases with an increase of temperature. At 95 and 138 °F, for the materials and conditions involved, extraction is insignificant for extraction pressures below 1100 and 1600 psig, respectively.
5. The presence of solution gas in the oil used in the study did not affect either the CO_2 -oil extraction performance or the CO_2-oil MMP.
6. In an extended extraction test, CO_2 can extract approximately 70 wt.% or 64 vol.% of the original oil in place (OOIP). The CO_2 extraction capacity decreased from around 0.3 g oil/g CO_2 injected at the beginning of the extraction to 0.006 g oil/g CO_2 injected at time of termination. The average value of the extraction capacity was 0.0509 g oil/g CO_2 injected.
7. Small hydrocarbon molecules of the oil partition into a CO_2-rich phase more efficiently than large molecules. Therefore, oils obtained through extraction have lower molecular weight than the corresponding original oils.
8. Much of the produced hydrocarbons lighter than C_9 were not condensed in the liquid separator used in the extraction experiment. Instead, they were vaoiruzed with the produced CO_2. In the future, if an experimental setup and procedures similar to those in this study are used, compositional analysis of the produced gas is recommended.

Experiments—CO_2 Foam Coreflood Tests

Introduction

Application of foam to a reservoir involves injecting a surfactant along with water and gas into the reservoir. To enable the selection of a suitable surfactant for a reservoir, laboratory test data have to be collected to characterize the surfactant performance. One of the most important criteria used in the surfactant selection process is the effectiveness of the surfactant in reducing the mobility of CO_2. The foam resistance factor (R_f) is a parameter used to assess the magnitude of mobility reduction.[42,81] The R_f is defined as the total mobility of CO_2/brine divided by the total mobility of CO_2/surfactant solution (foam mobility), where both mobility measurements are conducted at the same gas-liquid volumetric injection ratio (CO_2 fraction). If foam is not generated, the R_f is unity. If foam is generated, the value of the R_f quantifies the effect of the presence of foam. Therefore, once the surfactant selection process is completed, the R_f data of the selected surfactant generated from various foam tests should be readily available. The relationships of surfactant concentration,

injection flow rate, foam quality (CO_2 fraction), and rock permeability with R_f have been elucidated by recent laboratory foam tests.[5,42,82] Based on these relationships, a predictive foam model has been developed[11] and will be presented in the following section.

Efficient application and evaluation of candidate reservoirs for CO_2 foam processes requires a predictive foam model. To provide input data to the predictive foam model, quantitative information on foam-flow behavior at various foam-test conditions is required. However, some of the information available in the literature is inconclusive and some of the information is not complete. For example, there are discrepancies in the literature regarding foam mobility behavior with increasing foam quality (CO_2 fraction) and with increasing flow rate. Also, the foam-flow behavior in the lower range of foam quality (below 50%) has never been reported. Therefore, the objectives of this study are to examine further the inconsistent information on foam-flow behavior and to explore the information on the lower range of foam quality.

Experimental Descriptions

A schematic diagram of the test apparatus is shown in Fig. 61. Brine, surfactant solution (SS), and CO_2 were loaded into floating piston accumulators and then displaced into the system by a pump filled with distilled water. The pressure drop across the core was measured by a Honeywell differential pressure transducer (DPT) and by two Sensotec pressure transducers (PT) located upstream and downstream, respectively, from the core. System pressure was provided by a Temco backpressure regulator (BPR) controlled to the desired run pressure. The test apparatus was housed in an oven to maintain a constant temperature. A wet test meter outside the oven was used to monitor gas production. Either CO_2 and brine or CO_2 and surfactant solution could be coinjected into the system by turning their corresponding pumps on simultaneously. For the purpose of this study, foam was generated in situ in the core and the foam generator upstream to the core was bypassed.

Foam tests were conducted on fired Berea sandstone cores at conditions of 101°F and 2100 psig. As a standard procedure for the foam tests, the core was first saturated with brine by injecting brine overnight at a flow rate of 5 cc/hr. Then the brine permeability was determined by regression based on several brine injection rates varying from 5 to 40 cc/hr. Next, baseline experiments were performed at various flow rates by coinjecting CO_2 and brine into the core at various gas-liquid volumetric injection ratios (CO_2 fractions). Note that a gas-liquid volumetric injection ratio of 4:1 corresponds to a CO_2 fraction of 0.8. Each baseline experiment lasted until a steady-state pressure drop across the core was achieved. After the baseline experiments, the core was flushed with brine to displace CO_2 and then the brine permeability was redetermined. Prior to the foam experiments, the core was saturated with surfactant solution at a surfactant concentration of 2500 ppm to bring the adsorption level to a constant value. Then the surfactant-solution permeability was determined. The foam experiments were performed at various flow rates by coinjecting CO_2 and surfactant solution at various CO_2 fractions similar to those of the baseline experiments. Each foam experiment lasted until a steady-state pressure drop across the core was achieved. After the last foam experiment, the core was depressurized to the ambient condition and flushed with brine to completely displace CO_2 and surfactant solution. The core was then pressurized and saturated with brine for a final brine

permeability determination. The brine permeability was used to determine whether the conditions of the core had been altered during the foam tests.

In all the tests, a synthetic brine with the composition shown in Table 12 was used. The surfactant used in this study was Chaser™ CD-1045. The surfactant solution was prepared by mixing CD-1045 in the synthetic brine. Information on the fired Berea cores used in the tests is listed in Table 13.

Results and Discussion

Test Series I.

In this test series, core A was used. The initial brine permeability of the core was 36.9 md. The results of the baseline experiments are summarized in Table 14 for total flow rates of 4.2, 8.4, and 16.8 cc/hr, each at CO_2 fractions of 0.2, 0.333, 0.5, 0.667, and 0.8. There was little or no effect of flow rate on the total mobility of CO_2/brine for each tested CO_2 fraction, as shown in Fig. 62. When the CO_2 fraction was higher than 0.333, the total mobility of CO_2/brine increased with increasing CO_2 fraction for all tested flow rates, as shown in Fig. 63. When CO_2 fraction was lower than 0.5, the effect on the total mobility of CO_2/brine was less obvious. After the baseline experiments, the brine permeability was determined to be 45.6 md.

During the injection of surfactant solution into core A, a steady-state pressure drop across the core was never achieved for all the tested flow rates. To check the conditions of the core, the core was depressurized, flushed with brine, pressurized, and flushed with brine for a final brine permeability determination. The initial brine permeability could not be restored (about 1/3 of the initial value) and core A was abandoned.

Test Series II.

In this test series, core B was used. The initial brine permeability of the core was 195.6 md. The results of the baseline experiments are also summarized in Table 14. The total mobility of CO_2/brine increased with CO_2 fraction when the CO_2 fraction was higher than 0.333, as shown in Fig. 64. When CO_2 fraction was lower than 0.5, the effect on the total mobility of CO_2/brine was less obvious. This observation was consistent with the results of core A. For each tested CO_2 fraction, the total mobility of CO_2/brine at 16.8 cc/hr is higher than those at 8.4 and 4.2 cc/hr, as shown in Fig. 65. There was little or no effect of flow rate on the total mobility of CO_2/brine at 8.4 and 4.2 cc/hr. After the baseline experiments, the brine permeability was determined to be 182.5 md.

Although a steady-state pressure drop across the core was never achieved for all the tested flow rates during the injection of surfactant solution, foam experiments were still carried out and conducted at 4.2 cc/hr for various CO_2 fractions (foam qualities). Note that a CO_2 fraction of 0.5 in a foam test corresponds to a foam quality of 50%. The results of the foam experiments are summarized in Table 15 for CO_2 fractions of 0.2, 0.333, 0.5, 0.667, and 0.8 and also plotted in Fig. 64 (indicated by the legend CO2/SS). The total mobility of CO_2/surfactant solution (foam mobility) decreased with increasing CO_2 fraction (foam quality), as clearly shown in Fig. 64.

When the CO_2 fraction of the foam experiment was decreased from 0.667 to a previous value of 0.2, the pressure drop of the foam experiment was greater than that obtained previously (171 vs. 127 psi), see Table 15. There were two possible reasons for this irreversible behavior. The effect might be due to the foam generated at a previous higher CO_2 fraction, such that foam would not return to a state corresponding to a current lower CO_2 fraction. It might also be attributed to the generation of plugging products from the effects of surfactant and foam on the core, such that the permeability of the core was reduced. After the foam experiments, the initial brine permeability of the core could not be restored (about 1/5 of initial value) and the core was abandoned. Even though the core could not be restored to the original permeability, the mobilities of CO_2/surfactant solution (foam mobilities) were always two orders of magnitude lower than that of the baseline experiments, as clearly shown in Fig. 64.

It is interesting to note that, when examining the pressure drop response of the foam experiments, the pressure curves cycled up and down significantly with a peak-to-peak amplitude that varied from 50 psi to 100 psi for the cases of 0.2, 0.33, and 0.5 CO_2 fraction (20%, 33.3% and 50% foam quality), as shown in Figs. 66-68. But the pressure curves were very smooth with a peak-to-peak amplitude of about 5 to 10 psi for the cases of 0.667 and 0.8 CO_2 fraction (66% and 80% foam quality), as shown in Figs. 69 and 70. Similar pressure responses were also observed for the baseline experiments with much smaller peak-to-peak amplitudes. This kind of cycling pressure response might be due to the formation and the breakthrough of a CO_2 bank. The existence of foam would enhance the cycle interval and amplitude compared to baseline experiments.

Test Series III.

In this test series, core C was used. The initial brine permeability of the core was 139.28 md. The results of the baseline experiments are also summarized in Table 14. When the CO_2 fraction was higher than 0.333, the total mobility of CO_2/brine increased with CO_2 fraction, as shown in Fig. 71. When CO_2 fraction was lower than 0.5, the effect on the total mobility of CO_2/brine was less obvious. This observation was consistent with the results of cores A and B, as shown in Figs. 63 and 64. The effect of flow rate on the total mobility of CO_2/brine for each tested CO_2 fraction was inconclusive, as shown in Fig. 72. When CO_2 fraction was lower than 0.5, the total mobility of CO_2/brine decreased with increasing flow rate. When CO_2 fraction was higher than 0.667, the total mobility of CO_2/brine increased with increasing flow rate.

Prior to the foam experiments, the core was saturated with surfactant solution with a concentration of 2500 ppm active surfactant. The surfactant solution was injected until a steady-state pressure drop across the core was achieved. The surfactant-solution permeability was determined to be 121.8 md, which was very close to the brine permeability of 126.0 md measured prior to the injection of surfactant solution. This steady-state behavior was not observed during the surfactant-solution saturation of cores A and B. Thus the surfactant-solution permeability was not determined for both cores A and B.

The results of the foam experiments are also summarized in Table 15 for total flow rates of 4.2, 8.4, and 16.8 cc/hr and CO_2 fractions of 0.2, 0.333, 0.5, 0.667, and 0.8. The total mobility of CO_2/surfactant solution (foam mobility) decreased with increasing CO_2 fraction (foam quality), as

clearly shown in Fig. 73. When comparing foam resistance factors (Fig. 74), the resistance factor increased with increasing CO_2 fraction for all tested flow rates when CO_2 fraction was higher than 0.2; there appeared to be a minimum resistance factor between CO_2 fractions of 0.2 and 0.333, except the case of 4.2 cc/hr. For the tested CO_2 fractions of 0.666 and 0.8, the total mobility of CO_2/surfactant solution increased with increasing flow rate and the resistance factor decreased with increasing flow rate, as shown in Figs. 75 and 76, respectively. For the tested CO_2 fractions of 0.2, 0.333, and 0.5, the effects of flow rate on the total mobility of CO_2/surfactant solution and foam resistance factor were inconclusive. When the patterns of both Figs. 75 and 76 are examined carefully, it appears that there might be some uncertainties for the foam experiments at 4.2 cc/hr for tested CO_2 fractions of 0.2, 0.333, and 0.5. Therefore, based on the test results of 8.4 and 16.8 cc/hr, the total mobility of CO_2/surfactant solution increased with increasing flow rate and the resistance factor decreased with increasing flow rate for the tested CO_2 fractions of 0.2, 0.333, and 0.5.

During the foam experiments at a flow rate of 4.2 cc/hr, the CO_2 fraction was decreased from 0.8 to a previous value (0.2) but the steady-state pressure drop of the foam experiment was greater than that obtained previously (63.73 vs. 19.91 psi), see Table 15. This irreversible behavior was consistent with that observed in core B in Test Series II. To further investigate this behavior, a second series of foam experiments were initiated after the brine permeability of the core was determined. Even though the core could not be restored to the original permeability, the second series of foam experiments at 4.2 cc/hr for CO_2 fractions of 0.2, 0.5, and 0.667, were still conducted. The results are also summarized in Table 15 and plotted in Fig. 73 (indicated by the legend CO2/SSII). For each tested CO_2 fraction, the pressure drop across the core was greater than that of the previous experiment (see Table 15). This indicated that the permeability of the core was altered and reduced due to the generation of plugging products from the effects of surfactant and foam on the core. The final brine permeability of the core was 59.18 md, determined after the second series of foam experiments, confirmed the permeability was decreased.

Test Series IV.

In this test series, core D was used. Instead of following the previous procedure for the foam test, a foam experiment was initiated at 4.2 cc/hr for the CO_2 fraction of 0.8 after the surfactant-solution permeability was determined. After the foam experiment, the brine permeability was determined to be 74.4 md, which was close to the surfactant-solution permeability of 61.7 md measured prior to the foam experiment. This indicated that there was little or no permanent plugging. To further investigate this behavior, a second series of foam experiments at 4.2 cc/hr and CO_2 fractions of 0.2, 0.5, and 0.8 were conducted after the baseline experiments were performed. The results of both baseline and foam experiments are also summarized in Tables 14 and 15. The results from the foam experiments at 4.2 cc/hr for CO_2 fraction of 0.8 before and after the baseline experiments were almost identical (see Table 15). In addition, the final brine permeability of the core (78.76 md), determined after the second series of foam experiments, confirmed that the permeability was not reduced. Why the permeability of the core was not reduced in this test series was not clear because all the cores used in this study were Berea cores fired under similar conditions. One possible reason might be that core D was much shorter than the other cores (see Table 13) so the plugging products generated from the effects of surfactant and foam on the core were displaced.

The total mobility of CO_2/brine is plotted against CO_2 fraction in Fig. 77 for cores A, B, C, and D. The total mobility of CO_2/brine for each core, except core D, was determined by regression based on all tested flow rates of 4.2, 8.4, and 16.8 cc/hr. These values are reported as WAG mobility in Column 7 in Table 15. At zero CO_2 fraction, the average brine mobility was used for each core. Figure 77 clearly shows that, when CO_2 fraction was higher than 0.333, the total mobility of CO_2/brine increased with increasing CO_2 fraction. There appeared to be a minimum mobility between the CO_2 fractions of 0.2 and 0.333. In Fig. 78, the total mobility of CO_2/surfactant solution was plotted against the CO_2 fraction for cores B, C, and D at a total flow rate of 4.2 cc/hr. The total mobility of CO_2/surfactant solution (foam mobility) decreased with increasing CO_2 fraction (foam quality). When comparing foam resistance factors at 4.2 cc/hr (see Fig. 79) the foam resistance factor increased with increasing CO_2 fraction (foam quality). However, at tested flow rates of 8.4 and 16.8 cc/hr, a minimum foam resistance factor appeared in core C between the CO_2 fractions of 0.2 and 0.333 (see Fig. 74).

Conclusions for CO_2 Foam Coreflood Tests

When the CO_2 fraction was higher than 0.333, the total mobility of CO_2/brine increased with increasing CO_2 fraction; a minimum mobility appeared between the CO_2 fractions of 0.2 and 0.333. The total mobility of CO_2/surfactant solution (foam mobility) decreased with increasing CO_2 fraction (foam quality).
For the tested CO_2 fractions ranging from 0.333 to 0.8, the resistance factor increased with increasing CO_2 fraction (foam quality) for all tested flow rates of 4.2, 8.4, and 16.8 cc/hr.
A minimum foam resistance factor appeared between CO_2 fractions of 0.2 and 0.333 for tested flow rates of 8.4 and 16.8 cc/hr.
The total mobility of CO_2/surfactant solution increased with increasing flow rate.
The resistance factor decreased with increasing flow rate.

Modeling and Simulation

With the ever-present concern that recovery mechanism efficiencies are greatly reduced below the MMP (even though the extent is under consideration), it is wise to look for mechanisms that would counter the reduction. These can include both foams and other methods such as horizontal wells. Thus, when developing models to simulate reservoir flow development, the models should include foam features and various injection methods such as horizontal wells. CO_2-foam has been studied in previous laboratory work[1,2,42,83] and field foam tests[84-86] conducted by the PRRC. The reservoir models that simulate mass transfer in CO_2 floods involve compositional transfer capabilities that require considerable phase behavior development. Included in this work are the modeling of phase behavior using equation of state and neural networks, and modifications for reservoir models to simulate CO_2 foam and horizontal wells.

Phase Behavior-Preprocessor for Reservoir Simulations

Compositional models based on cubic equations of state[87] are commonly employed for simulation of the reservoir performance in CO_2 flooding processes. Generally, with a large number of pseudocomponents used in characterizing the heptanes-plus (C_{7+}) fraction of an oil, a satisfactory prediction of the phase behavior can be obtained. In compositional models, however, the cost and computing time can increase significantly with the increased number of components in the system. Therefore, there are limitations on the maximum number of components that can be used in compositional models and the original multicomponents in an oil have to be lumped into a smaller number of pseudo-components. That is one of the objectives of C_{7+} characterization: to obtain the best possible description of the C_{7+} fraction using a minimum number of pseudo-components. Tuning of the equation-of-state parameters to experimental equilibrium data generated at static conditions prior to the reservoir simulation studies is the current practice in the industry. One objective of this work was to set up a preprocessor program to generate input parameters for compositional simulators. In this preprocessor program, the equation-of-state parameters and other parameters such as the average molecular weight of the C_{7+} fraction are tuned to match the equilibrium data generated at static conditions. A compositional model which is tuned to these static data, nevertheless, may not be adequate to predict the phase behavior around the critical region or close to the minimum miscibility pressure. This is still an important issue which merits special attention.

Currently, the preprocessor is able to match the bubblepoint pressure data by tuning the average molecular weight of C_{7+} fraction. After matching the bubblepoint pressure, the preprocessor program will generate parameters that can be used as input to compositional simulators. Our goal is to improve the preprocessor to match not only the bubblepoint pressure data but also other equilibrium data generated at static conditions.

During the development of the preprocessor program, a new and effective method was proposed for estimating the specific gravities of pseudocomponents that are required to characterize the heavy components of crude oils. This method uses the most often available data of the heavy components of crude oils: average molecular weight and specific gravity of the C_{7+} fraction. The proposed method makes use of the definition of the Watson characterization factor, which is the cube root of boiling point in Rankine (ºR) divided by specific gravity, and the corrected Riazi-Daubert relation for the boiling point[88]:

$$T_{bi} = \frac{6.77857\ M_i^{\,0.401673}\ \gamma_i^{\,-1.58262}}{\exp[\ -\ (b\ M_i\ +\ c\ \gamma_i\ +\ d\ M_i\ \gamma_i)]} \tag{2}$$

where T_{bi} is the boiling point (ºR), γ_i is the specific gravity (at 60ºF relative to water at 60ºF), M_i is the molecular weight of the pseudo-component, and constants b, c, and d are equal to 0.00377409,

2.984036, and -0.00425288, respectively. Using the definition of the Watson characterization factor, K_W, the specific gravity of the pseudo-component is given as:

$$\gamma_i = \frac{T_{bi}^{1/3}}{K_w} \tag{3}$$

By solving the previous two equations with the successive substitution method, we can obtain the specific gravity of the pseudocomponent. If the calculated average specific gravity of the C_{7+} fraction does not match the measured value, a new value of the Watson characterization factor is calculated using the Newton method. The whole calculation is iterated until a value of the Watson characterization factor gives specific gravities of pseudocomponents that can match the measured value. In order to evaluate the new method and compare it with the existing estimation methods, a procedure has been implemented, without using any tuning techniques, for the phase equilibrium predictions of crude oil-CO_2 systems. The phase equilibrium predictions, based on the specific gravities estimated by the new method and the existing methods proposed by Whitson *et al.*[89] and Yarborough,[90] were all reasonably accurate and of the same magnitude. The specific gravities estimated by the new method and the method proposed by Whitson *et al.*[89] always provided similar phase behavior predictions. Chang *et al.*[91] describe in detail the proposed method and comparisons with the existing methods.

Phase Behavior using Neural Networks

Introduction

Phase behavior, such as bubblepoint pressure (P_b), bubblepoint oil formation volume factor (B_{ob}), and phase boundaries versus composition change such as in CO_2 injection, are critical in reservoir engineering for predicting fluid flow.[92] Both correlations and equations of state (EOS) have been used to predict phase behavior. Correlations are usually too general and are developed based on regional oil samples. In many instances EOS require extensive data and parameter tuning to model phase behavior. As more data and advanced computational techniques become available, improvement becomes increasingly rapid and more accurate. We will show that neural networks (NN) can be applied for predicting P_b, B_{ob}, and the phase behavior of CO_2-crude oil systems with specific emphasis in the low temperature, high-CO_2 concentration region, where three CO_2-crude oil phases exist.

Three regional correlations, used for calculating PVT properties,[93-96] will be used in this study for comparison. These correlations treat oil and gas as two components, each having a fixed composition.[92] The specific gas and oil gravities, pressure, and temperature are used to characterize the oil's PVT properties. Crude oils exhibits regional trends in chemical composition; thus, regional correlations are not expected to provide satisfactory results when applied to crude oils from other regions.

The displacement efficiency in CO_2 floods depends on many factors,[97] including phase behavior and mass interchange between phases.[98] Mixtures of CO_2 and crude oil show complex phase behavior, particularly near the critical pressure and temperature of CO_2, that include liquid-liquid (L1-L1) and liquid-liquid-vapor (L1-L2-V) behavior.[97] Methods for predicting this phase behavior with cubic EOS have been presented in the literature.[99] Most tune the EOS parameters to match each experimental phase diagram.[100,101] Models displaying a more predictive character have also been attempted,[67,102,103] but are either of limited applicability, or require significant tuning. The requirement of significant parameter tuning[104] destroys the predictive power of the equation,[105] especially when predicting the three-phase region in CO_2 -crude systems that occurs in proximity to a critical region.[103,106-108] This method has found only marginal success.

The emerging technology of NN offers two advantages: fast computation and accuracy.[109] We will show the potential of using NN for predicting P_b, B_{ob}, and CO_2-oil mixtures phase behavior near the critical three-phase region. Artificial neural systems, or NN, are physical cellular systems that can acquire, store, and use experiential knowledge.[110] The knowledge is stable states or mapping embedded in networks that can be recalled in response to the presentation of cues. In a typical neural data processing procedure, the database is divided into two sets: training and test. The training set is used to develop the desired network. Depending on the paradigm used, the desired output in the training guides the network in learning by adjusting the weights between its neurons or processing elements.

Once the network has learned the information in the training set, the test set is applied to the network for verification. Although the user has the desired output of the test set, it has not been seen by the network. This ensures the integrity and robustness of the trained network.[110] NN help the user by addressing petroleum engineering problems: both those that have and those that have not been easily solved through other methods. NN techniques with error-back propagation[111] have proved to be valuable pattern recognition tools. They are capable of finding highly complex patterns within a large data base. Al-Kaabi and Lee[112] used the method to identify a transient pressure well test interpretation model. The error-back propagation technique can also be applied to problems in function approximation. Hecht-Nielsen[113] proved that the error-back propagation is capable of approximating any function. Pao[114] showed how it can approximate a Gaussian function. Accarain and Desbrandes[115] applied it to estimate pore pressure from sonic velocity measurements. Ouenes *et al.*[116] applied NN to fractured reservoir and characterization problems. Mohaghegh[110] applied it to estimate permeability of a highly heterogeneous formation in West Virginia and Habiballah *et al.*[109] applied it to predict vapor/liquid equilibrium *K* values for light-hydrocarbon mixtures.

The basic idea in neurocomputing is to provide the neural net with training records that allow the abutment of the neural net parameters—the weight matrix—through an optimization procedure called training.[116] The training process consists of estimating the weights that minimize the error function, as described in the following paragraphs. The equations used in this training process were developed by Hertz *et al.*[117] and Liuc.[118] The gradient descent technique has been commonly used in the error-back propagation. It has the disadvantages of slow convergence and user-dependent parameters (learning rate and momentum constants). A better approach to the learning problem is

to use the scaled conjugate gradient (SCG) technique developed by Mϕller.[119] The SCG method uses second-order information defined by the Hessian matrix (the second derivative of error function with respect to network weights). The SCG has no user-dependent parameters and is capable of scaling weight changes. This makes it considerably faster than the gradient descent approach.

Correlations of P_b and B_{ob}

The P_b and B_{ob} correlations used in this study to compare with NN are functions of solution gas R_s, gas gravity γ_g, oil API gravity or oil gravity γ_o, and temperature T. In this work we used three different correlations for each property:

(1) The Standing Correlations:[93,94]

$$P_b=18.2[(R_s/\gamma_g)^{0.83}(10)^a-1.4] \quad (4)$$

with

$$a = 0.00091T - 0.0125(API) \quad (5)$$

and

$$B_{ob} =0.9759+0.00012[R_s(\gamma_g/\gamma_o)^{0.5}+1.25T]^{1.2}, \quad (6)$$

based on 105 experimentally measured values from 22 oils from California oil fields.

(2) The Glaso Correlations:[95]

$$Log(P_b)=1.7669+1.7447\ Log(P_b^*)-0.30218[Log(P_b^*)]^2 \quad (7)$$

where

$$P_b^* =(R_s/\gamma_g)^a(T)^b(API)^c \quad (8)$$

with a=0.816, b=0.172, c=-0.989.

or volatile oils, Glaso recommends that the temperature exponent, b, be reduced to the value of 0.130. Also,

$$B_{ob} = 1.0 + 10^A \quad (9)$$

where

$$A= -6.58511 + 2.91329LogB_{ob}^* - 0.27683(LogB_{ob}^*)^2 \quad (10)$$

and

$$B_{ob}^{*} = R_s(\gamma_g/\gamma_o)^{0.526} + 0.968T. \quad (11)$$

These correlations are based on 45 oil samples, mostly from North Sea oils.

(3) The Al-Marhoun Correlations[95]:

$$P_b = a\, R_s^{\,b}\, \gamma_g^{\,c}\, \gamma_o^{\,d}\, (T+460)^e \quad (12)$$

where a=0.00538088, b=0.715082, c=-1.87784, d=3.1437,and e=1.32657

and

$$B_{ob} = 0.497069 + 0.862963\times10^{-3}T + 0.182594\times10^{-2}F + 0.318099\times10^{-5}F^2 \quad (13)$$

with

$$F = R_s^{\,a}\, \gamma_g^{\,b}\, \gamma_o^{\,c} \quad (14)$$

and $a = 2390$, $b = 0.323294$, and $c = -1.20204$.

These correlations are based on 160 points from 69 Middle Eastern hydrocarbon mixtures.

The accuracy of NN predictions and the above correlations relative to experimental values was determined using average percent relative error, average absolute percent relative error, minimum/maximum absolute percent relative error, standard deviation, correlation coefficient, and two graphical techniques: crossplots and absolute relative percent error. One hundred sixty data points from Middle East oils[96] were used for training and the other 80 samples from the Middle East with 11 North Sea oils[95] were the test set. The NN inputs are solution gas-oil ratio, average gas relative density, stock-tank oil gravity, and temperature. The ranges of the data used are shown in Table 16.

Bubblepoint Pressures. Eighty Middle East system data points and systems from Glaso's set[95] that fell within the range of the training set, as outlined in Table 16, were used for testing. The error analysis for the NN estimation and for each correlation are summarized in Table 17. The P_b estimation using NN achieved the lowest average absolute relative error of 3.72% and standard deviation of 4.944%, with the highest correlation coefficient accuracy of 0.998. Since 80 of the 91 test points were the same used to develop the Al-Marhoun correlation, it was not surprising that it had the second best overall fit. Standing's correlation stood third in accuracy. The Glaso correlation showed poor accuracy, with the highest average absolute relative error of 23.99 and the lowest correlation coefficient of 0.900.

Table 18 shows the statistical results for the 11 North Sea oils[95] only. The NN again achieved the highest accuracy, with the lowest average absolute relative error of 3.094%, standard deviation

of 3.602%, and highest correlation coefficient of 0.998. Again, not surprisingly, Glaso's correlation, partially based on these North Sea systems, had the second best average fit. It is significant that the NN had a better fit then Glaso, even though none of the eleven oils, nor any North Sea oil, were included in the training group.

The crossplot of estimated versus experimental values for P_b are presented in Figs. 80 through 83. Circles and squares represent Middle East and North Sea oils, respectively. Most of the plotted points of the NN fall very close to the 45° line. The crossplot of Al-Marhoun's correlation is fairly close to that of the estimation of the NN. On the other hand, the correlations of Standing and Glaso reveal a general overestimation, which might be expected when comparing fluid from one region to a correlation developed using fluid in a different region. Figures 84 through 87 show plots of relative absolute percent error for the four systems. It is quite obvious that the NN was superior to the other correlations, even Al-Marhoun's correlation that was developed using the bulk of these data, and is visually shown to be superior even on the North Sea fluids.

When the three correlations are compared to NN, NN provided the best estimation of P_b, even for the North Sea oils when no North Sea oils were used for training. Thus, it can be concluded that NN should be valid for predicting P_b of reservoir fluids from any region with properties falling within the range of data used in training. Though only two different regional oils were tested in this study, with a larger range of experimental data for training, NN could be a standard method for the prediction of P_b.

Formation Volume Factor. The results of comparing calculated B_{ob} and the experimentally obtained B_{ob} for the 89 test data points are summarized in Table 19. The same 80 Middle East samples used for P_b, were used to train for B_{ob} and the same Middle East oil and the nine North Sea oil used previously that had reported B_{ob} were used for testing the NN. Again, the estimation of B_{ob} using the NN method achieved the lowest average absolute relative error of 0.662% and standard deviation of 0.889%, with the highest correlation coefficient accuracy of 0.998. Again, Al-Marhoun's correlation had the second highest accuracy. The Glaso correlation was third followed by Standing. Table 20 summarizes the statistical results for the nine North Sea oils that had B_{ob} given and the system was within the range of data in Table 16. The NN approach achieved the highest accuracy, with the lowest average absolute relative error of 0.664% and standard deviation of 0.996%.

The crossplot of estimated versus experimental values for B_{ob} are presented in Figs. 88 through 91. Circles and squares represent Middle East and North Sea oils, respectively. Most of the plotted points of NN estimations fall very close to the 45° line. The crossplot of Al-Marhoun's correlation is fairly close to that of the NN estimation. On the other hand, the correlations of Standing and Glaso reveal a general overestimation, see Figs. 89 and 90, with Glaso's correlation generally appearing to be a little better than Standing's correlation. Figures 92 through 95 show plots of relative absolute percent error for the four systems. It is quite obvious that the NN was superior to the other correlations. It was surprising that the NN used on North Sea oils worked better than the correlation developed using oils from that region, even when none were used to train the NN.

In summary, comparing the four correlations, NN provided the best estimation of B_{ob} . Even for the nine North Sea oils which were not used for training, NN still worked better than any correlation. Thus, it can be concluded that NN should be valid for predicting B_{ob} of reservoir fluids from any region with properties falling within the range of data used in training. Though only two different regional oils were tested in this study, the results suggest that with a larger range of experimental data for training, NN could be a global method for the prediction of B_{ob}.

Using NN to Predict Phase Behavior of CO_2-Crude Oil Mixtures

It is well established that CO_2-crude oil mixtures form vapor-liquid-liquid ($V\text{-}L_1\text{-}L_2$) equilibria at high CO_2 concentrations and at pressures and temperatures close to the critical pressure (1070 psig) and temperature (88°F) of CO_2. The three phases in equilibrium are an oleic liquid phase, a CO_2-rich liquid phase, and a CO_2-rich vapor phase. An accurate prediction of this type of phase behavior is important for the success of numerical simulations of processes where CO_2 is injected into oil reservoirs. The description of the phase behavior such as phase boundaries with an EOS presents some difficulties. EOS approaches require extensive computational time, may have convergence problems, and require correctly tuned binary interaction parameters.

The NN appeared to be a good candidate for an improved predictive method to examine the three-phase envelope of CO_2-crude oil mixtures. The input to the NN is the mole fraction of crude oil components (CO_2, N_2, H_2S, C_1, C_2, C_3, iC_4, nC_4, iC_5, nC_5, C_6, and C_{7+}), C_{7+} molecular weight, C_{7+} specific density, CO_2 mole fraction and system temperature. Ten oil systems with reported phase diagrams were used for training. Oils A, B_1, B_2, C_2, and D were from Turek *et al.*;[73] oil B is from Shelton and Yarborough;[71] oil G is from Creek and Sheffield;[26] and oils JEMA and NWE are from Jorgensen and Stenby.[120] Two systems, oil F[73] and oil BSB,[120] were used for testing. Table 21 lists the input parameters for each of these reservoir fluid systems. In the training systems the temperature ranged from 83°F to 110°F. In each test the critical point was predicted first; then the saturation curves. Since there are no phase boundaries reported in the literature between liquid and liquid-liquid regions for oils of B_1, C_2, and D, this boundary was not predicted in this study. Table 22 lists the critical point experimental results and NN estimations for the two test systems. The average absolute relative errors of critical CO_2 mole fraction and critical pressure estimated by NN are 6.25% and 0.99%, respectively.

The predicted and experimental phase diagrams of oils F and BSB are shown in Figs. 96 and 97. The predicted P_b for oil F are very good from 0 to 25 mole % injected CO_2. Above 25 mole % CO_2 the predictions are a little high and the critical point is at a few mole % CO_2 too low, but at the right experimental pressure. The three-phase region is a good match with the phase boundaries being a little higher over some regions and a little low over the others. For oil BSB, the bubblepoint values were a little low at low CO_2 concentration and then crossed at about 40 mole % CO_2 (see Fig. 97). The three-phase region matched well from 60 to 70 mole % CO_2 and was generally low over the entire envelope, but more extensively above 70 mole % CO_2.

Jorgensen and Stenby[120] and Coutinho *et al.*[99] have demonstrated that EOS predictions of the three-phase region are good without tuning any parameter for some oil systems, but for others tuning of the binary interaction parameters to match the experimental three-phase region is necessary.

Generally, 10 points are considered a limited data base, especially with the number of variables considered. Though there were inaccuracies in the prediction of the phase boundaries due to the limited data base used for training and scatter in experimental data presented by various authors in the literature, the results are encouraging when compared with EOS predictions.

Conclusions and Recommendations for Phase Behavior Simulations

A preprocessor for reservoir compositional simulators has been developed to match the bubblepoint pressure data by tuning the average molecular weight of C_{7+} fraction.
NN appear to be valid for predicting P_b and B_{ob} of all types of gas/oil mixtures with properties falling within the range of data used in training. In this case 80 Middle East crude oils were used for training, and another 80 Middle East and 11 North Sea crude oils that fell within the training system range were tested with excellent result.
NN were superior to correlations when both were used on systems that were not included to train or develop the correlation. Therefore, NN appear to be a better method for estimating oil properties with increased accuracy over traditional methods.
With a larger range of experimental data for training, NN could be a standard method for the prediction of P_b and B_{ob}.
Though there were inaccuracies in the prediction of the phase boundaries due to the limited data base used for training and the difficulty of obtaining accurate experimental data, the NN results are acceptable compared to EOS predictions. With more data points and more accurate experimental data for training, NN is a possible method to improve predictions in critical areas such as the CO_2-crude oil mixture three phase region.

Foam Simulations

Efficient application and evaluation of candidate reservoirs for CO_2-foam processes require a predictive foam model. Accurate prediction is difficult because the mobility of CO_2 is complex, depending on bubble size or foam texture, and foam texture itself depends on many factors.[121] Despite the complexity of foam behavior, several approaches for modeling foam displacement can be found in the literature. The first approach uses a semiempirical expression for gas mobility in the presence of foam as a function of flow rate, gas fraction, surfactant concentration, and other factors.[122-126] The parameters associated with the expression can be obtained from various foam tests. Even though foam texture controls gas mobility,[127] there is no explicit reference to foam texture or foam bubble size in the semi-empirical expression. The second approach[82,83,121,128-131] uses a bubble population balance model[132] to allow the effect of foam texture to be directly incorporated into an expression for gas mobility in the presence of foam. The bubble population balance model accounts for changes in foam texture caused by mechanisms that create, destroy, or propagate foam in addition to foam trapping and mobilization. Nevertheless, the model parameters of the functional forms chosen for each mechanism need to be fitted to coreflood data from foam tests. The third approach[133,134] relies on the relation between capillary pressure, foam texture, and gas mobility. It is a local-equilibrium version of the bubble population balance model for strong foams under

conditions where capillary pressure dominates foam texture and gas mobility. However, as a local equilibrium model, it does not describe some of the foam behavior that depend on flow rate, e.g., foam mobility increases with increasing gas rate.[5,82]

The foam resistance factor[42,81] is a parameter commonly used to assess the magnitude of mobility reduction. If foam is not generated, the resistance factor is unity. If foam is generated, the value of the resistance factor quantifies the effect of the presence of foam. The objective of this study is to develop a predictive foam model that can make use of the resistance factor data available from the surfactant selection process. Recent laboratory foam tests[5,42,82] elucidated the relationships of surfactant concentration, injection flow rate, foam quality, and core permeability with the foam resistance factor. Based on these relationships, a foam model was developed and incorporated into two reservoir simulators. The first is a pseudo-miscible simulator, MASTER,[135] obtained from the Department of Energy, and the second is an equation-of-state, compositional simulator, UTCOMP,[136,137] provided by the University of Texas at Austin. Both simulators have been successfully modified to simulate CO_2-foam flooding processes where the foam resistance factor data are input as data tables.

Foam Model

A semi-empirical approach is used to calculate the gas mobility in the presence of foam instead of using a mechanistic approach based on bubble population balance. The gas mobility in the presence of foam is modeled based on resistance factor data that are readily available once the surfactant selection process is done.

The following major assumptions were used in the foam model:

1 Foam affects only the gas mobility.

2. Foam cannot exist if any of the following foam existing conditions are not met:

$$S_g > S_g^{\lim} \qquad S_o < S_o^{\lim}$$
$$C_s > C_s^{\lim} \qquad S_w > S_w^{\lim}$$

   where C_s is the surfactant concentration in the water phase, and S_g, S_o, and S_w are the gas,- oil-, and water-phase saturations, respectively. The variable with superscript *lim* corresponds to the limiting value of each variable.

3. Foam generation will occur only if: the gas-liquid volumetric ratio is greater than a limiting value, the gas saturation is increasing, and the foam existing conditions in 2 are satisfied.

4. Surfactant adsorption on the rock can be modeled with a Langmuir-type model and is unaffected by the presence of foam.

By definition, the resistance factor R_f can be written as

$$R_f = \frac{M_{CO_2+BR}}{M_{CO_2+SS}} \tag{15}$$

where M_{CO2+BR} is the total CO_2/brine mobility of obtained from the experiment of simultaneous injection of CO_2 and surfactant-free brine, M_{CO2+SS} is the total mobility of CO_2/surfactant solution obtained from the experiment of simultaneous injection of CO_2 and surfactant solution, and both mobility measurements are conducted at the same gas-liquid volumetric injection ratio. The total mobility of CO_2/brine is a combination of the mobility of CO_2 (gas phase) and the mobility of surfactant-free brine (water phase), hence,

where M_w is the water mobility and M_g is the gas mobility. Similarly, the total mobility of CO_2/surfactant solution is equal to the sum of the mobility of surfactant solution (water phase) and the mobility of CO_2 (gas phase) in the presence of foam. Because the water mobility is not affected by the presence of foam, therefore, the gas mobility in the presence of foam is

$$M_g^{foam} = \frac{1}{R_f}\left(M_w + M_g\right) - M_w \tag{16}$$

If foam can be generated, the foam resistance factor is determined from the lookup tables and the gas mobility in the presence of foam is calculated. The calculated value of gas mobility in the presence of foam will not be modified until foam ceases to exist. Gas mobility can be altered by changing either the gas relative permeability or viscosity or changing both together. For convenience, the effect of foam on gas mobility is represented by altering only the gas relative permeability.

Foam Simulators

Two reservoir simulators have been modified to include the foam model. The first is UTCOMP, described by Chang,[134] and the second is MASTER, described by Ammer *et al*. [133] The resistance factor data, which depend on interstitial velocity, foam quality (gas-liquid volumetric injection ratio or gas fraction), surfactant concentration, and rock permeability, are input as lookup tables in the simulators. The routines that use the lookup tables in the simulators will first locate the intervals for interpolations by checking conditions in the order of permeability, foam quality, surfactant concentration, and interstitial velocity. Then the interpolations are done in the order of velocity, concentration, quality, and permeability. The resistance factor is assumed to be log-linear over velocity and permeability but linear over concentration and quality. At the edges of these tables, simple two-point extrapolation method is used.

Compositional Foam Simulator. The basis of the compositional foam simulator is UTCOMP. By utilizing the tracer features in UTCOMP, the compositional foam simulator is developed without the addition of a surfactant conservation equation into UTCOMP. The tracer adsorption model has been modified to account for the adsorption isotherm. The surfactant movement is tracked by treating the surfactant as the first aqueous tracer component. The major modifications that were made to

UTCOMP include (1) the addition of lookup tables for the resistance factor data and (2) the addition of an algorithm to calculate the gas mobility in the presence of foam.

Pseudomiscible Foam Simulator. MASTER is a pseudomiscible simulator that is an extension of the so-called black-oil model and uses the mixing-rule approach to calculate effective fluid densities and viscosities. For technical details of the equations and miscible features included in MASTER, we refer the reader to the original report by Ammer *et al*.[133] [A report for the new version of MASTER is being prepared and will be available from the Department of Energy.] The major modifications that were made to MASTER include: (1)the addition of a conservation equation including the adsorption isotherm to permit the simulation of surfactant movement; (2) the addition of lookup tables for the resistance factor data; and (3) the addition of an algorithm to calculate the gas mobility in the presence of foam.

Validation Results

To assess the adequacy of the included foam features in UTCOMP and MASTER, several validation tests have been performed. Note that these simulation tests did not necessarily represent a real field application and the simulation results have been published earlier.[139]

Test Problem I. The initial conditions for test problem I was established by simulating a 10-year water flood and then a 5-year CO_2 flood from an initial pressure of 1500 psia and an initial water saturation of 25%. In this test problem, UTCOMP was used to perform the simulation tests on a three-dimensional quarter of a five-spot pattern of a reservoir with five physical layers. The production and injection wells were located in opposite corners of the pattern and were completed in all five layers. A detailed description of the reservoir data is given in Table 23. The reservoir temperature was 90°F. The reservoir fluid description reported by Lim *et al.*[138] was used because the phase behavior and properties of the oil and CO_2 are typical of those of multiple-contact, miscible field condition of West Texas. A modified Corey relative permeability model with water, oil, and gas endpoints of 0.21, 0.71, and 1, respectively, was used. The water injection rate was 130 STB/D (2500 lb-mole/day) during water injection period and the gas injection rate was 300 MSCF/D (800 lb-mole/day) during gas injection period. The production well was limited by a bottomhole pressure of 1500 psia. The wellbore radius was 0.33 ft for both injection and production wells. The foam test was performed using the following injection schedule:

Surfactant solution (2500 ppm active) injection for 122 days.

Six rapid cycles of alternating injection of surfactant solution and gas/solvent (SAG) for a total of 90 days. Each SAG cycle consisted of three days of surfactant solution injection and 12 days of gas/solvent injection,

Gas/solvent injection for 153 days.

This schedule was also specifically selected to mimic the injection schedule used in a CO_2 foam pilot test at the East Vacuum Grayburg-San Andres Unit (EVGSAU).[140]

In order to evaluate the foam test, a base case was needed. The injection schedule of the base case was identical with that of the foam test except the injection of surfactant solution was replaced with the injection of water (surfactant-free brine). Figure 98 shows the oil rate history for the foam

test and the base case. Observe the significant increase in the oil rate at 250 days from about 10 STB/D to about 85 STB/D. Then the oil rate dropped and leveled off at about 60 STB/D for the foam test compared to the base case. This kind of response is similar to that observed in the EVGSAU field pilot test as shown by Martin *et al.*[140] in their Fig. 7. Figure 99 shows a corresponding decrease in the instantaneous gas-oil ratio (GOR). Figure 100 shows higher oil recovery for the foam test with an incremental oil of 5 MSTB. To better illustrate the results, the injection profile for the two cases at 263 days of simulation are shown in Fig. 101. Note that layer 4 is the most permeable layer with a permeability of 1000 md, while layers 2 and 5 are the least permeable layer at 70 md. Figure 102 shows that, for the base case, most of the injected CO_2 would be injected through the highest permeable layer, while the least amount of CO_2 would be injected through the least permeable layers. Consequently, the sweep was poor and the oil rate was low for the base case (Fig. 98). However, for the foam test, there were significant increase in the amount of CO_2 injected through layers 2 and 5. At the same time, the amount of CO_2 injected through layer 4 was reduced significantly from 76.6% to 1.8% of the total moles injected. Therefore, the profile modification due to the presence of the foam significantly improved the sweep and thus resulted in higher oil rate (Fig. 98). These results show that UTCOMP has been successfully modified to simulate foam flooding processes. Figures 102–104 show the resistance factor data used in the simulations, which have been modified from the experimental data reported by Chang and Grigg.[42] The effect of the magnitude of the foam resistance factor on the oil rate was examined by using a scaling parameter F. As shown in Fig. 105, the response to the foam for the oil rate to increase was delayed when the magnitude of the foam resistance factor data was scaled down by the parameter F from 1 to 0.35.

Test Problem II. Because of extensive modifications and additions that were made to the code of MASTER, test problem II was designed to validate the capability of MASTER using the results from UTCOMP. In order to compare the results from an equation-of-state compositional simulator and a pseudo-miscible simulator, the so-called black-oil PVT properties used in the pseudo-miscible simulator should correspond with the equation-of-state characterization parameters used in the equation-of-state compositional simulator. To satisfy this condition, the reservoir fluid descriptions reported in the fifth Comparative Solution Project[141] were used. In this reservoir system, the oil contained the following mole percents: 50% C_1, 3% C_3, 7% C_6, 20% C_{10}, 15% C_{15}, and 5% C_{20} and the injection gas/solvent contained 77% C_1, 20% C_3, and 3% C_6. The PVT properties were generated from the simulations of constant composition expansion and differential liberation expansion for both the oil and the injection gas/solvent. The minimum miscibility pressure is 3000 psia. For detailed reservoir fluid descriptions including the PVT properties and characterization parameters, we refer the reader to the original paper by Killough and Kossack.[141]

Test Problem II involved five cycles of alternating injection of water and gas/solvent (WAG) for a total of 5 years. Each WAG cycle consisted of 122 days of water injection and 243 days of gas/solvent injection. The water injection rate was 770 STB/D (15000 lb-mole/day) during water injection period and the gas injection rate was 1100 MSCF/D (2900 lb-mole/day) during gas injection period. The production well was constrained to a bottomhole pressure of 3000 psia. The wellbore radius was 0.25 ft for both production and injection wells. The reservoir model is the same one used in Test Problem I (Table 23). The reservoir had a temperature of 160ºF, an initial water

saturation of 20%, and an initial reservoir pressure of 4000 psia. The simulation results from MASTER and UTCOMP were in excellent agreement for the oil rate and the cumulative oil production as shown in Figs. 106 and 107. Besides the validation of MASTER, this problem also provided a check on the fluid descriptions taken from the fifth Comparative Solution Project such that the black-oil PVT properties used in MASTER did correspond with the equation-of-state characterization parameters used in UTCOMP.

Test Problem III. To test the foam features in MASTER, the five-year WAG injection schedule used in Test Problem II was modified by substituting the foam test schedule used in Test Problem I for the WAG schedule at the third year. Similarly, the injection schedule for the base case was identical to that of the foam test, except the injection of surfactant solution was replaced with the injection of water (surfactant-free brine). Figure 108 shows the oil rate history from the completion of the SAG injection (900 days of simulation) for the foam test and the base case. The oil rate for the foam test was able to maintain above 100 STB/D for 300 more days as compared to the base case. The corresponding reduction in GOR can be observed in Fig. 109. By the end of the five-year injection, the incremental oil was about 25 MSTB as shown in Fig. 110. These results show that MASTER has been successfully modified to simulate foam flooding processes. This is also confirmed by comparing the foam test results with those of UTCOMP. The foam test results from MASTER and UTCOMP were in good agreement for the oil rate and the cumulative oil production, as shown in Figs. 111 and 112.

EVGSAU Pilot History Match

In order to calibrate the foam model with field data, the production history prior to the foam tests has to be matched. The history match model was constructed based on the EVGSAU pilot data. The field pilot pattern of nine wells, as shown in Fig. 113, and the surrounding 16 wells were included in the history match model (see Fig. 14). Well 3332-001 (#13), located at the center of the pattern, was the foam injection well. Well 3332-032 (#12) was the "offending" production well. The history match model consisted of a 16 x 16 grid (see Fig. 114) in seven separate layers for a total of 1792 grid blocks. These seven layers were based on the type-log zonation (C-3, C-2, C-1, D, E, G, and H). The history match simulations involved three phases of simulations: primary depletion from 1959 to 1979, waterflood from 1980 to 1985, and CO_2-flood (water alternating CO_2) from 1986 to 1992. Figure 115 compares historical and simulated cumulative production for the offending production well of the pilot area from 1959 to 1985. As shown in the figure, the match of the cumulative gas production was very good (Gas (s) vs Gas (h)) and the cumulative water production (Water (s)) was less than the field data (Water (h))although the breakthrough of water was virtually identical.

Currently, the third phase of the history match simulations is still in progress because we did not have a satisfactory match for this phase of simulations. However, a preliminary foam test simulation was performed based on the history match model obtained from the match of primary depletion and waterflood (1959–1985). The foam test simulation was performed using exactly the same EVGSAU injection schedule from January 1985 to November 1991 for all the injection wells except the foam injection well 3332-001 (#13). The injection schedule for the foam injection well

were modified as following:

Surfactant solution (2500 ppm active) injection for three months from August to October 1988.

Five rapid cycles of alternating injection of surfactant solution and CO_2 (SAG) for a total of 75 days. Each SAG cycle consisted of 3 days of surfactant solution injection and 12 days of CO_2 injection, The surfactant solution injection rate was 1703.53 STB/D and the CO_2 injection rate was 3862.05 MSCF/D. These rates were obtained by averaging the rates of the 75-day period so that the whole material balance in the pilot pattern could be maintained.

Figure 116 shows the oil rate history of the offending production well from the initiation of the SAG injection (1400 days of simulation) for the foam test and the base case. The oil rate for the foam test was reduced during 1450 to 1550 days of simulation but was increased later during 1750 to 1950 days of simulation as compared to the base case. The reduction of the gas rate of the offending production well for the foam test was clearly shown in Fig. 117 during 1450 to 1750 days of simulation as compared to the base case. The reduction of both the oil and gas rate at 1450 days of simulation indicated that foam was generated at the path from the foam injection well to the offending well, and the continue reduction of gas rate until 1750 days of simulation indicated CO_2 was diverted away from the path and resulted in the higher oil rate during 1750 to 1950 days of simulation. By the end of the simulation, the incremental oil of the offending production well was about 1.7 MSTB. Note that the incremental oil of the foam pilot area was about 9 MSTB as shown in Fig. 118. This indicated that foam treatment on the pilot area increased the oil production for all the production wells, not just the offending production well. Therefore, the presence of the foam significantly improved the sweep and thus resulted in higher oil production. The corresponding reduction in instantaneous gas-oil ratio and cumulative gas production can be clearly observed in Figs. 119 and 120.

Conclusions

1. A foam model based on the foam resistance factor was developed.
2. Both UTCOMP and MASTER have been successfully modified to simulate foam flooding processes where the resistance factor data are input as lookup tables.
3. The simulation results show an increase in the oil production rate attributed to the effects of foam, and are consistent with the observations from the EVGSAU field pilot.
4. The results also show successful profile modification because of the presence of foam, thus resulting in significant sweep improvement.

Horizontal Well Simulations

Important technological advances during the last decade have made it possible to drill and complete horizontal well economically.[142] Because of the better sweep efficiencies and higher injectivities possible with horizontal wells, all improved oil recovery (IOR) methods would benefit from their use.[143-147] To successfully apply horizontal wells, reliable and accurate tools are needed to aid in the design. A reservoir simulator with horizontal well capabilities can provide guidance into

the design of well lengths, locations, and other factors associated with horizontal wells. However, the pseudo-miscible reservoir simulator, MASTER (discussed in the previous section), was only able to handle vertical well simulations; that is, only the vertical well parallel to the z-axis was considered in MASTER. Therefore, one of the objectives of this work was to incorporate the horizontal well modeling capability into MASTER. The primary motivation of this study was to conduct a systematic investigation of CO_2 flooding using horizontal wells in conjunction with foam.

Well Model

We have implemented the equivalent wellblock radius formulation of Babu *et al.*[148] into MASTER, because the equation is general and is valid for both vertical and horizontal wells, for any well locations and for any anisotropy. Furthermore, the equation is still accurate for anisotropic grids of high aspect ratio whereas other well model equations required modifications. However, this formulation is very sensitive to nonuniform grids. For a detailed description of the general analytical formula for the equivalent wellblock radius, we refer the reader to the original paper of Babu *et al.*[148]

Modifications to MASTER

In the original MASTER code, the well was represented only as a vertical well parallel to the z-axis. The wellblock productivity index were input from the users. Therefore, the first task was to modify the code to allow for flexible well orientation, that is, wells can be parallel to the x-, y-, or z-axis. Horizontal wells are parallel to the x- or y-axis, whereas vertical wells are parallel to the z-axis. The second major modification involved incorporating Babu *et al.*'s well model into the simulator.

Validation Results

Cases 3a and 3b of the problem given in the Seventh SPE Comparative Solution Project[149] were used to validate the horizontal well model implemented in MASTER. This problem deals with oil recovery by bottom water drive in a thin reservoir where coning is important. Fluids are produced from a horizontal well drilled in the top layer (layer 1), and a constant pressure line source is used to simulate the bottom water drive. The horizontal well produces at a constant liquid rate of 9000 STB/D. Cases 3a and 3b were designed to examine the effect of well length on the recovery. The length of the horizontal producer was 900 ft in case 3a and 2100 ft in case 3b. The length of the constant pressure injector was kept constant at 2700 ft in both cases. For a detailed description of the problem, we refer the reader to the original paper of Nghiem *et al.*[149]

Figure 121 compares the oil rate history obtained from MASTER with those of the participants in the project for Case 3a. Since there were a total of fourteen participants in this project, we have only used the highest and the lowest results from the band of results produced by the participants indicated as SPE (High) and SPE (Low), respectively, in the legend. The corresponding water-oil ratio (WOR) obtained from MASTER is shown in Fig. 122 compared to the results from the SPE project. For Case 3b, the results are shown in Figs. 123 and 124. It is clear that the results predicted by MASTER fall within the range of the results predicted by the fourteen participants in this project.

Conclusions

The horizontal-well feature has been successfully incorporated into MASTER based on the simulation results validated by the solutions of the Seventh SPE Comparative Solution Project.

TASK 3: LOW IFT MECHANISMS WITH APPLICATIONS TO MISCIBLE FLOODING IN FRACTURED RESERVOIRS

Introduction

Interfacial tension (IFT) provides a logical link between miscibility criteria such as MMP and the flow behavior of near-miscible CO_2/oil systems in heterogeneous reservoirs. The objective of Task 3 primarily concerns facilitating the determination of IFT of CO_2/oil systems and its application to CO_2 injection into reservoirs under a wide range of conditions. The accomplishment of Task 3 would provide reservoir engineers with a reliable method for estimating IFT of CO_2/oil under a wide range of reservoir conditions. Of particular interest are low and high values of gas/oil IFT, gas/brine IFT at reservoir conditions, and oil/brine IFT at reservoir conditions.

We rigorously investigated both the origin and evolution of the methodologies developed for IFT prediction. We found that there is no systematic method for calculation of any of the above stated systems. We found considerable confusion in the literature, even for the calculation of simple gas/oil systems via the parachor method. Here is a summary of the results of our research into IFT predictions:

1) Many past methodologies were developed with implicit, and incorrect, assumptions regarding the scaling exponent between IFT and density difference which is the key to parachor calculations.

2) Recent theoretical research in the physics literature appears to have isolated and verified the scaling exponents, yet the petroleum industry has been unaware of the advances.

3) We have investigated scaling behavior near and far from the critical point and found that the scaling exponents are unique; therefore, they should not be used as adjustable parameters.

4) Parachors for pure components and C_{7+} fractions have been recalculated from carefully selected data found in over 250 technical papers. The parachors are based on current understanding of critical phenomena; thus, neither should these be used as adjustable parameters.

5) The modified parachor method presented in this report has proven superior to other parachor calculations for application in low and high IFT systems, both CO_2/oil and gas-condensates.

After completing our investigation into IFT prediction methodologies, we experimentally investigated surface tension of CO_2 near the critical point. A more accurate method for the determination of low IFT from pendant drop measurements was developed. Low IFT CO_2 gravity drainage in naturally fractured reservoirs was studied experimentally and theoretically. Promising

experimental results were matched by a newly developed mathematical model. The results of Task 3 address both fundamental research and research with direct applications to CO_2 flooding.

Investigation on Parachor Method For IFT Prediction

Background

Interfacial tension (IFT) is one of the key parameters controlling recovery from oil reservoirs. In a low IFT region that occurs around the critical point close to dew and bubblepoint lines, the IFT dominates relative permeabilities and residual liquid saturations. Prediction of IFT is essential for modeling many secondary and tertiary oil recovery processes. However, there is no consistent standard by which this may be accomplished.

Prediction of the IFT of multicomponent systems using thermodynamics of adsorption at the interface has been demonstrated by Guggenheim and Adam[150] at low pressures where the vapor density is negligible. The commonly used methods in the petroleum industry for predicting IFT are empirical correlations called parachor methods because of their simplicity. Although recently, the gradient theory has been demonstrated to be superior to the parachor method, it may be applied accurately to interfaces at only conditions far from the critical region according to Cornelisse *et al.*[151] We are interested in calculations of IFT of reservoir fluids, both in the low and high IFT regions. Therefore, only parachor methods are discussed in this report.

Based on experimental observations, Macleod[152] recognized the following relation between surface tension and densities:

$$\frac{\sigma}{(\rho_l - \rho_v)^4} = C \tag{19}$$

where σ is surface tension, ρ_l and ρ_v are densities of the liquid and vapor phases, respectively, and C is a constant. The exponent 4 was adopted from Van der Waal's equation, which is based on the assumption that the force of attraction between molecules falls off as the 4th power of distance between them. Sugden[153] related the constant C to chemical composition of the substance. He defined a parameter by

$$P = \frac{M}{\rho_l - \rho_v}\sigma^{\frac{1}{4}} \tag{20}$$

where M is molecular weight and P is called *parachor,* which was believed to be a measure of the molecular volume and chemical composition. After Sugden's definition of the parachor in 1924, many researchers have interpreted and evaluated parachors for a variety of pure substances. Quayle[154] provides a summary of these investigations.

The parachors had been limited to calculations of surface tensions of pure substances until the 1940s when the concept was introduced to the petroleum industry. Weinaug and Katz[155] employed the pure substance parachors to calculate the IFT of mixtures; Katz *et al.*[156] utilized the parachors to determine the IFT of crude oils; and Reno and Katz[157] tried to determine the IFT of hydrocarbons containing dissolved nitrogen. The equation they used for the multicomponent systems is essentially a linear combination of equations for pure substances with mole fraction weighting:

$$\sigma = \left[\sum_{i=1}^{n} P_i \left(x_i \frac{\rho_l}{M_l} - y_i \frac{\rho_v}{M_v} \right) \right]^4 \tag{21}$$

where x_i and y_i are mole fractions of component i in liquid phase and vapor phase, respectively. Based on experimental observations for propane and normal butane, Hough and Stegemeier[158] proposed the following equation for mixture IFT calculations:

$$\sigma = \left[\sum_{i=1}^{n} P_i \left(\frac{x_i}{V_l} - \frac{y_i}{V_v} \right) \right]^{3.67} \tag{22}$$

where V_l and V_v are molar volumes of liquid phase and vapor phase, respectively. Equation (22) is identical to Eq. (21), with the only difference of scaling exponent 3.67 rather than 4. Lee and Chien[159] also presented an equation for mixture IFT calculations:

$$\sigma = \left[\sum_{i=1}^{n} P_i \left(x_i \frac{\rho_l}{M_l} - y_i \frac{\rho_v}{M_v} \right) \right]^{3.91} \tag{23}$$

According to Lee and Chien, the parachor can be determined based on critical properties of the components. A slight modification to the Weinaug-Katz equation was made by Hugill and Van Welsenes[160] using a correlation for pure component parachors and a two-parameter mixing rule for mixture parachors.

Firoozabadi *et al.*[161] compared calculated surface tensions of reservoir crude oil/gas systems using the Weinaug-Katz method with experimental data and claimed that for reservoir-fluid systems that do not contain asphalt materials, a quadratic parachor correlation would suffice for computation of interfacial tension. Gasem *et al.*[162] tested the prediction methods proposed by Weinaug and Katz, the modifications by Hugill and Van Welsenes, and Lee and Chien for IFT of CO_2 and ethane in hydrocarbon solvents. They concluded that the Weinaug-Katz method gives IFT results with an average error of less than 10% when a scaling exponent of 3.66, instead of 4, is used. Many linear and non-linear correlations for parachors have been developed since 1936. Ali[163] compared these parachor methods and modifications using ten parachor correlations. He concluded that the Weinaug-Katz method with a linear parachor correlation that appears in Fanchi[164] yields the best IFT predictions for reservoir oil/gas systems with a mean absolute deviation of 22.2%. Ali also showed that the Lee-Chien method can produce large errors in reservoir fluid calculations where the critical properties of the heavy fluid components are uncertain. Based on statistical analysis, Fawcett[165] evaluated correlations and parachors to predict low IFT in condensate systems. He concluded that the Hough-Stegemeier method with a linear correlation for crude cut parachors gives low IFT predictions with small systematic errors for multicomponent systems.

Obviously there has been considerable confusion in the literature concerning the parachor method for estimating IFT. The confusion is primarily based upon the lack of precise definition of the scaling exponent and parachors derived based on this exponent. We addressed: (1) clarification of the confusion about the scaling exponent, (2) derivation of parachors for pure species occurring in petroleum fluids and oil cuts, and (3) verification of the validity of these derived parachors in IFT prediction of reservoir fluids.

Scaling Exponent

This section discusses the origin of various values of the scaling exponent that appear in the literature. The applicability of the scaling exponent 3.88 established in the modern physics literature is evaluated using experimental data for 23 compounds and compound mixtures occurring in petroleum fluids.

Origin of Various Values

From the last section, the exponent 4 in the Weinaug-Katz equation (Eq. 21) was adopted, through Macleod and Sugden, from the Van der Waal's equation without any justification. Macleod assumed that since the Van der Waal's equation is based on the assumption that the force of attraction between molecules falls off as the 4th power of distance between them, then the value 4 should be the scaling exponent. We have re-examined Macleod's original data and found this exponent 4 to be a rough approximation. The actual values of Macleod's exponent are less than 4 as shown in Fig. 125 and Table 24.

Another means of quantifying the exponent is to use the critical scaling theory for IFT:

$$\sigma = \sigma_0 \left(1 - \frac{T}{T_c} \right)^{\gamma} , \tag{24}$$

and density difference:

$$\Delta\rho = \Delta\rho_0 \left(1 - \frac{T}{T_c} \right)^{\beta} \tag{25}$$

Dividing Eq. (24) by Eq. (25) gives a relationship between IFT and $\Delta\rho$.

$$\sigma = C(\Delta\rho)^{\frac{\gamma}{\beta}} \tag{26}$$

The constant *C* is related to the parachor and the ratio of the two critical scaling exponents, γ/β , is equivalent to the exponent in the parachor equation.

Based on empirical relations given by Guggenheim,[166] Hough and Stegemier[158] proposed values of 1/3 (or 0.33) for β and 11/9 (or 1.22) for γ. The ratio of these two values gives Hough-Stegemeier's scaling exponent of 11/3 (or 3.67). The empirical relations provided by Guggenheim originally appeared in Guggenheim's[167] early work published in 1945. These relations were established based on limited measurement of $\Delta\rho$ and IFT. The eight fluids used were *Ne, Ar, Kr, Xe, N_2, O_2, CO*, and CH_4.

At one time, many researchers believed that all materials have the same β exponent—1/3. However, until the 1970s, this had not been rigorously demonstrated as pointed out by Stanley.[168] It can be seen that the 1/3 proposed by Guggenheim had not been accepted by physicists as a general value for β when it was adopted by Hough and Stegemeier. The γ value 11/9 was also established by Guggenheim's work[166] based on limited measurements on *Ne, Ar,* N_2 and O_2. Again, the scaling exponent 11/9 had not been accepted in the physics literature as a general value for β when it was adopted by Hough and Stegemeier in 1961. Therefore, it appears that the exponent 3.67 proposed by Hough and Stegemeier is not applicable to all fluids. Lee and Chien[159] adopted β and γ values from different sources. They used the empirical value 11/9 (or 1.22) for γ given by Guggenheim[166] and theoretical value 0.3125 for β given by Fisher.[169] The ratio of these two values gives Lee-Chien's

scaling exponent of 3.91. The 0.3125 is based on one of a class of decorated Ising models described by Fisher.[170] According to this model, the γ value is 1.25 rather than 1.22. This reveals that the scaling exponent 3.91 in Lee-Chien's equation may not be reliable because it was established based on inconsistent data sources.

Sengers and Sengers[171] summarized theoretical values of these critical scaling exponents found in the physics literature as shown in Table 25. The currently accepted values for β and γ in modern physics are 0.325 and 1.26, respectively (Rowlinson and Widom,[172] Widom,[173] and Moldover[174]) yielding 3.88 for the critical scaling exponent in the parachor equation.

Applicability of Exponent 3.88

The question of applicability of critical scaling exponents well away from the critical point has been speculated upon, but in the literature no evidence can be found that proves or disproves the extent of critical scaling and what governs deviations from critical scaling far from the critical point. From Macleod's data shown in Fig. 125, we could assume that the theoretically derived critical exponent (3.88) may be applicable over a wide range of conditions, while other more recent papers have suggested this number should be altered away from the critical region.

Haniff and Pearce[175] discussed the four exponents (4, 3.67, 3.91 and 3.88) that appear in parachor equations. They also measured IFT and $\Delta\rho$ of C_1/C_3 mixtures at different temperatures. By fitting their experimental data to the parachor equation, they found that the exponent in the parachor equation increases with temperature. This exponent increases from 3.70 to 3.83 as temperature increases from 29.6º C to 39.2º C for the C_1/C_3 mixture. Since all these values are less than 3.88, they believed that the experimental points were outside the critical region. They also considered the value 3.70, which was derived at a temperature of 29.6ºC, to correspond to Hough-Stegemier's exponent 3.67. They concluded that along the critical isotherm and, more particularly, in the vary narrow region close to the critical point, the exponent is equal to 3.88. They referred to exponent values that are less than 3.88 as "effective" critical exponents. Huygens *et al.*[176] plotted IFT-density data taken from studies by Haniff and Pearce,[175] Wagner and Leach,[177] Firoozabadi and Ramey,[178] and Satherley *et al.*[179] in one graph. They found that when all the data points are considered in a wide range of IFT below 1 mN/m, the data exhibits a linear relationship on a log-log scale with a slope of 3.88, which is consistent with the theoretical value of the scaling exponent. Accordingly, they define the critical region as the region where the IFT is less than 1 mN/m.

To explore the applicability of the scaling exponent 3.88, we first plotted IFT versus reduced temperature ($1-T/T_c$) data in the low IFT region for methyl ether and CO_2 as demonstrated in Fig. 126. The slope is very close to 1.26. We then plotted IFT versus reduced temperature ($1-T/T_c$) data for 57 pure components. Data are cited from Vargaftik.[180] The measured IFT data were mostly between 10 mN/m and 30 mN/m. IFT was measured at reduced temperatures mostly ranging from 0.2 to 0.6. Although most of data points fall far beyond the critical region defined by Huygens *et al.*, distribution analysis shown in Fig.127 indicates that most of the slope values are still in the neighborhood of 1.25, which is close to the critical scaling exponent 1.26.

Figure 128 shows a plot of density difference versus reduced temperature for the iso-butyric acid/water system studied by Greer.[181] This figure demonstrates the validity of the scaling exponent $\beta = 0.325$ near to the critical point. While similar data are lacking in literature, more IFT-density data for multicomponent mixtures are available from previous investigations. Figure 129 shows a plot of IFT vs. $\Delta\rho$ for methane-propane mixtures at various temperatures. Data used to generate this plot are from Weinaug and Katz's[155] paper for the C_1/C_3 binary system. The experimental data conforms closely to the slope derived by critical scaling theory, even well away from what is considered "near critical." Figure 129 indicates that for this gas condensate system the slope of 3.88 holds at least up to an IFT value of 10 mN/m. Figure 130 shows experimental data presented by Satherley *et al.*,[182] Morrow *et al.*,[183] and Cuiec *et al.*[184] for oil/brine systems containing alcohol. This figure tends to confirm the definition Huygens *et al.* of the near-critical region. Shown in Fig.131 are data obtained by Huygens *et al.* and Satherley and Schiffrin for three nitrogen/hydrocarbon systems. This figure indicates that the near-critical region for the nitrogen/hydrocarbon systems may be much narrower than that defined by Huygens *et al.* The slope drops below 3.88 when the IFT is greater than 0.1 mN/m. Figure 132 shows experimental data provided by Hsu *et al*.,[185] Nagarajan and Robinson,[186,187] and Gasem *et al.*[188,189] for some CO_2 hydrocarbon systems. The experimental data match the slope derived by critical scaling theory closely, even well away (IFTs up to 10 mN/m) from what is considered "near critical," except for the C_{14}/CO_2 system which has a relatively narrow critical region.

It must be emphasized that near the critical point, the slope has a theoretical value of 3.88 regardless of the path taken to the critical point, whether by change in temperature or pressure (as in the case of CO_2-hydrocarbon mixtures) or adding a third component such as alcohol. Figures 125 and 129 through 132 clearly demonstrate that as low IFT values are achieved (approximately below 1.0 dyne/cm), the slope of the plot is very near the theoretical value of 3.88. Figures.130 and 131 show that alcohol/oil/water and N_2/hydrocarbon systems deviate from a slope of 3.88 at higher values of IFT. The deviation of the nitrogen/hydrocarbon and alcohol/oil/water systems from critical exponents are explained by the following: If a single drop of alcohol is added to an oil/water system, the alcohol will rapidly adsorb at the interface. The IFT will be significantly reduced yet the density difference between the bulk phases will change very little. The result is that the slope of the IFT/$\Delta\rho$ plot is greater than 3.88. Conversely, nitrogen weakly adsorbs at the interface, thereby requiring high pressures for significant solubility and mass transfer between the phases before the IFT is lowered. In addition, the molecular weight of nitrogen is lower than that of most hydrocarbons in oil; therefore, it usually has a negative contribution to gas density, which keeps IFT high. Thus, the nitrogen/hydrocarbon slopes are seen to be less than 3.88. These special systems are discussed in a separate section in this report.

In summary, for strongly interacting systems, *e.g*., brine/oil/alcohol, weakly interacting systems, *e.g.*, N_2/oil, or molecules with a large size discrepancy, *e.g.*, CO_2/C_{14}, the scaling exponent may not be valid outside the critical region as defined by Huygens *et al*. However, for CO_2, crude, or gas condensate systems, the scaling exponent's wide range of validity ensures relatively accurate IFT predictions by the parachor method.

New Parachors

This section presents parachors of pure components derived using 3.88 as the scaling exponent. These parachors are correlated to molecular weight. Correlations have been developed for hydrocarbon mixtures with different composition. Parachors of oil cuts are determined utilizing these correlations.

Pure Substance

Parachors of CO_2, N_2, H_2S and 136 hydrocarbons commonly encountered in crude oils are back calculated from measured density and interfacial tension data. The experimental data are found in the literature.[152-154,190-221] These experimental data are carefully screened from 259 technical papers. Experimental data consistently provided by different investigators are selected for parachor determinations in this work. The resultant parachors are presented in Table 26. With some mixing rules, these parachor data can be utilized for predicting IFT of well defined hydrocarbon systems with known exact compositions.

Hydrocarbon Mixtures

It is convenient to lump or sometimes split hydrocarbon components in analyzing hydrocarbon "plus fractions" of crude oil systems. Usually, the plus fractions, commonly known as the C_{7+} fractions, contain an indefinite number of components with a carbon number higher than six. Molecular weight and specific gravity of the C_{7+} fraction may be the only measured data available. Therefore, it is desirable to assign parachors to the plus fractions based on the molecular weights. We have plotted molecular weight vs. parachor data for different hydrocarbon mixtures as shown in Figs. 133–138. These figures indicate that a fairly good linear relationship exists for a variety of hydrocarbons. This linear relationship can be expressed as

$$P = a\,M + b \tag{27}$$

Correlation coefficients and standard error of estimation for these hydrocarbons are summarized in Table 27. It is evident from Table 27 that normal paraffins remarkably obey the linearity, while adding cyclic and aromatic compounds causes scatter of data. It is recommended that these correlations be used for estimating parachors of the plus fractions. One of the correlations should be chosen based on an estimation of the composition of the plus fraction. The estimation may be made through PONA (paraffin/olefin/naphthalene/aromatic) analysis of stock-tank oil.

Parachors of Oil Cuts

Although it is possible to get reliable parachors for pure components, the applications of pure component parachors are limited to simple fluid systems with known exact compositions. This is particularly true in petroleum reservoir simulation where hydrocarbons are treated in their groups (oil cuts). For example, the C_6 group includes normal hexane, 2-methylpentane, 3-methylpentane, 2,2-dimethylbutane, 2,3-dimethylbutane, etc. With currently available technologies, it is difficult, if not impossible, to measure the exact composition of a crude oil. Also, it is not feasible to simulate crude oil systems using all the exact components. Even if this could be done, physical properties

(such as critical pressure) of all the pure components are not readily available. Therefore, it is desirable to assign parachors to hydrocarbon groups (oil cuts) for uses in compositional reservoir simulators. Based on equivalent molecular weights of oil cuts proposed by Ahmed,[222] parachors of hydrocarbon groups are estimated using a linear correlation. The results are shown in Table 28.

Comparisons

Several parachor correlations have been reported to be successful for predicting IFT of reservoir fluids. Firoozabadi *et al.*[161] claimed that for reservoir-fluid systems that do not contain asphalt materials, the following quadratic parachor correlation would suffice for the computation of surface tension when Weinaug-Katz parachor method is used:

$$P = -11.4 + 3.23\,M - 0.0022\,M^2. \tag{28}$$

Through comparison of ten parachor correlations, Ali[163] concluded that the linear parachor correlation determined by Fanchi[164] best fits the Weinaug-Katz parachor method and yields the least error in IFT predictions. The linear parachor correlation is given by

$$P = 69.9 + 2.3\,M. \tag{29}$$

Fawcett[165] claimed that the Hough-Stegemeier method gives good IFT predictions if the following linear correlation for crude cut parachors is employed:

$$P = 81.2 + 2.448\,M. \tag{30}$$

In this section, measured IFTs of six reservoir oil/CO_2 mixtures are compared with the IFTs predicted by Peng-Robinson equation of state (PREOS) using the following approaches:

1. Use scaling exponent 4 and Eq. (28)
2. Use scaling exponent 4 and Eq. (29)
3. Use scaling exponent 3.67 and Eq. (30)
4. Use scaling exponent 3.88 and Eq. (27)

The last approach is proposed by this work. The Lee-Chien method is not compared here because of uncertainties involved in determination of critical properties of heavy components.

The six reservoir oil/CO_2 systems with given IFT measurements are

I. Asphalt-free oil used by Firoozabadi *et al.*[161]
II. Oil A used by Firoozabadi *et al.*[161]

III Oil C used by Firoozabadi *et al.*[161]
IV. Oil D used by Firoozabadi *et al.*[161]
V. Oil A plus 55% CO_2 used by Simon *et al.*[223]
VI. Recombined Oil plus 55.55% CO_2 used by Gasem *et al.*[189]

Measured compositions and characterizations of C_{7+} of these reservoir oils and experimental temperatures when IFTs were measured are summarized in Table 29.

Using the PREOS and the four approaches, the IFT of six reservoir oil/CO_2 mixtures at different pressures is predicted. For the first five fluid systems, the predicted IFT data are compared with measured IFT data in Table 30. When Approach 4 was used, the last set of correlation coefficients in Table 27 was employed. Table 30 indicates that Approach 4 yields the least error in IFT predictions. The predicted and measured IFT data for System VI are compared in Fig. 139. This figure again shows that Approach 4 allows better prediction of IFT compared to other approaches, especially in the near critical region.

As an example of the application of Approach 4, we have computed IFT for mixtures of CO_2 and oil from the Spraberry Trend Area in West Texas. Equi-IFT maps are generated for modeling fluid flow in the reservoir. These maps are shown in Figs. 140 and 141 for CO_2 stock tank oil and CO_2/recombined reservoir oil, respectively. This figure also demonstrates the range of convergence for density calculations via the PREOS.

Discussion of Scaling Exponent

This section presents our arguments about the treatment of the scaling exponent, parachor, and special systems that do not obey the scaling law under conditions normally encountered in petroleum reservoirs. From recent work such as Danesh *et al.,*[224] researchers have proposed the critical scaling exponent in the parachor equation as a function of density difference. They used the critical scaling exponent as an adjustable parameter to fit the experimental data. We do not think this is a theoretically correct approach. The critical scaling exponent has a unique value in what is typically considered the critical region. Many parachor values found in the literature were derived based on constant scaling exponents (mostly 4). If a constant parachor and varying exponents are utilized, the inconsistency will result in inaccurate IFT predictions of unknown systems. We believe that outside the critical region, where the critical scaling exponent 3.88 is not valid, correlations such as the one proposed by Firoozabadi and Ramey[178] should be developed for IFT predictions. Also adsorption theory may be suitable for IFT calculations in such cases.

Parachors

Reno and Katz[157] measured IFT of normal heptane and normal butane containing dissolved nitrogen at different pressure and temperatures. They calculated IFT using the parachor method presented by Eq. (21). The calculated IFT data match the measured IFT data only when the parachor of nitrogen in the mixture is adjusted from pure nitrogen parachor of 60 to 41. Huygens *et al.*[176] measured the IFT of four hydrocarbon mixtures containing nitrogen. They found that Eq. (22) fails

to predict IFT of the nitrogen/hydrocarbon systems if the parachor of pure nitrogen is used. In order to match the measured IFT, they had to vary nitrogen parachor for different mixtures. Since parachor is a property of the pure component, we argue that each component should have its unique parachor no matter whether the component exists in its pure state or in mixtures with other substances. We believe that varying the parachor for a given component is not consistent with critical scaling.

Special Systems

Systems like brine/alcohol/oil, N_2/hydrocarbon, and CO_2/C_{14} are considered special systems because the critical region, where critical scaling theory is valid, is narrow. These systems are strongly interacting, weakly interacting, or molecules with a large size discrepancy. Since the parachor method fails to predict the IFT of these systems under conditions that normally occur for petroleum fluids, the IFT can be better predicted using adsorption theory.

We have re-calculated the IFT of the nitrogen/hydrocarbon systems that were investigated by Reno and Katz[157] and Huygens *et al.*[176] using new parachors. We confirmed the observations by the above researchers: the parachor method does not work well for some hydrocarbon systems containing dissolved nitrogen if the pure nitrogen parachor is used. We speculate that the parachor method for mixtures represented by Eqs. (21), (22) and (23) is an approximation extended from the parachor method for pure substance using a linear mixing rule. Although it works well for some hydrocarbon and CO_2/hydrocarbon mixtures, it is not generally applicable to all mixtures, such as nitrogen/hydrocarbon mixtures that behave very differently from hydrocarbon compounds due to their different chemical properties, adsorption and solubility behavior.

To support our argument, let us examine Eq. (21) carefully. This equation was proposed by Weinaug and Katz[155] based on equations derived by Sugden[153] and Fowler[225] for pure substances. When this equation was formed, it was assumed that the parachor is a linear, additive, and constitutive property, which may not be true for all mixtures, especially nitrogen and hydrocarbons that are chemically very different. Also, it was conceived by Weinaug and Katz that a method of applying mole fraction of each constituent in its respective phase to molal volumes of phases is valid. It was expected that each constituent contributes a positive IFT component to the total IFT of the system. However, we have found that the term $x_i \frac{\rho_l}{M_l} - y_i \frac{\rho_v}{M_v}$ in Eq. (21) could be negative for some gaseous constituents such as nitrogen. This is mainly because y_i is significantly higher than x_i for these constituents and M_v is significantly lower than M_l in the system. When these terms are negative, negative contributions of these constituents to the IFT of the mixture are calculated, which physically makes no sense.

This argument can also be justified by considering the adsorption mechanism. Chemical properties of a component of a mixture govern adsorption of the component at the liquid-vapor interface of the system. Consider two systems: the first one is a propane/IPA (2-propanol) mixture, and the second one is propane containing dissolved nitrogen. To compare the two systems, let us define relative interface adsorption, I_l and I_v, for component i as

$$I_l = \frac{x_i^s}{x_i} \tag{31}$$

and

$$I_v = \frac{x_i^s}{y_i} \tag{32}$$

where x_i^s is mole fraction of component *i* at the liquid-vapor interface. By these definitions, I_l and I_v reflect the relative amount of a component adsorbed at the two-phase interface compared to that in each phase. The x_i^s for the two systems at different pressures are computed. The result of the computation shows that the mole fraction of the IPA at the interface is high compared to that in the vapor phase *($I_v > 1$),* and it increases quickly with elevated pressure. However, the mole fraction of the IPA at the two-phase interface is almost the same as that in the liquid phase *($I_l \approx 1$),* and it is not sensitive to pressure. This indicates that IPA in the vapor phase is favorable to be adsorbed at the interface, and pressure helps this adsorption. This is expected because IPA is a surfactant which reduces interfacial tension by active adsorption at the interface. From this point of view, it is anticipated that the IFT of mixtures containing IPA should decrease rapidly with increased pressure.

The result of the computation also shows that the mole fraction of the nitrogen at the two-phase interface is low compared to that in the vapor phase ($I_v < 1$), and it increases slowly with elevated pressure. However, the mole fraction of the nitrogen at the two-phase interface is higher than that in the liquid phase ($I_l > 1$), and it decreases slowly when pressure is increased. This indicates that nitrogen in the vapor phase is neither favorable to be adsorbed at the interface nor favorable to be dissolved in the liquid phase, and pressure does not effectively help the adsorption or the solubility of the nitrogen. In other words, nitrogen is not surface-active. Based on this reasoning, it is anticipated that the IFT of mixtures containing much nitrogen should not decrease rapidly with increased pressure in some pressure range. This is consistent with experimental data (Fig. 131) showing slow decline of IFT of N_2/toluene and N_2/n-C_{14} systems outside of the critical region as pressure increases.

The preceding analysis shows that the adsorption behavior of nitrogen is very different from the adsorption behavior of IPA at the liquid/vapor interface. Since the adsorption mechanism governs IFT of the system through surface excess, it is necessary to analyze the IFT of nitrogen/hydrocarbon or alcohol/oil/brine systems using adsorption theory.

Conclusions

1. According to current understanding in the physics literature, the critical scaling exponent in the parachor equation is 3.88.

2. The scaling exponent and parachors calculated based on critical scaling should not be used as adjustable parameters in prediction of multicomponent IFT.

3. Based on the exponent 3.88, new parachors of pure substances commonly encountered in petroleum fluids are obtained from carefully selected density and surface tension data. The parachors of hydrocarbon mixtures are linearly correlated to their molecular weights. Normal paraffins remarkably obey the linearity, while adding cyclic and aromatic compounds to the mixture causes scatter of data. Parachors of hydrocarbon groups (oil cuts) are assigned to their equivalent molecular weights using a linear correlation.

4. These newly developed pure component parachors, parachor correlations, and oil cut parachors are tested for IFT predictions using six reservoir oil/CO_2 mixtures. These tests indicate that the new parachors and correlations are better than those proposed by previous investigators for IFT prediction of reservoir fluids. When the parachor method and the new parachors and correlations are employed, IFT of reservoir fluids can be predicted using Peng-Robinson equation of state with an acceptable error.

5. The parachor method worked well combined with the PREOS for CO_2/crude and gas condensates, but it failed to predict IFT of some special systems such as nitrogen/hydrocarbon mixtures. Subsequent research included analysis of IFT of such special mixtures using adsorption theory.

Experimental Measurement of IFT

Background

Determination of IFT is important in various aspects of chemistry, chemical engineering, and petroleum engineering.[226] Many techniques of IFT measurements are currently used at different conditions. Detachment techniques, such as de No ring[227] and Wilhelmy slide,[228] rely on the condition of perfect wetting of the withdrawing surface. Capillary rise,[229] maximum bubble pressure,[230] and drop weight[231] techniques require calibration with liquids of known IFT. They also involve a three phase contact that introduces systematic error. The spinning drop technique[232] is not easy to use for reservoir temperature and pressure applications. Although laser light scattering[233] has been used successfully in IFT measurement, it involves systematic error with a high pressure cell where it is not practical for a diffraction grating to be located very close to the liquid surface. The traditional pendant/sessile drop technique, which is not affected by a three phase boundary, has been revived by advances in digital video and image analysis.

The principle of the pendant drop technique relies on measurement of the coordinates of an asymmetric shaped drop and its match to the solution of the Laplace equation. All the information on the value of the IFT is contained in the shape assumed by the drop. Our literature survey indicates that six calculation methods have been developed to extract IFT information from the drop shape in the past six decades: shape factor method, inflection plane method, regression method, direct method, spline-fitting method, and growing-drop method.

The shape factor method is also referred to as the selected plane method. It is essentially based on methodology proposed by Andreas *et al*.[234] who characterized the shape of a drop through the knowledge of various shape factors. Fordham[235] tabulated a parameter (β) relating to IFT with the shape factors proposed by Andreas. Girault *et al*.[236] fit a polynomial to Fordham's data, enabling solutions on the computer. Hansen and Rodsrud[237] solved the Laplace equation and derived a new polynomial for determination of β and IFT from shape of the drop. The shape factor method is easy to use. However, inherent in the method itself are sources of error that scatter the results. Huygens *et al*.[238] reported that the theoretical accuracy of the method is 0.5%; which, however, in practice may increase to 5%. Stauffer[239] concluded that the accuracy of the method for the usual-size drops encountered in practice was of 2–6%, with a 1% error in the measurement of the drop dimensions.

The inflection plane method was first proposed by Girault *et al*.[240] based on the location of the inflection plane. It was applied to the measurement of ultra-low IFT for oil/water systems. The researchers claimed that this method is suitable for determination of IFT from pendant drops that do not have equators (and therefore, necks), although the equation for calculating IFT was derived for a sufficiently long pendant drop. Results from this method are very sensitive to the measured location of the inflection, and it is difficult to determine accurately the inflection plane.[235]

The regression method was proposed by Girault *et al*.[236] and was used by several researchers.[241–243] This method involves solving the Laplace Equation to obtain a theoretical drop edge. The observed edge is matched to the theoretical edge by adjusting parameters in the theoretical drop. IFT is then extracted from the matching parameters. The main disadvantage of this method is that the solution is not unique due to strong interdependence of multiple parameters. Another disadvantage is the long computation time required due to the iterative nature of the method.

A direct method was proposed by Huygens *et al*.[238] Instead of solving the Laplace equation as done by previous investigators, Huygens *et al.*[238] applied the equation on two points on the drop profile. They measured the variables that appear in the equation and substituted their values into the equation for two points. The IFT was determined from solving the two simple equations corresponding to the two points. This method is easy to use compared to other methods. However, Huygens *et al*.[238] reported that this method is not as accurate as the regression method of Rotenberg *et al.*[242]

The spline-fitting method was presented by Lopez de Ramos.[244] This method requires plotting mean curvature versus elevation using drop profile data. IFT is determined from the slope of the plotted line. The drawback of this method is that sometimes the measured data are so noisy that it is

impossible to get a linear plot between mean curvature and elevation even if a high smoothing factor is used.

The growing-drop method was proposed by MacLeod and Radke[245] for measuring dynamic IFT. The method was developed on the basis of an assumption that the growing-drop is spherical, which is not always observed in practice. Another drawback of the method is that wetting behavior of the needle tip has a critical impact on the growing-drop measurement. MacLeod and Radke[245] found that with strongly wetting liquids against air in stainless steel capillaries, they were unsuccessful in overcoming drop climbing.

As IFT gets lower, pendant drops tend to be small and flat.[242,246] In this case the shape factor method is difficult to apply because the diameter of the drop (D_s) at the elevation of equator diameter (D_e) from the apex is strongly affected by the presence of the tip (see Fig.142). Also wetting behavior deforms the shape of the pendant drop.[245] We have observed that the IFT is erroneous if it is determined based on drop edge above the equator in low IFT systems. The objective of this study was to develop a simple method for low IFT determination using half of the drop profile, i.e., drop edge data below the equator. To avoid the difficulties involved in solving the second-order, non-linear differential (Laplace) equation, we developed a new method based on a static force balance on the lower half of the pendant drop. A simple equation relating the IFT, fluid densities, and drop geometry was formulated. With known profile data from the lower half of the pendant drop, IFT can be calculated quickly from the equation.

It is generally recognized[238,242,244] that the drop information at and near the apex is vitally important because it defines the origin of the drop curve and the curvature information is used to calculate IFT. Unfortunately, as the tangent line at the apex is horizontal, video digitization always gives considerable error in measured coordinates. Our new method requires high quality drop-profile data near the apex of the drop to determine curvature of the drop surface at the apex. We confirmed the observation by a previous investigator[244] that the results can be completely distorted by experimental noise and noise introduced during digitizing the drop profile. We solved this problem by digitizing rotated drop images, fitting a smoothed spline to the drop profile data, and differentiating this smoothed spline in curvature calculations.

The result of IFT determined using this new method was compared with that given by other methods in the literature for water, normal decane, decyl alcohol, 2,2,4 trimethyl pentane, normal heptane, hexadecane and toluene under ambient conditions. This comparison shows very good consistency among the methods in the high IFT region (IFT > 10 mN/m). Using our pendant drop generating apparatus and image processing system, we tested the new method under various conditions for water, normal decane, ethane, and CO_2. We found that the new method is more accurate than the shape factor method, especially in the low IFT region (IFT < 1 mN/m). This is because the new method allows calculations of IFT from very small droplets as long as the droplets have equators developed. The lowest IFT that we have measured so far is 0.09 mN/m. We believe that by using more powerful lenses for magnifying drop images, even lower IFT can be measured.

Method Description

Figures 142 and 143 demonstrate the geometry of and forces acting on the lower half of a pendant drop. The forces are drop weight W, interfacial tension σ from the upper half of the drop, pressure P_{He} from the upper half of the drop, and buoyancy force P_o from the outer phase. At any equilibrium condition, applying Newton's second law of motion to the lower half of the drop yields:

$$-\frac{\pi}{4}D_e^2 P_{He} - W + \pi D_e \sigma + \int_{x=0}^{x=D_e/2} 2\pi x P_o \cos(a)\, dS = 0 \tag{33}$$

where D_e is equator diameter, P_{He} is pressure in the drop at equator elevation H_e from the apex, P_o is pressure in the outer phase at an elevation corresponding to radial distance x, a is inclination angle of the drop surface at the elevation corresponding to radial distance, and S is the arc length from the apex to the elevation corresponding to radial distance x. P_{He} can be expressed as

$$P_{He} = P_{ai} - \rho_i g H_e \tag{34}$$

where P_{ai}, ρ_i, and g are pressure immediately above the apex, density of the inner phase and gravitational acceleration, respectively. Since

$$P_{ai} = P_{ao} + P_{ca} \tag{35}$$

and

$$P_{ca} = \frac{2\sigma}{R_a} \tag{36}$$

where P_{ao}, P_{ca}, and R_a are pressure immediately below the apex, capillary pressure at the apex, and radius of curvature at the apex (two principal radii of curvature, r_1 and r_2, are the same and equal to R_a at the apex), respectively, Eq. (34) can be rearranged:

$$P_{He} = P_{ao} + \frac{2\sigma}{R_a} - \rho_i g H_e \tag{37}$$

The weight can be expressed as

$$W = \int_0^{He} \pi \rho_i g x^2 dy \tag{38}$$

The arc length is

$$dS = \frac{dx}{\cos(a)} \tag{39}$$

The outer pressure can be expressed as

$$P_o = P_{ao} - \rho_o g y \tag{40}$$

where ρ_o is the density of the outer phase. Substitutions of Eqs. (37), (38), (39) and (40) into Eq. (33) give

$$-\frac{\pi}{4} D_e^2 \left(P_{ao} + \frac{2\sigma}{R_a} - \rho_i g H_e \right) - \int_0^{H_e} \pi \rho_i g x^2 dy + \pi D_e \sigma + \int_0^{D_e/2} 2\pi x \left(P_{ao} - \rho_o g y \right) dx = 0 \tag{41}$$

Interfacial tension σ can be solved from this equation to yield:

$$\sigma = \frac{\frac{g}{D_e}\left(\int_0^{H_e} \rho_i x^2 dy + \int_0^{D_e/2} 2\rho_o x y dx \right) - \frac{1}{4} D_e \rho_i g H_e}{1 - \frac{D_e}{2R_a}} \tag{42}$$

If the drop profile $y = f(x)$ is measured, R_a and integral in Eq. (41) can be evaluated to determine interfacial tension σ.

Experimental Apparatus

Figure 144 shows a sketch of our experimental setup for pendant drop measurement. Up to 18 needles can be installed in a high pressure cell for forming pendant and sessile drops of different sizes. Fluids are circulated by a pump through the measuring cell, where pendant drops are formed, and a density meter to measure the densities of the two phases. A circulating water bath is used to control the temperature of the measuring cell and the density meter. Pressure and temperature are measured by a pressure indicator and a thermometer. The big box represents the air bath. The temperature in the water and air bath are regulated at measuring conditions. Pendant/sessile drops are imaged by a CCD video camera. Drop images such as the one in Fig.143 are sent to the VCR, monitor and computer for data processing. The computer calculates IFT from the image profile. The density meter is a PAAR mPDS 2000. The Video camera is a SANYO VCB-3524 with a 1.5 Tele conversion lens, C-Mount Lens Adaptor, and a video monitor. The image processing software is EPIX SVIP version 7.0 for windows. The circulating pump is a high-speed LDC analytical miniPump. Needle sizes range from 0.23 mm to 0.90 mm. For calibration uses, accurately cut metal collars are attached around the needles.

Results and Discussion

The new method was first tested using experimental data obtained under ambient conditions. Pendant drop profile data were taken from Lopez de Ramos.[244] Drop dimension parameters, D_e and H_e, were determined from the drop profiles. The radius of curvature at the apex R_a was numerically calculated using the profile data. Parameter values for seven pure substances are shown in Table 31. Surface tensions of the seven substances were calculated with Eq. (42) and are shown in the last column of Table 32. Table 33 also contains surface tension data reported in the literature for comparison. Jasper's[247] data was collected from the physical chemistry literature. Hansen and Rodsrud's[237] data was obtained using the shape factor method. Lopez de Ramos'[244] data was calculated from the spline method. Comparisons between literature reported surface tension data and that obtained using the new method indicate consistency in the high tension region. Also included in Tables 31 and 32 are experimental data obtained from our laboratory for water and decane under various conditions for comparison. The data indicate that the result given by the new method is lower than that given by the shape factor method at elevated pressure and temperature. Figure 145 shows experimental data obtained for the brine/heptane/iso-propanol system. This figure indicates that the IFT determined using the shape factor method begins to deviate from the theoretical trend (scaling law) at an IFT approximately equal to 0.2 mN/m. In order to assure that the deviation is a result of application of the method used for extracting IFT from pendant drops, rather than fluid properties, we also measured IFT of pure CO_2. The result is shown in Fig. 146, which indicates the divergence of calculated IFT by the shape factor method from the theoretical trend when IFT is below 0.5 mN/m.

Surface tension of ethane was also measured in our laboratory for comparison. Figure 147 presents measured density data for ethane. Figure 148 shows a plot of phase density difference versus reduced temperature. It can be seen from this plot that the measured data follow the theoretical trend

defined by a theoretical slope of 0.325 on the log-log scale. Surface tensions determined by the shape factor method and the new method are plotted in Fig. 149 against reduced temperature. It is seen from the plot that the surface tensions calculated by the new method follow the theoretical trend with a slope of 1.26 on the log-log scale, while the surface tensions calculated by the shape factor method deviate from the theoretical slope when IFT is lower than 0.2 mN/m. Figure 150 demonstrates a log-log plot of surface tension versus phase density difference. Again, it indicates that the surface tensions given by the new method follow the theoretical trend with a slope of 3.88, while the surface tensions given by the shape factor method deviate from the theoretical slope in the low tension region.

In order to know at what conditions the shape factor method fails to extract accurate IFT information from CO_2 drops, we conducted a second set of IFT measurements for pure CO_2. Figure 151 shows measured density data for CO_2 liquid and vapor phases along the vapor pressure curve. Phase density difference versus reduced temperatures are plotted in Fig. 152. It is seen from this plot that the measured data honors the theoretical trend with a slope of 0.325. Surface tensions determined by the shape factor method and the new method are plotted in Fig. 153 against reduced temperature. The plot demonstrates that the surface tensions calculated with the new method follow the theoretical trend with a slope of 1.26, while surface tensions calculated by the shape factor method deviate from the theoretical slope when IFT is below 0.5 mN/m. Figure 154 shows a plot of surface tension versus phase density difference. It also indicates that the surface tensions given by the new method follow the theoretical trend with a slope of 3.88, while surface tensions from the shape factor method deviate from the theoretical slope in low tension region.

The reason the shape factor method fails in the low IFT region is probably due to the effect of the needle tip for small pendant drops. This effect on the drop shape may be reflected by the value of the shape factor (D_s / D_e) of the drop. As IFT gets lower, the pendant drop gets smaller, and the shape factor gets larger (approaching unity). Fordham[235] claimed that the shape factor method is accurate for β values between 0.25 and 0.6, which corresponds to shape factor values between 0.6 and 0.95 according to his two-term correlation between β and the shape factor. Hansen and Rodsrud [237] claimed that the shape factor method is accurate for β values between 0.1 and 0.5, which corresponds to shape factor values between 0.46 and 0.91 according to their four-term correlation between β and the shape factor. Figure 155 presents some actual drop images from which IFT of CO_2 was determined in our first CO_2 experiment. Listed below the drop images are corresponding shape factors and IFT. These drops were obtained using a needle size of 0.305 mm in outer diameter. We evaluated shape factor values corresponding to IFT values where calculated IFT deviates from theoretical trend. Comparison of shape factors for these CO_2 drops indicates that a surface tension of 0.5 mN/m corresponds to a shape factor of 0.85. Similar comparison of shape factors of drops obtained from our second CO_2 experiment using a 0.406 mm needle indicates that a surface tension of 0.5 mN/m for the system corresponds to a shape factor of 0.86. Comparison of shape factors of ethane drops obtained using a 0.254 mm needle indicates that a surface tension of 0.2 mN/m corresponds to a shape factor of 0.85. Experimental data obtained for the brine/heptane/iso-propanol using a 0.559 mm needle indicates that a surface tension of 0.2 mN/m for the system corresponds to a shape factor of 0.88. It appears evident from this analysis that the shape factor method should fail to extract accurate IFT information from pendant drops that have average shape factor greater than 0.86.

Conclusions

In the low IFT region, pendant drops tend to be small and flat. The upper portion of the pendant drop is strongly affected by the wetting behavior of the tip. In this case, calculation methods such as the traditional shape factor method are erroneous because drop edge information from the upper, distorted portion of the pendant drop is included in the calculation. A new method for determination of low IFT has been developed based on a static force balance on the lower half of the pendant drop. The result of surface tension determined using this new method was compared with that given by the shape factor method for water, normal decane, decyl alcohol, 2,2,4 trimethyl pentane, normal heptane, hexadecane and toluene under ambient conditions. This comparison shows consistency between the results given by the shape factor method and the new method in the high IFT region (IFT > 10 mN/m). Testing of the new method with IFT measured under various conditions for water, normal decane, ethane, and CO_2 indicates that the new method is more accurate than the shape factor method in the low IFT region (IFT < 1 mN/m).

Investigations on CO_2 Gravity Drainage

Background

Because fractures are highly conductive to injected gas and gas is the nonwetting phase in the rock matrix, gas injection into fractured reservoirs has been traditionally considered as an inefficient method for enhancing oil recovery from fractured reservoirs. However, the Midale Pilot[248] indicated that the efficiency of CO_2 injection into fractured reservoirs is not as low as expected. The only explanation is that when a non-equilibrium gas is injected into the fracture system at elevated pressure, compositional effects become active between the gas in the fractures and oil in the matrix. Due to the multi-contact mechanism, light hydrocarbons in the oil can be extracted from the virgin oil bank forming a “gas”-rich light liquid phase and an oil-rich heavy liquid phase. This kind of phase split has been reported by several investigators.[45,51] The interfacial tension (IFT) between phases is low compared to that between the virgin oil and gas phases. Therefore, the capillary pressure threshold may be overcome by gravity resulting in gravity drainage of oil from the matrix blocks. In order to understand the mechanism of gravity drainage and predict the response of fractured reservoirs to gas injection, a mathematical model of the process is desirable.

Equilibrium Gravity Drainage

Studies on gravity drainage were conducted a century ago when King investigated the principles and conditions of aquifer motion. Investigations of gravity drainage of oil in oil reservoirs were initiated in the early 40's. Leverett[250] and Katz[251] presented data and discussed the theory relating capillary and gravitational forces acting on liquids contained in a sand body. Stahl *et al*.[252] conducted experiments to investigate behavior of free-fall gravity drainage of water and oil in an unconsolidated sand. Elkins *et al*.[253] presented a simplified theory of regional drainage of oil from an upstructure to downstructure location due to gravity assuming zero capillary pressure gradient. Cardwell and

Parsons[254] presented a governing equation for the free-fall gravity drainage process. They could not solve the equation because of its non-linearity. By neglecting the term involving the product of permeability and variation of capillary pressure with saturation, they derived a solution for simplified cases using the concept of a demarcator. Terwilliger *et al.*[255] conducted experimental and theoretical investigations on gravity drainage performance under controlled flow rates. Their theory was based on the Buckley-Leverett[256] approach. Nenniger and Storrow[257] presented an approximate series solution for free-fall gravity drainage based on film flow theory. The results accurately matched experimental data obtained from a highly permeable pack of glass beads. Essley *et al.*[258] analyzed the gravity drainage process and final oil recovery in a steeply dipping reservoir. Templeton and Nielsen[259] experimentally investigated the counterflow segregation of fluids under the gravitational force field using glass beads. Dumore and Schols[260] performed experimental studies of free-fall gravity drainage of oil in the laboratory and developed a drainage capillary pressure function. Dykstra[261] generalized the approximate theory presented by Cardwell and Parsons[254]. His mathematical model matched some experimental data with assumed permeability values. Hagoort[262] theoretically analyzed vertical displacement efficiencies of forced and free-fall gravity drainage processes. He derived a governing equation for saturation in free-fall gravity drainage, which is identical to that given by Cardwell and Parsons[254] except that he used the Leverett J-function for expressing capillary pressure. He again did not solve the saturation equation because of its non-linearity. Haldorson *et al.*[263] evaluated the gravity drainage mechanism in an oil field using compensated neutron logs, centrifugal displacements and an analytical stochastic approach. Nectoux[264] investigated the velocity influence on sweep efficiency in oil drainage experiments. Compositional effects were also discussed in his paper.

Low IFT and Nonequilibrium Gravity Drainage

Jacquin *et al.*[265] investigated gravity drainage with fluids not in equilibrium. Their laboratory experiments show that the oil recovery by gravity drainage increases if the content of intermediate components in the gas or in the liquid phase increases. Pavone *et al.*[266] conducted experiments to investigate free-fall gravity drainage at low IFT. The IFT of the C_1/C_7 mixture utilized in their experiments was 0.53 dyne/cm. They found that the gravity drainage process can be divided into two time periods. During the first period, almost 50% of the oil in place was produced. The second period of slow drainage began suddenly at a breakpoint whereby the production rate was low but led to more than 20% additional oil recovery. They also presented a non-linear governing equation for gas saturation during drainage. Their governing equation is similar to the one given by Cardwell and Parsons[254]. The governing equation was linearized by assuming straight-line permeability and logarithmic capillary pressure curves. They solved the linearized governing equation analytically assuming that the minimum gas saturation is always at the outlet of the core (the demarcator is always at the bottom of the core). They matched some experimental data by dual use of the analytical solution, i.e., the analytical solution was used twice for early and later times, respectively, to match the same set of experimental data.

Stensen *et al.*[267] performed experiments for analyzing the effect of IFT on gravity drainage. They employed brine and a $C_1/n - C_7$ mixture having IFT ranging from 76 (reported in the paper) to

0.5 dyne/cm. Suffridge and Renner[268] investigated gravity drainage experimentally under constant and varying IFT in fractured and non-fractured cores. The varying IFT was obtained by first placing C_{10} in the core, and then letting C_1 to diffuse into the core. da Vilva and Meyer[269] presented a formulation for oil desaturation curves used for reservoir simulation. Schechter *et al*.[270] reported experimental results of investigations on low IFT imbibition and drainage. They utilized brine/isopropanol/ i–C_8 systems with IFT of 0.1, 1.07, and 38.1 dynes/cm and density differences of 0.11, 0.21, and 0.33 g/cc, respectively. They also presented analyses of imbibition and drainage mechanisms. It was concluded that gravity drainage of wetting phase from fully saturated vertical cores occurs for inverse bond numbers less than 1. Luan[271] discussed theoretical aspects of free-fall gravity drainage in naturally fractured reservoirs. He solved the governing equation given by Hagoort analytically and numerically. However, he used the same boundary condition as that utilized by Pavone *et al.*; that is, the demarcator is assumed to be always at the bottom of the core. Espie *et al*.[272] investigated gravity drainage/waterflood interaction in the laboratory. They found that injection of water into a gravity drained oil column with high gas saturation improves the mobilization of a dry oil bank. Catalan *et al*.[273] reported their results of investigations on the effects of wettability and heterogeneities on the recovery of waterflood residual oil with low pressure inert gas injection assisted by gravity drainage. Experiments on forced gravity drainage by gas injection under varying pressures were performed and analyzed. They concluded that tertiary gravity drainage in water-wet systems is most efficient when the oil spreads on the water phase in the presence of gas. Blunt *et al*.[274] presented a theoretical and experimental treatment of three phase flow in water-wet porous media from the molecular level upwards. They found that oil spontaneously spreads as a layer between water and gas in most three-phase systems. Their experimental data on gravity drainage in a capillary matched predictions by their theoretical model. Recently Øyno *et al*.[275] conducted laboratory experiments on composite cores at reservoir conditions using recombined reservoir fluids to investigate the potential of secondary and tertiary recovery using gas injection, where gravity drainage is regarded as an important recovery mechanism. Although they recognized that the time required to reach capillary/gravity equilibrium depends on oil/gas density difference, gas/oil IFT, and molecular diffusion in both gas and oil phases, they could not identify conditions whereby each factor dominates.

In summary, the literature reveals that three different gravity drainage processes in porous media have been investigated: (1) forced gravity drainage by gas injection and controlled flow rate, which occurs when gas is injected into steeply dipping reservoirs, (2) simulated gravity drainage by centrifuging, which exists only in laboratories, and (3) free-fall gravity drainage, which takes place in naturally fractured reservoirs after depletion of oil in the fractures or after gas injection into the fractures. The free-fall gravity drainage, which is representative of gas injection into a depleted fractured reservoir, has been investigated by Leverett,[250] Stahl *et al*.,[252] Cardwell and Parsons,[254] Nenniger and Storrow,[257] Templeton and Nielsen,[259] Dumore and Schols,[260] Dykstra,[261] Hagoort,[262] Jacquin *et al*.,[265] Pavone *et al*.,[266] Stensen *et al*,[267] Suffridge and Renner,[268] Schechter *et al*.,[270] Luan,[271] and Øyno *et al*.[275]

Unlike forced gravity drainage, free-fall gravity drainage cannot be modeled using a Buckley-Leverett approach because flow rate is not prespecified. A survey of the literature reveals four mathematical models that have been developed for describing the process of free-fall gravity

drainage of equilibrium fluids. They are the Cardwell-Parsons-Dykstra (C-P-D) model, the Nenniger-Storrow (N-S) model, the Pavone-Bruzzi-Verre (P-B-V) model, and the Luan Model. The accuracy of these models are found to be poor, based on our comparisons with experimental data. Therefore, we have developed a new mathematical model to simulate equilibrium and non-equilibrium gravity drainage. Comparison of recovery data computed using the new model to experimental data found from both the literature and experiments conducted in our laboratory indicates that the new model can better describe the process of free-fall gravity drainage of both equilibrium and non-equilibrium fluids.

Laboratory Experiments

Laboratory experiments were conducted to simulate vertical free-fall gravity drainage from a matrix block in a naturally fractured reservoir. Core samples were first saturated with synthetic reservoir brine. The brine was then horizontally displaced by separator oil to S_{wi}. On one of the cores, brine was injected into the core again to simulate waterflooding. The oil and brine saturated core was transferred to a vertical core holder with an inner diameter 0.2 cm greater than the core diameter. During the experiment, CO_2 was injected into the 0.1-cm wide annulus (simulating a fracture) between the core sample and core holder at reservoir pressure and temperature. Oil recovered from the core sample was collected at ambient conditions. The key parameter of interest is oil recovery as a function of time.

Core Samples

Two Berea cores with high and low permeabilities and two whole reservoir cores with extremely low permeability were tested. The cores were 21.75 in. long. The high permeability Berea core had an absolute permeability of 500 md. The low permeability Berea had a 50 md absolute permeability. One of the reservoir cores had a 0.01 md permeability to water. The other reservoir core had a 0.38 md permeability to water. Core porosities and water saturations are summarized in Table 33.

Oil

A separator oil was used in the experiments. The oil composition was obtained from GC analysis. The average molecular weight of the oil is 219.39. Composition of the oil is shown in Table 34. The oil sample was tested at 100°F and 1000 psig. The density was 0.8329 g/cc and the viscosity was equal to 2.956 cp. As will be shown later, the MMP of the oil was measured and found to be 1550 psig using slim tube at the reservoir temperature of 138°F.

Results

The experiments were conducted at a reservoir temperature of 138°F. Oil recovery data from the four cores are presented in Fig. 156. The experiment with the 500 md permeability Berea core was carried out under pressure of 1450 psig. The experiment was terminated at six days. The produced oil looks like original separator oil. The experiment with the 50 md permeability Berea core was carried out under pressures ranging from 1,700 psig to 2,000 psig. The experiment was terminated at 220 days. The produced oil are black, brown, and yellow in color. The experiment with the 0.01

md permeability reservoir core was also performed at pressures starting at about 2,000 psig and eventually dropped to 1,500 psig as shown in Fig. 157. The produced oils are yellow, light brown, and brown in color. Composition of the yellow and brown oils are also shown in Table 34. Density and viscosity of the yellow oil are measured at 60°C and atmospheric pressure. They are 0.82 g/cc and 2.1 cp, respectively. The experiment with the 0.38 md permeability reservoir core was performed at pressures between 1900 psig and 2100 psig. The produced oils are black, light brown, and brown in color.

Discussion

Figure 156 indicates fast drainage of oil from the high permeability Berea core during CO_2 injection into the core holder annulus. This is expected because the capillary pressure is already low in the high permeability Berea core and a slight decrease in IFT can reduce capillary pressure to less than the gravitational force. The black color of the produced oil confirms that oil drained before much of CO_2 diffused into the oil bank. This figure also indicates slow oil recovery from low permeability reservoir cores. This is again expected because of high capillary pressure in the low permeability cores. Comparison of compositions of injected separator oil and produced yellow and blown oils (see Table 34) clearly shows that the produced light-color oils contain much less heavy hydrocarbons than separator oil does. The light-color oils were probably produced due to molecular diffusion mechanism, while the black oil may be produced due to gravity drainage mechanism.

Another notable phenomenon is that the oil recovery from the 0.38 md reservoir core was slower than that from the 0.01 md reservoir core. This is believed to be the result of the water saturation effect. The initial water saturation in the reservoir is usually less than 0.40, while the water saturation in the 0.38 md permeability core was 0.45 after waterflood. Unlike other cores, this core produced water in the early time of experiment until a water saturation of 0.36 was reached. It is believed that the existence of mobile water in the core delayed the oil recovery due to competing relative permeabilities.

Model Description

Derivation of the new model is detailed in Appendix A. A summary of the resultant equations is presented in this section. Based on the fact that the volumetric drainage rate is equal to the derivative of draining-phase volume in porous media with respect to time, the following governing equation for the wetting/non-wetting phase demarcator has been formulated:

$$\phi\left[S_{wi}-S_{wr}-\sqrt{\frac{F_s\phi z_D}{5t_D}}\right]\frac{dz_D}{dt_D}+\frac{\phi z_D}{3t_D}\sqrt{\frac{F_s\phi z_D}{5t_D}}-\left[1-\frac{H_D}{1-z_D}\right]=0 \qquad (43)$$

where

$$z_D = \frac{z_d}{L} \tag{44}$$

where

$$H_D = \frac{H}{L} \tag{45}$$

$$t_D = \frac{k_e \Delta\rho g t}{\mu L} \tag{46}$$

where z_d = demarcator depth, L = length of porous medium column, H = capillary pressure threshold, ϕ = porosity, S_{wr} = residual wetting phase saturation, S_{wi} = initial wetting phase saturation, F_s = correction factor to Kozeny equation, t = time, k_e = effective permeability, g = gravitational acceleration, $\Delta\rho = \rho_i - \rho_o$, and μ = viscosity.

Equation (43) is non-linear and is difficult, if not impossible, to solve. Therefore, we solved the equation numerically by rearranging it into the following form:

$$\Delta z_D = \frac{-\frac{\phi z_D}{3t_D}\sqrt{\frac{F_s \phi z_D}{5t_D}} + \left[1 - \frac{H_D}{1 - z_D}\right]}{\phi\left[S_{wi} - S_{wr} - \sqrt{\frac{F_s \phi z_D}{5t_D}}\right]} \cdot \Delta t_D \tag{47}$$

Using initial condition of 0 for z_D at a very small time t_D (0.0001 for example) and a small time step Δt_D, the increment of demarcator (Δz_D) can be calculated from this equation. Then z_D and t_D can be updated by

$$z_{D_{new}} = z_{D_{old}} + \Delta z_D \tag{48}$$

and

$$t_{D_{new}} = t_{D_{old}} + \Delta t_D \tag{49}$$

Repeated use of Eqs. (47), (48) and (49) gives a numerical solution to Eq. (43). Based on the position of the demarcator and the volume distribution of the liquid above the demarcator, the draining-phase recovery R with time t is calculated utilizing Eq. (50).

$$R = \left(1 - \frac{S_{wr}}{S_{wi}}\right) z_D - \frac{2z_D}{3S_{wi}} \sqrt{\frac{F_s \phi z_D}{5t_D}} \tag{50}$$

Derivation of Eq. (50) is also detailed in Appendix A. Two typical solution curves are presented in Figs. 158 and 159 for $\phi = 0.1$, $S_{wr} = 0.1$, $H_D = 0.1$, and $F_s = 1$ and 0.5, respectively. It is clearly seen from Figs. 158 and 159 that the equilibrium gravity drainage process can be divided into two periods. During the first period, the demarcator drops and the total drainage rate is a combination of the rates of full-pore flow and film flow. During the second period, the demarcator is stabilized and the total drainage rate is the rate of film flow only. It is interesting to note the effects of the parameter F_s on the shapes of demarcator and recovery curves indicated by the two figures. When F_s is greater (less homogeneous rock), as shown in Fig.158, the demarcator stabilizes gradually during bulk flow, leaving more recoverable fluid behind for pure film flow to occur. When F_s is small (homogeneous rock), as shown in Fig.159, the demarcator stabilizes sharply at the end of bulk flow, leaving less recoverable fluid behind for pure film flow.

Nonequilibrium gravity drainage occurs when a porous medium saturated with one phase is surrounded by another phase not in equilibrium, for instance, injected gas and resident oil. In this case, the surrounding phase migrates into the porous medium due to molecular diffusion causing the IFT of the fluid in the porous medium to change with time. For example, when an oil-saturated, vertically oriented core is surrounded by CO_2 during gravity drainage, the CO_2 diffuses into the core. This process results in continuous reduction of IFT between the CO_2-rich phase and the oil phase as CO_2 moves toward the interior of the core. Thus the IFT at any point in the core is time-dependent.

Although the new mathematical model is derived assuming that the wetting phase and non-wetting phase are in thermodynamic equilibrium, it is possible to apply the model to simulation of a nonequilibrium gravity drainage process if some modifications are made to account for the nonequilibrium effect due to diffusion. If we divide the core length into many elements along the direction of diffusion, then it is possible to apply the mathematical model to each individual element where uniform fluid properties are assumed. We have developed the following steps to simulate the nonequilibrium gravity drainage processes:

Estimate the concentration of the gas phase in each element at a diffusion/drainage time;

2. Estimate the average fluid viscosity, density, IFT and capillary pressure in each element at that time based on the composition of the fluid mixture;
3 Apply the mathematical model to each element to estimate liquid recovery from the element at a given time;
4. Sum up the recoveries calculated from each element to get the total liquid recovery at a given time;
5. Update the time by adding a time step and repeat 1, 2, 3, and 4 until a desired ultimate drainage time is reached.

In order to estimate gas concentration in each element, it is necessary to solve the diffusion equation (Fick's second law). Different analytical solutions to the diffusion equation are available from literature such as Crank[277] and Carslaw and Jaeger.[278] It is not clear which of the solutions is more suitable for analyzing gas diffusion into reservoir matrix. To avoid difficulties involved in programming these solutions, a simple numerical solution to the diffusion equation is used in this study. It has been found that the numerical result matches the analytical solution given by Crank[277] when the time step is less than 0.5 day for $D_0 = 1 \times 10^{-7}$ cm^2/s. This comparison is shown in Fig. 160. Numerical procedures for the solution are detailed in Appendix B.

Comparisons

Equilibrium Gravity Drainage

The new mathematical model is derived assuming constant capillary pressure at the demarcator, i.e., the wetting phase and non-wetting phase are in thermodynamic equilibrium. This model is compared with existing models and 20 sets of experimental drainage data obtained under thermodynamic equilibrium. In these experiments, IFT varies between 76 and 0.1 dynes/cm, density difference changes from 1.25 to 0.11 g/cc, the effective permeability to wetting phase covers a wide range from 6602 D to 6.1 md, porosity varies from 42.72% to 18.4%, and connate water saturation ranges from 0 to 15.8. Figure 161 shows comparisons of model calculated and observed C_1/C_7 recoveries from a Fontainebleau sandstone core.[266] Other comparisons similar to Fig. 161 were previously presented.[276] These comparisons indicate that the new model yields better accuracy than other models. The Cardwell-Parsons-Dykstra model and the Nenniger-Storrow (N-S) model consider a moving demarcator, while the Pavone-Bruzzi-Verre (P-B-V) model and the Luan model assume a fixed demarcator at the bottom of the porous media, which is not a true physical representation of drainage behavior. The C-P-D model neglects an important capillary term that appears in the governing equation. The N-S model is an approximate series solution, and the accuracy depends on the number of terms (Nenniger and Storrow[257] provide expressions for only three terms). The P-B-V model was obtained by assuming straight-line relative permeability and logarithmic capillary pressure curve, which also may not be representative of the true behavior. It is believed that these unrealistic assumptions used in model development cause inaccuracies of the models in describing the free-fall gravity drainage process.

Nonequilibrium Gravity Drainage

The concentration of CO_2 in the simulated fracture (annular space around core sample) is estimated based on an Equation of State (EOS):

$$c_f = \frac{p}{RzT} \tag{50}$$

The CO_2 concentration in each matrix element is obtained by multiplying c_f by dimensionless concentration calculated from the numerical solution to the diffusion equation presented in Appendix B. Then EOS was used again to determine volume of CO_2 in each element. Oil production due to horizontal diffusion was assumed to be equal to the volume of CO_2 that had diffused into the rock.

The match between experimental data obtained from the four cores and the mathematical model is demonstrated in Fig. 162. It is seen from this figure that a better match exists for Berea cores, while discrepancies exist for the reservoir cores. Parameters used in the match are described in the following section.

Based on our measurement, a viscosity of 2 cp for oil was utilized in our model. Density and IFT data used in the model were from our measurement results as shown in Figs. 163 and 164. Figure 163 suggests that a phase density difference of 0.2 g/cc should be used for the CO_2/separator oil system under experimental conditions. Figure 164 indicates that the IFT of the CO_2/separator oil system should be about 2 mN/m under the experimental conditions. The capillary pressure threshold was calculated using Eq. 51.

$$H = \frac{0.2\sigma}{\Delta\rho g}\sqrt{\frac{\phi}{k_e}} \tag{51}$$

Based on Renner's measurements,[280] the molecular diffusion coefficient of CO_2 in a decane-saturated Berea core at 100°F and 850 psig varies from 5.05×10^{-5} to 1.08×10^{-4} cm^2/s. The molecular diffusion coefficient of CO_2 in the pure decane may be back calculated from the following equation:

$$D = \frac{D_0}{F\phi} \tag{52}$$

Using $0.81/\phi^2$ as an approximation to the formation factor F and 0.20 porosity for the Berea core, the molecular diffusion coefficient of CO_2 in the pure decane is estimated to be $D_0=2\times10^{-4}$ to 4×10^{-4} cm^2/s. This value may be optimistic if applied to CO_2/STO system at 138 °F and 2,000 psig. In the petroleum industry, a practical value of $D_0=2\times10^{-5}$ cm^2/s for a molecular diffusion coefficient for reservoir liquids is commonly used in simulation of CO_2 miscible flooding.[281] However, we have found that the $D_0=2\times10^{-5}$ cm^2/s results in an over-estimation of oil recovery by our mathematical model. The oil

recoveries from our CO_{22}gravity drainage experiments were matched by our mathematical model when the molecular diffusion coefficient was tuned to $D_0=6x10^{-7}$ cm^2/s.

Discussion. Also shown in Figs. 163 and 164 are densities and IFT of a CO_2/recombined reservoir oil system. These figures imply that, compared to the CO_2/separator oil system, higher pressures are required to reduce IFT and density difference for achieving the same miscibility. Figure 165 demonstrates the relation between measured phase density difference and IFT for the CO_2/separator oil system and the CO_2/recombined reservoir oil system. It is not surprising that the same relation holds for both of the systems because both oils were from the same reservoir. Since the IFT-density relation governs gravity drainage in a given porous medium, it is speculated that CO_2 gravity drainage using a reservoir oil should give the same results as that using a separator oil except that higher pressures are required for miscibility. As shown in Fig. 166, the MMP of the separator oil is about 1550 psig. Figures 163 and 164 imply that the MMP of the reservoir oil should be slightly higher than that of the separator oil. This was proved by our measurement showing that the MMP of the reservoir oil is about 1565 psig.

Conclusions

1. The efficiency of CO_2 gravity drainage in naturally fractured reservoirs has been investigated experimentally. The result indicates that oil drains fast in high permeability cores, while the drainage efficiency decreases with increased water saturation.

2. A literature survey reveals that four mathematical models have been developed by previous investigators for describing free-fall gravity drainage of equilibrium phases in porous media. Comparison of wetting phase recoveries calculated by these models with experimental data indicates these models to be inaccurate. Discrepancies are believed to be due to unrealistic assumptions made in formulation of these models. Based on Darcy's law and film flow theory, a new mathematical model has been developed to describe free-fall gravity drainage with equilibrium fluids. Comparisons of wetting phase recoveries given by the new model with 20 sets of experimental data obtained under thermodynamic equilibrium show better accuracy of the model over the existing models.

3. The diffusion equation has been solved numerically to estimate gas concentration in the porous media. A procedure has been developed to couple equilibrium gravity drainage with diffusion in order to describe non-equilibrium gravity drainage. Using this procedure and measured fluid properties, experimental data obtained from four CO_2 gravity drainage experiments under thermodynamic non-equilibrium conditions have been matched.

Appendix A. Formulation of Free-fall Gravity Drainage

Assumptions

The following assumptions are made in this analysis:

1. The porous medium is homogeneous and isotropic
2. Draining phase flows only in the vertical direction.
3. The draining phase is incompressible.
4. Capillary pressure is constant at the moving demarcator.

Governing Equation

The total volume of draining phase (V_t) in the saturated zone (full pore drainage zone) and phase volume in the unsaturated zone (above phase demarcator). That is

$$V_t = V_s + V_{us} \qquad \text{A-1}$$

The phase volume in the unsaturated zone (V_{us}) includes residual phase volume (V_r) and phase volume in the film (V_f):

$$V_{us} = V_r + V_f \qquad \text{A-2}$$

If the initial and residual saturations of the draining phase are S_{wi} and S_{wr}, respectively, we have

$$V_s = S_{wi}\phi A(L - z_d) \qquad \text{A-3}$$

and

According to Nenniger and Storrow,[257] the phase volume in the film can be estimated by integrating Jeffrey's[279] equation:

$$V_f = \frac{2}{3} b \sqrt{\frac{\mu z_d^3}{\Delta \rho g t}} \qquad \text{A-5}$$

Substitutions of Eqs. (A-2) through (A-5) into Eq. (A-1) give

$$V_t = S_{wi}\phi A(L - z_d) + S_{wr}\phi A z_d + \frac{2}{3} b \sqrt{\frac{\mu z_d^3}{\Delta\rho g t}} \qquad \text{A-6}$$

Darcy velocity in the saturated zone can be expressed as

$$v_s = -\frac{1}{A}\frac{dV_t}{dt} \qquad \text{A-7}$$

The volumetric flow rate, dV_t/dt, in Eq. (A-7) can be determined by taking the derivative of Eq. (A-6) with respect to time:

$$\frac{dV_t}{dt} = -S_{wi}\phi A\frac{dz_d}{dt} + S_{wr}\phi A\frac{dz_d}{dt} + b\sqrt{\frac{\mu}{\Delta\rho g}}\left(\sqrt{\frac{z_d}{t}}\frac{dz_d}{dt} - \frac{1}{3}\sqrt{\frac{z_d^3}{t^3}}\right) \qquad \text{A-8}$$

Substituting Eq. (A-8) into Eq. (A-7) yields:

$$v_s = \left(S_{wi} - S_{wr}\right)\phi\frac{dz_d}{dt} + \frac{b}{A}\sqrt{\frac{\mu}{\Delta\rho g}}\left(\frac{1}{3}\sqrt{\frac{z_d^3}{t^3}} - \sqrt{\frac{z_d}{t}}\frac{dz_d}{dt}\right) \qquad \text{A-9}$$

The Darcy velocity (v_s) can also be expressed using Darcy's law. This was done by Cardwell and Parsons[254]:

$$v_s = \frac{k_e \Delta\rho g}{\mu}\left(1 - \frac{H}{L - z_d}\right) \qquad \text{A-10}$$

Substituting Eq. (A-9) into Eq. (A-10) and rearranging the latter gives:

$$\left[\left(S_{wi} - S_{wr}\right)\phi - \frac{b}{A}\sqrt{\frac{\mu z_d}{\Delta\rho g t}}\right]\frac{dz_d}{dt} + \frac{b}{3A}\sqrt{\frac{\mu z_d^3}{\Delta\rho g t^3}} - \frac{k_e \Delta\rho g}{\mu}\left(1 - \frac{H}{L - z_d}\right) = 0 \qquad \text{A-11}$$

Now let us define the following dimensionless variables:

$$t_D = \frac{k_e \Delta \rho g t}{\mu L} \qquad \text{A-12}$$

$$z_D = \frac{z_d}{L} \qquad \text{A-13}$$

$$H_D = \frac{H}{L} \qquad \text{A-14}$$

and

$$H_{dD} = \frac{H_d}{L} \qquad \text{A-15}$$

Introducing Eqs. (A-12), (A-13) and (A-14) into Eq. (A-11) and rearranging the latter give:

$$\left[\left(S_{wi} - S_{wr}\right)\phi - \frac{b\sqrt{k_e}}{A}\sqrt{\frac{z_d}{t_D}}\right]\frac{dz_D}{dt_D} + \frac{b\sqrt{k_e}\, z_D}{3At_D}\sqrt{\frac{z_D}{t_D}} - \left(1 - \frac{H_D}{1 - z_D}\right) = 0 \qquad \text{A-16}$$

If the breadth of the film, b, is estimated using Kozeny equation, then

$$\frac{b\sqrt{k_e}}{A} = \sqrt{\frac{F_s \phi^3}{5}} \qquad \text{A-17}$$

Substituting Eq. (A-17) into Eq. (A-16) yields:

$$\phi\left[S_{wi} - S_{wr} - \sqrt{\frac{F_s \phi z_D}{5t_D}}\right]\frac{dz_D}{dt_D} + \frac{\phi z_D}{3t_D}\sqrt{\frac{F_s \phi z_D}{5t_D}} - \left(1 - \frac{H_D}{1 - z_D}\right) = 0 \qquad \text{A-18}$$

Eq. (A-18) is the governing equation for demarcator depth z_D.

Solution

Using initial condition at $z_D=0$ at $t_D=0$, Eq. (A-18) is solved numerically. Typical solution curves are presented in Figs. 159 and 160 for $\phi=0.1$, $S_{wr}=0.1$, $H_D=0.1$, and $F_s=1$ and 0.5, respectively.

Based on the position of the demarcator and the volume distribution of the liquid in the porous medium, the draining-phase recovery (R) with time can then be determined as follows:

$$R=\frac{V_{ti}-V_s-V_r-V_f}{V_{ti}} \qquad \text{A-19}$$

The initial phase volume is

$$V_{ti}=S_{wi}\phi AL \qquad \text{A-20}$$

Substituting Eqs. (A-20), (A-3), (A-4), and (A-5) into Eq. (A-19) and rearranging the latter give

$$R=\left(1-\frac{S_{wr}}{S_{wi}}\right)\frac{z_d}{L}-\frac{2b}{3S_{wi}\phi AL}\sqrt{\frac{\mu z_d^3}{\Delta\rho g t}} \qquad \text{A-21}$$

Introducing dimensionless variables and Eq. (A-17) into Eq. (A-21) results in

$$R=\left(1-\frac{S_{wr}}{S_{wi}}\right)z_D-\frac{2z_D}{3S_{wi}}\sqrt{\frac{F_s\phi z_D}{5t_D}} \qquad \text{A-22}$$

Typical recovery curves are also shown in Figs. 159 and 160 corresponding to the demarcator curves presented in the figure.

Appendix B: Numerical Solution of Diffusion Equation

Assumption

Since the height of the porous medium under consideration is vertically exposed to a diffusing phase, we assume that (1) vertical diffusion is negligible, i.e., horizontal (one-dimensional) diffusion prevails in the porous medium, and (2) diffusion coefficient is constant during gravity drainage throughout the porous medium.

Governing Equation

The governing equation to the 1-D diffusion problem is Fick's second law:

$$D\frac{\partial^2 c}{\partial x^2} = \frac{\partial c}{\partial t} \qquad \text{B-1}$$

Initial Condition

Initially the concentration of the diffusing phase in the porous medium is assumed to be a constant c_i. The initial condition may be expressed as

$$c|_{t=0,\,x>0} = c_i \qquad \text{B-2}$$

Boundary Conditions

The inner boundary is the lateral surface of the porous medium. The gas concentration at the boundary may be assumed to be the gas concentration in the fracture:

$$c|_{t>0,\,x=0} = c_f \qquad \text{B-3}$$

The outer boundary is at the center of the porous medium. Because of symmetry, the following boundary condition should be used:

$$\left[\frac{\partial c}{\partial x}\right]_{t\geq 0,\,x=x_{\max}} = 0 \qquad \text{B-4}$$

By introducing dimensionless concentration defined as

$$C_D = \frac{c - c_i}{c_f - c_i} \qquad \text{B-5}$$

Eqs. (B-1) through (B-4) can be written as

$$D\frac{\partial^2 C_D}{\partial x^2} = \frac{\partial C_D}{\partial t} \qquad \text{B-6}$$

$$C_D|_{t=0, x>0} = 0 \qquad \text{B-7}$$

$$C_D|_{t>0, x=0} = 1 \qquad \text{B-8}$$

$$\left[\frac{\partial C_D}{\partial x}\right]_{t\geq 0, x=x_{\max}} \qquad \text{B-9}$$

Numerical Solution

Using the implicit differentiation scheme, Eq. (B-6) can be discretized at point and time step as:

which can be rearranged to be:

$$A_i C_{D_{i-1}}^{n+1} + B_i C_{D_i}^{n+1} + C_i C_{D_{i+1}}^{n+1} = D_i \qquad \text{B-11}$$

where $A_i = C_i = 1$ and

$$B_i = -2 - \frac{\Delta x^2}{D\Delta t} \qquad \text{B-12}$$

$$D_i = -\frac{\Delta x^2}{D\Delta t} C_{D_i}^n \qquad \text{B-13}$$

For i=1 (first cell), after applying boundary condition given by Eq. (B-8), Eq. (B-11) becomes

$$\left(A_1 + B_1\right)C_{D_1}^{n+1} + C_1 C_{D_2}^{n+1} = D_1 \qquad \text{B-14}$$

For i=2 (second cell), Eq. (B.11) becomes

$$A_2 C_{D_1}^{n+1} + B_2 C_{D_2}^{n+1} + C_2 C_{D_3}^{n+1} = D_2 \qquad \text{B-15}$$

If the length is discretized into m cells, for i=m (last cell), after applying boundary condition given by Eq. (B-9), Eq. (B-11) becomes

$$A_m C_{D_{m-1}}^{n+1} + \left(B_m + C_m\right)C_{D_m}^{n+1} = D_m \qquad \text{B-16}$$

Equations (B-14) through (B-16) are m equations with m unknowns $(C_{D_i}^{n+1}, i = 1,2,...,m)$, and can be written in the form of matrices. These unknowns can be easily solved using the matrix solver subroutine THOMAS. The numerical result is comparable to analytical result given by Crank[277] as shown in Fig. 161.

NOMENCLATURE

a = inclination angle, degree, or constant in various equations

A = cross sectional area, L^2, cm^2

A_i = coefficient of term $C_{D_{i-1}}^{n+1}$ for grid i

b = total breadth of film, L, cm, or constant in various equations.

B_i = coefficient of term $C_{D_{i-1}}^{n+1}$ for grid block i

B_{ob} = formation volume factor

c = concentration, mole/L^3, mole/cm^3, or constant in various equations

C = constant in Macleod Equation

CO_2 = carbon dioxide

C_D = dimensionless concentration

c_f = fracture concentration, mol/L^3, mole/cm^3

c_i = initial concentration, mole/L^3, mole/cm^3

C_i = coefficient of term $C_{D_{i-1}}^{n+1}$ for grid i

C_s = surfactant concentration ppm

d = constant in various equations

D = effective diffusion coefficient, L^2/t, cm^2/s

D_e = pendant drop diameter at equator, cm

D_i = coefficient for grid block i

D_s = pendant drop diameter at elevation D_e, cm

D_0 = molecular diffusion coefficient, L^2/t, cm^2/s

EOS = equation of state

F = formation factor, dimensionless

F_s = correction factor to Kozeny equation

g = gravitational acceleration, L/t^2

H = capillary pressure threshold, L, cm

H_D = dimensionless capillary pressure threshold

H_d = height of demarcator, L, cm

H_{dD} = dimensionless height of demarcator

H_e = elevation of the equator from apex, cm

i = space index of grid block

I = relative adsorption index

k_e = effective permeability, L^2, md

K_w = Watson characterization factor

L = length of porous medium column, L, cm

m = the maximum number of grid blocks

M = molecular weight

M_{CO2+BR} = total mobility of CO_2 /brine

M_{CO2+SS} = total mobility of CO_2 /surfactant

M_g = gas mobility

M_g^{foam} = gas mobility in the presence of foam

M_i = molecular weight of pseudocomponent i

M_w = water mobility

MMP = minimum miscibility pressure

n = time step index or number of components

NN = neural networks

p = pressure, m/Lt^2, atm

Δp = pressure drop across a core

P = parachor

P_{ai} = inner phase pressure above apex, dyne/cm^2

P_{ao} = outer phase pressure below apex, dyne/cm^2

P_b = bubblepoint pressure, psig

P_{ca} = capillary pressure at the apex, dyne/cm^2

P_{He} = inner phase pressure at H_e, dyne/cm^2

P_l = liquid phase density, g/cm^3

P_o = outer phase pressure at elevation y, dyne/cm^2

$P\nu$ = gas phase density, g/cm^3

PVT = pressure-volume-temperature

Q = flow rate

R = dimensionless fluid recovery

R_a = radius of curvature at the apex, cm

R_f = resistance factor

R_s = solution gas

S = arc length from the apex to elevation y, cm

S_g = gas saturation

S_o = oil saturation

S_w = water saturation

S_{wc} = connate wetting phase saturation, fraction

S_{wi} = initial wetting phase saturation

S_{wr} = residual wetting phase saturation, fraction

SAG = surfactant solution alternating with gas

SMR = selective mobility reduction

T = temperature, °K (unless °C, °F, or °R is stated)

t = time, s

T_{bi} = boiling point temperature

T_c = critical temperature

t_D = dimensionless time

t_c = critical temperature, °K

Δt = time step size, s

v_s = Darcy velocity in saturated zone, L/t, cm/s

V = convection coefficient, L/t cm/s

V_f = phase volume in the film, L^3, cm^3

V_g = gas phase molar volume

V_l = liquid phase molar volume

V_r = residual phase volume, L^3, cm^3

V_s = phase volume in saturated zone, L^3, cm^3

V_t = total phase volume, L^3, cm^3

V_{ti} = initial total phase volume, L^3, cm^3

V_{us} = phase volume in unsaturated zone, L^3, cm^3

W = drop weight, dyne

WAG = water alternating with gas

x = radial distance, cm

x_i = mole fraction of component *i* in the liquid phase

x_{max} = maximum diffusion distance, L, cm

x^s_i = mole fraction of component *i* at the liquid-vapor interface

Δx = length of grid block, L, cm

y = elevation from apex, cm

y_i = mole fraction of component *i* in the vapor phase

z = depth from the top of the core, L, cm

z_d = demarcator depth, L, cm

z_D = dimensionless demarcator depth

z_{CO2} = mole fraction of CO_2

β = $\Delta\rho\ g\ R^2_a/\sigma$, dimensionless or density scaling exponent

γ = interfacial tension scaling exponent

γ_o = oil specific gravity

γ_{oi} = oil specific gravity of pseudocomponent *i*

γ_g = gas gravity

$\Delta\rho$ = density difference

$\Delta\rho_0$ = reference density difference

χ = mobility

δ = solubility parameter

μ = viscosity, m/Lt, cp

ρ_i = density of the inner phase, g/cm^3

ρ_l = liquid phase density, g/cm^3

ρ_o = density of the outer phase, g/cm^3

ρ_v = gas phase density, g/cm^3

σ = interfacial tension, m/t^2, dyne/cm or N/m

σ_0 = reference interfacial tension

ϕ = porosity

lim = limiting values of the associated variable

REFERENCES

1. Lee, H.O., Heller, J.P., and Hoefer, A.M.W.: "Change in Apparent Viscosity of CO_2 Foam with Rock Permeability," *SPERE* (Nov. 1991) 421-428.
2. Tsau, J.S. and Heller, J.P.: "Evaluation of Surfactants for CO_2-Foam Mobility Control," paper SPE 24013 presented at the 1992 Permian Basin Oil and Gas Recovery Conference, Midland, March 18-20.
3. Dixit, A., Tsau, J.S., and Heller, J.P.: "Laboratory Study on Surfactant-Based Selective Mobility Control," paper SPE 27729 presented at the 1994 Permian Basin Oil and Gas Recovery Conference, Midland, March 16-18.
4. Tsau, J.S., Heller, J.P., Moradi-Araghi, A., Zornes, D.R., and Kuehne, D.L.: "CO_2 Foam Field Verification Pilot Test at EVGSAU: Phase IIIA-Surfactant Performance Characterization and Quality Assurance," paper SPE 27785 presented at the 1994 SPE/DOE Ninth Symposium on Improved Oil Recovery, Tulsa, Apr. 17-20.
5. Yaghoobi, H. And Heller, J.P.: "Laboratory Investigation of Parameters Affecting CO_2-Foam Mobility in Sandstone at Reservoir Conditions," paper SPE 29168 presented at the 1994 Eastern Regional Meeting, Charleston, Nov. 8-10.
6. Tsau, J.S. and Heller, J.P.: "How Can Selective Mobility Reduction of CO_2-Foam Assist in Reservoir Floods?" paper SPE 35168 presented at the 1996 Permian Basin Oil and Gas Recovery Conference, Midland, March 27-29.
7. Yang, S.H. and Reed, R.L.: "Mobility Control Using CO_2 Foams," paper SPE 19689 presented at the 64th Annual Technical Conference, San Antonio, Oct. 8-11, 1989.
8. Yaghoobi, H. and Heller, J.P.: "CO_2-Foam Mobility Behavior in Heterogeneous System," paper SPE 35169 presented at the 1996 Permian Basin Oil and Gas Recovery Conference, Midland, March 27-29.
9. Kovscek, A.R., and Radke, C.J.: "A Comprehensive Description of Transient Foam Flow in Porous Media," presented at the 1993 DOE/NIPER Symposium on Field Application of Foams for Oil Production, Bakersfield, CA, Feb. 11-12.
10. Ammer, J.R., Brummert, A.C., and Sams, W.N. *Miscible Applied Simulation Techniques for Energy Recovery-Version 2.0, User's Guide and Technical Report*, DOE Contract No. DOE/BC-91/2/SP (February 1991).
11. Chang, S.H. and Grigg, R.B.: "Foam Displacement Modeling in CO_2 Flooding Precesses," paper SPE 35401 presented at 1996 SPE/DOE Symposium on Improved Oil Recovery, Tulsa, Apr. 21-24.
12. L. Lake, *Enhanced Oil Recovery*, Prentice Hall, Inc., Englewood Cliffs, New Jersey (1989) 201-205.
13. Ettinger, R.A. and Radke, C.J.: "Influence of Texture on Steady Foam Flow in Berea Sandstone," *SPERE* (Feb. 1992) 83-90.
14. Martin, F.D. : "Enhanced Oil Recovery for the Independent Producer," paper SPE/DOE 24142 presented at the 1992 SPE/DOE Symposium on Enhanced Oil Recovery, Tulsa, April 22-24.
15. Hadlow, R.E.: "Update of Industry Experience with CO_2 Flooding," paper SPE 24928 presented at the 1992 SPE Annual Technical Conference and Exhibition, Washington, D.C., October 4-7.

16. Shyeh-Yung, J-G.J.: "Mechanisms of Miscible Oil Recovery: Effects of Pressure on Miscible and Near-Miscible Displacements of Oil by Carbon Dioxide," paper SPE 22651 presented at the 1991 SPE Annual Technical Conference and Exhibition, Dallas, October 6-9.
17. Shyeh-Yung, J-G. J *et al*.: "Effect of Solvent Composition and Pressure on Displacement of Oil by Enriched Hydrocarbon Gases," paper SPE 28264 presented at the 1994 SPE Annual Technical Conference & Exhibition, New Orleans, Sept. 25-28.
18. Burger, J.E. *et al*, "Effect of Phase Behavior on Bypassing in Enriched Gasfloods," *SPERE* (May 1994) 112.
19. Bardon, C. *et al*: "Gas/Oil Relative Permeabilities and Residual Oil Saturations in a Field Case of a Very Light Oil, in the Near-Miscibility Conditions," paper SPE 28625 presented at the 1994 SPE Annual Technical Conference & Exhibition, New Orleans, Sept. 25-28.
20. Pande, K.K.: "Effect of Gravity and Viscous Crossflow on Hydrocarbon Miscible Flood Performance in Heterogeneous Reservoirs," paper SPE 24935 presented at the 1992 SPE Annual Technical Conference and Exhibition, Washington, D.C., October 4-7.
21. Mizenko, G.J., "North Cross (Devonian) Unit CO_2 Flood: Status Report," paper SPE 24210 presented at the 1992 SPE/DOE Symposium on Enhanced Oil Recovery, Tulsa, April 22-24.
22. Liu, E.C. *et al*.: "A Numerical Evaluation of the Effectiveness of Single Slug, WAG, and Hybrid CO_2 Injection Processes for the Dollarhide Devonian Unit, Andrew County, Texas," paper SPE 20098 presented at the 1990 Permian Basin Oil and Gas Recovery Conference, Midland, March 8-9.
23. Vargaftik, E.C. *Tables on the Thermophysical Properties of Liquids and Gases*, Hemisphere Publishing Corp., Washington, D.C., (1975).
24. Ely, J.F. *et al*.: *NIST Thermophysical Properties of Hydrocarbon Mixtures Databases*, Version 1.0 National Institute of Standards and Technology, Standard Reference Data Program (1990).
25. Yellig, W.F. *et al.*, "Determination and Prediction of CO_2 Minimum Miscibility Pressure," *JPT* (Jan. 1980) 160.
26. Creek, J.L. and Sheffield, J.M.: "Phase Behavior, Fluid Properties, and Displacement Characteristics of Permian Basin Reservoir Fluid.CO_2 Systems," *SPERE* (Feb. 1993) 34-42.
27. Chang, S-H., Martin, F.D., and Grigg, R.B.: "Effect of Pressure on CO_2 Foam Displacement: A Micromodel Visualization Study," paper 27784 presented at the 1994 SPE/DOE Ninth Symposium on Improved Oil Recovery, Tulsa, April 17-20.
28. Grigg, R.B., Gregory, M.D., and Purkaple, J.D.: "The Effect of Pressure on Improved Oilflood Recovery from Tertiary Gas Injection," SPERE (August 1997) 179–187.
29. Holm, L.W. *et al*.: "Mechanisms of Oil Displacement by Carbon Dioxide," *JPT* (Dec. 1974) 1427.
30. Harmon, R.A., and Grigg, R.B. "Vapor-Density Measurements for Estimating Minimum Miscibility Pressure," *SPERE* (Nov. 1988) 1215.
31. Orr, F.M. *et al.* "Interpretation of Pressure-Composition Phase Diagrams for CO_2/Crude-Oil Systems," *SPEJ* (Feb. 1984) 485.
32. Holm, L.W. *et al*.: "Effect of Oil Composition on Miscible Type Displacement by Carbon Dioxide," *SPEJ* (Feb. 1982) 87.
33. Orr, F.M., *et al*.: "Effect of Oil Composition on Minimum Miscibility - Part 2: Correlation," *SPERE* (Nov. 1987) 479.

34. Hagedorn, K.D. and Orr, F.M.: "Component Partitioning in CO_2/Crude Oil Systems: Effects of Oil Composition on CO_2 Displacement Performance," paper SPE 25169, presented at the 1993 SPE International Symposium on Oilfield Chemistry, New Orleans, March 2-5.
35. Prausnitz, J.M.: *Molecular Thermodynamics of Fluid-Phase Equilibria*, Prentice-Hall, Englewood Cliffs, N.J. (1969).
36. Lange, E.A.: "Correlation and Prediction of Residual Oil Saturation for Gas Injection EOR Processes," paper 35425 presented at the 1996 SPE/DOE Symposium on Improved Oil Recovery, Tulsa, April 21-24.
37. Thomas, F.B. *et al*.: "Miscible or Near-Miscible Gas Injection, Which Is Better?" paper SPE 27811 presented at the 1994 SPE/DOE Symposium on Improved Oil Recovery, Tulsa, April 17-20.
38. Schechter, D.S. and Guo, B.: "Parachors Based on Modern Physics and Their Uses in IFT Prediction of Reservoir Fluids," paper SPE 30785 presented at the 1995 SPE Annual Technical Conference & Exhibition, Dallas, October 22-25.
39. Wu, R.S. *et al*.: "Evaluation of Miscibility From Slim Tube Tests," *J. Canadian Pet. Tech*., (Nov-Dec 1990) 63.
40. Grigg, R.B., Heller, J.P., and Schechter, D.S.: "Improved Efficiency of Miscible CO_2 Floods and Enhanced Prospects for CO_2 Flooding Heterogeneous Reservoirs," annual report, Contract No. DE-FG22-94BC14977, U.S. DOE (April 1995).
41. Stevens, J.E. and Martin, F.D.: "CO_2 Foam Field Verification Pilot Test at EVGSAU: Phase IIIB - Project Operations and Performance Review," paper SPE 27786 presented at the 1994 SPE/DOE Symposium on Improved Oil Recovery, Tulsa, April 17-20.
42. Chang, S-H. and Grigg, R.B.: "Laboratory Flow Tests Used to Determine Reservoir Simulator Foam Parameters for EVGSAU CO_2 Foam Pilot," paper SPE 27675 presented at the 1994 Permian Basin Oil and Gas Recovery Conference, Midland, March 16-18.
43. Martin, F.D. *et al*.: "Field Verification of CO_2 Foam," final report, DOE Contract No. DE-FG21-89MC26031 (April 1995).
44. Orr, F.M., Jr., Silva, M.K., and Lien, C.-L.: "Equilibrium Phase Compositions of CO_2/Crude Oil Mixture-Part 2: Comparison of Continuous Multiple-Contact and Slim-Tube Displacement Tests," *SPEJ* (April 1983) 281-291.
45. Lansangan, R.M. and Smith, J.L. "Viscosity, Density, and Composition Measurements of CO_2/West Texas Oil Systems," *SPERE* (Aug. 1993) 175-182.
46. Weiss, W.W., Buckley, J.S. and Ouenes,A. : "Integration of Advanced Geoscience and Engineering Techniques to Quantify Interwell Heterogeneity in Reservoir Models," final report, Contract No. DE-AC22-93BC14893, U.S. DOE (January 1997).
47. Elsharkawy, A.M., Poettmann, F.H., and Christiansen, R.L.: 'Measuring Minimum Miscibility Pressure: Slim-Tube or Rising Bubble?" pper SPE presented at the 1992 SPE/DOE Symposium on Enhanced Oil Recovery, Tulsa, April 22-24.
48. Orr, F.M., Jr., Siva, M.K., Lien, C.L., and Pelletier, M.T.: "Laboratory Experiments to Evaluate Field Prospects for carbon Dioxide Flooding,: *JPT,* **34** (1982) 888-898.
49. Johnson, J.P. and Pollin, J.S.: "Measurement and Correlation of CO2 Miscibility Pressures" paper SPE 9790 presented at the 1981 SPE/DOE Enhanced Oil Recovery Symposium, Tulsa, April 5-8

50. Nighswander, J.A., Chang-Yen, D.A., Perez, J., and Kalra, H.: "Experimental Measurement and Modeling of Transition Zone Fluids," paper SPE 27813 presented at the 1994 SPE/DOE Symposium on Enhanced Oil Recovery, Tulsa, April 17-20.
51. Grigg, R.B.: "Dynamic Phase Composition, Density, and Viscosity Measurements During CO_2 Displacement of Reservoir Oil," paper SPE 28974 presented at the 1995 SPE International Symposium on Oilfield Chemistry, San Antonio, Feb. 14-17.
52. Grigg, R.B. and Fritchman, D.M.: "Continuous Phase Equilibrium Data for CO_2 Wasson Line Oil: Supplement to Paper SPE 28974," PRRC Report 95-22, New Mexico Petroleum Recovery Research Center, May 1995, Socorro, NM.
53. Grigg, R.B., Kernodle, J.L., and Onimole, A.: "Data from Minimum Miscibility and CO_2 Swelling Tests for Spraberry Crude," PRRC Report 95-21, New Mexico Petroleum Recovery Research Center, May 1995, Socorro, NM.
54. Orr, F.M., Jr., and Lien, C.L. "Phase Behavior of CO_2 and Crude Oil in Low Temperature Reservoirs," *SPEJ* (Aug. 1981) 480-492.
55. Schechter, D.S. and Guo, B.: "Mathematical Modeling of Gravity Drainage After Gas Injection into Fractured Reservoirs," paper SPE 35170 presented at the 1996 SPE/DOE Improved Oil Recovery Symposium, Tulsa, Apr. 22-24.
56. Menzie, D.: "A Study of the Vaporization of Crude Oil by Carbon Dioxide Repressuring," PhD dissertation, Pennsylvania State University (1962).
57. Alsinbili, M.B.: "An Experimental and Theoretical Investigation of The Effect of API-Gravity Injection Pressure and Oil Composition on Oil Recovery by High Pressure Carbon Dioxide Injection," PhD dissertation, University of Oklahoma (1972).
58. Gardner, J.W., Orr, F.M., Jr., and Patel, P.D.: "The Effect of Phase Behavior on CO_2 Flood Displacement Efficiency," *JPT* (Nov.1981) 2067-81.
59. Silva, M.K and Orr, F.M, Jr. : "Effect of Oil Composition on Minimum Miscibility Pressure-Part 1: Solubility of Hydrocarbons in Dense CO2," paper SPE 14149 presented at the 1985 SPE Annual Technical Conference and Exhibition, Las Vegas, September 22-25.
60. Stewart, W.C. and Nielsen R.R.: "Phase Equilibria for Mixtures of Carbon Dioxide and Several Saturated Hydrocarbons," *Producer Monthly* (Jan. 1954) **18**(3), 27
61. Meldrum, A.H. and Nielsen, R.F.: "A Study of Three-Phase Equilibria for Carbon Dioxide-Hydrocarbon Mixtures," *Producer Monthly* (Aug. 1955) **19**(10), 22
62. Poettmann, F.H. and Katz, D.L.: "Phase Behavior of Binary Carbon Dioxide-Paraffin Systems," *Ind. Eng. Chem*. (1945) **37**, 847-853.
63. Reamer, H.H.; Olds, R.H., Sage, B.H., and Lacey, W.N.: "Phase Equilibria in Hydrocarbon Systems. Volumetric Behavior of the Ethane-Carbon Dioxide System," *Ind. Eng. Chem.* (1945)**37,** 688-691.
64. Zarah, B.Y.: "The Heterogenous Phase-Equilibria and the Solution Thermo-dynamics of The Ternary System Carbon Dioxide-N-Butylene-N-Eicosane," PhD dissertation, University of Notre Dame, Indiana (1974).
65. Francis, A.W.: "Ternary Systems of Liquid Carbon Dioxide," *J.Phys. Chem.* (1954), 1099-1114.
66. Larsen, L, Silva, M.K. and Taylor, M.A.: "Temperature Dependence of L1-L2-V Behavior in CO2-Hydrocarbon Systems," paper SPE 15399 presented at the 1986 SPE Annual Technical Conference and Exhibition, New Orleans, October 5-8.

67. Turek, E.A.; Metcalfe, R.S.; Yarborough, L., and Robinson, R.L., Jr.: "Phase Equilibria in CO2 -Multicomponent Hydrocarbon Systems: Experimental Data and Improved Prediction Technique," *SPEJ* (June 1984) 308–324.
68. Grigg, R.B. and Lingane, P.J.: "Predicting Phase Behavior of Mixtures of Reservoir Fluids With Carbon Dioxide," paper SPE 11960 presented at the 1983 SPE Annual Technical Conference and Exhibition, San Francisco, October 5-8.
69. Simon, R., Rosman, A. and Zana, E.: "Phase Behavior Properties of CO_2-Reservoir Oil Systems," *SPEJ* (Feb. 1978) **18**(1), 20.
70. Orr, F.M, Jr., Yu, A.D. and Lien, C.L.: "Phase Behavior of CO_2 and Crude Oil in Low Temperature Reservoirs," paper SPE 8813 presented at the 1980 SPE/DOE Symposium on Enhanced Oil Recovery, Tulsa, April 20-23.
71. Shelton, J.L. and Yarborough, L.: "Multiple Phase Behavior in Porous Media During CO_2 or Rich Gas Flooding," *JPT* (September 1977), 1171-1178.
72. Henry, R.L and Metcalfe, R.S.: "Multiple Phase Generation During CO_2 Flooding," paper SPE 8812 presented at 1980 SPE/DOE Symposium on Enhanced Oil Recovery, Tulsa, April 20-23.
73. Turek, E.A., Metcalfe, R.S. and Fishback, R.E.: "Phase Behavior of Several CO_2/West-Texas-Reservoir-Oil Systems," *SPERE* (May 1988) 505-516.
74. Orr, F.M, Jr. and Jensen, C.M: "Interpretation of Pressure Composition Diagram for CO_2/crude oil System," *SPEJ* (Oct. 1984) 485-97.
75. Hutchinson, C.A. and Braun, P.H.: "Phase Relations of Miscible Displacement in Oil Recovery," *AIChE J.*(March 1961) **7**(1), 64-72
76. Rathmel, J.J., Stalkup, F.I., and Hassinger, R.C.: "A Laboratory Investigation of Miscible Displacement by CO_2 ," paper SPE 3483 presented at the 1971 SPE Annual Fall Meeting, New Orleans, Oct. 3-6
77. Sigmund, P.M, Kerr, W. and McPherson, R.E.: "A Laboratory and Computer Model Evaluation of Immiscible CO_2 Flooding in a Low-Temperature Reservoir," paper SPE 12703 presented at the 1984 SPE/DOE Symposium on Enhanced Oil Recovery, Tulsa, April 16-18.
78. Bahralolom, I.M. and Orr, F.M, Jr.: "Solubility and Extraction in Multiple-Contact Miscible Displacements: Comparison of N_2 and CO_2 Flow Visualization Experiments," paper SPE 15079 presented at 1986 SPE California Regional Meeting, Oakland, CA, April 2-4.
79. Siagian, U.W.R.: "A Laboratory Study of the Extraction of Hydrocarbons from Crude Oil by High Pressure Carbon Dioxide," MS thesis, New Mexico Institute of Mining and Technology, Socorro, New Mexico (June 1997).
80. Holm, L.W. and Josendal, V.A.: "Mechanisms of Oil Displacenent by Carbon Dioxide," *JPT* (Dec. 1974), 1427.
!81. Kuehne, D.L. *et al.*, "Evaluation of Surfactant for the CO_2 Mobility Control in Dolomite Reservoirs," paper SPE 24177 presented at the 1992 SPE/DOE Symposium on Enhanced Oil Recovery, Tulsa, April 22-24.
82. Kovscek, A.R. and Radke, C.J. "A Comprehensive Description of Transient Foam Flow in Porous Media," paper presented at the 1993 DOE/NIPER Symposium on Field Application of Foams for Oil Production, Bakersfield, CA, February 11-12.
83. Chang, S-H., Owusu, L.A., French, S.B., and Kovarik, F.S.: "The Effect of Microscopic Heterogeneity on CO_2-Foam Mobility: Part 2—Mechanistic Foam Simulation," paper SPE

20191 presented at the 1990 SPE/DOE Symposium on Enhanced Oil Recovery, Tulsa, OK, April 22-25.
84. Heller, J.P., Boone, D.A., and Watts, R.J.: "Tertiary CO_2 Foam for Mobility Control at Rock Creek," paper SPE 14519 presented at the 1985 SPE Eastern Regional Conference, Morgantown, Nov. 5-8.
85. Martin, F.D. *et al*.: "CO_2 Foam Field Verification Pilot Test at EVGSAU Injection Project - Phase I: Project Planning and Initial Results," paper SPE 24176 presented at the 1992 SPE/DOE Symposium on Enhanced Oil Recovery, Tulsa, April 22-24.
86. Martin, F.D. et al.: "Field Verification of CO_2 Foam," final report, Contract No. DE-FG21-89 MC26031, U.S. DOE, (April 1995).
87. Peng, D.-Y., and Robinson, D. B.: "A new two-constant equation of state," *Ind. Eng. Chem. Fund.*, 15(1976): 59-64.
88. Riazi, M. R., and Daubert, T. E. : "Characterization parameters for petroleum fractions," *Ind. Eng. Chem. Res.*, 26(1987): 755-759.
89. Whitson, C.H., Anderson, T.F., and Soreide, I.: "C7+ characterization of related equilibrium fluids using the gamma distribution," *C7+ Fraction Characterization*, Chorn, L. G. and Mansoori, G. A. (eds.), Taylor and Francis, New York, 1989, pp. 35-56
90. Yarborough, L.: "Application of a generalized equation of state to petroleum reservoir fluids," in: Chao, K. C. and Robinson, R. L. Jr. (eds.), *Equation of State in Engineering and Research.* American Chemical Society, Washington, D. C., 1979, pp. 385-439.
91. Chang, S.-H., Grigg, R. B., and Huang, T.-C.: "Characterization and Multiphase Equilibrium Prediction of Crude Oil Heavy Components," *Fuel Science and Technology International* (1996).
92. Sutton, R.P. and Farshad, F.F., "Evaluation of Empirically Derived PVT Properties for Gulf of Mexico Crude Oils," SPE paper 13172 presented at the 1984 SPE Annual Technical Conference and Exhibition, Houston, Texas, September 16-19.
93. Standing, M. B.: "A Pressure-Volume-Temperature Correlation for Mixtures of California Oils and Gases" *Drilling and Production Practice, API (*1957) 275-287.
94. Standing, M. B.: *Volumetric and Phase Behavior of Oil Field Hydrocarbon Systems*, 9th ed. Society of Petroleum Engineers, Dallas (1981).
95. Glaso, O.: "Generalized Pressure-Volume-Temperature Correlations, " *JPT* (May 1980) 785-795.
96. Al-Marhoun, M.A.: "PVT Correlation for Middle East Crude Oils," *JPT*, (May 1988) 650-665.
97. Larsen, L.L.: "Prediction of Phase Behavior of CO_2-Hydrocarbon Mixtures," MS thesis New Mexico Institute of Mining and Technology, Socorro, NM (1984).
98. Gardner, J.W., Orr, F.M. and Patel, P.D.: "The Effect of Phase Behavior on CO_2-Flooding Displacement Efficiency," *JPT* (Nov. 1981) 2067-2081.
99. Coutinho, J. A. P., Jorgensen, M. and Stenby, E. H.: "Predictions of Three-phase Regions in Co_2-oil Mixtures," *Journal of Petroleum Science and Engineering* (1995)**12,** 201-208.
100. Khan, S.A., Pope, G.A and Sephernoori, K.: "Fluid Characterization of Three-phase Co_2/oil Mixtures," paper SPE 24130 presented at the 1992 SPE/DOE Symposium on Enhanced Oil Recovery, Tulsa, OK, April 22-24.
101. Negahban, S. and Kremesec, Jr.,V.J.: "Development and Validation of Equation of State Fluid Descriptions for CO_2/Reservoir-oil Systems," *SPERE* (1992) **7**(3), 363-368.

102. Nghiem, L.X. and Li, Y.K.: "Computation of Multiphase Equilibrium Phenomena with an Equation of State," *Fluid Phase Equilibria* (1984) **17**, 77-95.
103. Chaback, J.J. and Turek, E.A.: "Phase Behavior of Mixtures of San Andres Formation Oils with Acid Gases," *Equations of State: Theories and Applications,* K.C. Chaoand R.L. Robinson, Jr. (eds.), ACS Symp. Ser., (1986) **300,** 406-433.
104. Chorn, L.G. and Mansoori, G.A.: *C_{7+} Fraction Characterization*, Taylor and Francis, New York (1989).
105. Merril, R.C.: *EEC Summer School Notes*, IVC-SEP, DTH, Lyngby, Denmark (1993).
106. Katz, D.L. and Firoozabadi, A.: "Predicting Phase Behavior of Condensate/Crude-oil Systems Using Methane Interaction Coefficients," *JPT,* 1978 **30**(11), 1649-1655.
107. Gani, R. and Fredenslund, A.: "Thermodynamics of Petroleum Mixtures Containing Heavy Hydrocarbons: an Expert Tuning System," *Ind. Eng. Chem. Res.* (1987)**26**, 1304-1312.
108. Helle, S.C. and Friedmann, J.D.: "Different Effects of Characterization Methodologies. Formation Oils with Acid Gases," in *C_{7+} Fraction Characterization*, L.G. Chorn and G.A. Mansoori (eds.),Taylor and Francis, New York (1989) 11-35.
109. Habiballah, W.A., Startzman, R.A. and Barrufet, M.A.: "Use of Neural Networks for Prediction of Vapor/Liquid Equilibrium K Values for Light-Hydrocarbon Mixtures," *SPERE,* (May 1996) 121-126.
110. Mohaghegh, S.: "Neural Network: What It Can Do for Petroleum Engineers," *JPT* (Jan 1995) 42-43.
111. Rumelhart, D.E., Hinton, G.E. and Williams, R.J.: *Learning Internal Representations by Error Back Propagation*, MIT Press, Cambridge, MA (1988) 318-362.
112. Al-Kaabi, A.U. and Lee, W.J.: "Using Artificial Neural Networks Approach to Identify the Well Test Interpretation Model," paper SPE 20332 presented at the 1990 SPE Petroleum Computer Conference, Houston, June 25-28.
113. Hecht-Nielsen, R.: "Theory of the Backpropagation Neural Network," International Joint Conference on Neural Networks, Washington, DC, (1989)**1**, 593-606.
114. Pao, Y.: *Adaptive Pattern Recognition and Neural Networks*, Addison-Wesley, Reading, MA (1989) 113-140.
115. Accarain, P. and Desbrandes, R.: "Neuro-Computing Helps Pore Pressure Determination". *Petroleum Engineering International*, (Feb. 1993) 39-42.
116. Ouenes, A., Richardson, S. and Weiss, W.W.: "Fractured Reservoir Characterization and Performance Forcasting Using Geomechanics and Artificial Intelligence," paper SPE 30572, presented at the 1995 SPE Annual Technical Conference and Exhibition, Dallas, TX, Oct. 22-25.
117. Hertz, J., Krogh, A. and Palmer, R.G.: "Introduction to the theory of neural computation", Addison-Wesley, Redwood City, CA (1994).
118. Liu, K.J.: "Applications of New Backpropagation Algorithm in Petroleum Problems," MS thesis, New Mexico Institute of Mining and Technology, Socorro, NM (1996).
119. Moller, M.F.: "A Scaled Conjugate Gradient Algorithm for Fast Supervised Learning," *Neural Networks* (1993)**6**, 525-533.
120. Jorgensen, M. and Stenby, E.H.: "Phase Equilibrium Calculations CO_2-Hydrocarbon Mixtures," presented at the 1993 European IOR Symposium, Moscow, Oct.27-29.

121. Falls, A.H., *et al.*: "Development of a Mechanistic Foam Simulator: The Population Balance and Generation by Snap-Off," *SPERE* (Aug. 1988) 884-892.
122. Marfoe, C.H., Kazemi, H., and Ramirez, W.F.: "Numerical Simulation of Foam Flow in Porous Media," paper SPE 16709 presented at the 1987 SPE Annual Technical Conference and Exhibition, Dallas, TX, Sept. 27-30.
123. Islam, M.R., and Farouq Ali, S.M.: "Numerical Simulation of Foam Flow in Porous Media," *J. Can. Pet. Tech.* (July-Aug. 1990) **29**(4), 47-51.
124. Fisher, A.W., Foulser, R.W.S., and Goodyear, S.G.: "Mathematical Modeling of Foam Flooding," paper SPE 20195 presented at the 1990 SPE/DOE Symposium on Enhanced Oil Recovery, Tulsa, OK, April 22-25.
125. Law, D. H-S., Yang, Z-M. and Stone, T.W.: "Effect of the Presence of Oil on Foam Performance: A Field Simulation Study," *SPERE* (May 1992) 228-236.
126. Mohammadi, S.S., Coombe, D.A., and Stevenson, V.M.: "Test of Steam-Foam Process for Mobility Control in South Casper Creek Reservoir," *J. Can. Pet. Tech.* (Dec. 1993) 32, No. 10, 49-54.
127. Hirasaki, G.J. and Lawson, L.B.: "Mechanisms of Foam Flow in Porous Media: Apparent Viscosity in Smooth Capillaries," *SPEJ* (April 1985) 176-190.
128. Friedmann, F., Chen, W.H., and Gauglitz, P.A.: "Experimental and Simulation Study of High-Temperature Foam Displacement in Porous Media," *SPERE* (Feb. 1991) 37-45.
129. Ettinger, R.A. and Radke, C.J.: "Influence of Texture on Steady Foam Flow in Berea Sandstone," *SPERE* (Feb. 1992) 83-90.
130. Kovscek, A.R., Patzek, A.R., and Radke, C.J.: "Simulation of Foam Transport in Porous Media," paper SPE 26402 presented at the 1993 SPE Annual Technical Conference and Exhibition, Houston, TX, Oct. 3-6.
131. Kovscek, A.R., Patzek, A.R., and Radke, C.J.: "Mechanistic Prediction of Foam Displacement in Multidimensions: A Population Balance Approach," paper SPE 27789 presented at the 1994 SPE/DOE Symposium on Improved Oil Recovery, Tulsa,April 17-20.
132. Patzek, T.W. "Description of Foam Flow in Porous Media by the Population Balance Method,' *Surfactant-Based Mobility Control: Progress in Miscible-Flood Enhanced Oil Recovery*, D.H. Smith (ed.), ACS Symposium Series 373, Washington, D.C. (1988).
133. Rossen, W.R., Zhou, Z.H., and Mamun, C.K.: "Modeling Foam Mobility at the 'Limiting Capillary Pressure'," paper SPE 22627 presented at the 1991 Annual Technical Conference and Exhibition, Dallas, Oct. 6-9.
134. Rossen, W.R., Zeilinger, S.C., Shi, J-X., and Lim, M.T.: "Mechanistic Simulation of Foam Processes in Porous Media," paper SPE 28940 presented at the 1994 SPE Annual Technical Conference and Exhibition, New Orleans, Sept. 26-28.
135. Ammer, J.R., Brummert, A.C., and Sams, W.N.: "Miscible Applied Simulation Techniques for Energy Recovery—Version 2.0," quarterly report, Contract No. DOE/BC-91/2/SP, U.S. DOE (February 1991).
136. Chang, Y.: "Development and Application of an Equation of State Compositional Simulator," PhD dissertation, University of Texas, Austin, TX (1990).
137. Chang, Y., Pope, G.A., and Sepehrnoori, K.: "A Higher-Order Finite Difference Compositional Simulator," *J. Pet. Sci. Eng.* (Nov. 1990) **5**, No. 1, 35-50.

138. Lim, M.T., Khan, S.A., Sepehrnoori, K., and Pope, G.A.: "Simulation of Carbon Dioxide Flooding Using Horizontal Wells," paper SPE 24929 presented at the 1992 SPE Annual Technical Conference and Exhibition, Washington, D.C., Oct. 4-7.
139. Chang, S.-H. and Grigg, R.B.: "Foam Displacement Modeling in CO_2 Flooding processes," paper SPE 35401 presented at the 1996 SPE/DOE Tenth Symposium on Improved Oil Recovery, Tulsa, OK, April 21-24.
140. Martin, F.D., Stevens, J.E., and Harpole, K.J.: "CO_2-Foam Field Test at the East Vacuum Grayburg/San Andres Unit," *SPERE* (Nov. 1995) 266-272.
141. Killough, J.E., and Kossack, C.A. "Fifth Comparative Solution Project: Evaluation of Miscible Flood Simulators," paper SPE 16000 presented at the 1987 Symposium on Reservoir Simulation, San Antonio, TX, Feb. 1-4.
142. Joshi, S.D.: *Horizontal Well Technology*, PennWell, Tulsa, OK (1991).
143. Taber, J.J. and Seright, R.S. "Horizontal Injection and Production Wells for EOR or Waterflooding," paper SPE 23952 presented at the 1992 SPE Permian Basin Oil and Gas Recovery Conference, Midland, TX, March 18-20.
144. Hallenbeck *et al*., *Innovative Approach to CO_2 Project Development Holds Promise for Improving CO_2 Flood Economics in Smaller Fields Nearing Abandonment*, paper SPE 28334 presented at the 1994 SPE Annual Technical Conference and Exhibition, New Orleans, Sept. 25-28.
145. A.B. Speirs, and P.B. Warren, *Horizontal Well Experience in California Thermal Reservoirs*, paper HWC94-56 presented at the Canadian SPE/CIM/CANMET International Conference on Recent Advances in Horizontal Well Applications, Calgary, Canada, March 20-23, 1994.
146. Mungan, N.: "Further Recovery from Mature Reservoirs with Horizontal Wells," paper HWC94-07 Keynote Address presented at the Canadian 1994 SPE/CIM/CANMET International Conference on Recent Advances in Horizontal Well Applications, Calgary, Canada, March 20-23.
147. Dakhlia *et al*., "Simulation of Surfactant Flooding Using Horizontal Wells," paper 95-82 presented at the 1995 Annual Technical Meeting of The Petroleum Society of CIM, Banff, Alberta, Canada, May 14-17.
148. Babu *et al*., "The Relation Between Wellblock and Wellbore Pressures in Numerical Simulation of Horizontal Wells," *SPERE* (August 1991), 324-328.
149. Nghiem *et al*., "Seventh SPE Comparative Solution Project: Modeling of Horizontal Wells in Reservoir Simulation," paper SPE 21221 presented at the 1991 SPE Symposium on Reservoir Simulation, Anaheim, CA, Feb. 17-20.
150. Guggenheim, E.A. and Adam, N.K.: "The Thermodynamics of Adsorption at the Surface of Solutions," *Proc. Roy. Soc*. (1933), **A139**, 218-236.
151. Cornelisse, P.M.W., Peters, C.J., and de Swaan Arons, J. : "Application of the Peng- Robinson Equation of State to Calculate Interfacial Tensions and Profiles at Vapor- Liquid Interfaces," *Fluid Phase Equilibria* (1993), **82**, 119-129.
152. Macleod, D.B.: "On a Relation between Surface Tension and Density," *Trans. Faraday Soc*. (1923), **19**, 38-43.
153. Sugden, S.: "A Relation between Surface Tension, Density and Chemical Composition," *J. Chem. Soc.* (1924), **125**, 1177-1189.
154. Quayle, O.R.: "The Parachors of Organic Compounds," *Chem. Review* (1953), **53**, 439-586.

155. Weinaug, C.F. and Katz, D.L.: "Surface Tension of Methane-Propane Mixtures," *Ind. and Eng. Chemistry* (1943), **35**, No. 2, 239-246.
156. Katz, D.L., Mouroe, R.R., and Trainer, R.P.: "Surface Tension of Crude Oils Containing Dissolved Gases," *Petroleum Technology* (September 1943), 21-29.
157. Reno, G.J. and Katz, D.L.: "Surface Tension of n-Heptane and n-Butane containing Dissolved Nitrogen,"*Industrial and Engineering Chemistry* (October 1943), **35**, No. 10, 1091-1093.
158. Hough, E.W. and Stegemeier, G.L.: "Correlation of Surface and Interfacial Tension of Light Hydrocarbons in the Critical Region," *Soc. Pet. Eng. J.* (December 1961), 259-263.
159. Lee, S.T. and Chien, M.C.H.: "A New Multiple Component Surface Tension Correlation Based on Scaling Theory," paper SPE 12643 presented at the 1984 SPE/DOE Symposium on EOR, Tulsa, OK, April 15-18.
160. Hugill, J.A. and Van Welsenes, A.J.: *Fluid Phase Equilibria* (1986), **29**, 383.
161. Firoozabadi, A., Katz, D.L., Soroosh, H., and Sajjadian, V.A.: "Surface Tension of Reservoir-Crude Oil/Gas Systems Recognizing the Asphalt in the Heavy Fraction," *SPERE* (February 1988), 265-272.
162. Gasem, K.A.M., Dulcamara, P.B., Jr., Dickson, K.B., and Robinson, R.L., Jr.: "Test of Prediction Methods for Interfacial Tensions of CO_2 and Ethane in Hydrocarbon Solvents," *Fluid Phase Equilibria* (1989), **53**, 39-50.
163. Ali, J.K.: "Prediction of Parachors of Petroleum Cuts and Pseudocomponents," *Fluid Phase Equilibria* (1994), **95**, 383-398.
164. Fanchi, J.R.: "Calculation of Parachors for Compositional Simulation: An Update," *SPERE* (August 1990), 433-436.
165. Fawcett, M.J.: "Evaluation of Correlations and Parachors to Predict Low Interfacial Tension in Condensate Systems," paper SPE 28611 presented at the 1994 SPE Annual Technical Conference and Exhibition, New Orleans, September 26-28.
166. Guggenheim, E.A.: *Thermodynamics*, 3rd edition, North-Holland Publishing Company, Amsterdam (1957).
167. Guggenheim, E.A.: *J. Chem. Phys.* (1945), **13**, 253.
168. Stanley, E.H.: *Introduction to Phase Transitions and Critical Phenomena*, Oxford University Press, Oxford, U.K. (1982).
169. Fisher, M.E. and Scesney, P.E.: " Visibility of Critical-Exponent Renormalization," *Phys. Review A* (September 1970), **2**, 825-835.
170. Fisher, M.E.: *Phys. Review* (1968), 176, 257.
171. Sengers, J.M.H.L., and Sengers, J.V.: *How Close Is "Close to the Critical Point?"* North-Holland Publishing Company, Amsterdam (1981).
172. Rowlinson, J. and Widom, B.: *Molecular Theory of Capillarity*, Oxford University Press, Oxford, U.K. (1982).
173. Widom, B.: "Phase Equilibrium and Interfacial Structure," *Chemical Society Reviews* (1985), 121-139.
174. Moldover, M.R.: "Interfacial Tension of Fluids near Critical Points and Two Scale-factor Universality," *Phys. Review A* (1985), **31**, 1022-1033.
175. Haniff, M.D., and Pearce, A.J.: "Measuring Interfacial Tensions in a Gas Condensate System with a Laser-Light-Scattering Technique," *SPERE* (November 1990), 589-594.

176. Huygens, R.J.M., Ronde, H. and Hagoort, J.: "Interfacial Tension of Nitrogen and Volatile Oil Systems," paper SPE 26643 presented at the 1993 SPE Annual Technical Conference and Exhibition, Houston, TX, October 3-6.
177. Wagner, O.R. and Leach, R.O.: "Effect of Interfacial Tension on Displacement Efficiency," *SPEJ* (December 1966), 335-344.
178. Firoozabadi, A. and Ramey, H.J., Jr.: "Surface Tension of Water-Hydrocarbon Systems at Reservoir Conditions," *JCPT* (May-June 1988), **27**, No.3, 41-48.
179. Satherley, J., Girault, H.H.J. and Schiffrin, D.J.: "The Measurement of Ultralow Interfacial Tension by Video Digital Techniques," *J. Colloid & Interface Science* (May 1990), **136**, No.2, 574-583.
180. Vargaftik, N.B.: *Tables on the Thermophysical Properties of Liquids and Gases*, John Wiley & Sons, (1975).
181. Greer, S.C.: "Coexistence Curves at Liquid-Liquid Critical Points: Ising Exponents and Extended Scaling," *Physical Review A* (1976) **14**, No.5, 1770-1780.
182. Satherley, J. and Schiffrin, D.: "The Measurement of Low IFT Values for Enhanced Oil Recovery,", Progress Report to U.K. DOE, Winfrith (August 1986)
183. Morrow, N.R., Chatzis, I. and Taber, J.J.: "Entrapment and Mobilization of Residual Oil in Bead Packs," *Soc. Pet. Eng. Res. Eng.* (1988) **3**, 927-935.
184. Cuiec, L.E., Bourbiaux, B. and Kalaydjian, F.: "Imbibition in Low-Permeability Porous Media: Understanding and Improvement of Oil Recovery," paper SPE 20259 presented at the 1990 SPE/DOE Annual Symposium on Enhanced Oil Recovery, Tulsa, April
185. Hsu, J.C., Nagarajan, N. and Robinson, R.L., Jr.: "Equilibrium Phase Compositions, Phase Densities, and Interfacial Tension for CO_2 + Hydrocarbon Systems. 1. CO_2 + n-Butane," *J. Chem. Eng. Data* (1985), **30**, 485-491.
186. Nagarajan, N. and Robinson, R.L., Jr.: "Equilibrium Phase Compositions, Phase Densities, and Interfacial Tension for CO_2 + Hydrocarbon Systems. 2. CO_2 + n-Decane," *J. Chem. Eng. Data* (1986), **31**, 168-171.
187. Nagarajan, N. and Robinson, R.L., Jr.: "Equilibrium Phase Compositions, Phase Densities, and Interfacial Tension for CO_2 + Hydrocarbon Systems. 3. CO_2 + Cyclohexane. 4. CO_2 + Benzene," *J. Chem. Eng. Data* (1987), **32**, 369-371.
188. Gasem, K.A.M., Dickson, K.B., Dulcamara, P.B. Jr., Nagarajan, N. and Robinson, R.L., Jr.: "Equilibrium Phase Compositions, Phase Densities, and Interfacial Tension for CO_2 + Hydrocarbon Systems. 2. CO_2 + n-Tetradecane," *J. Chem. Eng. Data* (1989), **34**, 191-195.
189. Gasem, K.A.M., Dickson, K.B., Shaver, R.D. and Robinson, R.L., Jr.: "Experimental Phase Densities, and Interfacial Tension for CO_2 Synthetic-Oil and CO_2 Reservoir-Oil Systems," *SPERE* (1993) **8**, No. 3, 170-174.
190. Herz,W.: *Z. anorg. Chem.* (1927), **159**, 316.
191. Huygens, R.J.M., Ronde, H., and Hagoort, J.: "Interfacial Tension of Nitrogen/Volatile Oil Systems," paper SPE 26643 presented at the 1993 SPE Annual Technical Conference and Exhibition, Houston, TX, October 3-6.
192. Pearson, T.G. and Robinson, P.L.: *J. Chem. Soc.* (1934), 736.
193. Rossini, F.D.: *Selected Values of Physical and Thermodynamic Properties of Hydrocarbons and Related Compounds*, Carnegie Press, Pittsburgh (1953).

194. Sage, B.H. and Lacey, W.N.: *Thermodynamic Properties of the Light Paraffin Hydrocarbons and Nitrogen,* API, New York City (1950).
195. Katz, D.L.: *Bull. No. 114* (1949), The A&M College of Texas, 38.
196. Maass, O. and Wright, C.H.: *J. Am. Chem. Soc.* (1921), **43**, 1098.
197. Mumfod, S.A. and Phillips, J.W.C: *J. Chem. Soc.* (1928), 155.
198. Quayle, O.R., Day, A.R. and Brown, G.M: *J. Am. Chem. Soc.* (1944), **66**, 938.
199. Vogel, A.I.: *J. Chem. Soc.* (1946), 136.
200. Hunten, K.W. and Maass, O.: *J. Am. Chem. Soc.* (1929), **51**, 153.
201. Schenck, R. and Kintzinger, M.: *Rec. trav. Chem.* (1923), **42**, 759.
202. Godchot, M. and Cauquil, G.: *Compt. rend.*, 1931, **192**, 1560.
203. Sugden, S.: *The Parachor and Valency,* George Routledge and Sons, Ltd., London, 1930.
204. Robinson, A.E.: PhD dissertation, Emory University, 1950.
205. Vogel, A.I.: *J. Chem. Soc.* (1948), 1809.
206. Wibaut, J.P.: *Rec. Trav. Chim.* (1939), **58**, 375.
207. Wilson, R.C. and Henze, H.R.: *J. Am Chem. Soc.* (1941), **63**, 2112.
208. Manzoni-Ansidei, R.: *Boll. Sci. facolta chim.* (1940), ind. Univ. Bologna 4, 201.
209. Donaldson, R.E.: PhD dissertation, Emory University, 1950.
210. Tuot, M.: *Comp. rend.* (1933), **179**, 1434.
211. Lee, F.H.: *J. Chinese Chem. Soc.* (1943), **10**, 16.
212. Ruzicka, L., Boekenoogen, H.A., and Edelman, H.J.: *Helv. Chim.*(1933), Acta 16, 487.
213. Sugden, S.: *J. Chem. Soc.* (1924), **125**, 1177.
214. Jeffery, G.H. and Vogel, A.I.: *J. Chem. Soc.* (1948), 654.
215. Truchet, R.: *J. Am. Chem. Soc.* (1931), **16**, 309.
216. Buehler, C.A., Gardner, T.S., and Robinson, P.L.: *J. Chem. Soc.* (1929), 1048.
217. Manzoni-Ansidei, R.: *Giorn. biol. ind. agrar. aliment* (1937), **7**, No. 5, 234.
218. Vogel, A.I.: *J. Chem. Soc.* (1948), 607.
219. Donaldson, R.E. and Quayle, O.R.: *J. Am. Chem. Soc.* (1950), **72**,
220. Bhatnagar, S.S. and Singh, B.: *J. Chem. Phys.* (1928), **25**, 21.
221. Hammick, D.L. and Wilmut, H.F.: *J. Chem. Soc.* (1935), 207.
222. Ahmed, T.I.: *Hydrocarbon Phase Behavior*, Gulf Publishing Co., Houston (1989) 64-65.
223. Simon, R., Rosman, A. and Zana, E.: "Phase-Behavior Properties of CO_2 -Reservoir Oil Systems," *SPEJ* (February 1978) 20-26.
224. Danesh, A., Dandekar, A., Todd, A.C. and Tehrani, D.H.: "Modified Scaling Law and Parachor Methods for Improved Prediction of Interfacial Tension," paper SPE 22710 presented at the 1991 SPE Annual Technical Conference and Exhibition October.
225. Fowler, R.H.: *Proc. Roy, Soc.* (London), 159 **A**, 229 (1937).
226. Wagner, O.R. and Leach, R.O.: "Effect of Interfacial Tension on Displacement Efficiency", *SPEJ* (December 1966,) 335-344.
227. De No, P.L.:, *J. Gen. Physiol.*,(1919)**1,** 521; (1923)**5**, 429.
228. Wilhelmy, L:, *Ann. Phys.*, (1863)**119**, 177.
229. Sudgen, S.J.: *J. Chem. Soc.*, (1921) 1483.
230. Sudgen, S. J.: *J. Chem. Soc.*, (1922) 858.
231. Harkins, W.D., and Brown, F.F. : *J. Amer. Chem. Soc.*, (1919) **41,** 499.

232. Vonnegut, B.: *Rev. Sci. Instrum.*, (1942)**13**, 6.
233. Hannif, M.S., and Pearce, A.D.: "Measuring Interfacial Tensions in a Gas-Condensate System With a Laser-Light-Scattering Technique," *SPERE*, (November 1990) 589-594.
234. Andreas, J.M., Hauser, E.A., and Trucker, W.B.: "Boundary Tension by Pendant Drops," *J. Phys. Chem.,*(1938)**42**, 1001-1019.
235. Fordham, S.: " On the Calculation of Surface Tension from Measurements of Pendant Drops," *Proc. R. Soc*. (1948)**A194**, 1.
236. Girault, H.H., Schiffrin, D.J. and Smith, B.D.V.: "Drop Image Processing for Surface Tension and Interfacial Tension Measurements," *J. Electoanalytical Chemistry*, (1982)**137,** 207-217.
237. Hansen, F.K. and Rodsrud, G.: "Surface Tension by Pendant Drop," *J. Colloid Interfacial Science*, (1991)**141,** 1-9.
238. Huygens, R.J., Ronde, H., and Hagoort, J.: "Pendant Drop Interfacial Tension Measurements Using Image Processing Techniques," paper presented at the 1991 European IOR-Symposium in Stavanger, Norway, May 21-23.
239. Stauffer, C.E. : *J. Phys. Chem.,*(1965)**69**, 1933.
240. Girault, H.H., Schiffrin, D.J., and Smith, B.D.V.: "The Measurement of Interfacial Tension of Pendant Drops Using a Video Image Profile Digitizer," *J. Colloid Interfacial Science*, (September 1984) **101**, No. 1.
241. Jennings, J.W., and Pallas, N.R.: "An Efficient Method for the Determination of Interfacial Tension from Drop Profiles," *Langmuir*,(1988)**4,** 959-967.
242. Rotenberg, Y Boruvka, L., and Newmann, A.W.: "Determination of Surface Tension and Contact Angle from the shapes of Axisymmetric Fluid Interfaces," *J. Colloid Interfacial Science,* (1983) **93**(1), 169-183.
243. Pallas, N.R., and Harrison, Y.: "An Automated Drop Shape Apparatus and Surface Tension of Pure Water," *J. Colloid Surfaces*, (1990) **43**, 169-195.
244. Lopez de Ramos, A.L.: "Capillary-Enhanced Diffusion of CO_2 in Porous Media," PhD dissertation, University of Tulsa, Tulsa, OK (1993).
245. MacLeod, C.A., and Radke, C.J.: "A Growing-Drop Technique for Measuring Dynamic Interfacial Tension," Topical report DOE/BC/94000102 (1993).
246. Huh, C., and Reed, R.L.: "A Method for Estimating Interfacial Tensions and Contact Angles from Sessile and Pendant Drop Shapes," *J. Colloid Interfacial Science*, (February 1983) **91**(2), 472-484.
247. Jasper, J: "The Surface Tension of Pure Liquid Compounds," *J. Phys. Chem. Ref. Data*, (1971)**1**, 841-1009.
248. Beliveau, D., Payne, D.A., and Mundry, M: "Waterflood and CO_2 Flooding of the Fractured Midale Field," *JPET*, (September 1993), 881.
249. King, F.H.: "Principles and Conditions of the Movements of Ground Water," *Annual Report*, USGS (1899), 19.
250. Leverett, M.C.: "Capillary Behavior in Porous Solids," *Trans. AIME* (1941) **142**, 152.
251. Katz, D.L.: "Possibilities of Secondary Recovery for the Oklahoma City Wilcox Sand," *Trans. AIME* (1942) **146**, 28.
252. Stahl, R.F., Martin, W.A., and Huntington, R.L.: "Gravitational Drainage of Liquids from Unconsolidated Wilcox Sand," *Petroleum Technology* (January 1943).

253. Elkins, L.F., French, R.W., and Glenn, W.E.: " Lance Creek Sundance Reservoir Performance — a Unitized Pressure-maintenance Project," *Petroleum Technology*, (July 1948).
254. Cardwell, W.T. and Parsons, R.L.: "Gravity Drainage Theory," *Trans. AIME* (1949) **179**, 199.
255. Terwilliger, P.L., Wilsey, L.E., Hall, H.N., Bridges, P.M., and Morse, R.A.: "An Experimental and Theoretical Investigation of Gravity Drainage Performance," *Petroleum Transactions*, AIME (1951) **192.**
256. Buckley, S.E., and Leverett, M.C. "Mechanism of Fluid Displacement in Sands," *Trans. AIME* (1942) **146**, 107.
257. Nenniger, E., and Storrow, J.A.: "Drainage of Packed Beads in Gravitational and Centrifugal-force Fields," *AIChE* (1958) **4**(3), 305.
258. Essley, P.L., Hancock, G.L., and K. E. Jones,: Gravity Drainage Concepts in a Steeply Dipping Reservoir, paper SPE 1029-G (1958).
259. Templeton, E.E., and Nielsen, R.E.: "A Study of Gravity Counterflow Segregation," *SPEJ* (June 1962).
260. Dumore, J.M. and Schols, R.S.: *Drainage Capillary - Pressure Functions and the Influence of Connate Water*, *SPEJ* (October 1974).
261. Dykstra, H.: "The Prediction of Oil Recovery by Gravity Drainage," *JPT*, (May 1978).
262. Hagoort, J.: "Oil Recovery by Gravity Drainage," *SPEJ*, (June 1980).
263. Haldorsen, H.H., Rego, C.A., Chang, D.M., Mayson, H.J., and Creveling, D.M.: "An Evaluation of the Prudhoe Bay Gravity Drainage Mechanism by Complementary Techniques," paper SPE 13651 presented at the 1985 SPE California Regional Meeting, Bakersfield, California, March 27-29.
264. Nectoux, A. : "Equilibrium Gas Oil Drainage: Velocity, Gravitational and Compositional Effects," paper presented at the 4th European Symposium on Enhanced Oil Recovery, Hamburg, October 27-29, 1987.
265. Jacquin, C, Legait, B., Martin, J.M., Nectoux, A., Anterion, F., and Rioche, M. "Gravity Drainage in a Fissured Reservoir with Fluids not in Equilibrium," *Journal of Petroleum Science and Engineering* (1989) **2**, 217.
266. Pavone, D., Bruzzi, P., and Verre, R.: "Gravity Drainage at Low Interfacial Tension," paper presented at the 5th European Symposium on Enhanced Oil Recovery, Budapest, (1989) October 27-29.
267. Stensen, J.A., Skange, A. Monstad, P., and Graue, A.: "The Effect of Interfacial Tension on Gas Gravity Drainage," paper presented at the 2nd North Sea Chalk Symposium, (1990) Copenhagen, June 11-12.
268. Suffridge, E.E. and Renner, T.A.: "Diffusion and Gravity Drainage Tests to Support the Development of a Dual Porosity Simulator," paper presented at the 6th European IOR-Symposium, Stavanger, Norway (1991) May 21-23.
269. da Silva, F.V. and Meyer, B.: "Improved Formulation for Gravity Segregation in Naturally Fractured Reservoirs, paper presented at the 6th European IOR-Symposium, Stavanger, Norway (1991) May 21-23.
270. Schechter, D.S., Zhou, D., and Orr, F.M.: "Low IFT Gravity Drainage and Imbibition," *Journal of Petroleum Science and Engineering* (November 1994), 283.

271. Luan, Z.: "Some Theoretical Aspects of Gravity Drainage in Naturally Fractured Reservoirs, paper SPE 28641 presented at the 1994 SPE Annual Technical Conference and Exhibition, New Orleans, September 25-28.
272. Espie, A.A., Brown, C.E., Narayanan, K.R., and Wilcox, T.C.: "A Laboratory Investigation of Gravity Drainage/Waterflood Interaction in Prudhoe Bay," paper SPE 28614 presented at the SPE 1994 Annual Technical Conference and Exhibition, New Orleans, September 25-28.
273. Catalan, L.J.J., Dullien, F.A.L., and Chatzis, I.: "The Effects of Wettability and Heterogeneities on the Recovery of Waterflood Residual Oil with Low Pressure Inert Gas Injection Assisted by Gravity Drainage," *SPE Advanced Technology Series* (1994) **2**(2).
274. Blunt, M., Zhou, D., and Fenwick, D.: "Three Phase Flow and Gravity Drainage in Porous Media," *Transport in Porous Media* (1995) **20**, 77-103.
275. Øyno, L., Uleberg, K., and Whitson, C.H.: "Dry Gas Injection Fractured Chalk Reservoirs—An Experimental Approach," paper SCA 9527 presented at the 1995 SCA Conference, San Francisco, August 20-22.
276. Guo, B.: "Modeling of Gravity Drainage Under Constant and Varying Capillary Pressure," *Proc.*, 1995 Natural Fractured Reservoir Forum (paper PRRC 95-40), New Mexico Institute of Mining and Technology.
277. Crank, J. : *The Mathematics of Diffusion*, second ed. New York, Oxford University Press (1975).
278. Carslaw, H.S. and Jaeger, J.C.: *Conduction of Heat in Solids*, 2nd ed., New York, Oxford University Press (1959).
279. Jeffreys, H: *Proc. Cambridge Phil. Soc.*, 26, 204 (1930).
280. Renner, T.: "Measurement and Correlation of Diffusion Coefficient for CO_2 and Rich Gas Applications," *SPERE* (May 1988) 517–523.
281. Stalkup, F.I. Jr.: *Miscible Displacement*, SPE-AIME, New York (1984).
282. Ma, L.-K: *Modern Theory of Critical Phenomena*, Benjamin Cummings, London (1976).

Table 1. Slopes determined by the regression from the mobility measurements

Flow rate (cc/hr)	Rock type	Surfactant CD1045			Surfactant CD1050		
		0 ppm	500 ppm	1000 ppm	0 ppm	500 ppm	1000 ppm
7.5	Berea sandstone	1.09	0.30	0.36	1.03	0.71	0.76
	Baker dolomite	0.94	0.61	0.45	0.97	0.23	0.45
	Overall	0.82	0.39	0.26	0.95	0.60	0.65
15	Berea sandstone	1.12	0.45	0.34	1.16	0.72	0.72
	Baker dolomite	1.12	0.83	0.56	0.92	0.55	0.45
	Overall	0.90	0.49	0.34	0.99	0.67	0.70

Table 2. Foaming agents tested

Surfactant	Type	Active wt%	Formula	Manufacture
Chaser^{TM} CD1040	Anionic	40.0	Alpha Olefin Sulfonate	Chaser International
Chaser^{TM} CD1045	N/A	46.7	Proprietary	Chaser International
Chaser^{TM} CD1050	Nonionic	70.0	Alkyl Phenol Ethoxylate	Chaser International
Alipa^{R} CD128	Anionic	58.0	Ethoxylated alcohol sulfate	GAF
Dowfax^{TM} 8390	Anionic	35.0	C16-diphenylether disulfonate	Dow Chemical
Witcolate^{TM} 1259	Anionic	40.0	Alcohol ether sulfate	Witco Corp.
Witcolate^{TM} 1276	Anionic	40.0	Alcohol ether sulfate	Witco Corp.

Table 3. Mobility data in composite core #1 with 0.1 wt% surfactant concentration

Fluid Injected	Injection rate (cc/hr)	Mobility in section #1 (md/cp)	Mobility in section #2 (md/cp)	Mobility in section #3 (md/cp)	Mobility in section #4 (md/cp)
Brine	10	525	227	127	152
Brine/CO2	15	472.5	258.1	56	88.5
	10	452.8	239.8	49.1	78.6
	5	445.6	240.9	47.5	80.7
CD1050/CO2	15	3.41	2.88	1.6	N/A
	10	2.42	2.27	1.23	N/A
	5	1.77	1.63	0.95	N/A
CD128/CO2	15	2.91	2.23	1.29	N/A
	10	2.25	2	1.11	N/A
	5	1.92	1.67	0.97	N/A
CD1045/CO2	15	2.7	1.97	1.29	N/A
	10	1.99	1.58	1.07	N/A
	5	1.28	1.16	0.78	N/A
Dowfax 8390/CO2	15	83.01	34.61	20.93	N/A
	10	70.6	31.38	18.74	N/A
	5	55.34	25.92	14.95	N/A
CD1040/CO2	15	10.09	5.29	2.8	N/A
	10	8.14	3.57	2.36	N/A
	5	7.83	3.59	2.43	N/A
W1259/CO2	15	30.05	15.85	8.2	N/A
	10	23.4	14.32	6.38	N/A
	5	22.12	14.3	6.05	N/A
W1276/CO2	15	4.07	3.1	1.6	N/A
	10	3.5	2.59	1.4	N/A
	5	2.56	1.92	1.12	N/A

N/A : data not available because the pressure readings were beyond the limitation of the differential pressure transducer.

Table 4. Mobility data in composite core #2 with 0.05 wt% surfactant concentration

Fluid Injected	Injection rate (cc/hr)	Mobility in section #1 (md/cp)	Mobility in section #2 (md/cp)	Mobility in section #3 (md/cp)	Mobility in section #4 (md/cp)
Brine	10	819	440	106	130
Brine/CO2	15	808.2	198.1	48.3	55
	10	802.9	182	45.4	47.5
	5	819	157.5	43.6	49.5
Brine	10	802	435	106	120
Dowfax 8390	10	715.8	370.6	98	116
Dowfax 8390/CO2	15	317.4	91.3	30	N/A
	10	282.4	84.2	25.6	N/A
	5	265.9	77.4	25.7	N/A
Brine	10	688.2	322.4	74.3	**
CD1040	10	751.4	323.7	112.8	**
CD1040/CO2	15	310.2	80.5	29.0	N/A
	10	250.5	67.6	27.1	N/A
	5	202.7	57.4	25.4	N/A
Brine	10	751.4	321.2	102.9	**
CD1050	10	762.5	342.7	94.6	**
CD1050/CO2	15	7.1	6.2	2.4	N/A
	10	4.8	4.5	1.9	N/A
	5	3.6	3.4	1.6	N/A
Brine	10	758.3	269.4	80.4	**
CD128/CO2	15	10	6.8	2.2	N/A
	10	8.1	5.9	2	N/A
	5	7.7	6.4	2	N/A
Brine	10	720.3	289	90.4	**
CD1045	10	606.7	264.2	81.3	**
CD1045/CO2	15	7.3	4.9	2	N/A
	10	6.1	5.4	1.8	N/A
	5	4	3.2	1.3	N/A

Table 5. Slopes determined by the regression from the mobility measurements

Fluid type	Core #	Injection rate @ cc/hr (Darcy velocity @ ft/day)		
		15 (9.4)	10 (6.3)	5 (3.1)
CO2/brine	2	1.31	1.33	1.34
CO2/0.05 wt% Dowfax 8390	2	1.09	1.12	1.08
CO2/0.05 wt% Witcolate 1259	2	1.06	1.05	0.99
CO2/0.05 wt% CD1040	2	1.08	1.01	0.94
CO2/0.05 wt% Witcolate 1276	2	0.77	0.76	0.68
CO2/0.05 wt% CD128	2	0.75	0.70	0.69
CO2/0.05 wt% CD1045	2	0.63	0.63	0.56
CO2/0.05 wt% CD1050	2	0.55	0.48	0.42
CO2/brine	1	1.47	1.53	1.52
CO2/0.10 wt% Dowfax 8390	1	0.98	0.94	0.92
CO2/0.10 wt% Witcolate 1259	1	0.90	0.89	0.88
CO2/0.10 wt% CD1040	1	0.89	0.88	0.83
CO2/0.10 wt% Witcolate 1276	1	0.63	0.63	0.57
CO2/0.10 wt% CD128	1	0.56	0.47	0.46
CO2/0.10 wt% CD1050	1	0.51	0.45	0.41
CO2/0.10 wt% CD1045	1	0.51	0.43	0.33

Table 6. Spraberry recombined reservoir oil - CO_2 swelling test @ 138°F

Press. (psig)	Total Vol.cc	Rel. Vol. (1)	Rel. Vol. (2)	Vapor (cc)	% Vol. Vapor
		0 MOLE PERCENT CO_2			
3698	51.6	0.943	0.943		
2583	52.4	0.957	0.957		
1680	53.2	0.972	0.972		
1151	53.8	0.983	0.983		
875	54.5	0.996	0.996		
822	54.8	1.000	1.000	0.0	0.0
731	57.7	1.054	1.054	3.0	5.2
660	60.7	1.109	1.109	6.0	9.9
546	67.7	1.237	1.237	13.0	19.2
506	70.7	1.291	1.291	16.0	22.6
		14.9 MOLE PERCENT CO_2			
3302	54.0	0.960	0.986		
2636	54.6	0.971	0.997		
2031	55.2	0.982	1.008		
1371	56.0	0.996	1.023		
1225	56.3	1.001	1.028	0.0	0.0
1190	57.3	1.019	1.046	1.4	2.4
1074	61.0	1.085	1.114	6.0	9.8
932	67.0	1.191	1.224	12.5	18.7
870	70.0	1.245	1.278	15.0	21.4
736	80.0	1.422	1.461	25.0	31.3
633	90.0	1.600	1.644	35.0	38.9
		31.3 MOLE PERCENT CO_2			
3135	58.0	0.943	1.059		
2501	58.6	0.953	1.070		
2029	59.2	0.963	1.081		
1751	59.6	0.969	1.088		
1562	61.5	1.000	1.123	0.0	0.0
1390	66.0	1.073	1.205	6.5	9.8
1247	73.0	1.187	1.333	14.0	19.2
1086	83.0	1.350	1.516	24.0	28.9
1002	88.0	1.431	1.607	29.0	33.0
888	98.0	1.594	1.790	39.0	39.8
		42.3 MOLE PERCENT CO_2			
4671	61.0	0.949	1.114		
3524	62.2	0.968	1.136		
2599	63.2	0.983	1.154		
2055	64.0	0.996	1.169		
1835	64.3	1.000	1.174	0.0	0.0
1785	65.0	1.011	1.187	1.5	2.3
1652	68.0	1.058	1.242	6.0	8.8
1587	70.0	1.089	1.278	9.5	13.6
1483	74.0	1.151	1.351	14.0	18.9
1438	76.0	1.183	1.388	16.5	21.7
1310	83.0	1.291	1.516	25.0	30.1
1171	93.0	1.447	1.698	36.0	38.7
		51.1 MOLE PERCENT CO_2			
4773	66.0	0.940	1.205		
4300	66.6	0.948	1.216		
3257	68.0	0.968	1.242		
2104	69.8	0.994	1.275		
2025	70.3	1.000	1.283	0.0	0.0
1867	73.0	1.039	1.333	7.0	9.6
1701	78.0	1.110	1.424	15.5	19.9
1500	88.0	1.253	1.607	28.0	31.8
1357	98.0	1.395	1.790	39.5	40.3
1153	118.0	1.680	2.155	61.0	51.7
1012	138.0	1.964	2.520	82.0	59.4
		56.5 MOLE PERCENT CO_2			
4534	70.5	0.953	1.287		
3868	71.4	0.965	1.304		
3303	72.2	0.976	1.318		
2811	73.0	0.987	1.333		
2377	73.8	0.998	1.348		
2309	74.0	1.000	1.351	0.0	0.0
2100	75.5	1.021	1.379	7.5	9.9
1857	80.0	1.081	1.461	15.0	18.8
1794	82.0	1.108	1.497	17.5	21.3
1480	98.0	1.325	1.790	37.0	37.8
1382	108.0	1.460	1.972	48.0	44.4
1285	118.0	1.595	2.155	59.0	50.0
1145	138.0	1.865	2.520	80.5	58.3
		61.9 MOLE PERCENT CO_2			
4784	75.0	0.952	1.370		
4329	75.8	0.963	1.384		
3383	77.5	0.984	1.415		
2781	78.8	1.000	1.438	0.0	0.0
2706	79.0	1.003	1.443	4.5	5.7
2572	79.5	1.010	1.452	10.0	12.6
2224	81.5	1.035	1.488	16.5	20.2
1829	89.0	1.130	1.625	25.0	28.1
1725	94.0	1.194	1.717	30.5	32.4
1648	99.0	1.257	1.808	36.0	36.4
1520	109.0	1.384	1.991	47.5	43.6
1418	119.0	1.511	2.173	58.5	49.2
1258	139.0	1.765	2.538	80.0	57.6

Table 6 (Continued)

Press. (psig)	Total Vol.cc	Rel. Vol. (1)	Rel. Vol. (2)	Vapor (cc)	% Vol. Vapor
		67.7 MOLE PERCENT CO_2			
4750	83.0	0.979	1.516		
4091	83.8	0.988	1.530		
3715	84.6	0.998	1.545		
3621	84.8	1.000	1.549	0.0	0.0
3536	85.0	1.002	1.552	10.0	11.8
3448	85.2	1.005	1.556	20.0	23.5
3389	85.4	1.007	1.560	25.0	29.3
3327	85.6	1.009	1.563	29.0	33.9
2649	88.0	1.038	1.607	29.5	33.5
2118	92.0	1.085	1.680	30.5	33.2
1781	103.0	1.215	1.881	40.0	38.8
1710	108.0	1.274	1.972	45.0	41.7
1503	128.0	1.509	2.337	65.5	51.2
1351	148.0	1.745	2.703	86.0	58.1
		73.6 MOLE PERCENT CO_2			
5292	92.0	0.991	1.680		
5030	92.6	0.998	1.691		
4949	92.8	1.000	1.695	92.8	100.0
4862	93.0	1.002	1.698	85.7	92.2
4732	93.4	1.006	1.706	79.9	85.5
4560	93.8	1.011	1.713	74.1	79.0
4259	94.5	1.018	1.726	66.5	70.4
4069	95.0	1.024	1.735	62.5	65.8
3717	96.0	1.034	1.753	55.5	57.8
3154	98.0	1.056	1.790	49.5	50.5
2587	101.0	1.088	1.844	46.5	46.0
2122	106.0	1.142	1.936	47.0	44.3
1883	113.0	1.218	2.064	50.5	44.7
1738	123.0	1.325	2.246	58.5	47.6
1643	133.0	1.433	2.429	68.5	51.5
1493	153.0	1.649	2.794	88.5	57.8
		79.7 MOLE PERCENT CO_2			
5070	111.4	1.174	2.034	82.1	73.7
4999	112.0	1.180	2.045	81.8	73.0
4457	114.0	1.201	2.082	79.0	69.3
3520	118.0	1.243	2.155	75.5	64.0
2775	123.0	1.296	2.246	74.0	60.2
2192	131.0	1.380	2.392	76.0	58.0
1792	151.0	1.591	2.757	89.0	58.9

(1) Volume relative to the volume at the saturation pressure of the indicated mixture.
(2) Volume relative to the volume at the saturation pressure of the original fluid.

Table 7. Sulimar Queen separator oil—CO_2 swelling test @ 70°F

Press. (psig)	Total Vol, cc	Rel. Vol. (1)	Rel. Vol. (2)	Vapor (cc)	% Vol. Vapor	Upper Liq, cc
20.5 MOLE PERCENT CO_2						
1897	27.0	0.982	1.053			
1235	27.2	0.989	1.060			
800	27.3	0.993	1.064			
335	27.4	0.996	1.068			
201	27.5	1.000	1.072	0.0	0.0	
182	32.0	1.164	1.248	3.0	9.4	
168	36.0	1.309	1.404	7.0	19.4	
163	38.0	1.382	1.481	9.0	23.7	
149	43.0	1.564	1.676	13.5	31.4	
40.8 MOLE PERCENT CO_2						
2485	29.0	0.957	1.131			
1567	29.4	0.970	1.146			
911	29.7	0.980	1.158			
673	30.0	0.990	1.170			
437	30.3	1.000	1.181	0.0	0.0	
415	34.0	1.122	1.326	3.5	10.3	
393	38.0	1.254	1.481	7.5	19.7	
366	43.0	1.419	1.676	12.5	29.1	
60.8 MOLE PERCENT CO_2						
2632	33.5	0.957	1.306			
1843	34.0	0.971	1.326			
1201	34.5	0.986	1.345			
685	35.0	1.000	1.365	0.0	0.0	
667	38.0	1.086	1.481	4.0	10.5	
642	43.0	1.229	1.676	9.0	20.9	
614	48.0	1.371	1.871	15.0	31.3	
590	53.0	1.514	2.066	20.5	38.7	
568	58.0	1.657	2.261	25.5	44.0	
65.7 MOLE PERCENT CO_2						
1909	36.0	0.965	1.404			
1305	36.5	0.979	1.423			
998	36.7	0.984	1.431			
756	37.3	1.000	1.454	0.0	0.0	
747	40.0	1.072	1.559	4.0	10.0	
740	42.0	1.126	1.637	6.5	15.5	
723	47.0	1.260	1.832	11.5	24.5	
695	52.0	1.394	2.027	17.5	33.7	
70.7 MOLE PERCENT CO_2						
2586	38.0	0.950	1.382			
1381	39.0	0.975	1.418			
963	39.4	0.985	1.433			
785	40.0	1.000	1.455	0.0	0.0	
780	42.0	1.050	1.527	4.0	9.5	
768	47.0	1.175	1.709	11.0	23.4	
753	52.0	1.300	1.891	17.0	32.7	
733	57.0	1.425	2.073	22.0	38.6	
Press. (psig)	Total Vol, cc	Rel. Vol. (1)	Rel. Vol. (2)	Vapor (cc)	% Vol. Vapor	Upper Liq, cc

Press. (psig)	Total Vol, cc	Rel. Vol. (1)	Rel. Vol. (2)	Vapor (cc)	% Vol. Vapor	Upper Liq, cc
75.6 MOLE PERCENT CO_2						
2164	42.0	0.946	1.637			
1183	43.0	0.968	1.676			
820	44.4	1.000	1.731	0.0	0.0	
814	47.5	1.070	1.852	5.0	10.5	
808	53.0	1.194	2.066	10.5	19.8	
793	57.5	1.295	2.242	16.5	28.7	
779	62.0	1.396	2.417	22.5	36.3	
80.5 MOLE PERCENT CO_2						
1890	47.7		1.860			47.7
1386	48.2		1.879			48.2
1172	48.4		1.887			39.5
1037	48.6		1.895			34.0
919	48.8		1.903			32.0
828	49.0		1.910	0.0	0.0	30.5
825	51.0		1.988	4.0	7.8	28.0
824	53.0		2.066	7.0	13.2	27.0
820	57.0		2.222	11.5	20.2	26.5
812	62.0		2.417	17.0	27.4	26.0
85.4 MOLE PERCENT CO_2						
3235	54.9		2.140			45.4
2514	55.9		2.179			45.0
1796	56.9		2.218			42.5
1251	57.9		2.257			41.0
842	59.5		2.320	0.0	0.0	39.4
836	66.9		2.608	11.0	16.4	35.5
835	71.9		2.803	16.5	22.9	35.0
833	76.9		2.998	23.5	30.6	33.0
827	86.9		3.388	35.5	40.9	31.0
805	96.9		3.778	47.0	48.5	29.5
803	101.9		3.973	53.5	52.5	28.0
791	111.9		4.363	65.5	58.5	26.0
90.2 MOLE PERCENT CO_2						
5075	69.5		2.710			57.5
3695	71.5		2.788			59.0
2031	75.0		2.924			59.5
1547	77.0		3.002			60.0
846	80.0		3.119	0.0	0.0	60.8
845	82.0		3.197	3.5	4.3	58.5
841	92.0		3.587	16.5	17.9	55.0
836	102.0		3.977	29.0	28.4	51.5
830	112.0		4.366	42.0	37.5	48.5

(1) Volume relative to the volume at the saturation pressure of the indicated mixture.

(2) Volume relative to the volume at the saturation pressure of the original fluid (atmospheric pressure and 70 °F for this system).

Table 8. Variable pressure extraction experiment matrix

Oil Sample	Temperature, °F	Pressure, psig
Spraberry Separator Oil	95	1040, 1050, 1100, 1200, 1400, 1600
	138	1200, 1400, 1500, 1550, 1600, 1700, 1800, 1900
Sulimar Queen Stock Tank Oil	95	1000, 1050, 1065, 1075, 1080, 1100, 1200, 1300, 1400, 1600
	138	1200, 1400, 1450, 1500, 1550, 1600, 1650, 1700, 1800, 1900

Table 9. CO_2 extraction capacity of the variable pressure extraction experiments

Oil Samples	Temperature, 95 °F			Temperature, 138 °F			
	Pressure psig	Extraction Capacity g oil/g CO_2		Pressure psig	Extraction Capacity g oil/g CO_2		
		Samp. 1	Samp.2		Samp.1	Samp.2	Sampl.3
Spraberry Separator Oil	1040	0.0602		1200	0.0080		
	1050	0.0624		1400	0.0100		
	1100	0.0584	0.0671	1500	0.0274	0.0189	
	1205	0.1018	0.1081	1550	0.0442		
	1404	0.1189	0.1179	1600	0.0871		
	1600	0.1192	0.1152	1700	0.0958		
				1800	0.1081		
				1900	0.1052		
Sulimar Queen Stock Tank Oil				1203	0.0030	0.0022	
	1044	0.0040		1402	0.0090		
	1052	0.0716		1504	0.0130	0.0320	0.0266
	1065	0.0726		1608	0.0237	0.0362	0.0403
	1075	0.0971		1706	0.0436	0.0437	
	1105	0.1010		1800	0.0446	0.0543	
	1204	0.0935		1904	0.0482	0.0545	
	1302	0.0916		1800	0.0527		
	1407	0.0935		1700	0.0535		
	1608	0.0943		1650	0.0386		
				1601	0.0272		
				1550	0.0174		
				1452	0.0060		

Table 10. Slim tube MMP and critical extraction pressure ranges

Oil Sample	Temperature ^{o}F	Slim Tube MMP psig	Critical Ranges psig
Sulimar Queen Stock Tank Oil	95	1115	1040-1120
	138	1595	1520-1640
Spraberry Separator Oil	95	1190	1120-1220
	138	1540	1500-1640

Table 11. Compositions of Sulimar Queen and Spraberry oils

Components	Mole Fraction	
	Sulimar Queen	Spraberry
C_1		0.0211
C_2		0.0172
C_3		0.0351
C_4		0.0212
C_5-C_{10}	0.5477	0.5137
C_{11}-C_{20}	0.2660	0.2151
C_{21} -C_{30}	0.0856	0.0710
C_{30} -C_{36}	0.0326	0.0316
C_{37+}	0.0681	0.0740
Molecular Weight	194.8	180.9
API Gravity	40	38

Table 12. Composition of synthetic brine

Component	Weight* (g)
NaCl	61.26
KCl	0.58
CaCl2. 2H2O	10.86
MgCl2. 6H2O	5.19
Na2SO4	5.91
H2O	1916.20

* Based on 2000 g brine solution

Table 13. Berea core properties

Core	Length (cm)	Diameter (cm)	Porosity	Pore Volume (cc)	Initial Brine Perm. (md)
A	5.21	1.27	0.20	1.32	36.90
B	6.25	1.27	0.20	1.61	195.60
C	2.52	1.27	0.20	0.65	139.28
D	1.24	1.27	0.20	0.32	61.7*

* Initial surfactant-solution permeability (core D)

Table 14. Summary of baseline experiments

Core #	Total Flow Rate (cc/hr)	CO2 Fraction	Pressure Drop (psid)	Total Mobility (md/cp)	Total Interstitial Velocity (ft/day)
A	4.2	0.200	9.97	7.07	13.05
	4.2	0.200	9.85	7.15	13.05
	8.4	0.200	19.37	7.28	26.11
	16.8	0.200	41.84	6.74	52.21
	4.2	0.333	11.69	6.03	13.05
	4.2	0.333	9.49	7.43	13.05
	8.4	0.333	19.48	7.24	26.11
	16.8	0.333	33.78	8.35	52.21
	16.8	0.333	44.68	6.31	52.21
	4.2	0.500	9.49	7.43	13.05
	8.4	0.500	16.79	8.39	26.11
	16.8	0.500	38.90	7.25	52.21
	4.2	0.667	7.97	8.84	13.05
	4.2	0.667	7.58	9.30	13.05
	8.4	0.667	15.87	8.88	26.11
	16.8	0.667	28.37	9.94	52.21
	4.2	0.800	5.99	11.77	13.05
	4.2	0.800	6.46	10.91	13.05
	8.4	0.800	11.61	12.14	26.11
	16.8	0.800	24.85	11.34	52.21
B	4.2	0.200	5.60	15.10	12.85
	8.4	0.200	11.15	15.17	25.70
	16.8	0.200	14.25	23.74	51.39
	4.2	0.333	4.97	17.02	12.85
	8.4	0.333	9.86	17.15	25.70
	16.8	0.333	17.44	19.40	51.39
	4.2	0.500	4.55	18.59	12.85
	8.4	0.500	8.23	20.55	25.70
	16.8	0.500	15.55	21.75	51.39
	4.2	0.667	3.71	22.80	12.85
	8.4	0.667	7.03	24.06	25.70
	16.8	0.667	11.30	29.94	51.39
	4.2	0.800	2.97	28.47	12.85
	8.4	0.800	5.41	31.26	25.70
	16.8	0.800	7.71	43.88	51.39

Table 14, (cont'd)

Core #	Total Flow Rate (cc/hr)	CO2 Fraction	Pressure Drop (psid)	Total Mobility (md/cp)	Total Interstitial Velocity (ft/day)
C	4.2	0.200	1.43	23.85	12.85
	8.4	0.200	4.17	16.36	25.70
	16.8	0.200	8.63	15.81	51.39
	4.2	0.333	1.49	22.89	12.85
	8.4	0.333	3.92	17.40	25.70
	16.8	0.333	10.96	12.45	51.39
	4.2	0.500	1.46	23.36	12.85
	8.4	0.500	3.40	20.06	25.70
	16.8	0.500	6.47	21.08	51.39
	4.2	0.667	1.46	23.36	12.85
	8.4	0.667	3.19	21.38	25.70
	16.8	0.667	5.35	25.50	51.39
	4.2	0.800	1.29	26.44	12.85
	8.4	0.800	2.44	27.95	25.70
	16.8	0.800	4.07	33.52	51.39
D	4.2	0.200	1.11	15.18	13.05
	4.2	0.500	1.60	10.53	13.05
	4.2	0.800	1.35	12.48	13.05

Table 15. Summary of foam experiments

Core #	Total Flow Rate (cc/hr)	CO_2 Fraction	Pressure Drop (psid)	Total Mobility (md/cp)	Total Interstitial Velocity (ft/day)	WAG Mobility (md/cp)	Resistance Factor
B	4.2	0.200	127	0.67	12.85	20.00	30.00
	4.2	0.333	145	0.58	12.85	18.80	32.10
	4.2	0.500	172	0.49	12.85	21.30	43.30
	4.2	0.667	216	0.39	12.85	27.90	71.30
	4.2	0.200	171	0.50	12.85	20.00	40.50
	4.2	0.800	253	0.33	12.85	38.70	115.80
	4.2	0.667	254	0.33	12.85	27.90	83.80
C	4.2	0.200	19.91	1.71	12.85	16.08	9.39
	4.2	0.333	34.04	1.00	12.85	13.17	13.15
	4.2	0.500	34.37	0.99	12.85	20.96	21.12
	4.2	0.667	49.19	0.69	12.85	24.36	35.14
	4.2	0.800	56.01	0.61	12.85	31.66	52.00
	8.4	0.200	71.64	0.95	25.70	16.08	16.89
	8.4	0.333	73.51	0.93	25.70	13.17	14.19
	8.4	0.500	77.67	0.88	25.70	20.96	23.87
	8.4	0.667	88.97	0.77	25.70	24.36	31.78
	8.4	0.800	94.02	0.73	25.70	31.66	43.64
	4.2	0.800	77.31	0.44	12.85	31.66	71.77
	4.2	0.200	63.73	0.54	12.85	16.08	30.05
	16.8	0.200	92.50	1.47	51.39	16.08	10.90
	16.8	0.333	93.48	1.46	51.39	13.17	9.03
	16.8	0.500	105.62	1.29	51.39	20.96	16.23
	16.8	0.667	120.37	1.13	51.39	24.36	21.50
	16.8	0.800	122.59	1.11	51.39	31.66	28.45
	4.2	0.667	66.72	0.51	12.85	24.36	47.66
	4.2	0.500	62.20	0.55	12.85	20.96	38.23
	4.2	0.200	30.19	1.13	12.85	16.08	14.23
D	4.2	0.800	20.55	0.82	13.05	12.48	15.22
	4.2	0.800	20.32	0.83	13.05	12.48	15.05
	4.2	0.500	21.87	0.77	13.05	10.53	13.67
	4.2	0.200	11.85	1.42	13.05	15.18	10.68

Table 16. Range of data used in neural network tests

Property	minimum	maximum
Bubble point pressure, psia	130	3573
Bubble point pressure formation volume factor, RB/STB	1.032	1.997
Solution GOR, SCF/STB	26	1602
Average gas specific gravity (air=1)	0.752	1.367
Stock tank oil gravity, °API	19.40	44.60
CO_2 in surface gases, mole%	0.00	16.38
N_2 in surface gases, mole%	0.00	3.86
H_2S in surface gases, mole%	0.00	16.13
Reservoir temperature, °F	74	240

Table 17. Statistical accuracy of P_b estimated by neural networks and correlations from Standing, Glaso, and Al-Marhoun for 80 Middle East oils and 11 North Sea oils

	NN	Al-Marhoun	Standing	Glaso
Average relative error, %	1.067	0.222	7.596	18.12
Average absolute relative error, %	3.720	5.168	13.256	23.99
Minimum absolute relative error, %	0.000	0.000	0.052	0.474
Maximum absolute relative error, %	13.11	37.72	50.09	71.19
Standard deviation, %	4.944	7.576	15.47	21.98
Correlation coefficient	0.998	0.994	0.979	0.900

Table 18. Statistical accuracy of P_b estimated by neural networks and correlations from Standing, Glaso, and Al-Marhoun for 11 North Sea oils

	NN	Al-Marhoun	Standing	Glaso
Average relative error, %	-0.810	0.234	3.311	4.570
Average absolute relative error, %	3.094	14.19	15.94	9.498
Minimum absolute relative error, %	0.692	2.950	1.066	0.584
Maximum absolute relative error, %	5.988	37.72	50.09	24.48
Standard deviation, %	3.602	18.43	22.17	11.86
Correlation coefficient	0.998	0.980	0.986	0.995

Table 19. Statistical accuracy of B_{ob} estimated by neural networks and correlations from Standing, Glaso, and Al-Marhoun for 80 Middle East oils and 9 North Sea oils

	NN	Al-Marhoun	Standing	Glaso
Average relative error, %	0.045	-0.068	1.764	-0.317
Average absolute relative error, %	0.662	1.030	2.047	1.711
Minimum absolute relative error, %	0.031	0.000	0.000	0.000
Maximum absolute relative error, %	3.378	5.100	11.96	9.223
Standard deviation, %	0.889	1.442	2.291	2.266
Correlation coefficient	0.998	0.995	0.973	0.986

Table 20. Statistical accuracy of B_{ob} estimated by neural networks and correlations for nine North Sea oils

	NN	Al-Marhoun	Standing	Glaso
Average relative error, %	0.235	-0.476	0.312	-1.366
Average absolute relative error, %	0.664	1.986	2.065	2.160
Minimum absolute relative error, %	0.126	0.186	0.007	0.496
Maximum absolute relative error, %	2.564	5.100	4.913	5.336
Standard deviation, %	0.996	2.684	2.820	2.572
Correlation coefficient	0.998	0.988	0.983	0.985

Table 21. Reservoir fluid analysis, in mole fractions

component	A	B	B_1	B_2	C_2	C_2	D	G	JEMA	NWE
CO_2	0.0417	0.0011	0.0042	0.0056	0.0001	0.0001	0.0000	0.0019	0.0135	0.0044
N_2	0.0127	0.0048	0.0047	0.0052	0.0000	0.0000	0.0000	0.0029	0.0038	0.0019
H_2S	0.0169	0.0000	0.0000	0.0000	0.0000	0.0000	0.0169	0.0021	0.0020	0.0014
C_1	0.1608	0.1630	0.1265	0.1543	0.1834	0.1834	0.1262	0.1752	0.0693	0.2025
C_2	0.0843	0.0403	0.0665	0.0726	0.0778	0.0778	0.0380	0.0990	0.1004	0.0591
C_3	0.0748	0.0297	0.0691	0.0614	0.0791	0.0791	0.0480	0.1254	0.0738	0.0589
i C_4	0.0163	0.0036	0.0157	0.0049	0.0065	0.0065	0.0109	0.0176	0.0120	0.0146
n C_4	0.0385	0.0329	0.0461	0.0410	0.0474	0.0474	0.0292	0.0615	0.0650	0.0412
i C_5	0.0174	0.0158	0.0240	0.0136	0.0165	0.0165	0.0154	0.0213	0.0215	0.0253
n C_5	0.0211	0.0215	0.0284	0.0269	0.0178	0.0178	0.0186	0.0293	0.0415	0.0238
C_6	0.0430	0.0332	0.0292	0.0361	0.0382	0.0382	0.0244	0.0376	0.0544	0.0435
C_{7+}	0.4725	0.6541	0.5858	0.5784	0.5332	0.5332	0.6893	0.4162	0.5429	0.5234
MW_{7+}	253	227	226	233	230	230	247	215	248	229
ρ_{7+}	0.8896	0.8553	0.8822	0.8880	0.8763	0.8763	0.8917	0.8520	0.8883	0.8700
temp.(°F)	105	94	106	106	94	105	105	94	106	83

Table 22. Critical point estimated by neural networks

	Oil F		Oil BSB	
	Calculated	Measured	Calculated	Measured
Critical CO_2 Mole %	52	56	59	56
Critical Pressure (psia)	1569	1580	1291	1308

Table 23. Reservoir data

Reservoir size	660 ft by 660 ft by 160 ft
Mesh dimension	8 by 8 by 5
X-direction grid size	82.5 ft
Y-direction grid size	82.5 ft
Z-direction grid size of each layer	27, 40, 35,18,40 ft
Porosity of each layer	0.1, 0.06, 0.08, 0.15, 0.07
X-direction permeability of each layer	150, 70, 112, 1000, 70 md
Y-direction permeability of each layer	150, 70, 112, 1000, 70 md
Z-direction permeability of each layer	15, 7, 11.2, 100, 7 md

Table 24. Slopes of IFT vs $\Delta\rho$ data from Macleod.

Component Name	Reduced Temperature $(1-T/T_c)$	IFT (mN/m)	Slope
Ethyl Acetate	0.92–0.04	23.60–0.49	3.83
Ethyl Ether	0.90–0.07	16.49–0.64	3.94
Ethyl Alcohol	0.92–0.09	22.83–1.87	3.85
Phenol	0.72–0.06	20.28–0.99	3.84
Carbon Tetrachloride	0.93–0.12	25.68–1.93	3.91
Methyl Formate	0.91–0.07	24.62–0.87	3.90
Chlorobenzol	0.58–0.17	17.67–3.79	3.91
Acetic Acid	0.94–0.003	23.46–0.032	3.68

Table 25. Theoretical values of the critical exponents

Origin	β	γ	References
Van der Waal's Equation	0.5	1.5	
2-Dimensional Ising Model	0.125	1.0	[168] [282]
3-Dimensional Ising Model	0.325	1.26	[168] [282] [171]
Renormalization Group Theory	0.325	1.26	[171]
Currently Accepted Values	0.325	1.26	[172] [173] [174]

Table 26. Parachors of petroleum components

Component	Parachor		Component	Parachor
Carbon Dioxide	82.00		Nitrogen	61.12
Hydrogen Sulphide	85.50		Methane	74.05
Ethane	112.91		Propane	154.03
n-Butane	193.90		n-Pentane	236.00
n-Hexane	276.71		n-Heptane	318.44
n-Octane	359.33		n-Nonane	399.57
n-Decane	440.69		n-Undecane	482.00
n-Dodecane	522.26		n-Tridecane	563.77
n-Tetradecane	606.05		n-Pentadecane	647.43
n-Hexadecane	688.50		n-Eicosane	853.67
n-Hexacosane	1108.90		n-Dotriacontane	1355.89
n-Hexacontane	2541.84		2-Methylbutane	234.87
2-Methylpentane	276.87		3-Methylpentane	273.84
2,2-Dimethylbutane	272.20		2,3-Dimethylbutane	272.12
2-Methylhexane	316.29		3-Methylhexane	314.76
3-Methylpentane	312.49		2,2-Dimethylpentane	314.83
2,3-Dimethylpentane	310.48		2,4-Dimethylpentane	315.36
3,3-Dimethylpentane	309.57		2,2,3-Trimethylbutane	309.45
2-Methylheptane	356.93		3-Methylheptane	355.57

Table 26 (cont'd)

Component	Parachor		Component	Parachor
4-Methylheptane	355.45		3-Ethylhexane	353.16
2,2-Dimethylhexane	353.92		2,3-Dimethylhexane	351.90
2,4-Dimethylhexane	353.29		2,5-Dimethylhexane	355.05
3,3-Dimethylhexane	351.10		3,4-Dimethylhexane	350.82
3-Ethyl-2-methylpentane	346.20		3-Ethyl-3-methylpentane	352.41
2,2,3-Trimethylpentane	348.24		2,2,4-Trimethylpentane	351.55
2,3,3-Trimethylpentane	347.13		2,3,4-Trimethylpentane	348.82
2,4-Dimethylheptane	390.10		2,5-Dimethylheptane	394.08
3,3-Dimethylheptane	385.71		2,2,3-Trimethylhexane	389.56
2,2,4-Trimethylhexane	390.49		2,2,5-Trimethylhexane	392.87
2,3,3-Trimethylhexane	387.38		2,3,5-Trimethylhexane	390.80
2,4,4-Trimethylhexane	388.85		3,3,4-Trimethylhexane	387.11
2,2,3,3-Tetramethylpentane	382.09		2,2,3,4-Tetramethylpentane	385.08
2,2,4,4-Tetramethylpentane	387.39		2,3,3,4-Tetramethylpentane	382.70
2,4-Dimethyloctane	433.20		2,7-Dimethyloctane	436.04
4,5-Dimethyloctane	429.00		2,4-Dimethyloctane	426.34
2,4,6-Trimethylheptane	433.00		2,4,7-Trimethyloctane	473.01
Cyclopentane	210.05		Cyclohexane	247.89
Methylcyclohexane	289.00		Ethylcyclohexane	328.74
1,1-Dimethylcyclohexane	326.22		cis-1,2-Dimethylcyclohexane	325.26
trans-1,2-Dimethylcyclohexane	328.26		1,2-Dimethylcyclohexane	327.09
cis-1,3-Dimethylcyclohexane	329.09		trans-1,3-Dimethylcyclohexane	326.69
1,3-Dimethylcyclohexane	329.02		cis-1,4-Dimethylcyclohexane	326.88
trans-1,4-Dimethylcyclohexane	330.20		1,4-Dimethylcyclohexane	328.99

Table 26. (cont'd)

Component	Parachor		Component	366.16
1,1,3-trimethylcyclohexane	365.60		1,3,4-trimethylcyclohexane	364.93
n-Butylcyclohexane	410.51		Isobutylcyclohexane	407.71
sec-Butylcyclohexane	407.81		tert-Butylcyclohexane	404.73
Dicyclohexyl	460.41		Cycloheptane	285.24
Methylcycloheptane	325.19		Cyclooctane	322.56
Methylcyclooctane	362.33		2-Methylbicyclo[1,2,2]heptane	304.13
2-Methylbicyclo[2,2,2]octane	338.54		Decahydronaphthalene	381.58
trans-Decahydronaphthalene	379.41		cis-Decahydronaphthalene	375.32
Methylcyclopentadecane	638.23		Ethylene	101.53
Allylene	125.83		Propylene	143.02
2-Methyl-2-Butene	221.73		1-5-Hexadiene	254.35
3-Methyl-2-heptene	341.80		2,4-Dimethyl-4-hexene	338.55
2,5-Dimethyl-2-hexene	340.59		2,4-Dimethyl-4-heptene	381.98
2,5-Dimethyl-4-heptene	382.75		2,3,5-Trimethyl-2-hexene	379.41
2,4-Dimethyl-4-octene	422.05		2,4,6-Trimethyl-3-heptene	423.21
2,4,7-Trimethyl-4-octene	461.43		Acetylene	90.57
1-Octyne	335.26		3-Nonyne	373.10
3-Decyne	415.43		Phenylpropylacetylene	392.67
1-Undecyne	415.01		Butylpentylacetylene	456.59
Benzene	210.96		Toluene	252.33
Ethylbenzene	292.27		Indene	298.29
n-Propylbenzene	331.84		Isopropylbenzene	329.92
Naphthalene	321.01		n-Amylbenzene	412.32
n-Hexylbenzene	453.34		2-Amyl-1,4-dimethylbenzene	486.59
2-Hexyl-1,4-dimethylbenzene	527.97		2-Heptyl-1,4-dimethylbenzene	568.85
1,4-Dimethyl-2-octylbenzene	610.56		Triphenylmethane	602.29

Table 27. Correlation coefficients of hydrocarbon parachors

Hydrocarbons	*a*	*b*	SEOE
Normal Paraffins	2.97995377	18.17639160	4.617
Alkanes	2.98707461	11.73444748	5.884
Alkanes, Alkenes and Alkadienes	2.97924896	12.70571423	10.022
Alkanes, Alkenes, Alkadienes and Alkynes	2.97694945	11.37152950	12.594
Alkanes, Alkenes, Alkadienes, Alkynes and Cyclic Compounds	2.97649598	5.06389666	16.022
Alkanes, Alkenes, Alkadienes, Alkynes, Cyclic and Aromatic Compounds	2.95189214	3.71917152	21.941

SEOE = Standard Error Of Estimation.

Table 28. Parachors of oil cuts

Group	Parachor	Group	Parachor
C6	251.68	C7	287.10
C8	319.57	C9	360.90
C10	399.27	C11	437.65
C12	478.97	C13	520.30
C14	564.58	C15	611.81
C16	659.04	C17	703.32
C18	744.64	C19	780.07
C20	815.49	C21	862.72
C22	889.29	C23	924.7
C24	960.13	C25	998.51
C26	1033.93	C27	1066.40
C28	1101.82	C29	1131.34
C30	1166.76	C31	1196.28
C32	1228.75	C33	1261.23
C34	1293.70	C35	1317.31
C36	1349.78	C37	1373.40
C38	1405.87	C39	1432.43
C40	1464.91	C41	1485.57
C42	1515.09	C43	1541.66
C44	1571.17	C45	1594.79

Table 29. Composition and properties of reservoir fluids

Component, mol%	System I	System II	System III	System IV	System V	System VI
CO2	2.98	1.00	2.02	0.16	0.01	0.01
N2	0.12	0.02	0.03	0.45	0.00	0.00
C1	66.87	36.13	51.53	36.71	31.00	31.30
C2	6.86	5.95	8.07	8.44	10.41	10.32
C3	3.95	4.44	5.04	6.03	11.87	10.68
i-C4	0.73	0.79	0.83	1.24	2.32	0.44
n-C4	1.82	2.12	2.04	3.67	5.00	6.30
i-C5	0.83	1.03	0.84	1.80	1.41	1.22
n-C5	1.03	1.25	1.05	2.36	3.00	2.77
C6	1.40	1.97	1.38	3.03	2.55	2.79
C7+	13.40	45.30	27.17	36.11	32.43	34.17
Total	100.00	100.00	100.00	100.00	100.00	100.00
C7+ molecular weight	164.7	227.4	217.0	234.3	199.0	190.3
C7+ specific gravity		0.870		0.868		0.833
Temperature, °F	73	180	180	170	130	130
Bubble point pressure, psia	5,901	2,155	4,589	2,573	1,666	

Table 30. Comparison of IFT predictions with measured data

Fluid Mixture	Pressure psia	Experiment IFT dyne/cm	Predicted IFT, dyne/cm			
			Approach 1	2	3	4
System I	2275	2.7	2.03	0.98	1.25	2.38
System II	185	19.5	11.80	10.68	11.43	16.05
	1150	10.1	7.30	5.13	5.74	9.83
	1650	6.7	5.50	3.14	3.61	7.35
	2150	5.5	4.05	1.79	2.12	5.36
System III	2315	4.6	3.23	1.58	1.90	4.20
	2815	3.3	2.23	0.87	1.08	2.88
	3315	2.3	1.47	0.45	0.57	1.89
	3815	1.3	0.90	0.21	0.28	1.16
System IV	1110	10.3	6.47	5.01	5.66	8.85
	1610	8.5	4.80	3.15	3.65	6.54
	2010	6.0	3.71	2.08	2.47	5.04
System V	2000	0.434	0.395	0.312	0.462	0.445
	2270	0.0583	0.0618	0.0437	0.0778	0.0606
Maximum Error, %		0	43.53	83.85	78.46	23.06
Average Error, %		0	28.43	58.21	51.87	11.01

Table 31. Pendant drop parameters for seven pure substances

Liquid	ρ_l (g/cc)	ρ_v (g/cc)	D_e (cm)	H_e (cm)	R_a (cm)	Condition
Water	0.998	5.2E-3	0.336	0.182	0.156	20°C, 1 Atm
	0.997	6.6E-3	0.227	0.127	0.107	22°C, 1 Atm
	0.996	6.7E-3	0.211	0.109	0.106	23°C, 1 Atm
	0.993	7.6E-3	0.196	0.095	0.096	28°C, 1 Atm
Decane	0.730	4.1E-3	0.256	0.138	0.116	25°C, 1 Atm
	0.763	0.104	0.244	0.197	0.120	50°C, 22 Atm
	0.761	0.126	0.239	0.195	0.114	65°C, 23 Atm
Decyl alcohol	0.829	4.6E-3	0.256	0.135	0.115	25°C, 1 Atm
2-2-4 trimethyl pentane	0.692	3.9E-3	0.248	0.138	0.111	25°C, 1 Atm
Heptane	0.684	2.9E-3	0.253	0.132	0.114	25°C, 1 Atm
Hexadecane	0.773	6.5E-3	0.264	0.145	0.119	25°C, 1 Atm
Toluene	0.865	2.7E-3	0.254	0.132	0.115	25°C, 1 Atm

Table 32. Surface tension values in mN/m from pendant drop measurements

Liquid	Jasper[247]	Hansen & Rodsrud[237]	Lopez de Ramos[244]	Present	Condition
Water			(72.03)	72.10	20°C, 1 Atm
			71.23	71.50	22°C, 1 Atm
			72.05	70.36	23°C, 1 Atm
			71.23	70.29	28°C, 1 Atm
Decane	23.5	22.3	22.2	23.03	25°C, 1 Atm
			20.02	15.67	50°C, 22 Atm
			17.79	14.06	65°C, 23 Atm
Decyl alcohol	28.6	25.3	25.7	26.59	25°C, 1 Atm
2-2-4 trimethyl pentante	18.4	18.1	18.1	18.73	25°C, 1 Atm
Heptane	19.7	27.1	23.7	24.3	25°C, 1 Atm
Hexadecane	27.1	23.7	24.3	25.3	25°C, 1 Atm
Toluene	28.1	25.6	25.5	27.1	25°C, 1 Atm

Table 33. Core samples for CO_2 gravity drainage experiments

	Core #1	**Core #2**	**Core #3**	**Core #4**
Permeability, md	500	0.01	50	0.38
Porosity, %	18.7	10	13	11.1
Water Saturation, %PV	35	38.6	29.4	45

Table 34. Composition of oil produced by gravity drainage

Hydrocarbon Number	Mole Fraction STO	Yellow Oil	Brown Oil
5	0.09114	0.00122	0.00143
6	0.06631	0.00058	0.00103
7	0.14649	0.00190	0.00612
8	0.10466	0.00585	0.01799
9	0.06115	0.01425	0.03063
10	0.05053	0.03841	0.05731
11	0.03736	0.06110	0.07372
12	0.03561	0.08715	0.09773
13	0.03313	0.10453	0.11466
14	0.02572	0.08705	0.09355
15	0.02151	0.07932	0.08366
16	0.02020	0.07220	0.07295
17	0.02088	0.07893	0.07774
18	0.01485	0.05368	0.05020
19	0.01609	0.05446	0.04840
20	0.01142	0.03545	0.03029
21	0.01068	0.03057	0.02560
22	0.01016	0.02579	0.02109
23	0.00957	0.02142	0.01730
24	0.00898	0.01721	0.01382
25	0.00599	0.01051	0.00853
26	0.00846	0.01187	0.00952
27	0.00574	0.00682	0.00551
28	0.00852	0.00867	0.00711
29	0.00583	0.00488	0.00406
30	0.00566	0.00414	0.00354
31	0.00569	0.00363	0.00320
32	0.00555	0.00320	0.00293
33	0.00536	0.00291	0.00280
34	0.00540	0.00283	0.00283
35	0.00550	0.00285	0.00296
36	0.00822	0.00439	0.00472
37+	0.12763	0.06224	0.00709
Total	1.00000	1.00000	1.00000
MW	219.39	251.80	222.34

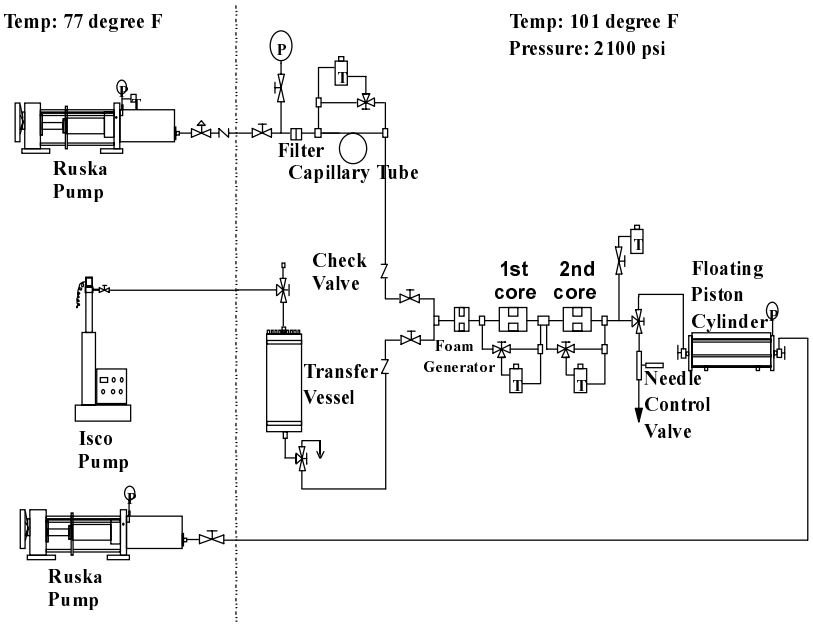

Fig. 1. Schematic of the mobility measurement experimental setup.

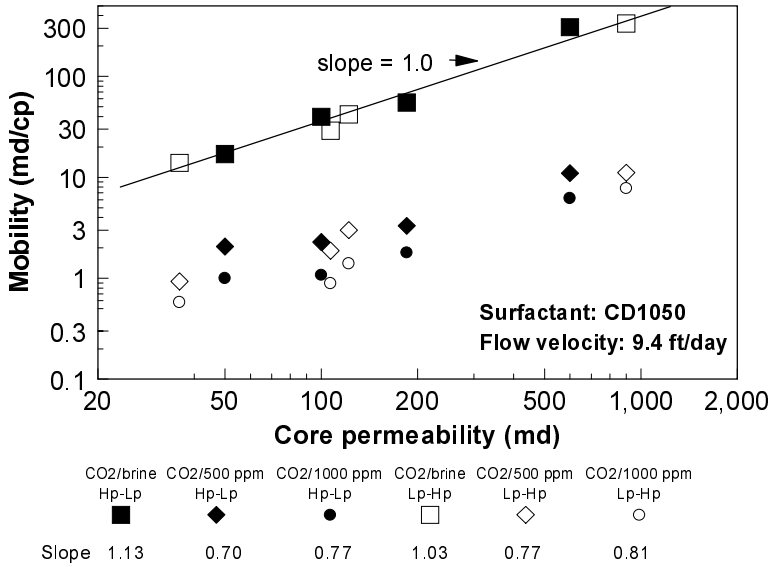

.

Fig. 2. Effect of core position on the mobility measurements.

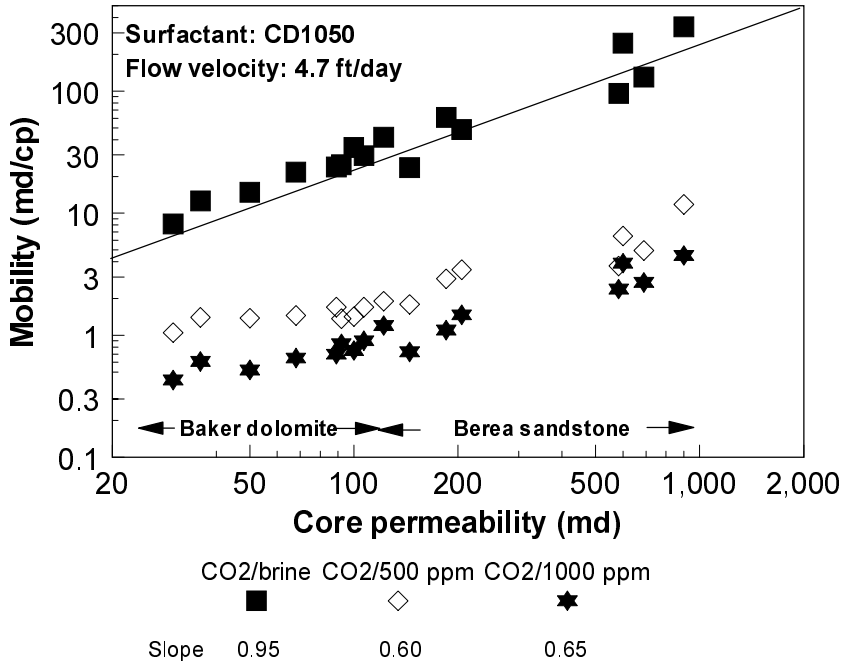

Fig. 3. Dependence of mobility on permeability.

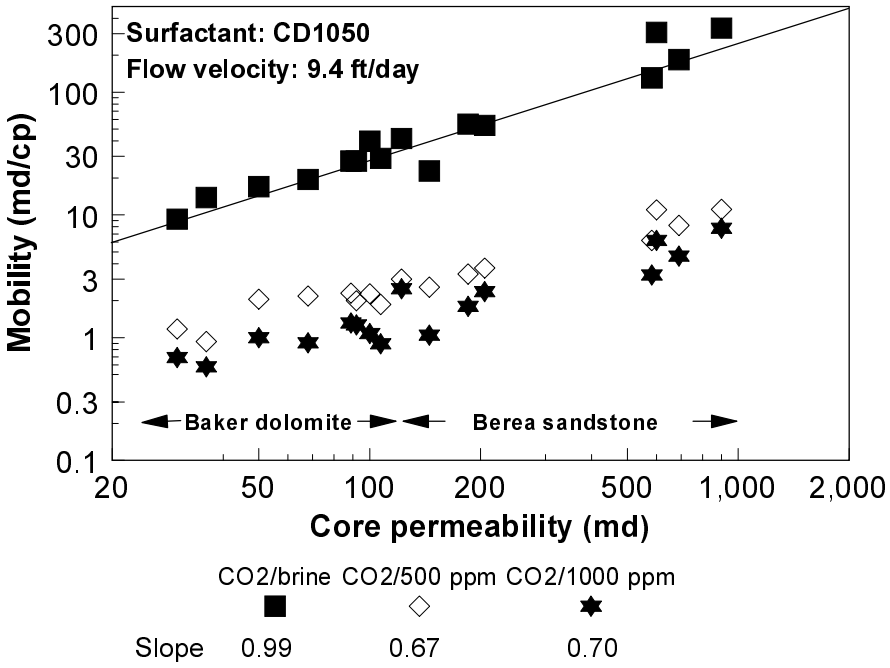

Fig. 4. Dependence of mobility on permeability.

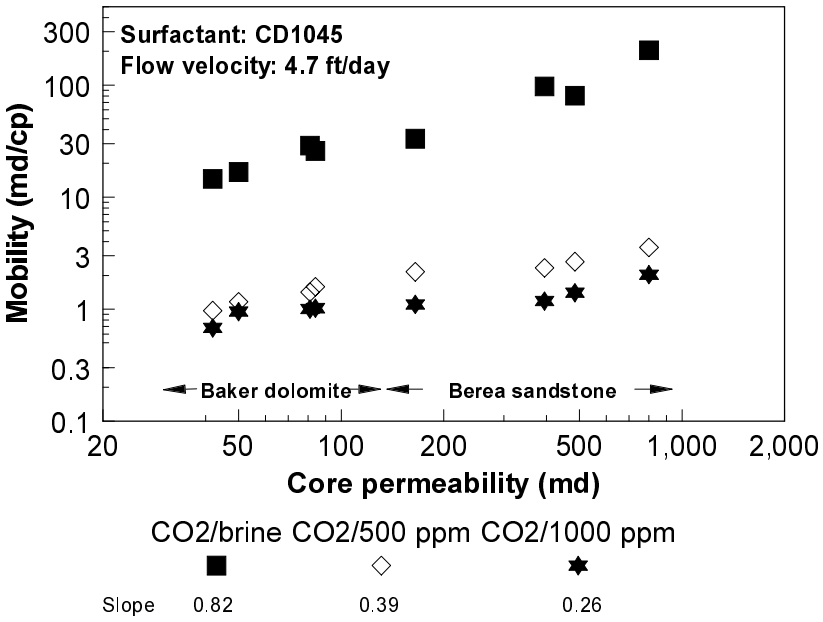

Fig. 5. Dependence of mobility on permeability.

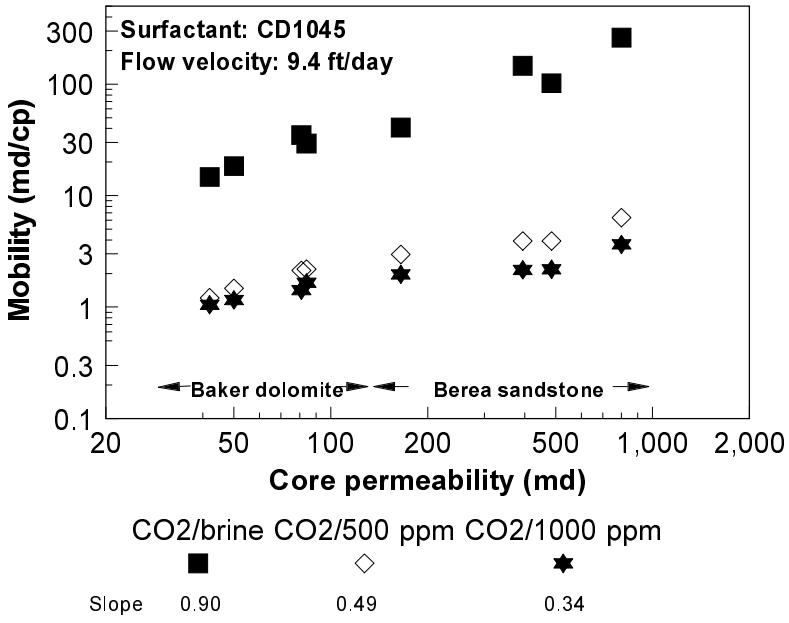

Fig. 6. Dependence of mobility on permeability.

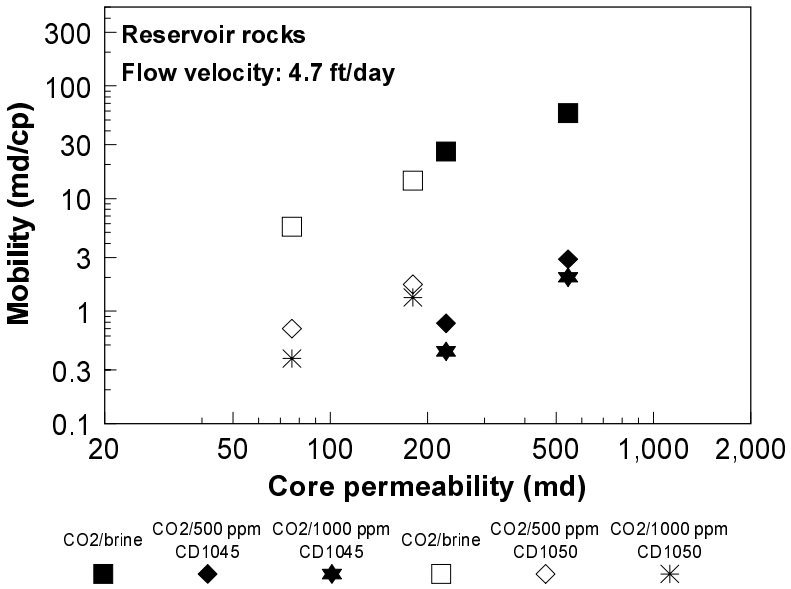

Fig. 7. Dependence of mobility on permeability.

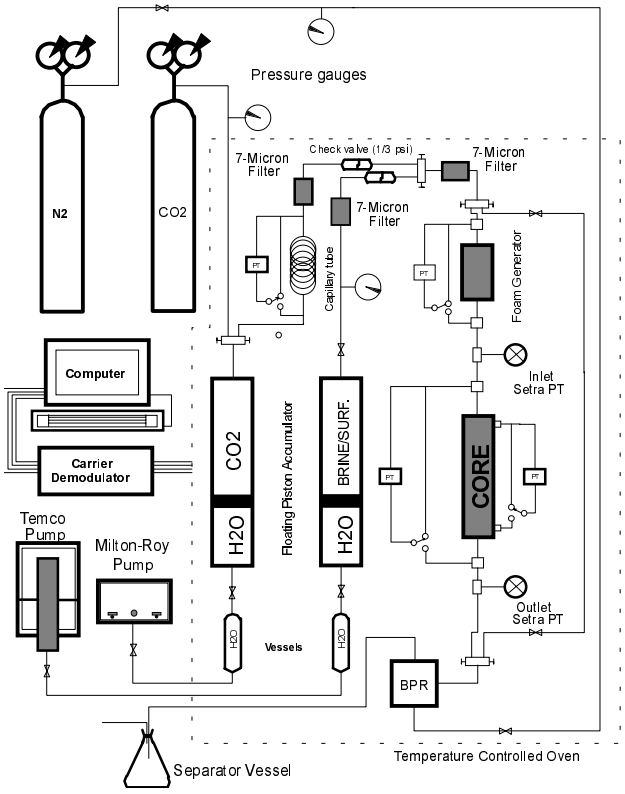

Fig. 8. Schematic diagram of the experimental apparatus (phase one).

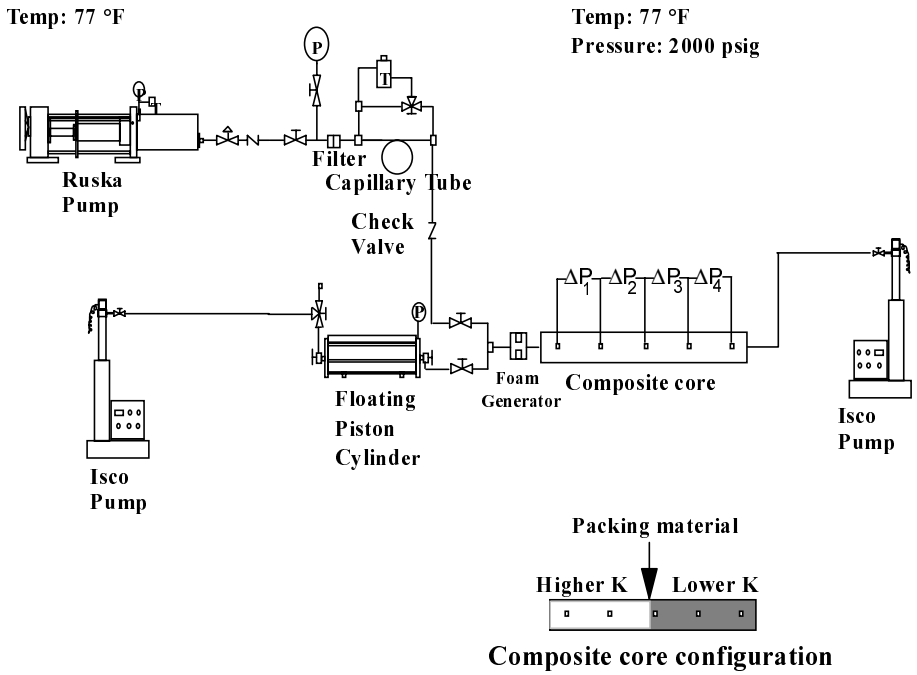

Fig. 9. Schematic of the mobility measurement experimental setup for a series composite core.

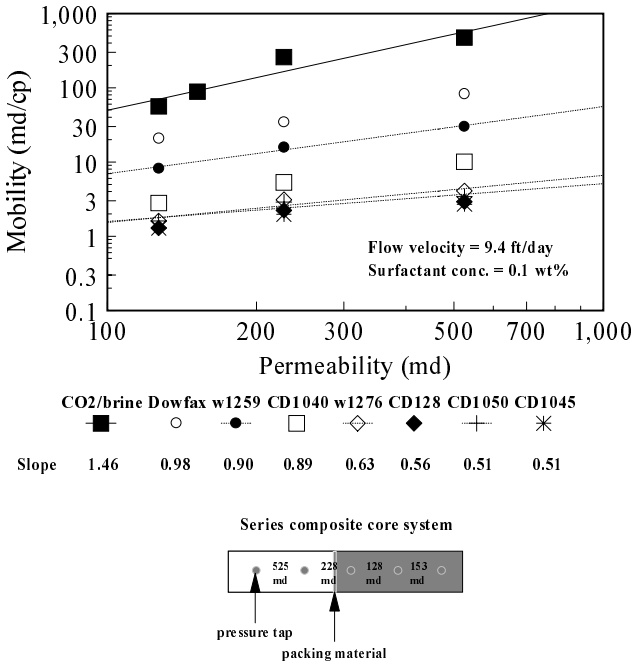

Fig. 10. Mobility dependence on permeability in a series composite core #1.

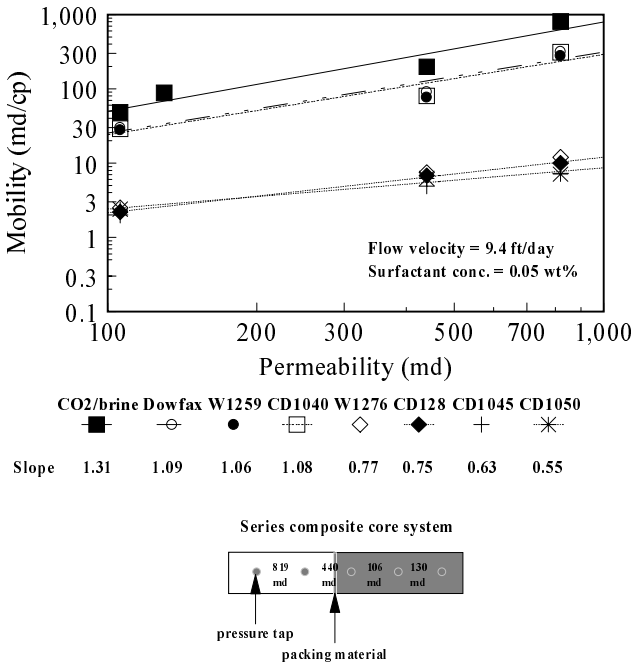

Fig. 11. Mobility dependence on permeability in a series composite core #2.

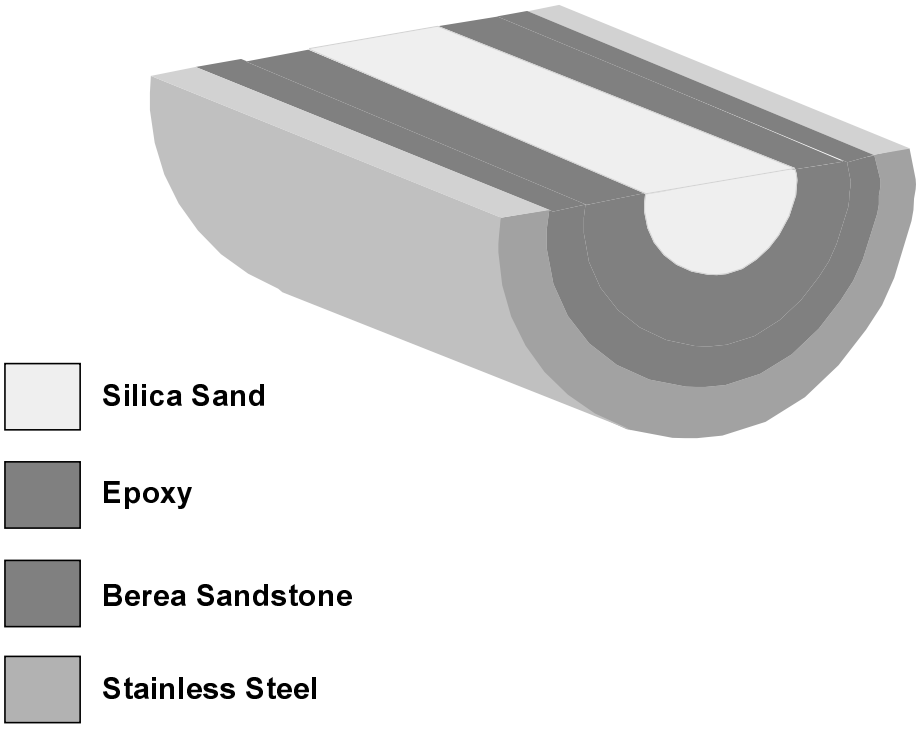

Fig. 12. Schematic diagram of the axial sectional area of a composite parallel core.

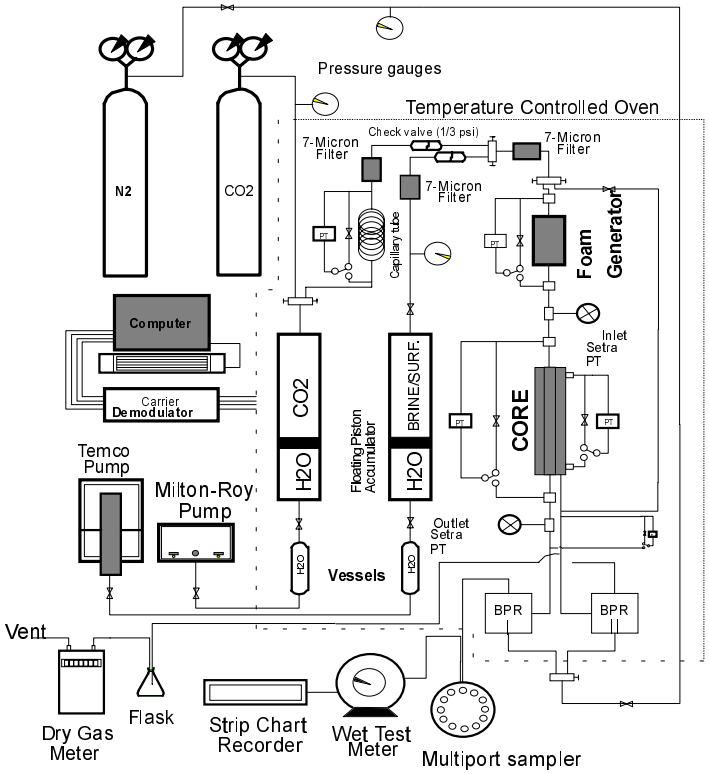

Fig. 13. Schematic diagram of the high pressure experimental apparatus for a parallel composite core.

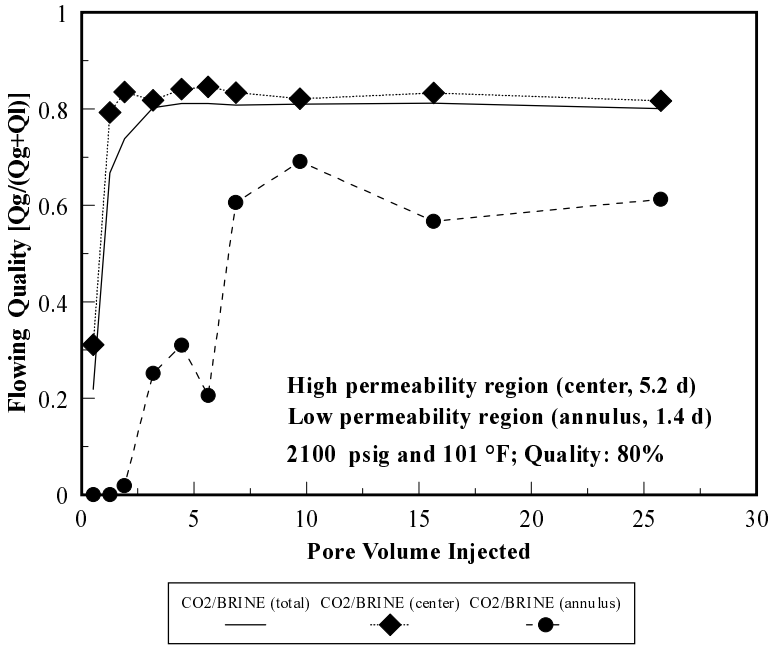

Fig. 14. Flowing quality behavior of CO_2/brine in a parallel Core (I).

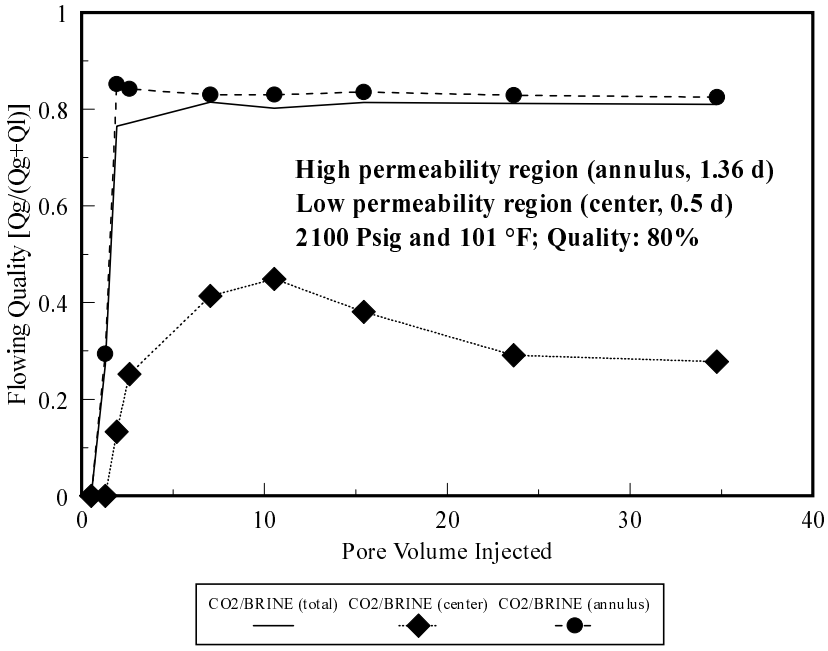

Fig. 15. Flowing quality behavior of CO_2/brine in a parallel Core (II).

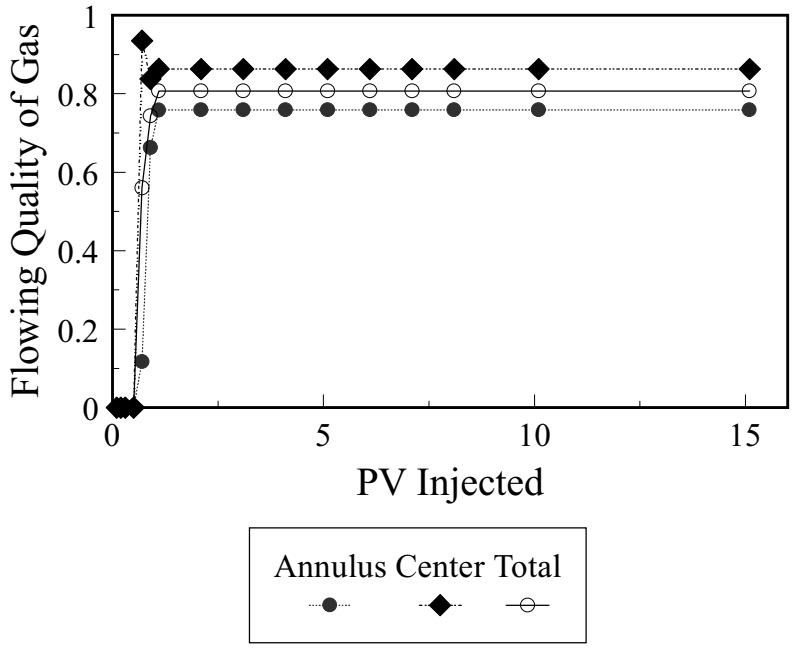

Fig. 16. Effluent profiles in a simulated parallel core with higher permeability region in the center.

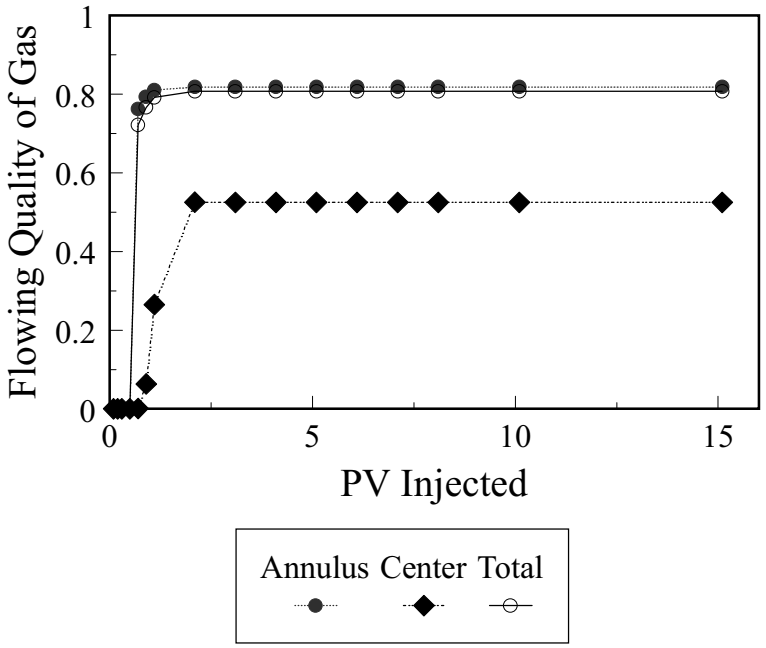

Fig. 17. Effluent profiles in a simulated parallel core with lower permeability region in the center.

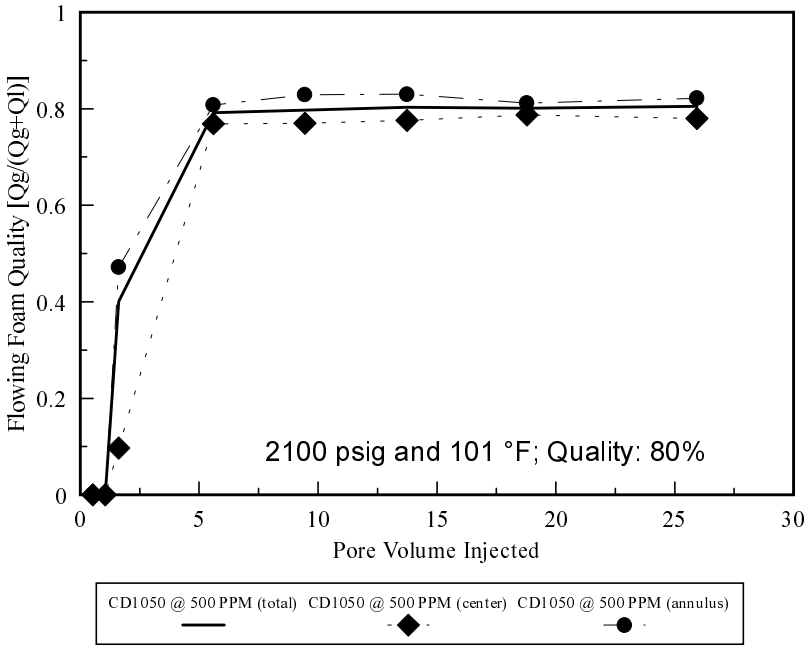

Fig. 18. Foam flowing quality behavior in a parallel core (II).

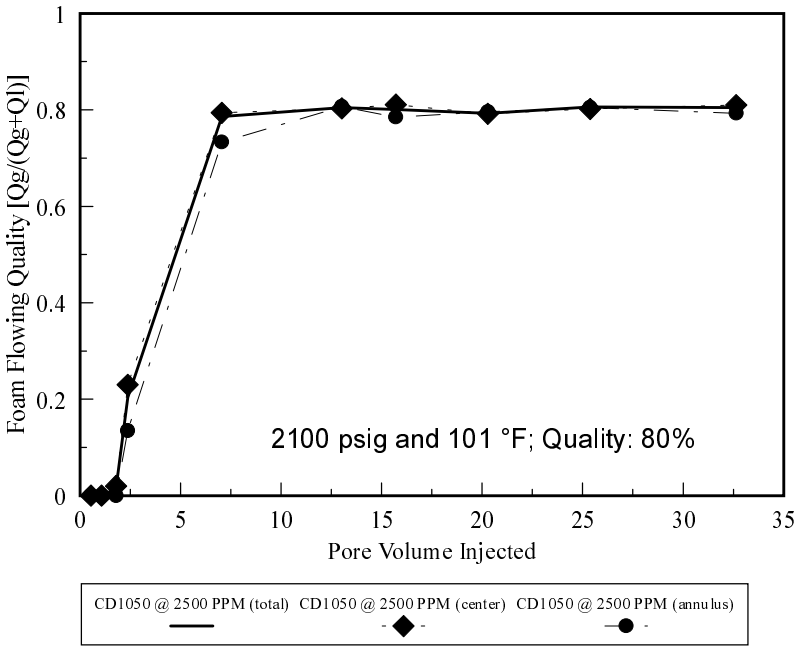

Fig. 19. Foam flowing quality behavior in a parallel core (I)

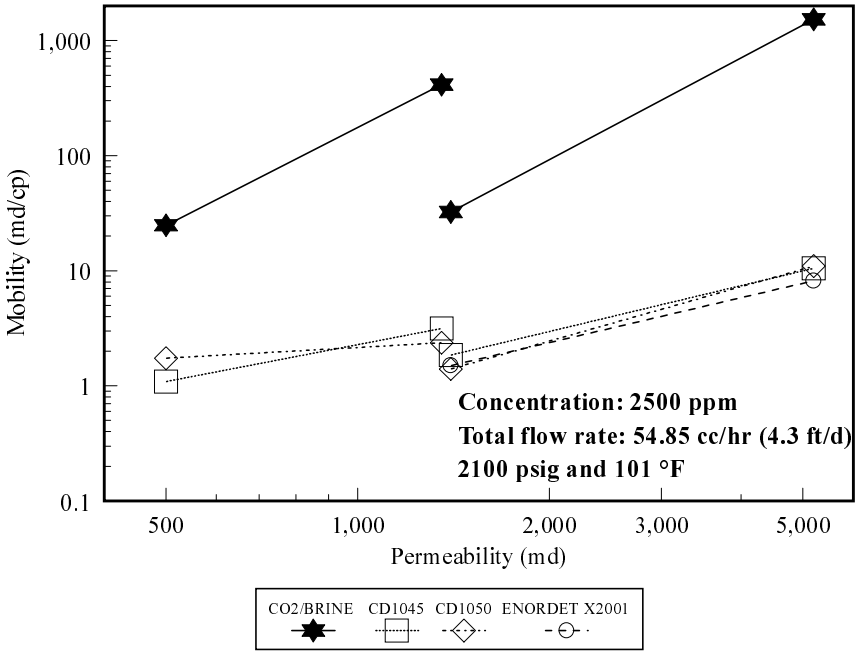

Fig. 20. Mobility dependence on permeability in parallel composite cores at darcy flow velocity of 4.3 ft/day.

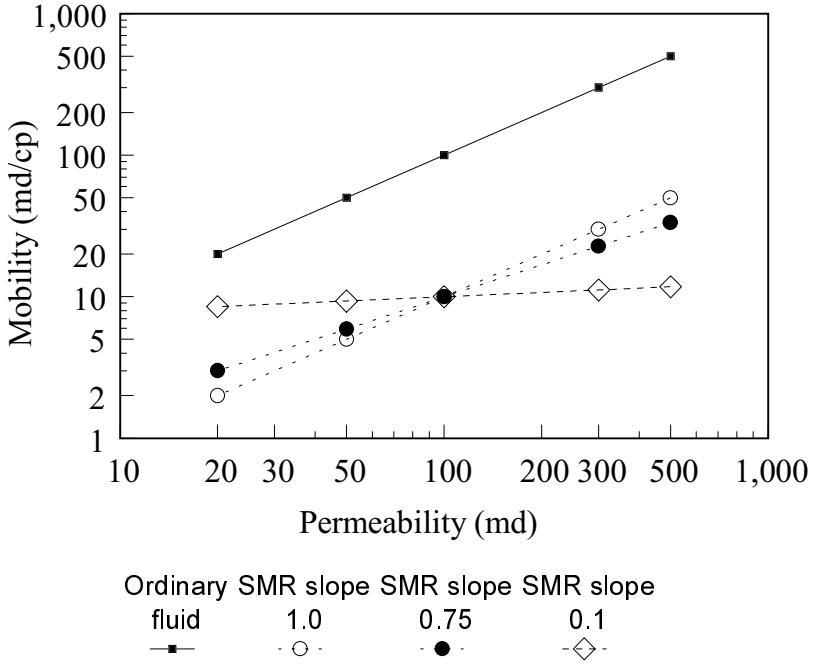

Fig. 21. Mobility dependence of displacing fluid on permeability.

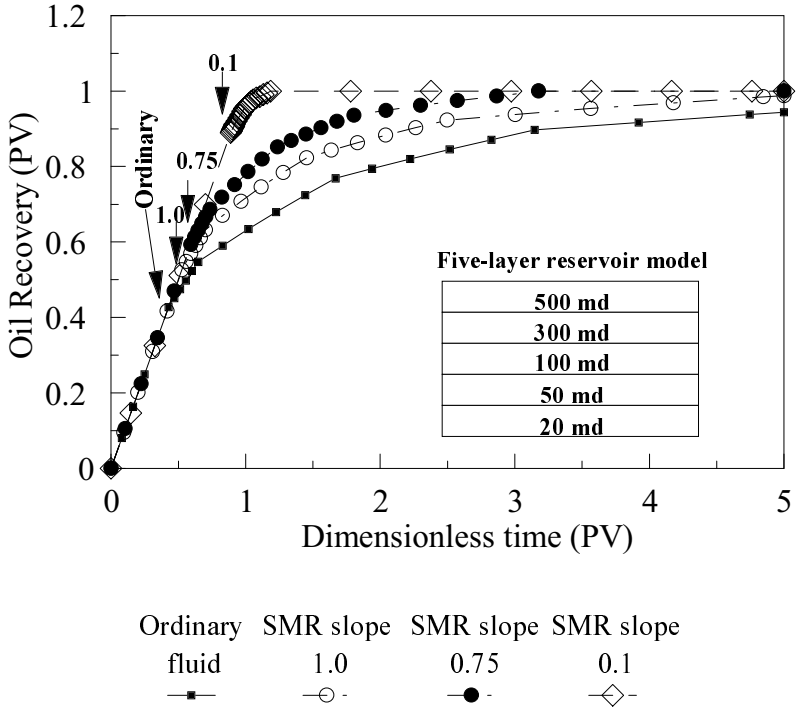

Fig. 22. Oil recovery or vertical sweep efficiency for a five-layer reservoir model. Arrows indicate CO_2 breakthrough in pore volume.

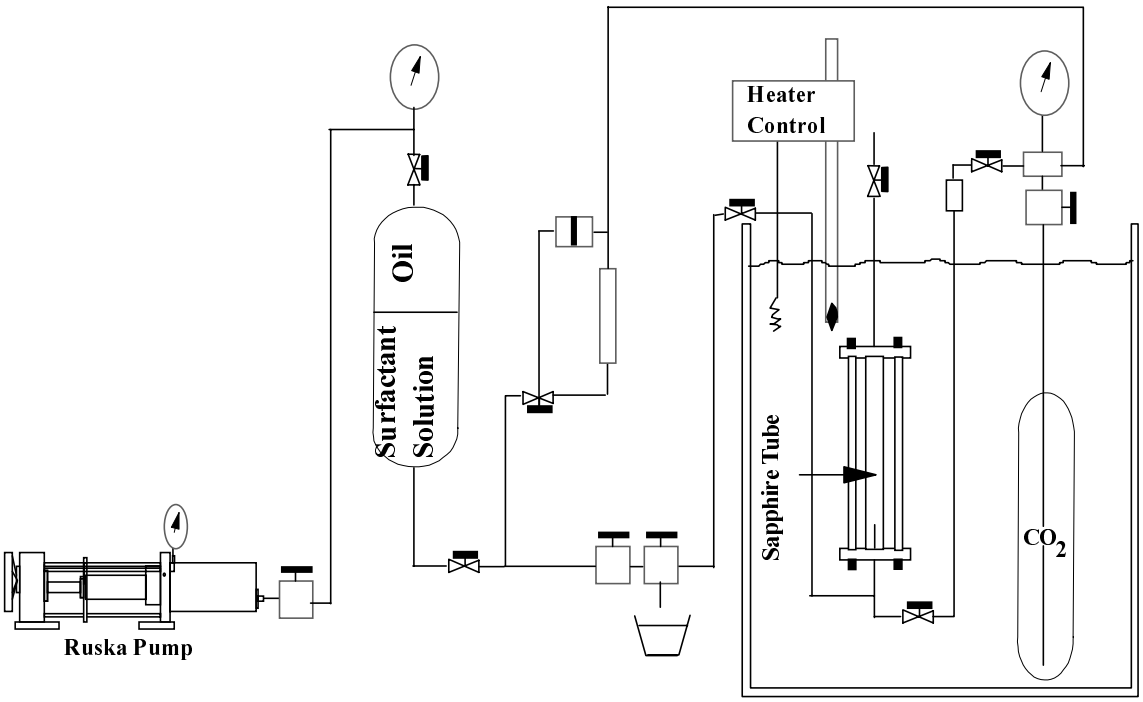

Fig. 23. Foam-durability apparatus.

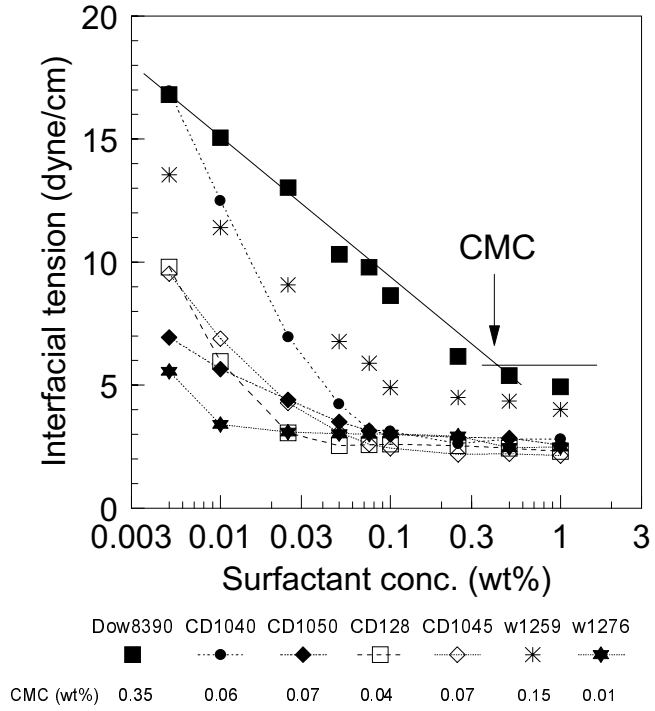

Fig. 24. IFT (dense CO_2 and surfactants) vs. surfactant concentration.

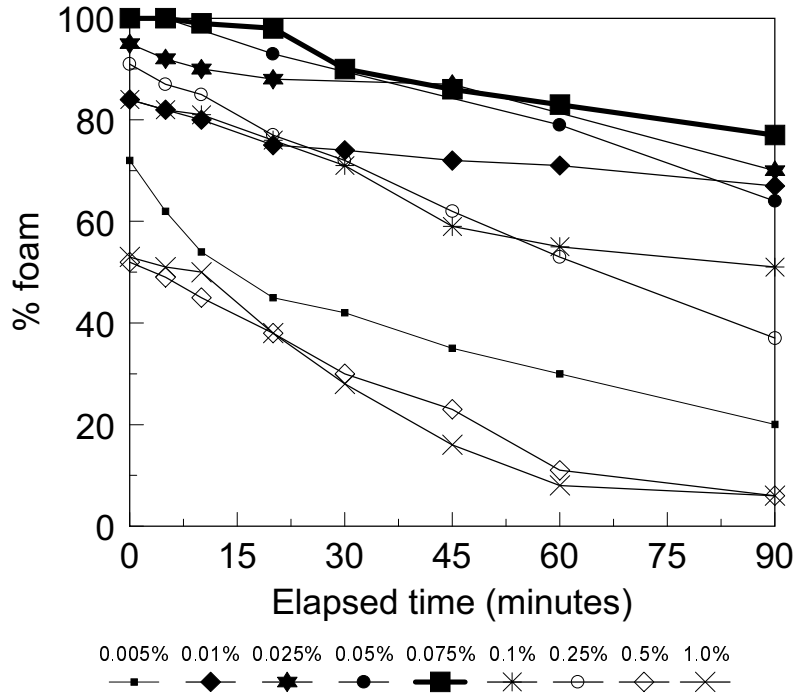

Fig. 25. Decay of CO foam with surfactant CD1050.

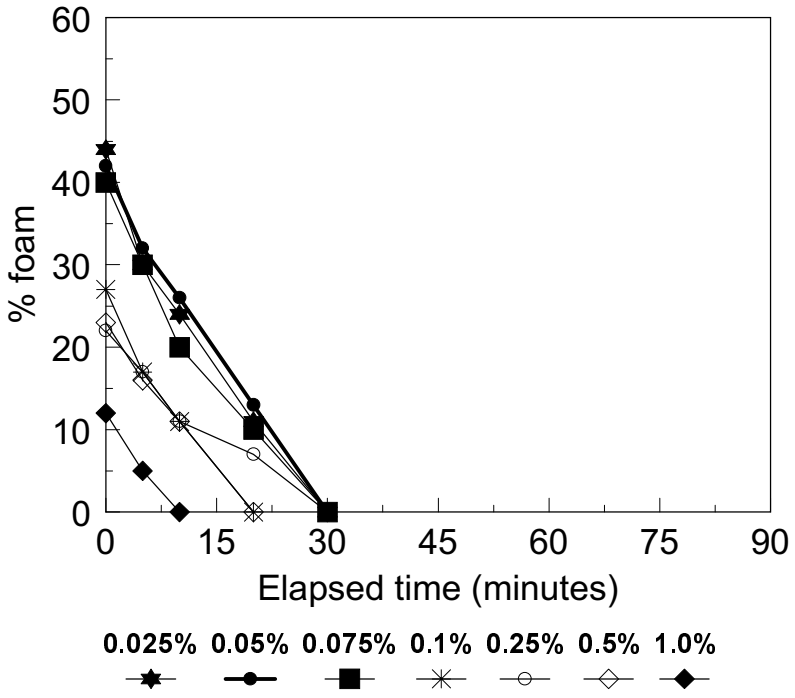

Fig. 26. Decay of CO_2 foam with surfactant CD128.

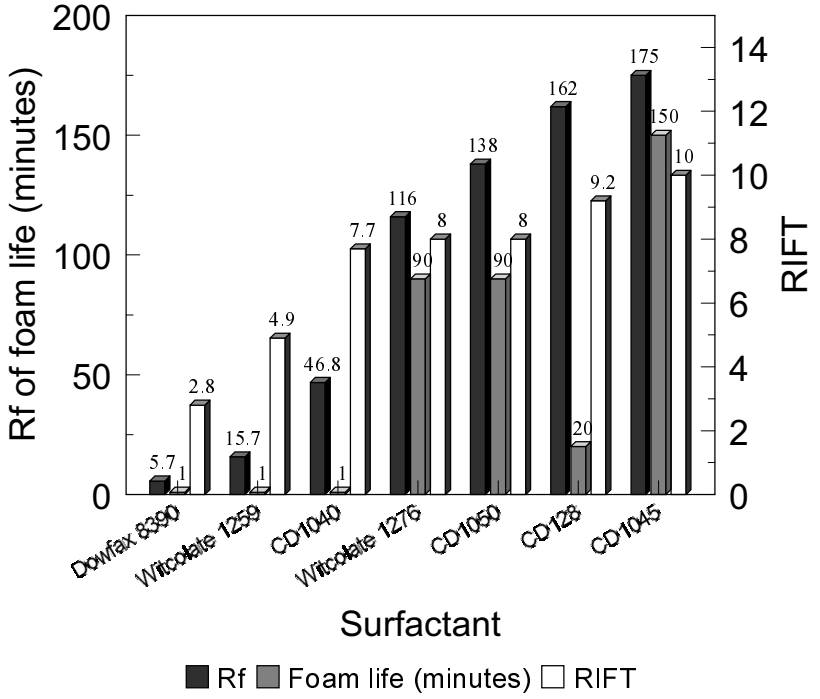

Fig. 27. Correlation between the property of foams and surfactants.

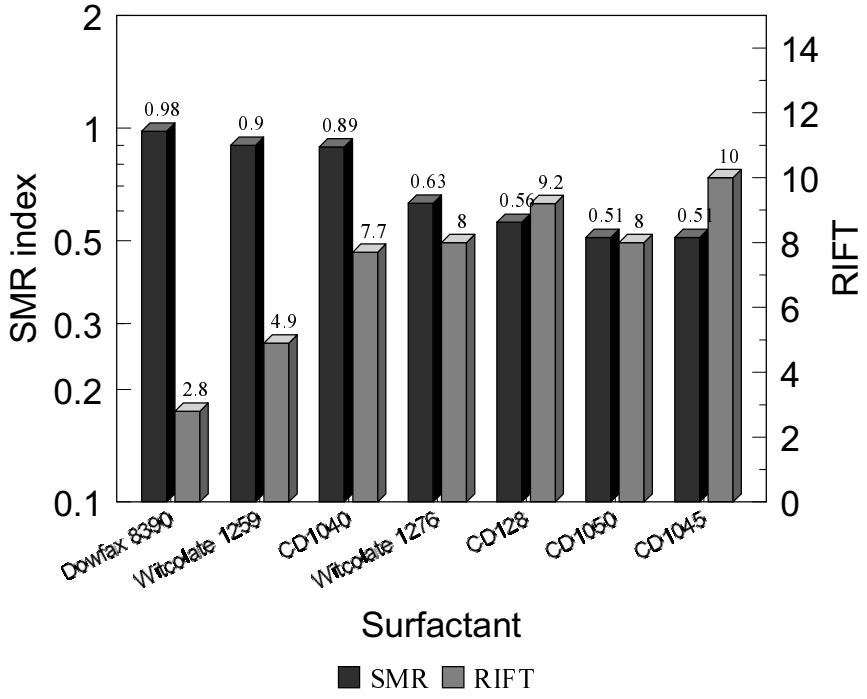

Fig. 28. Correlation between the SMR index and interfacial tension reduction factor.

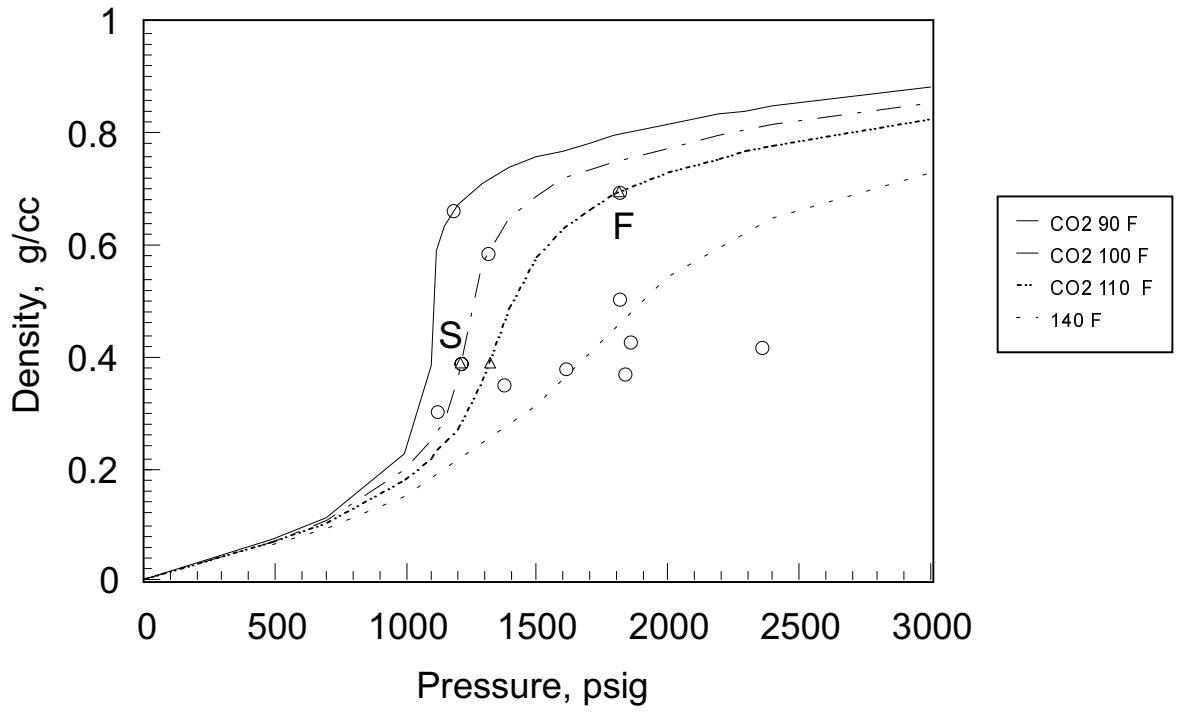

Fig. 29. CO_2 density versus pressure and temperature. The points indicate CO_2 density at a number of system MMPs.

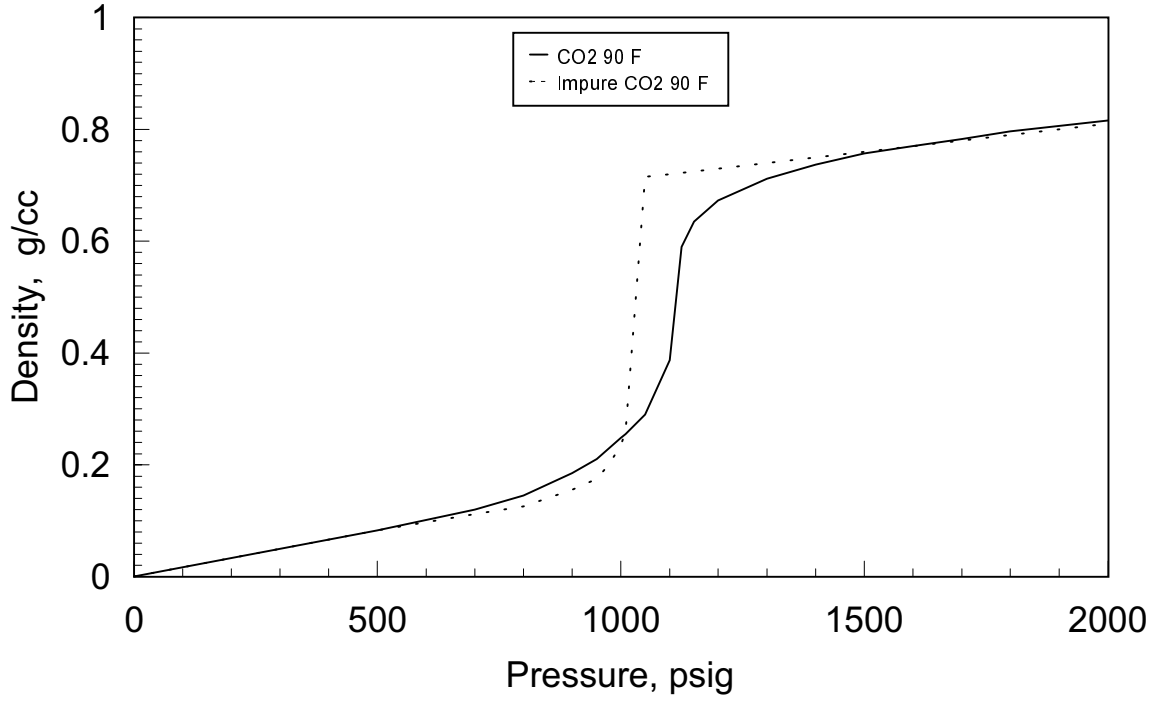

Fig. 30. CO_2 density versus temperature comparison for pure CO_2 and CO_2 with extracted hydrocarbon content.

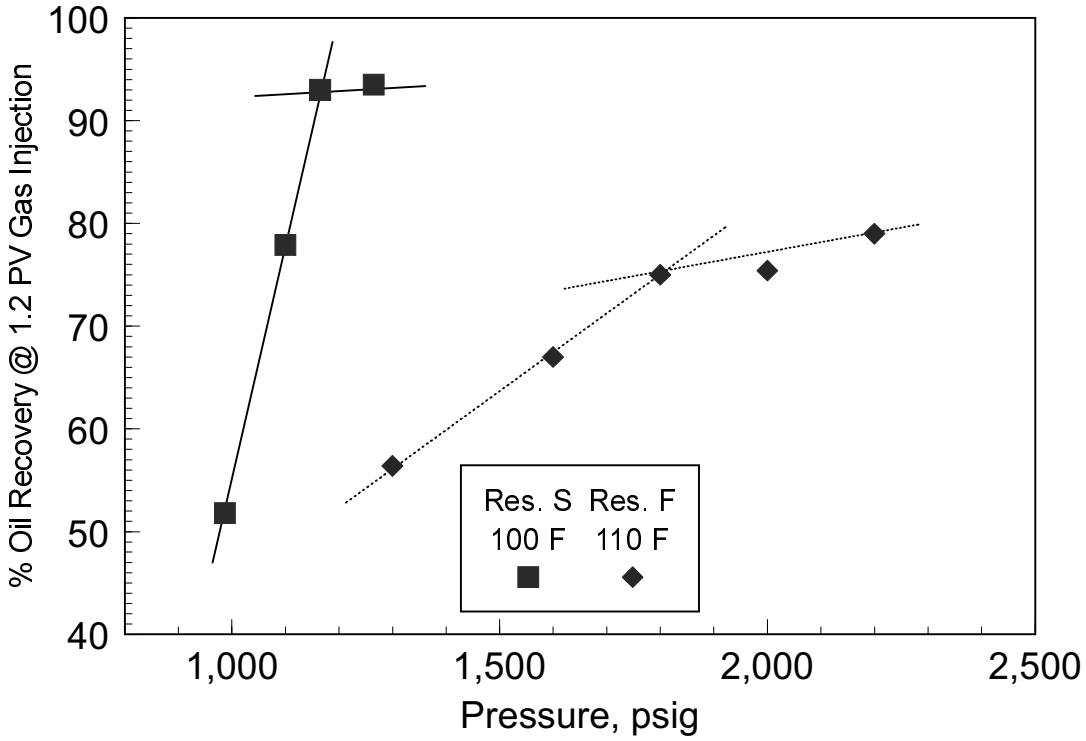

Fig. 31. Slim tube recovery versus pressure for reservoir oils S and F.[28]

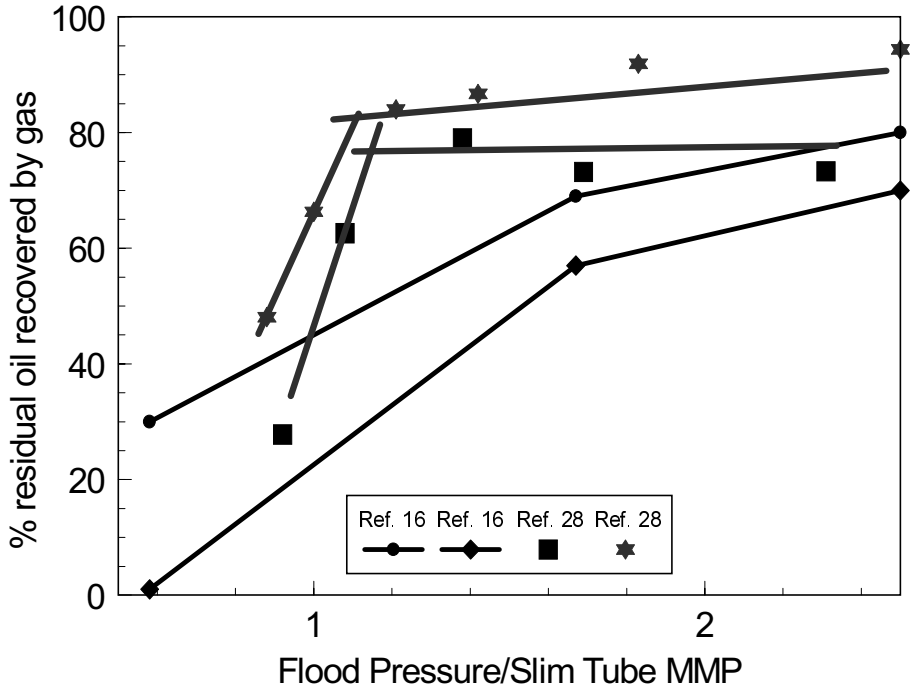

Fig. 32. Comparison of core-tertiary CO_2 floods from Refs. 16 and 28.

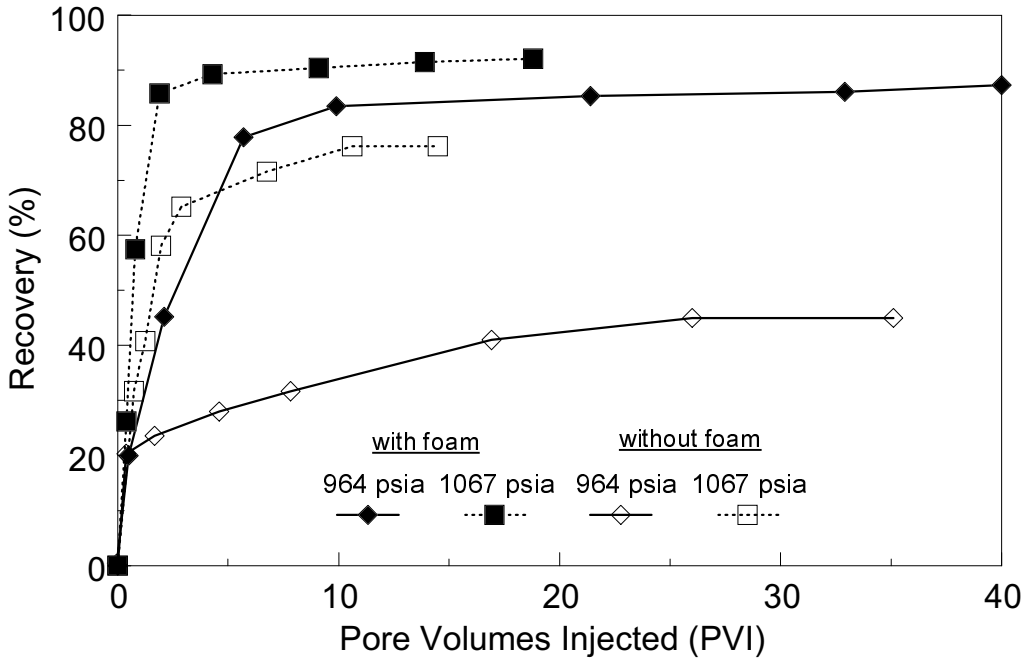

Fig. 33. Comparison of CO_2 floods in a visual micromodel with and without foam just above and below the MMP of about 1000 psig.

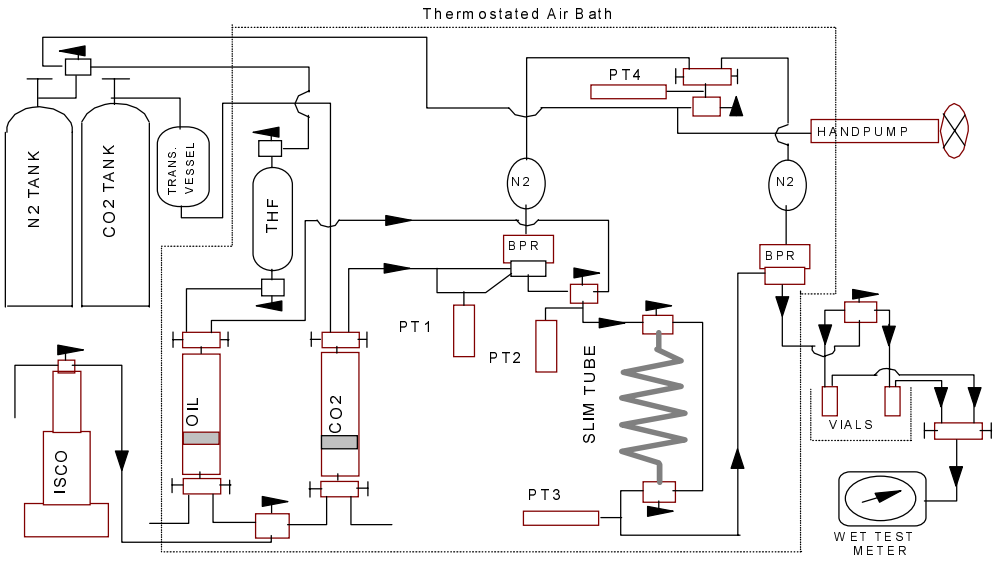

Fig. 34. Schematic diagram of the slim tube apparatus.

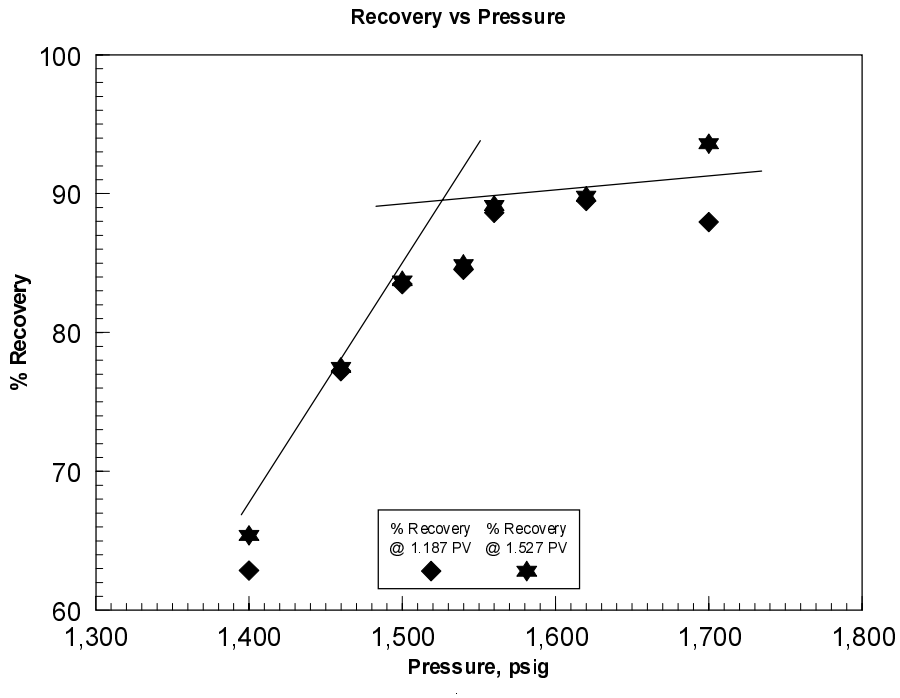

Fig. 35. Recovery vs pressure.

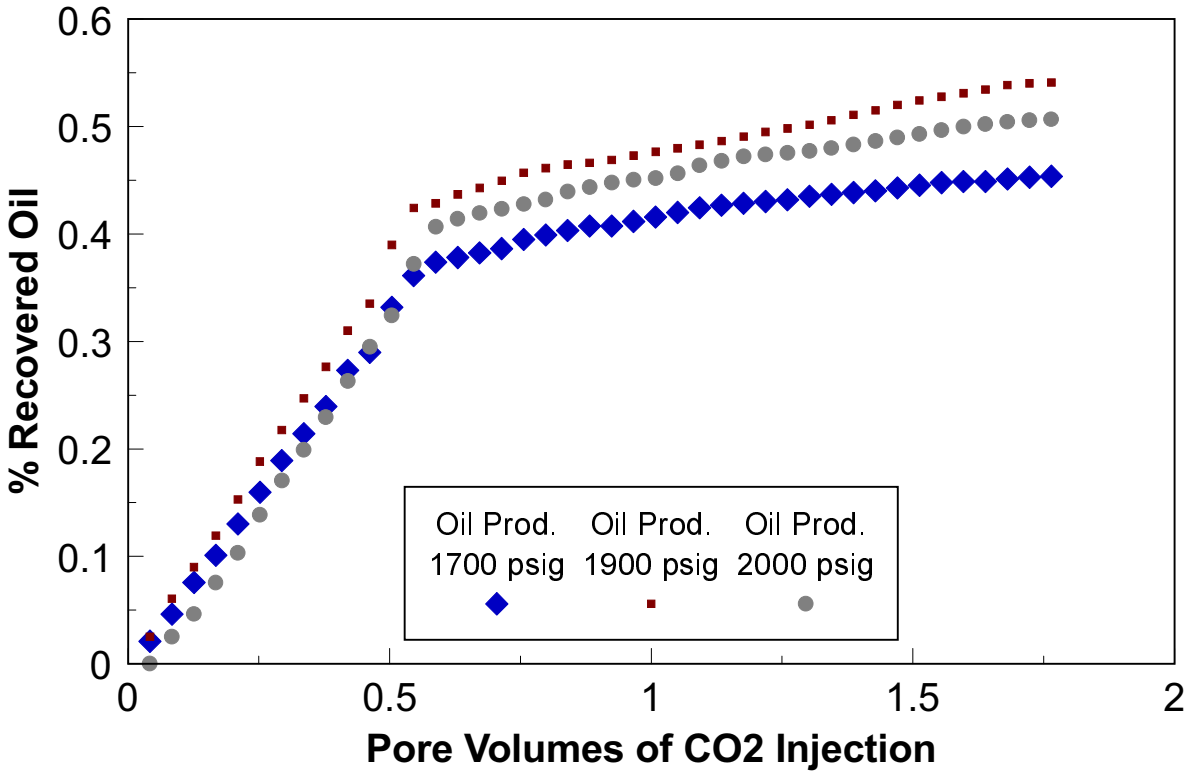

Fig. 36. Slim tube production comparisons vs pore volumes of CO_2 injected for three tests, 1700, 1900, and 2000 psig.

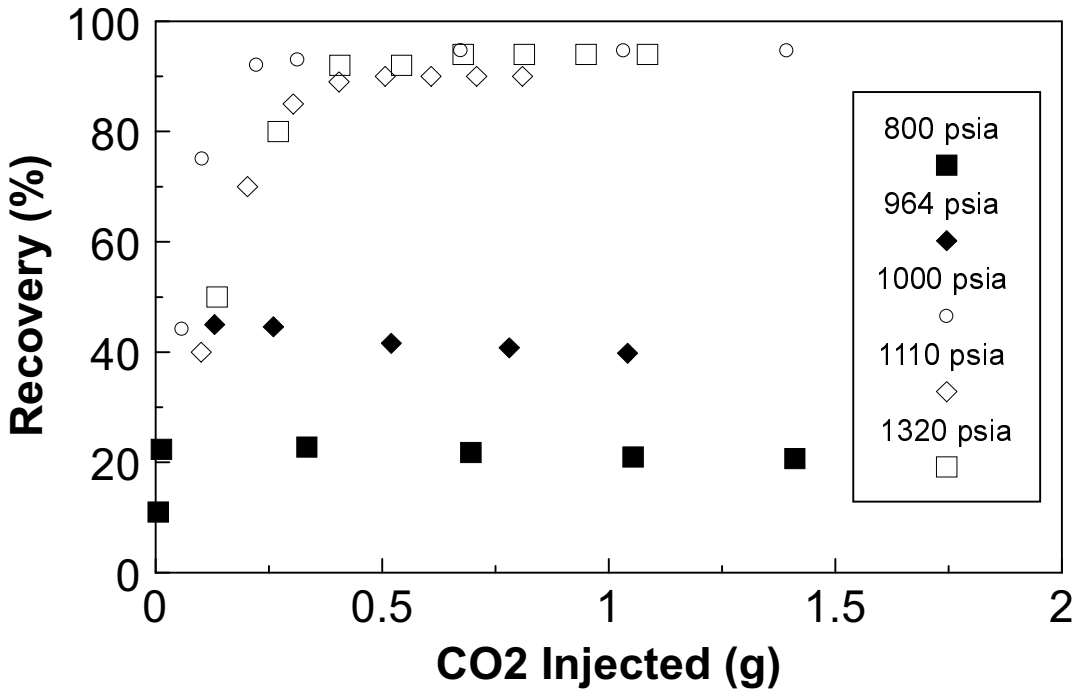

Fig. 37. Effect of pressure on sweep efficiency.

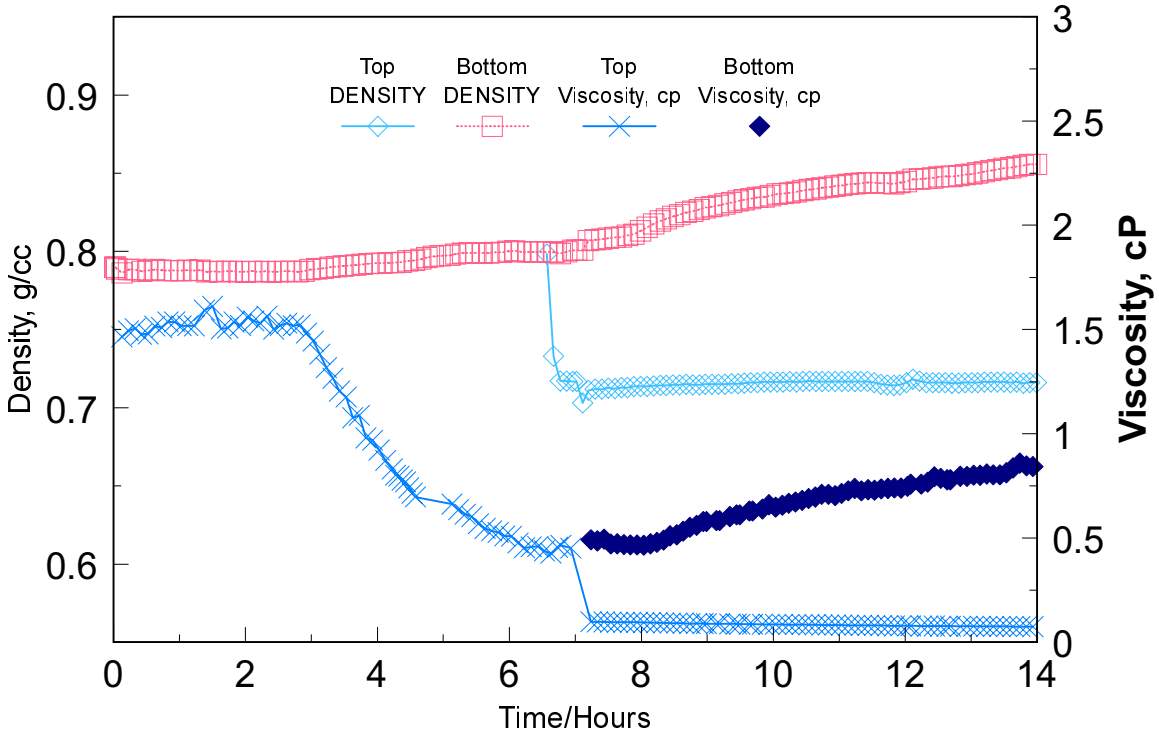

Fig. 38. Density and viscosity measurements versus time for both the top and bottom production. Spraberry recombined reservoir fluid with CO_2 at 2450 psig and 138°F.

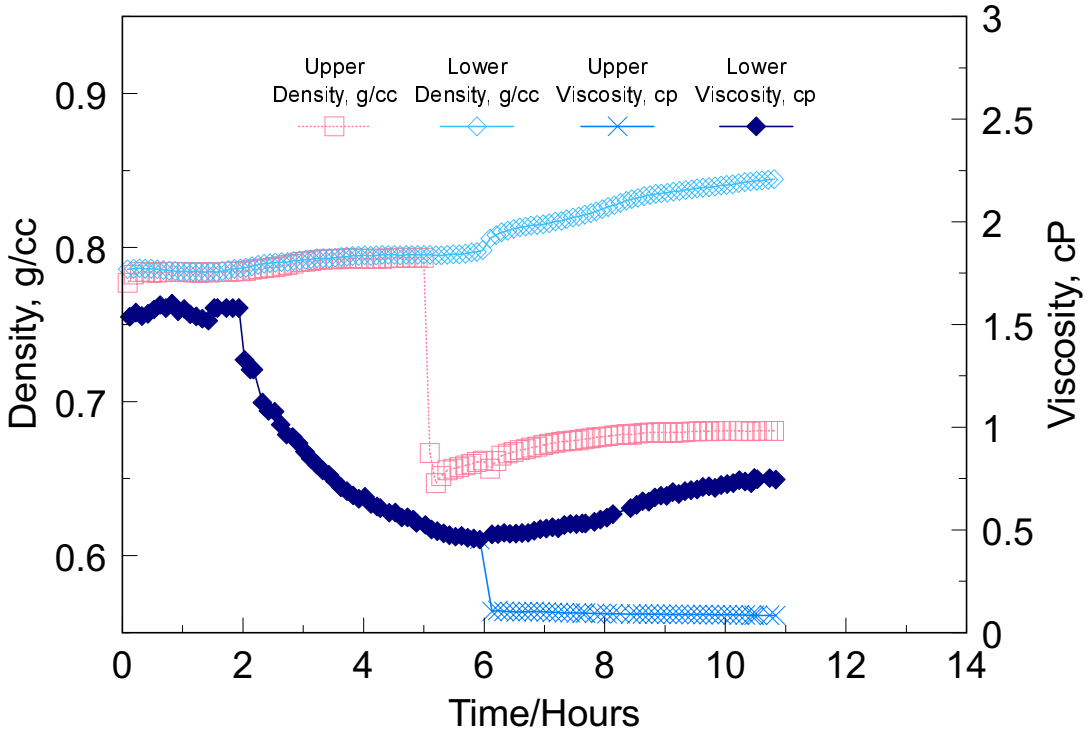

Fig. 39. Density and viscosity measurements versus time for both the top and bottom production. Spraberry recombined reservoir fluid with CO_2 at 2100 psig and 138°F.

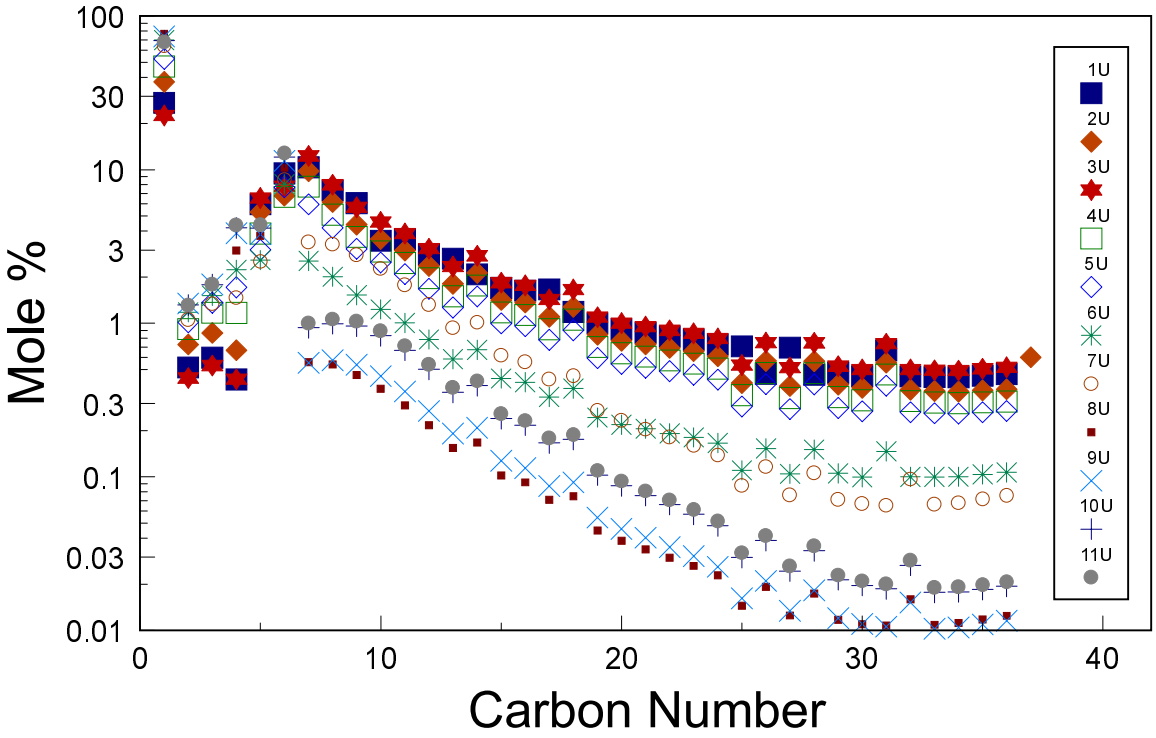

Fig. 40. Spraberry recombined reservoir oil: composition vs time in the CPE for the top production at 2100 psig and 138°F.

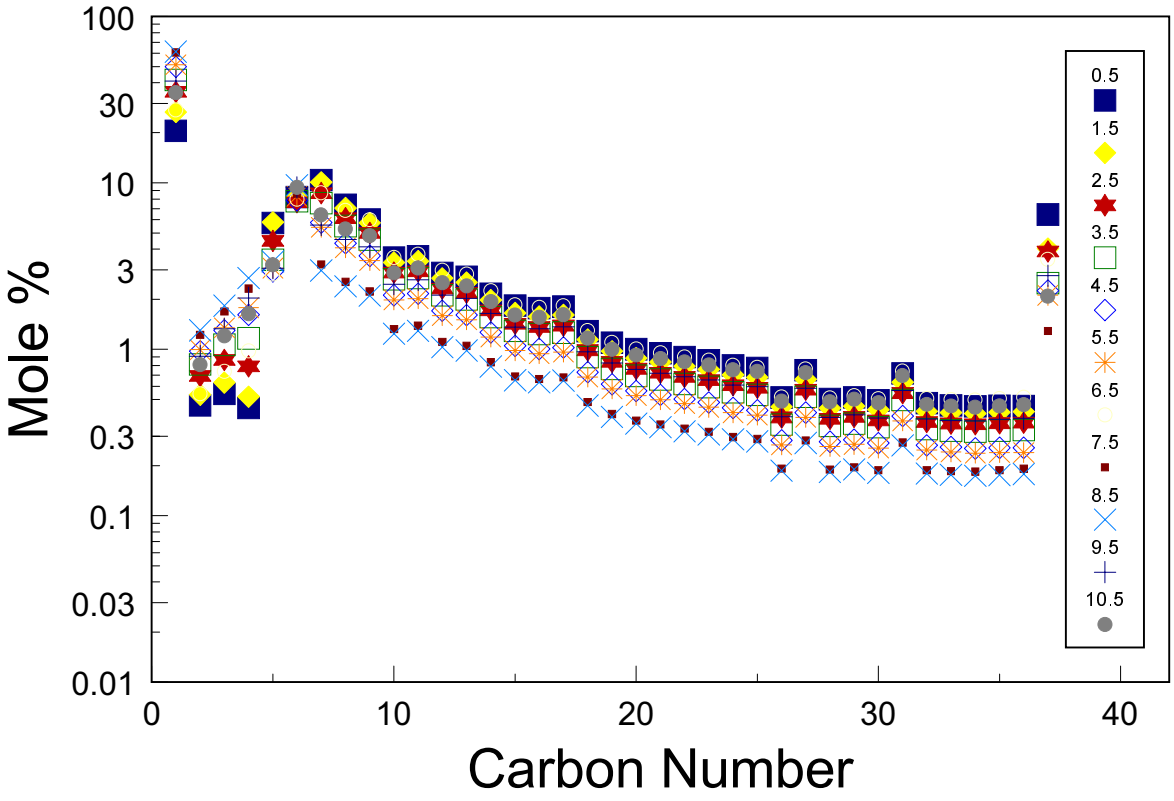

Fig. 41. Spraberry recombined reservoir oil: composition vs time in the CPE for the top production at 2100 psig and 138 °F.

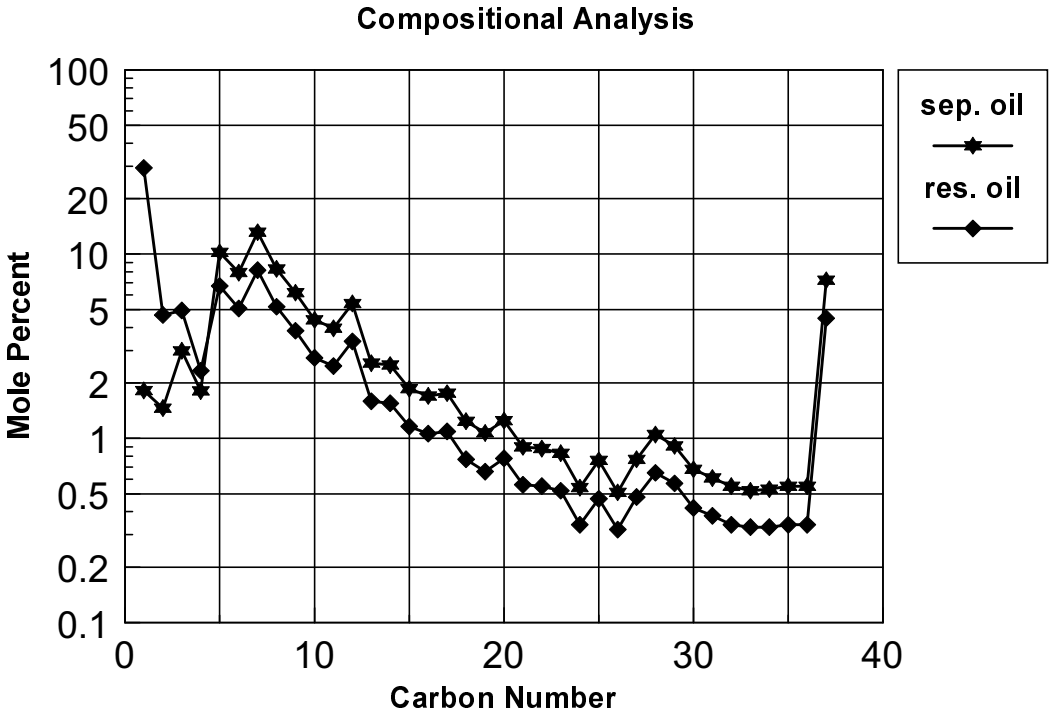

Fig. 42. Comparison of the compositions of the separator oil used in the slim tube tests and the recombined oil used in the swelling tests.

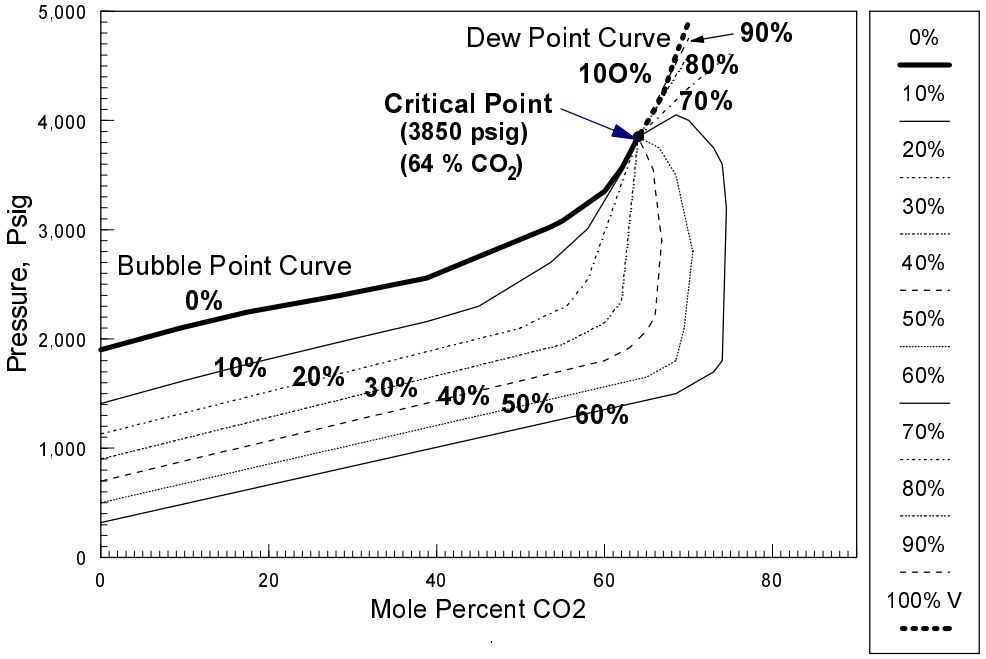

Fig. 43. CO_2-Spraberry recombined oil (1900 psig bubblepoint) Px diagrams with contant volume % vapor contour lines.

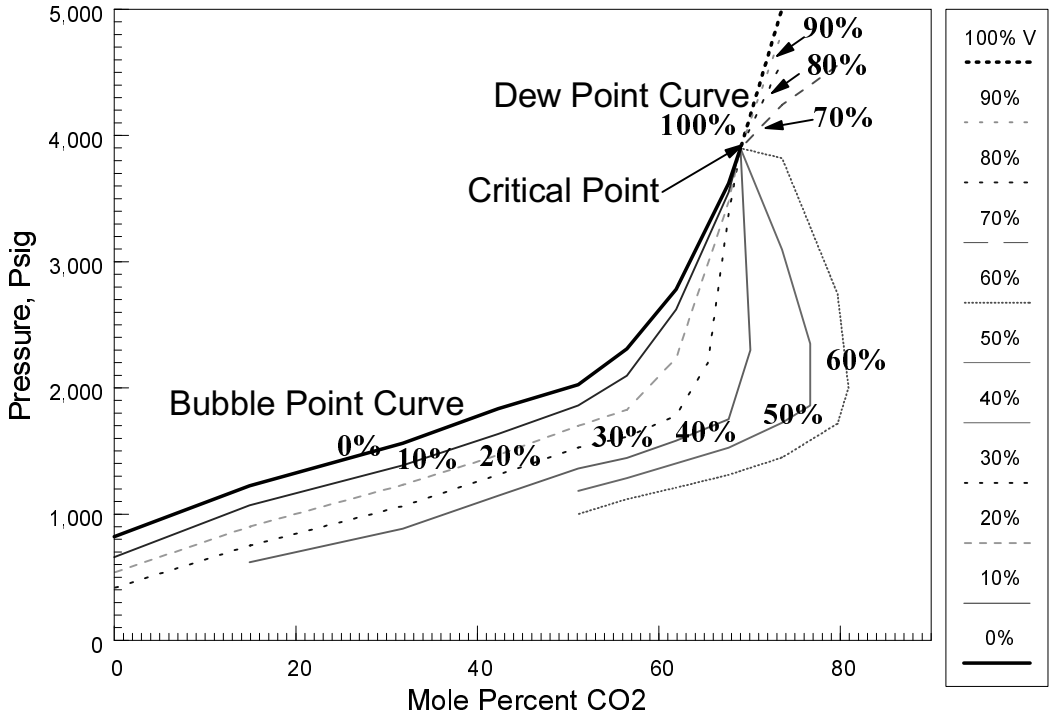

Fig. 44. CO_2-Spraberry recombined reservoir oil (800 psig bubblepoint) Px diagram with constant volume % vapor contour lines.

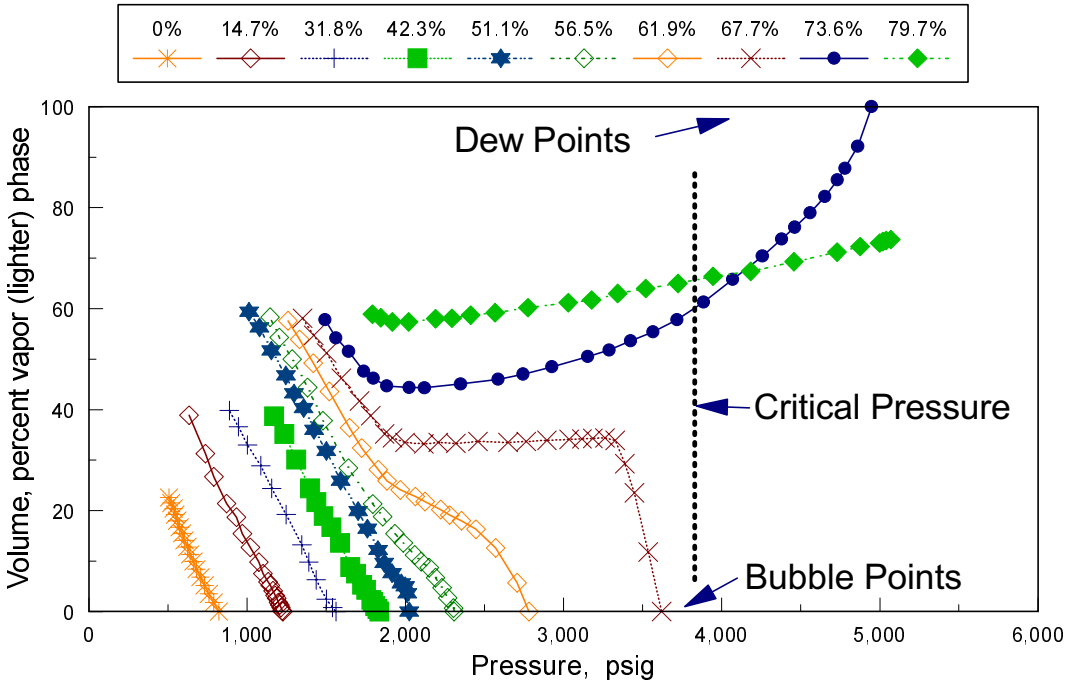

Fig. 45. Gas volume percent versus pressure for each CO_2 concentration with Spraberry recombined reservoir oil.

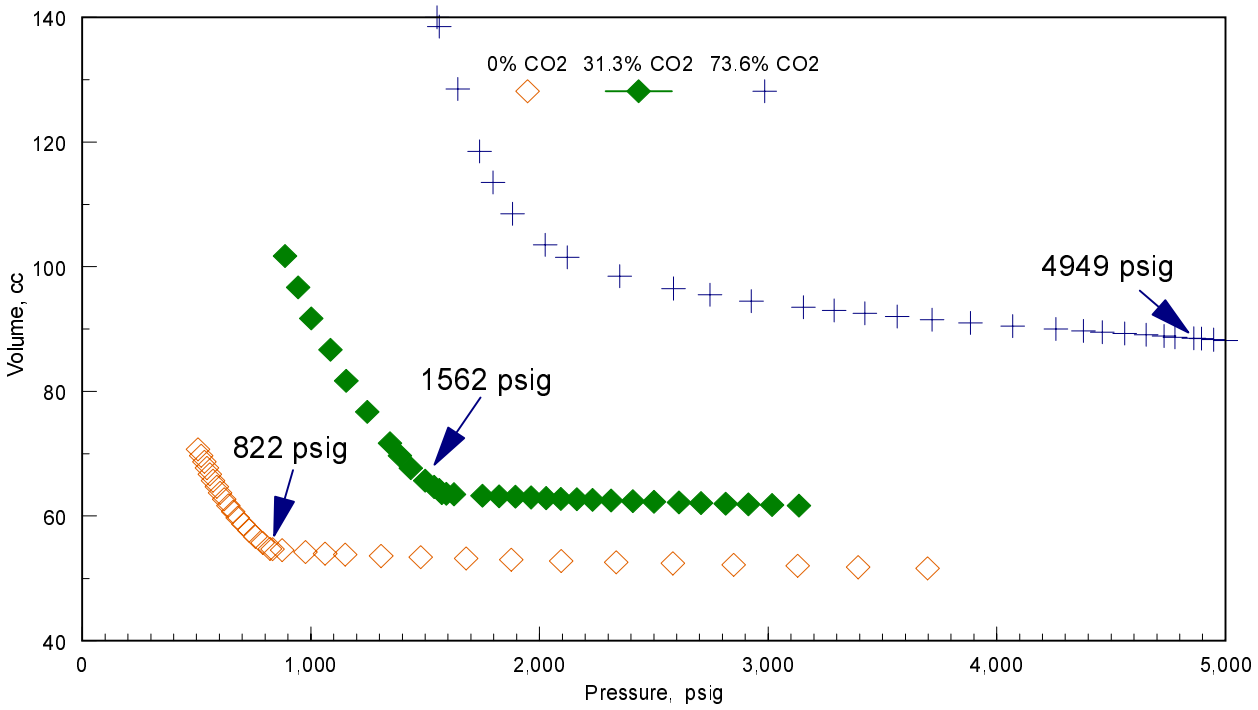

Fig. 46. PV (pressure-volume) curves from three Spraberry recombined reservoir oil with added CO_2.

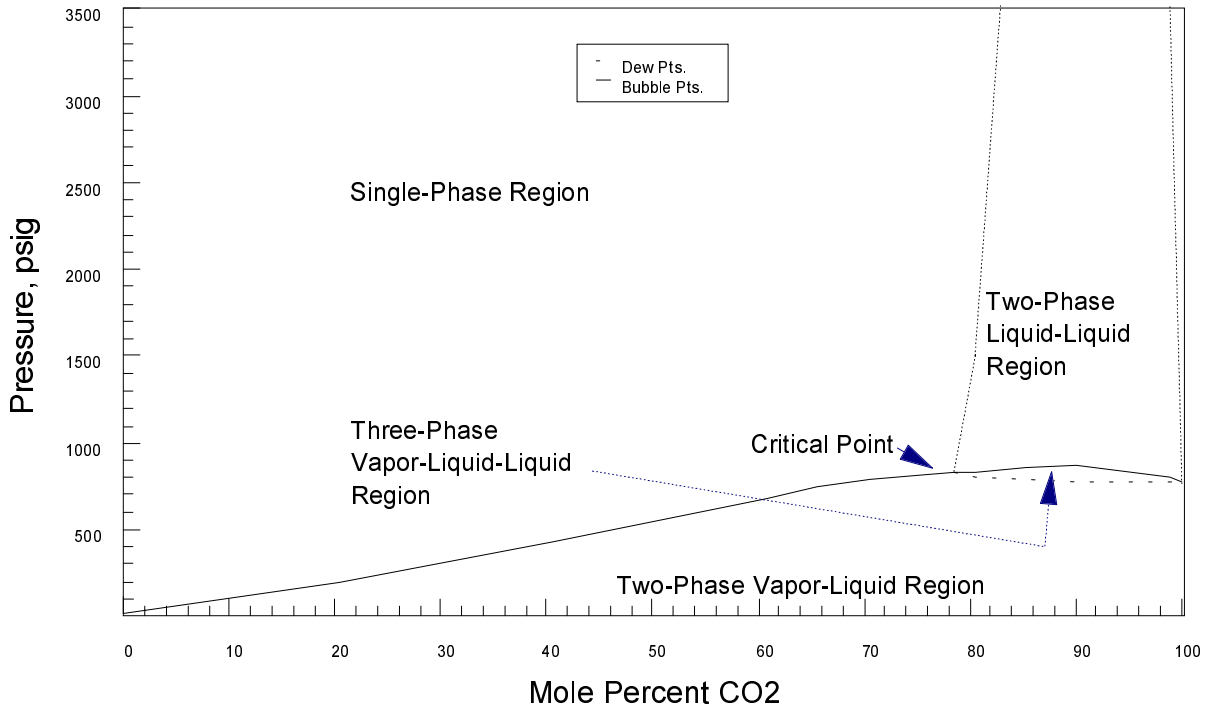

Fig. 47. Sulimar Queen phase behavior diagram using separator oil and CO_2.

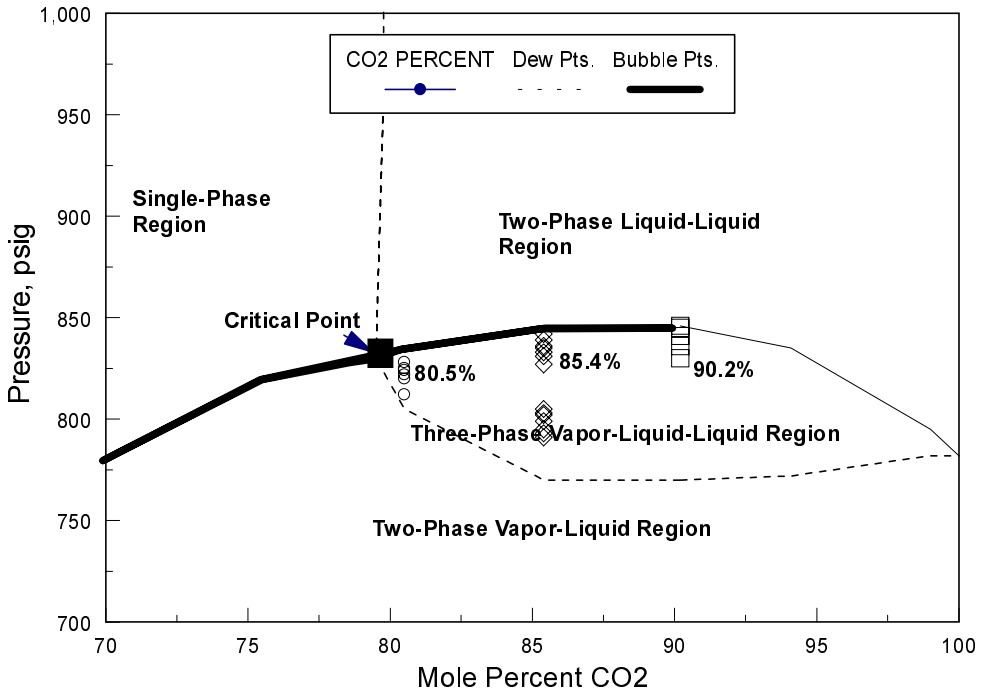

Fig. 48. Sulimar Queen phase behavior diagram expanded in the three-phase region for separator oil and CO_2.

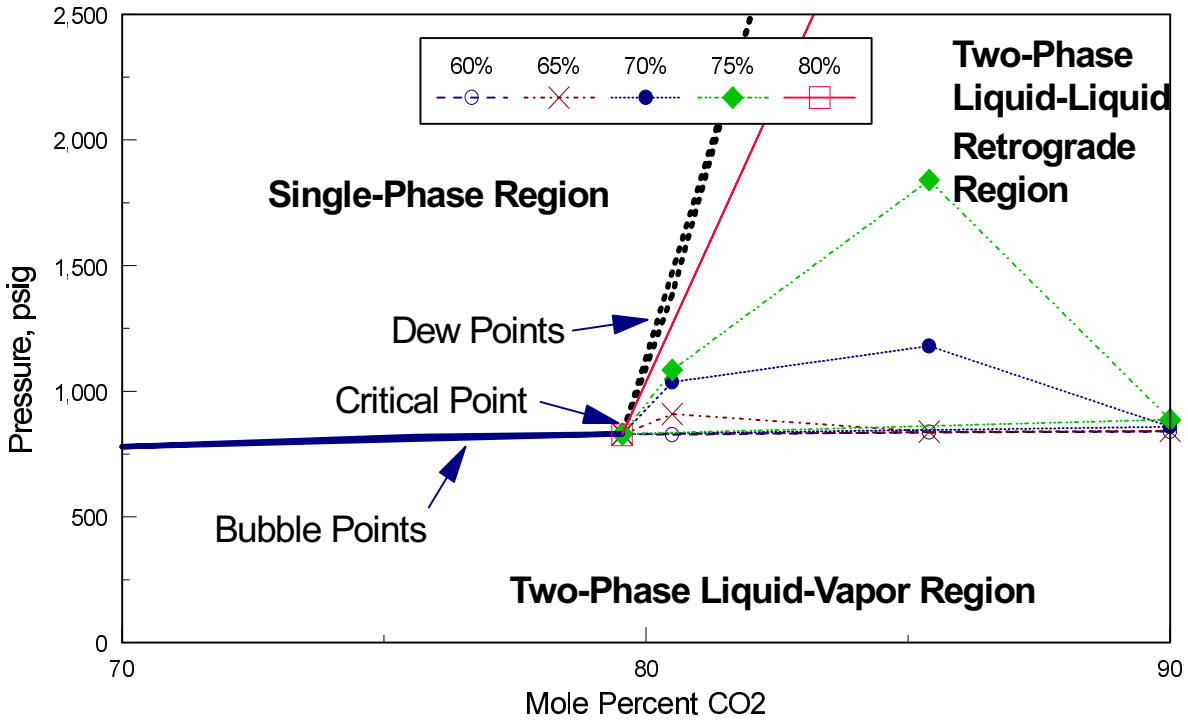

Fig. 49. Sulimar Queen Phase Diagram expanded in the liquid-liquid region. Constant upper phase contours shown.

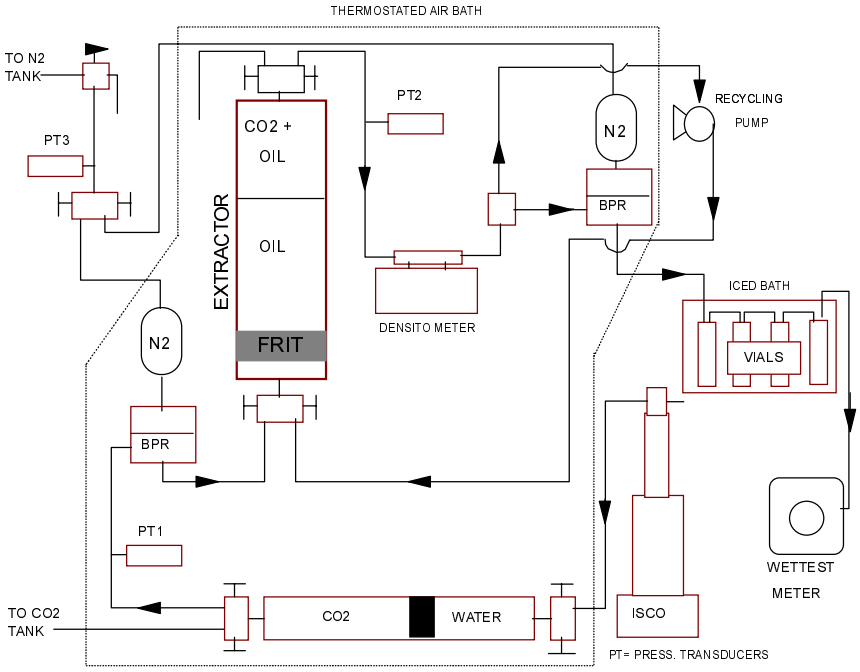

Fig. 50. Schematic diagram of the extraction apparatus.

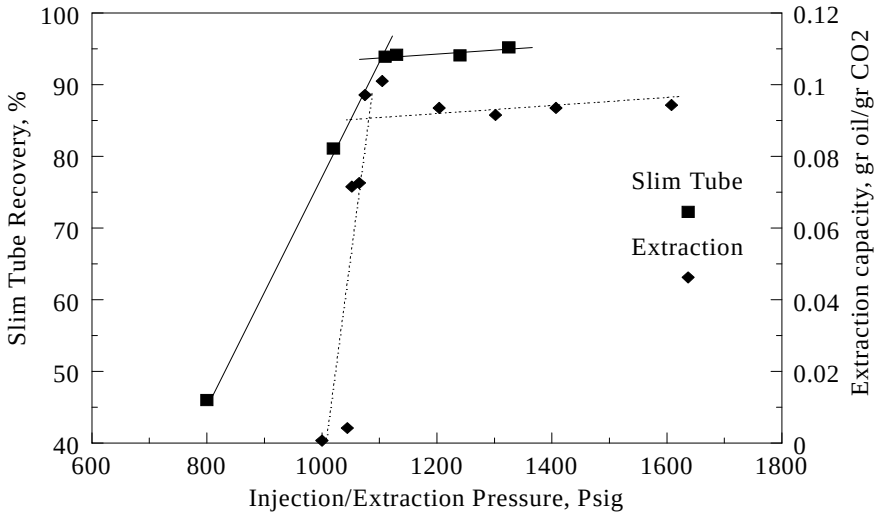

Fig. 51. Extraction capacity and slim tube recovery as a function of pressure for Sulimar Queen oil at 95ºF.

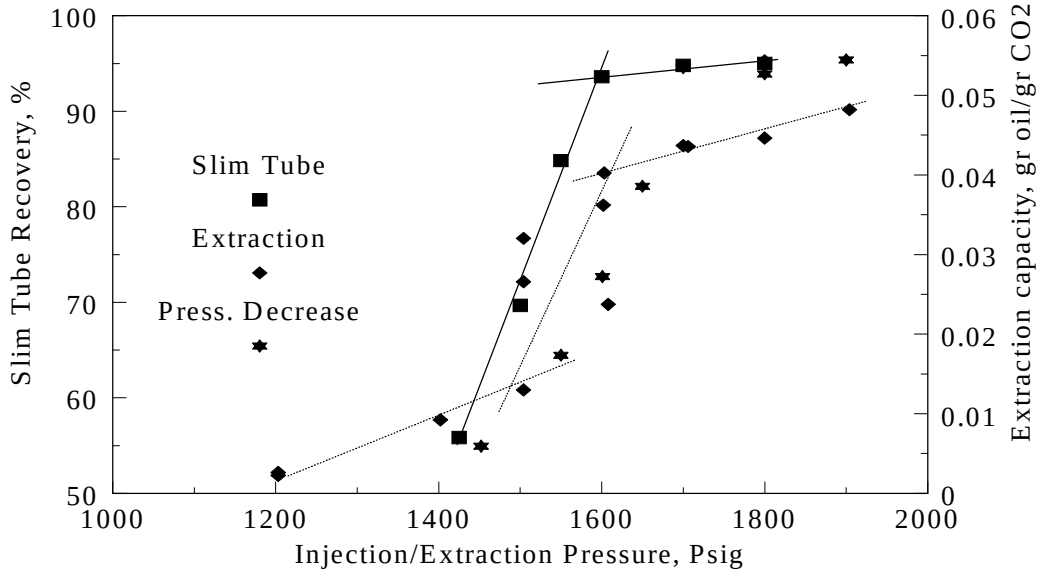

Fig. 52. Extraction capacity and slim tube recovery as a function of pressure for Sulimar Queen oil 138°F.

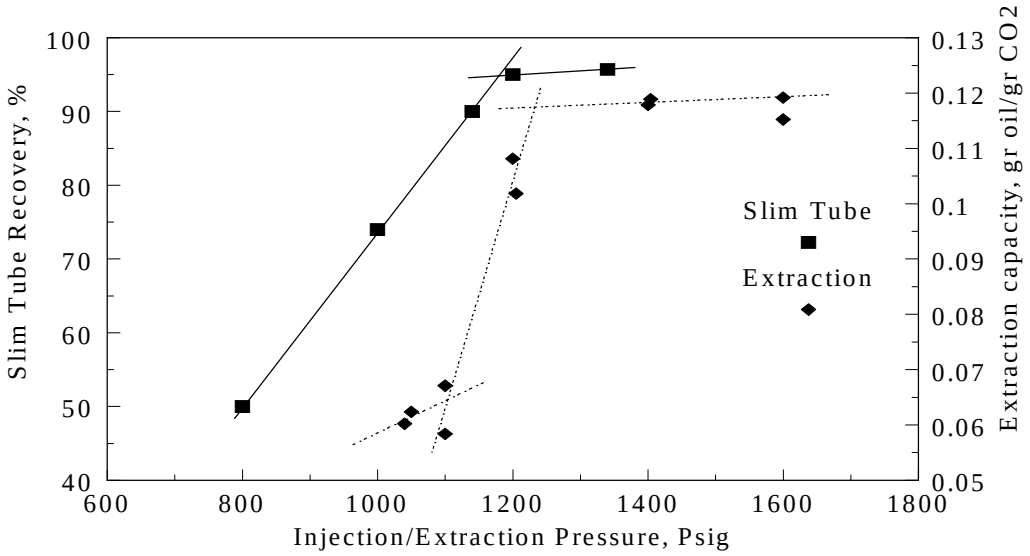

Fig. 53. Extraction capacity and slim tube recovery as a function of pressure for Spraberry oil at 95°F.

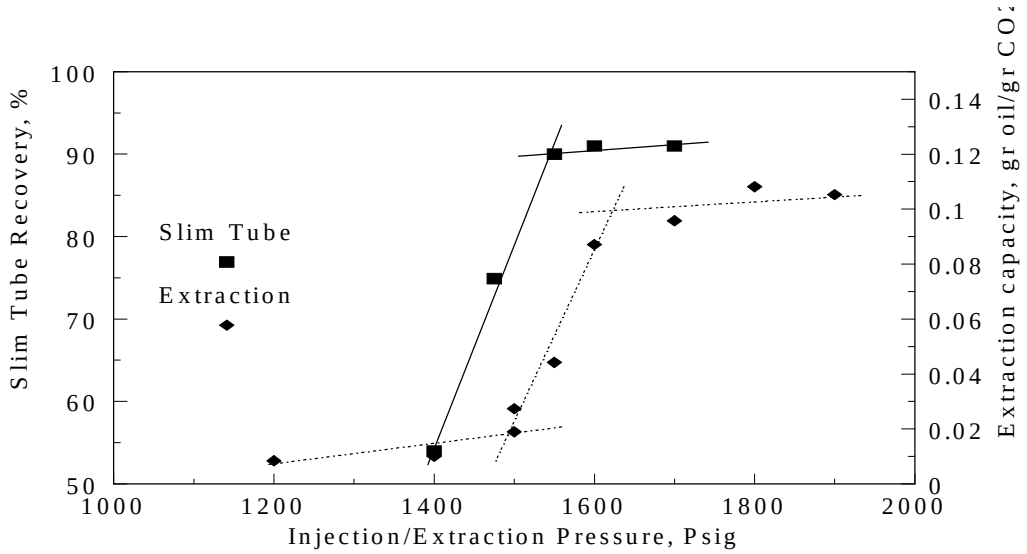

Fig. 54. Extraction capacity and slim tube recovery as a function of pressure for Spraberry oil at 138 °F

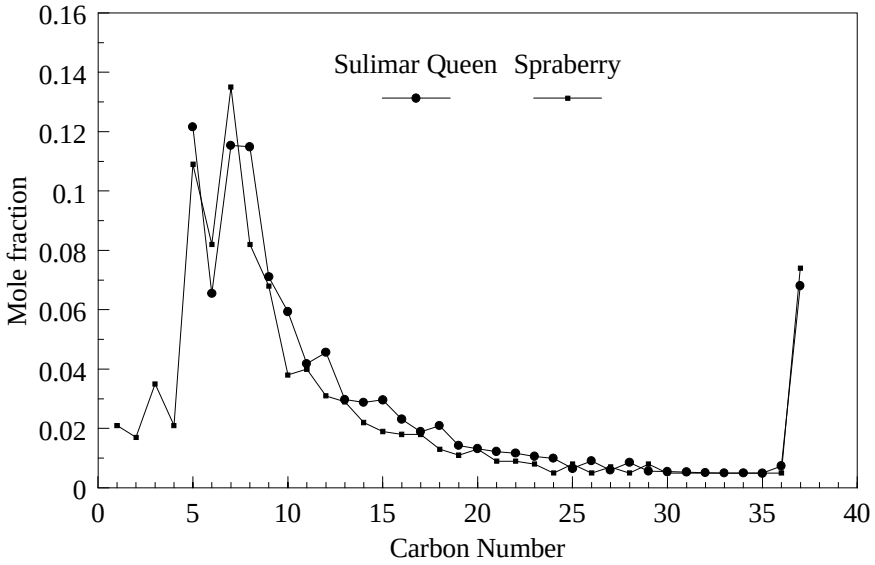

Fig. 55. Composition of Sulimar Queen and Spraberry oils.

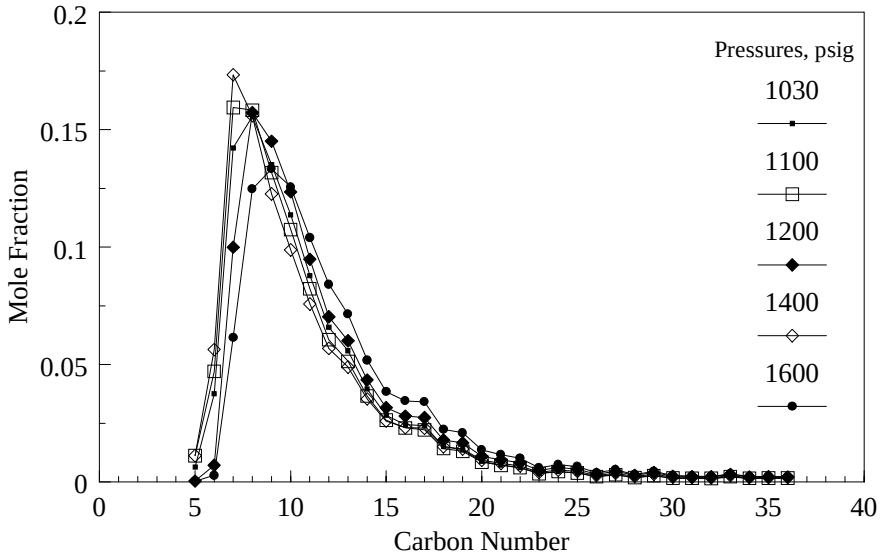

Fig. 56. Compositions of produced oils at different extraction pressure for Spraberry oil at 95°F.

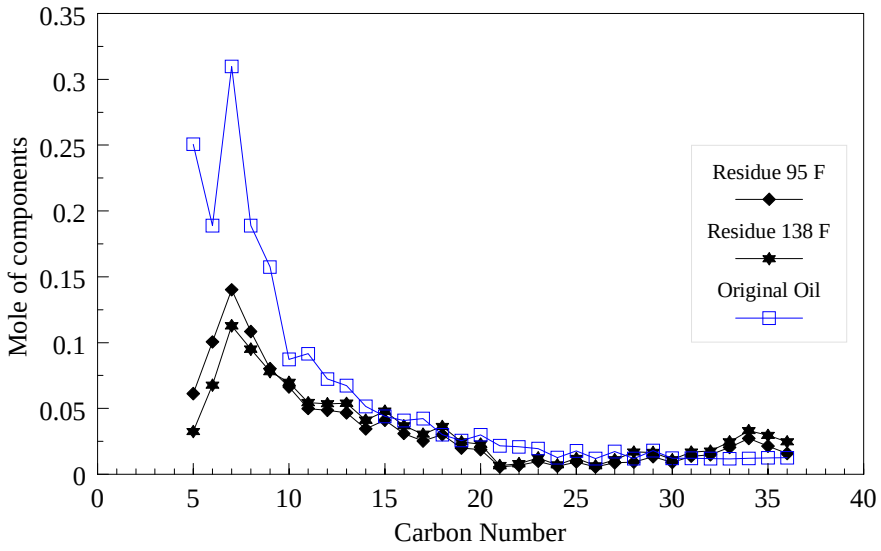

Fig. 57. Moles of original oil and extraction residues for Spraberry oil at 95°F and 138°F.

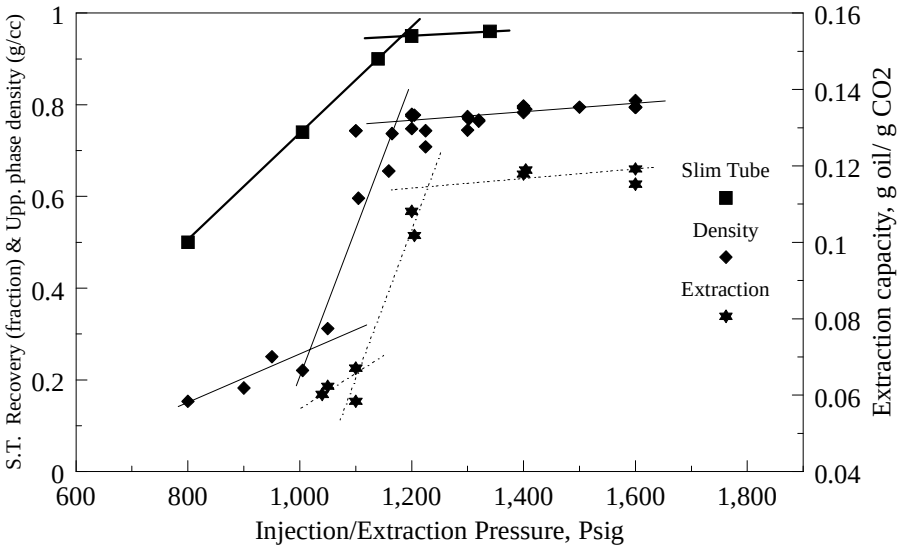

Fig. 58. Upper phase density, slim tube recovery and extraction capacity as a function of pressure for Spraberry Oil at 95°F.

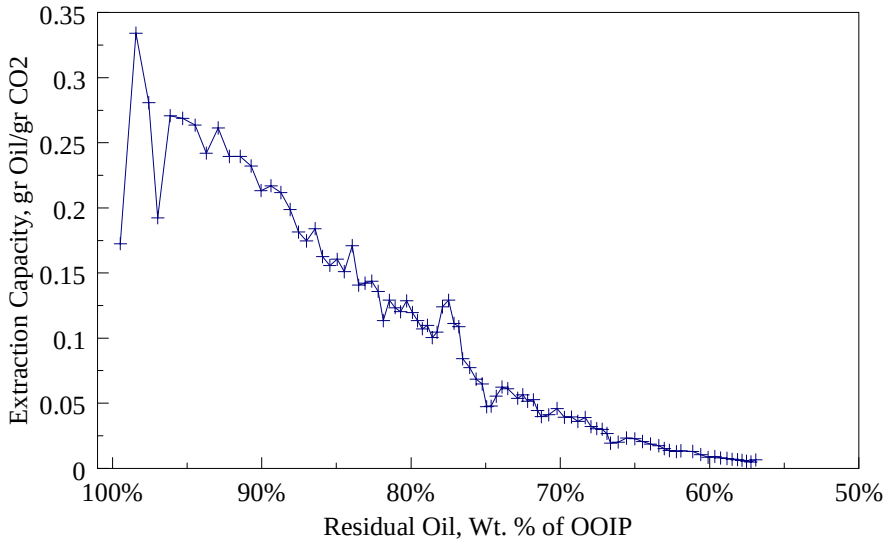

Fig. 59. Extraction capacity as a function of extraction stage for the extended extraction experiment.

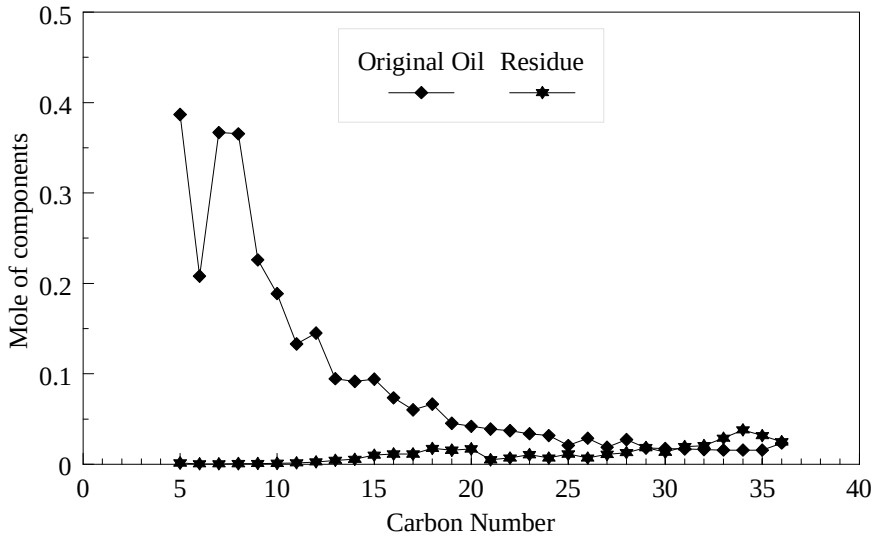

Fig. 60. Mole balance between original oil and extraction residue for the extended extraction experiment.

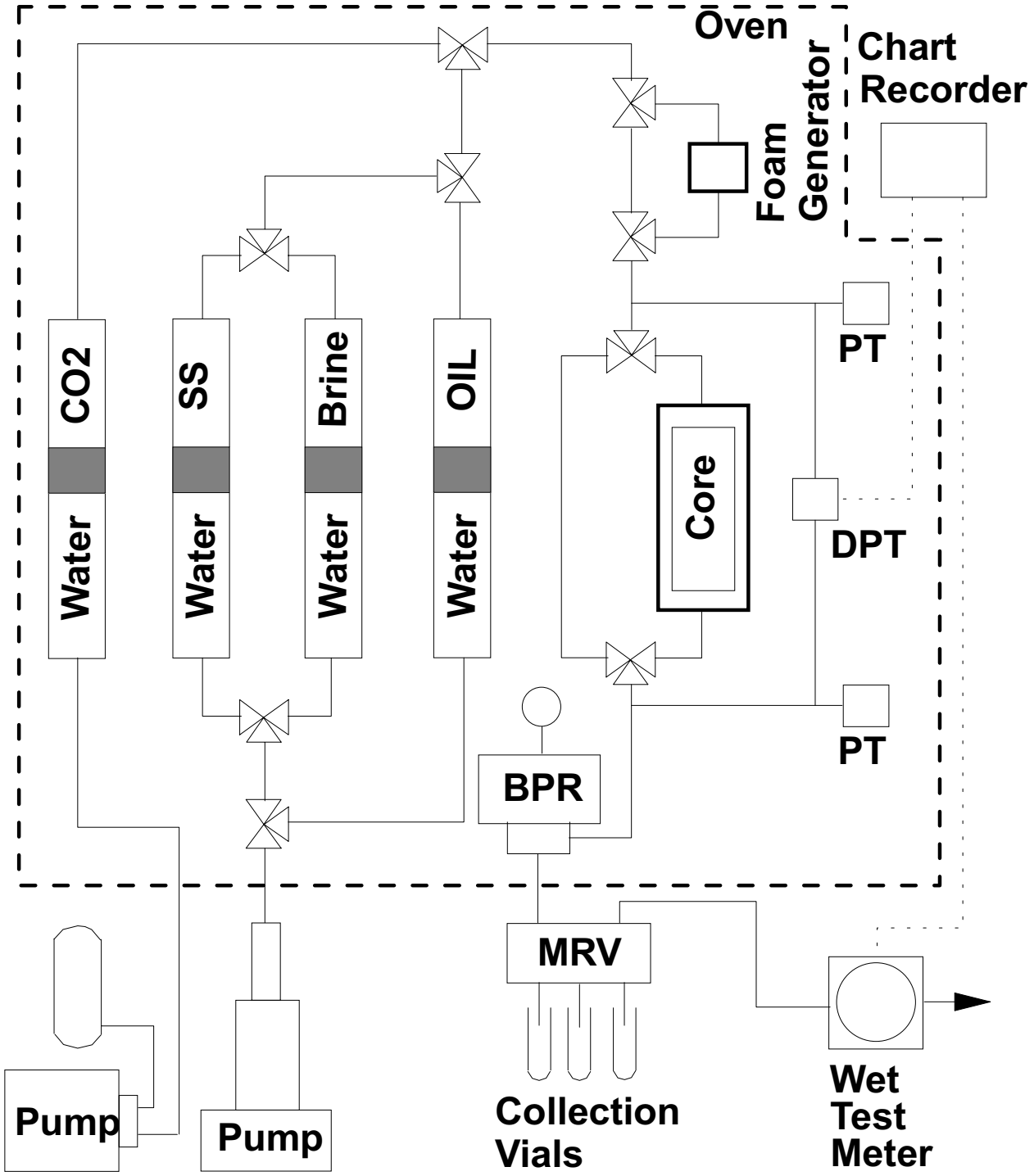

Fig. 61. Schematic of the coreflood test apparatus.

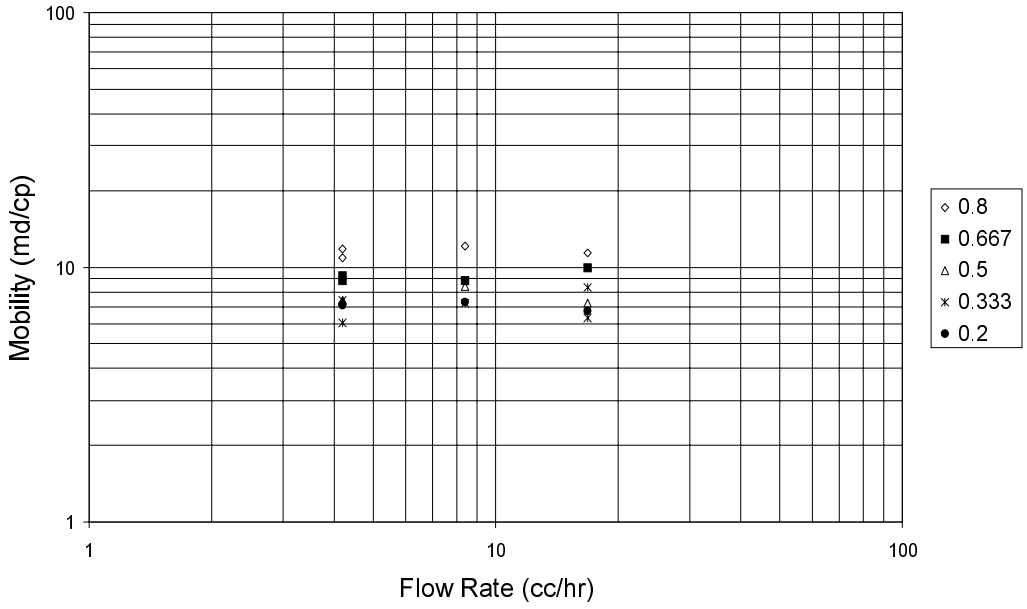

Fig. 62. Total mobility of CO_2/brine versus total flow rate for CO_2 fractions of 0.8, 0.667, 0.5, 0.333, and 0.2 (Core A).

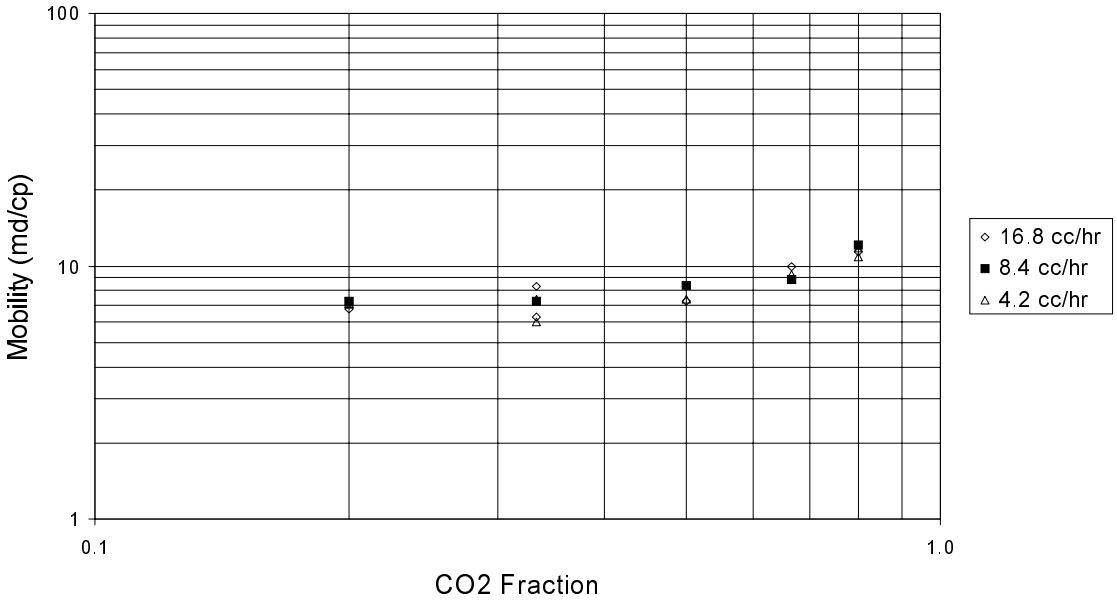

Fig. 63. Total mobility of CO_2/brine versus CO_2 fraction for total flow rates of 16.8, 8.4, and 4.2 cc/hr (Core A).

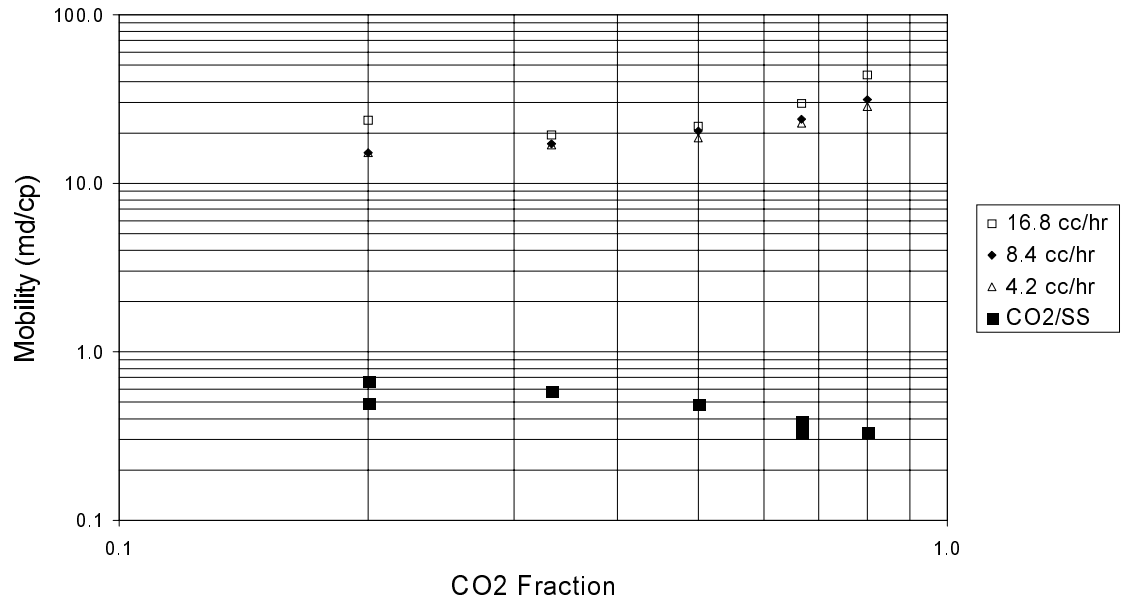

Fig. 64. Total mobility of CO_2/brine versus CO_2 fraction for total flow rates of 16.8, 8.4, and 4.2 cc/hr (Core B).

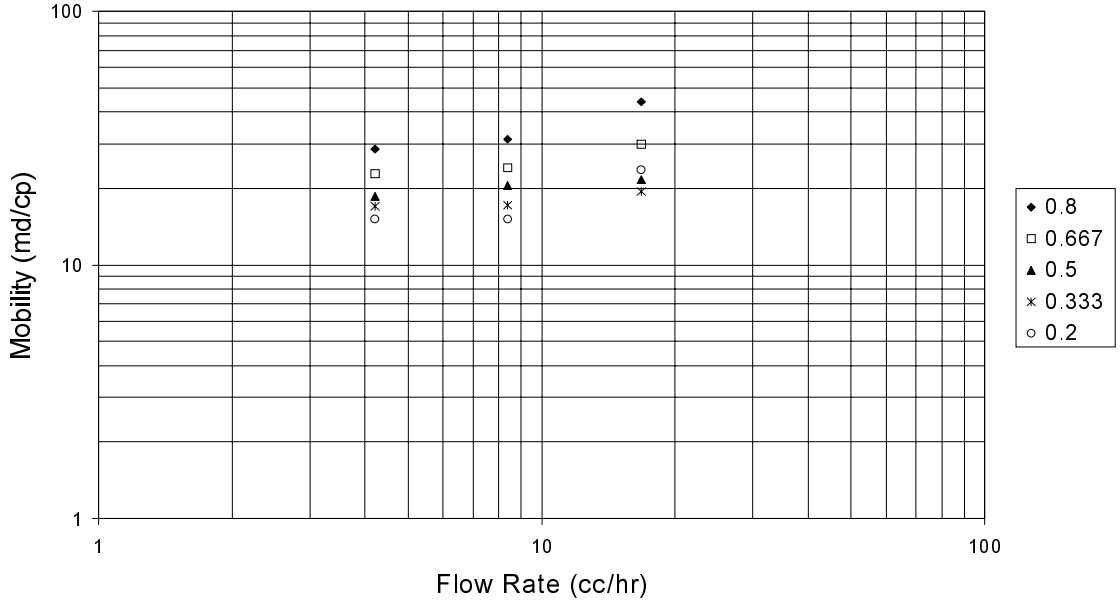

Fig. 65. Total mobility of CO_2/brine versus total flow rate for CO_2 fractions of 0.8, 0.667, 0.5, 0.333, and 0.2 (Core B).

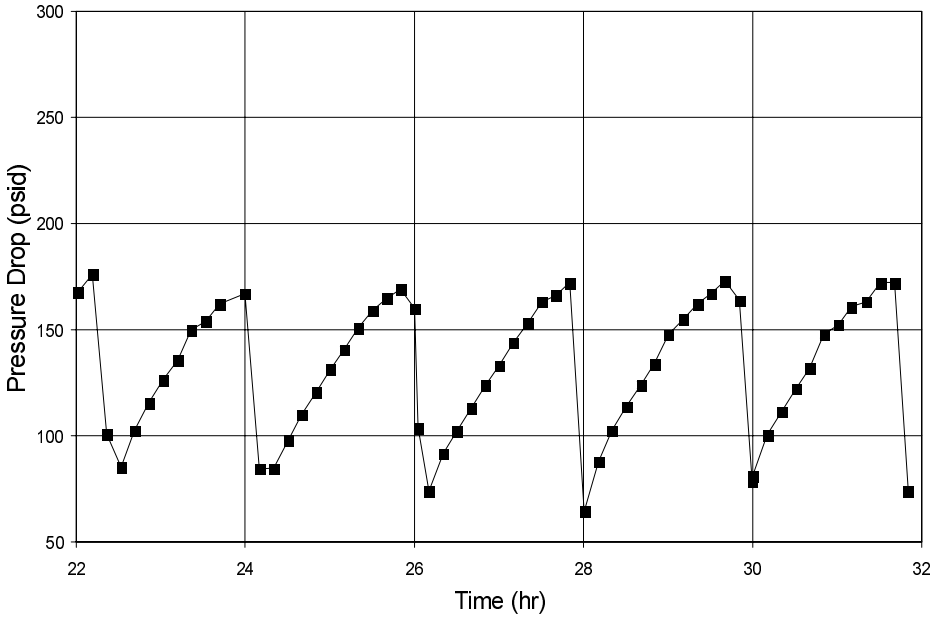

Fig. 66. Pressure drop response of the foam experiment with 20% foam quality.

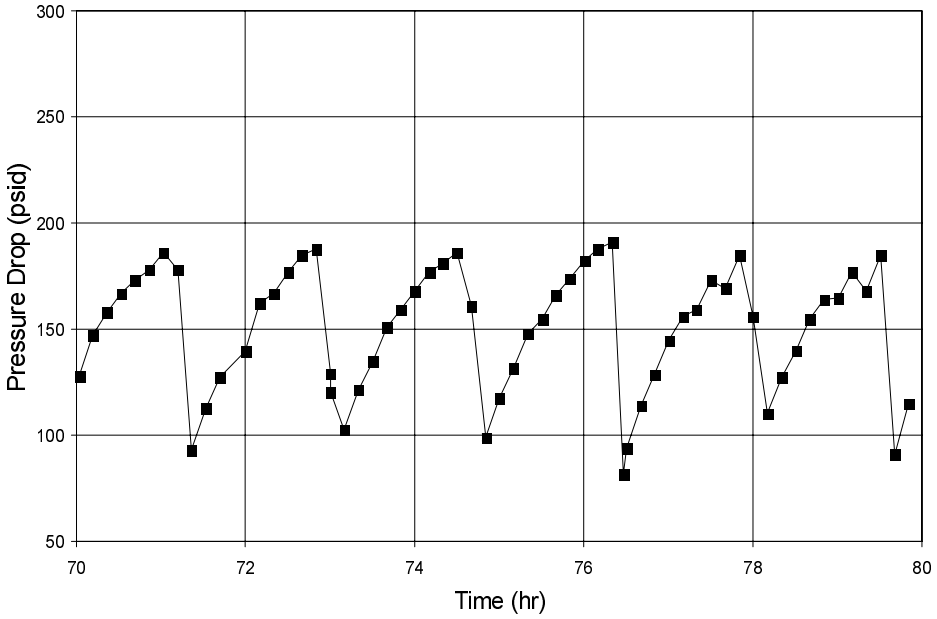

Fig. 67. Pressure drop response of the foam experiment with 33.3% foam quality.

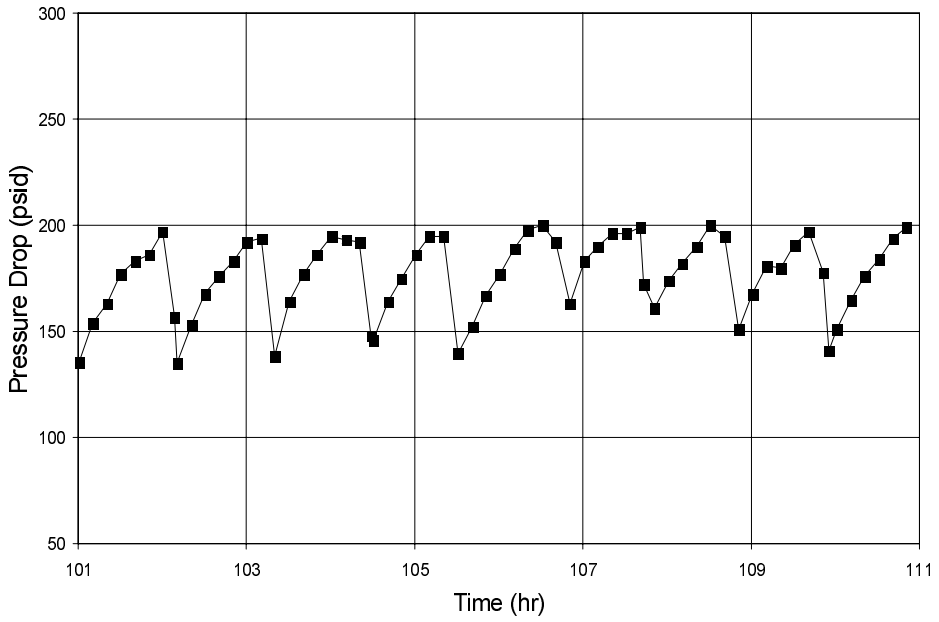

Fig. 68. Pressure drop response of the foam experiment with 50% foam quality.

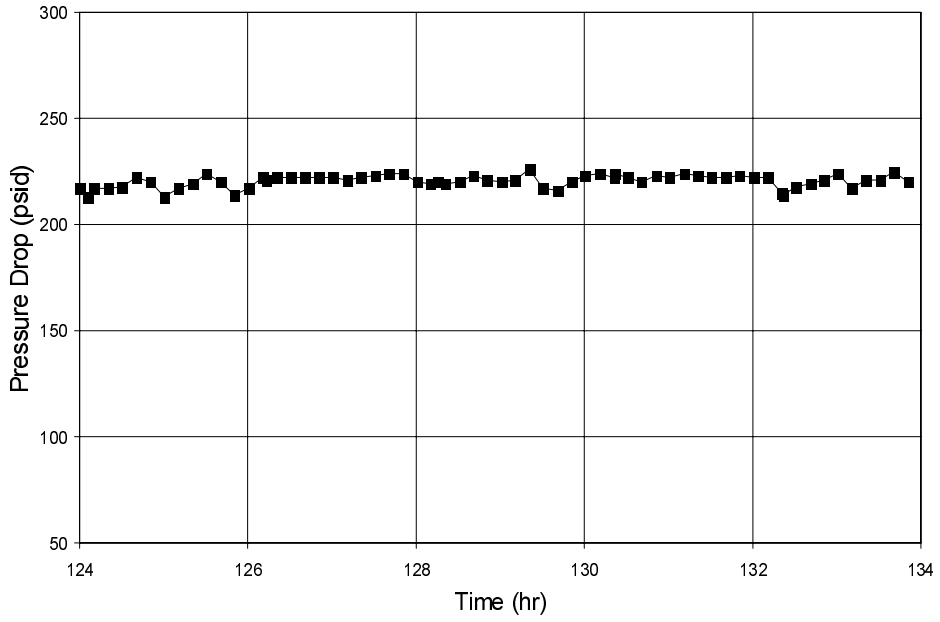

Fig. 69. Pressure drop response of the foam experiment with 66.7% foam quality.

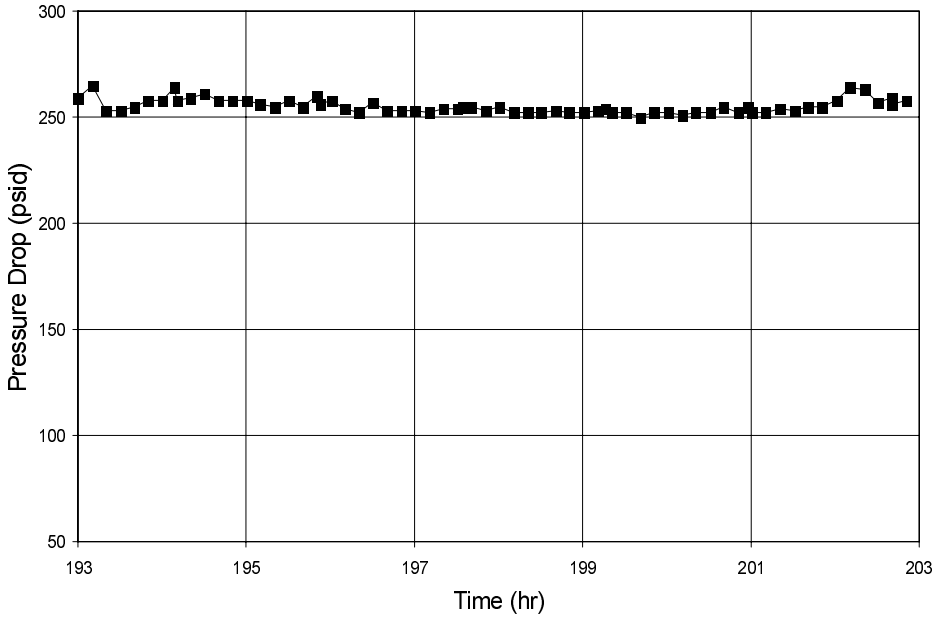

Fig. 70. Pressure drop response of the foam experiment with 80% foam quality.

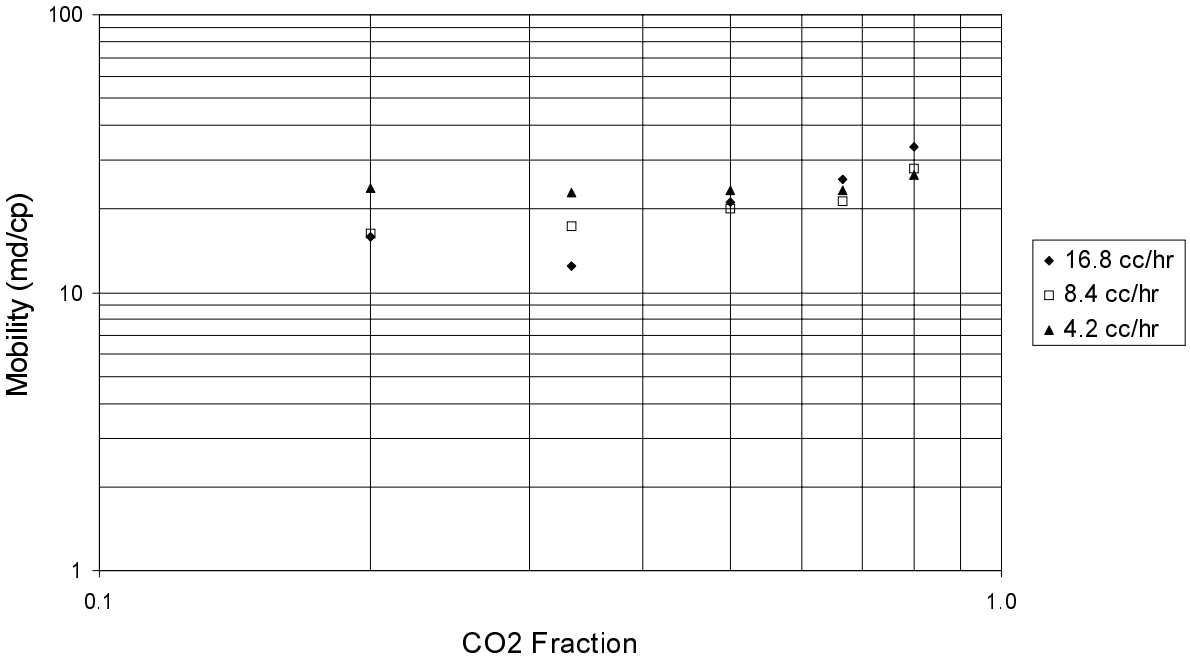

Fig. 71. Total mobility of CO_2/brine versus CO_2 fraction for total flow rates of 16.8, 8.4, and 4.2 cc/hr (Core C).

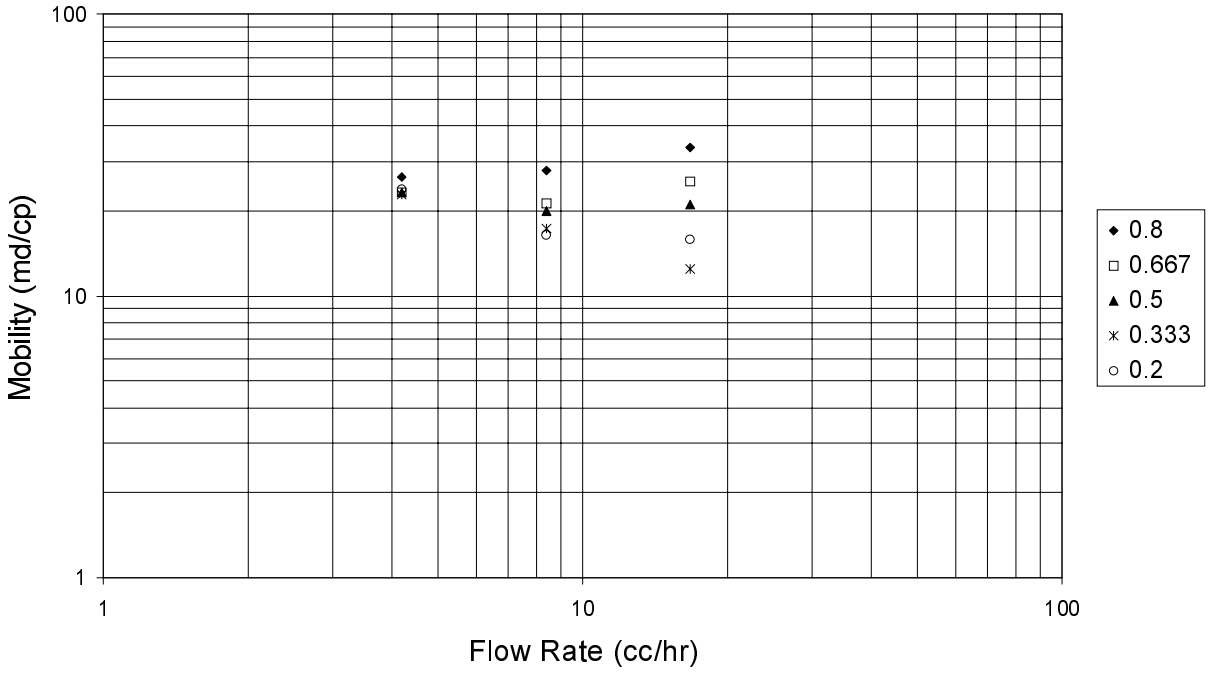

Fig. 72. Total mobility of CO_2/brine versus total flow rate for CO_2 fractions of 0.8, 0.667, 0.5, 0.333, and 0.2 (Core C).

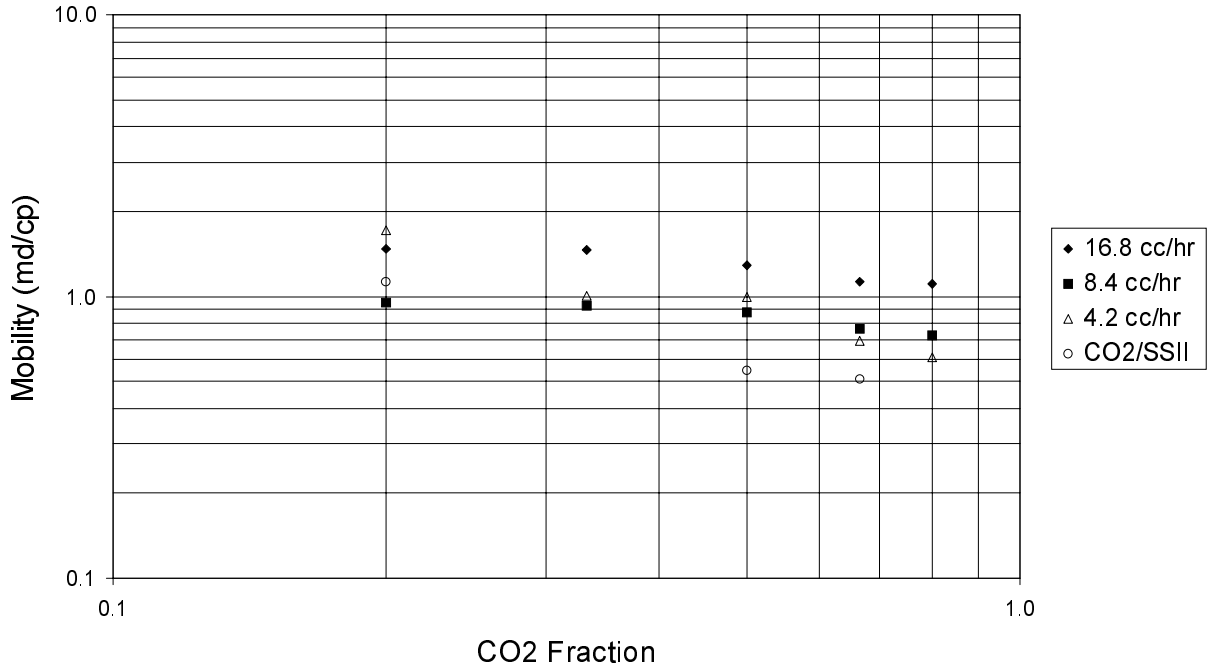

Fig. 73. Total mobility of CO_2/surfactant solution versus CO_2 fraction for total flow rates of 16.8, 8.4, and 4.2 cc/hr (Core C).

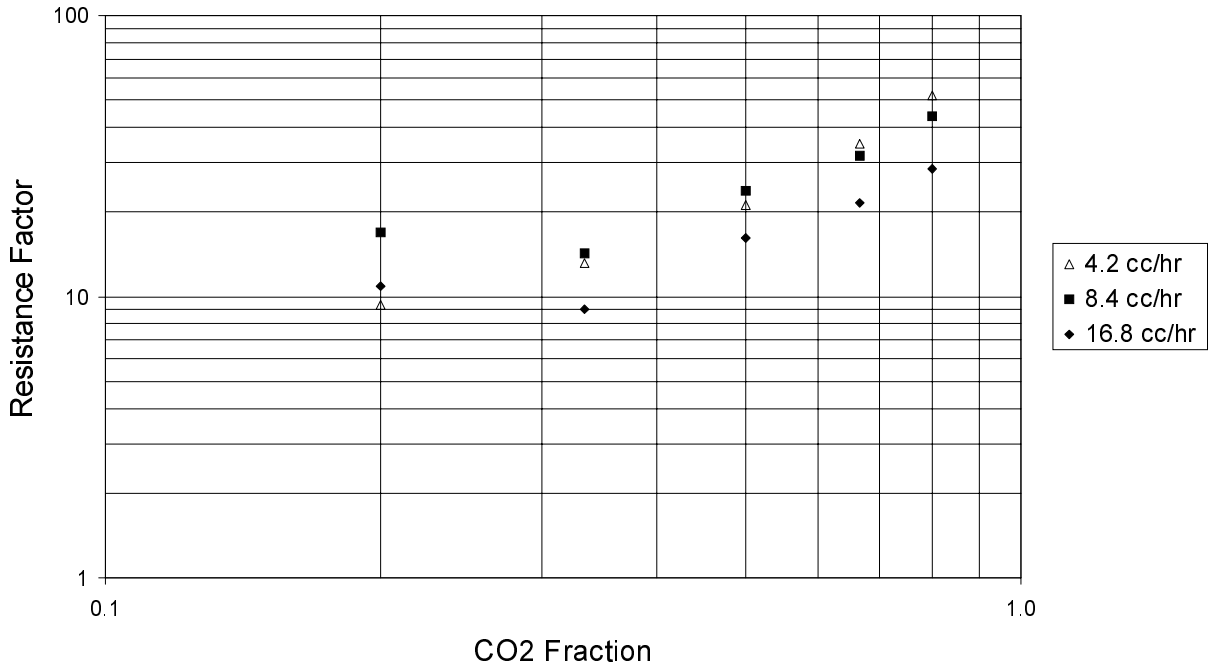

Fig. 74. Resistance factor versus CO_2 fraction for total flow rates of 16.8, 8.4, and 4.2 cc/hr (Core C).

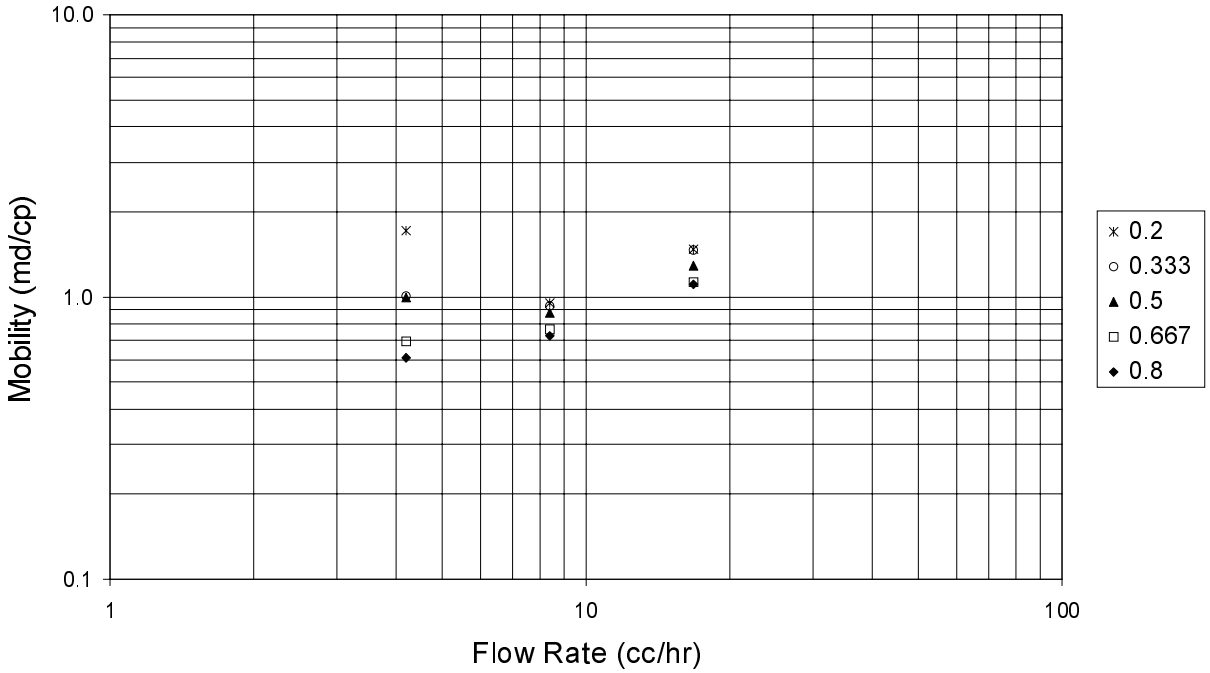

Fig. 75. Total mobility of CO_2/surfactant solution versus total flow rate for CO_2 fractions of 0.8, 0.667, 0.5, 0.333, and 0.2 (Core C).

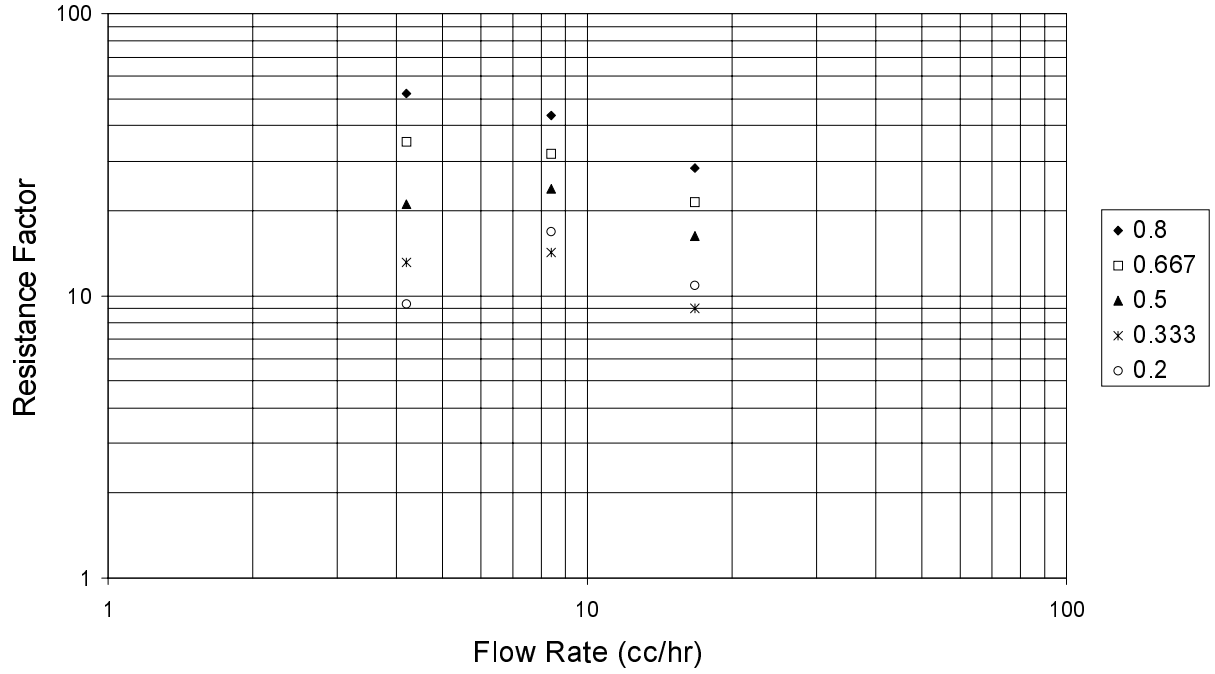

Fig. 76. Resistance factor versus total flow rate for CO_2 fractions of 0.8, 0.667, 0.5, 0.333, and 0.2 (Core C).

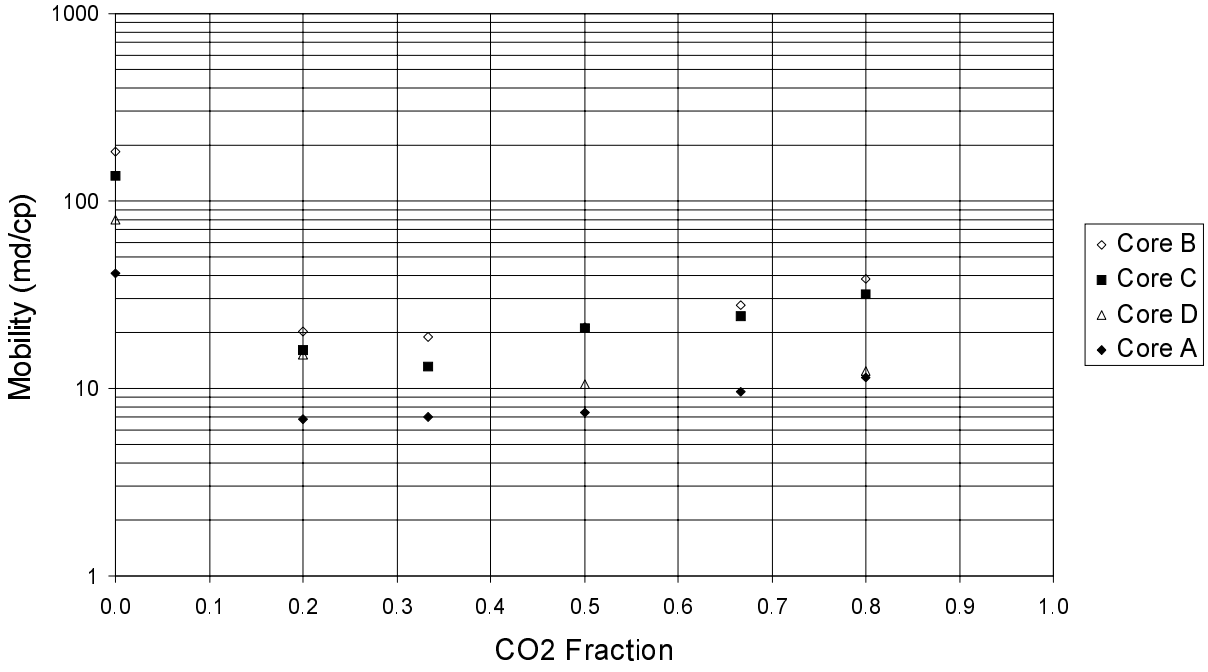

Fig. 77. Total mobility of CO_2/brine versus CO_2 fraction for cores A, B, C, and D.

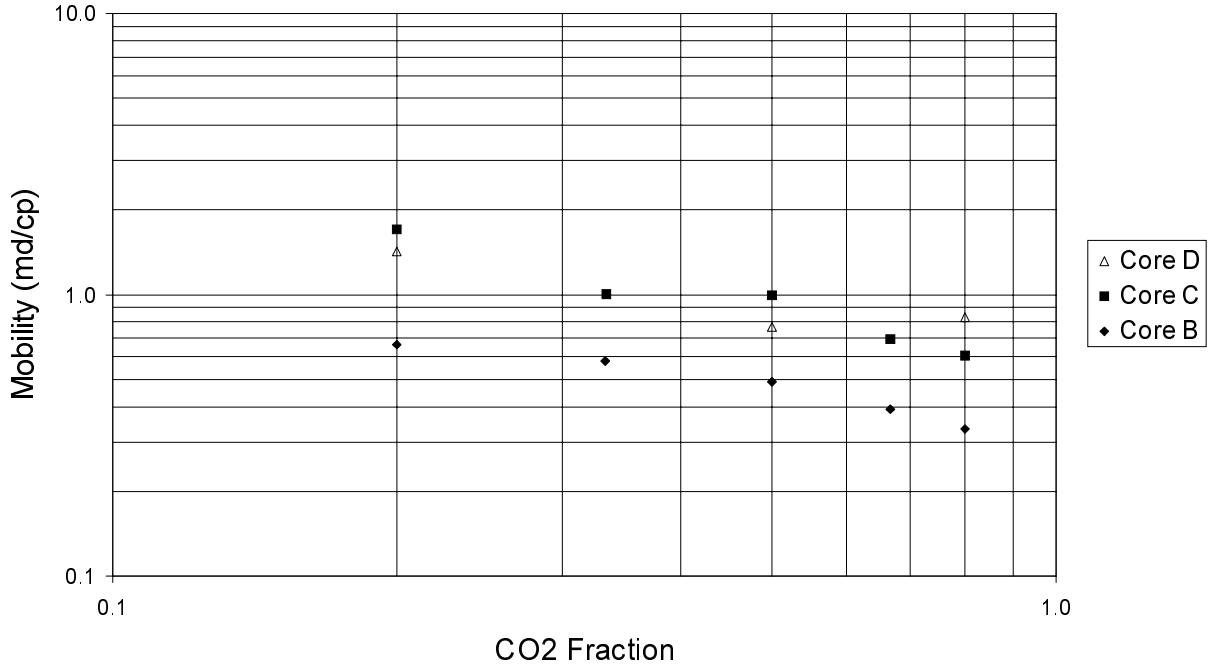

Fig. 78. Total mobility of CO_2/surfactant solution versus CO_2 fraction at 4.2 cc/hr for cores B, C, and D.

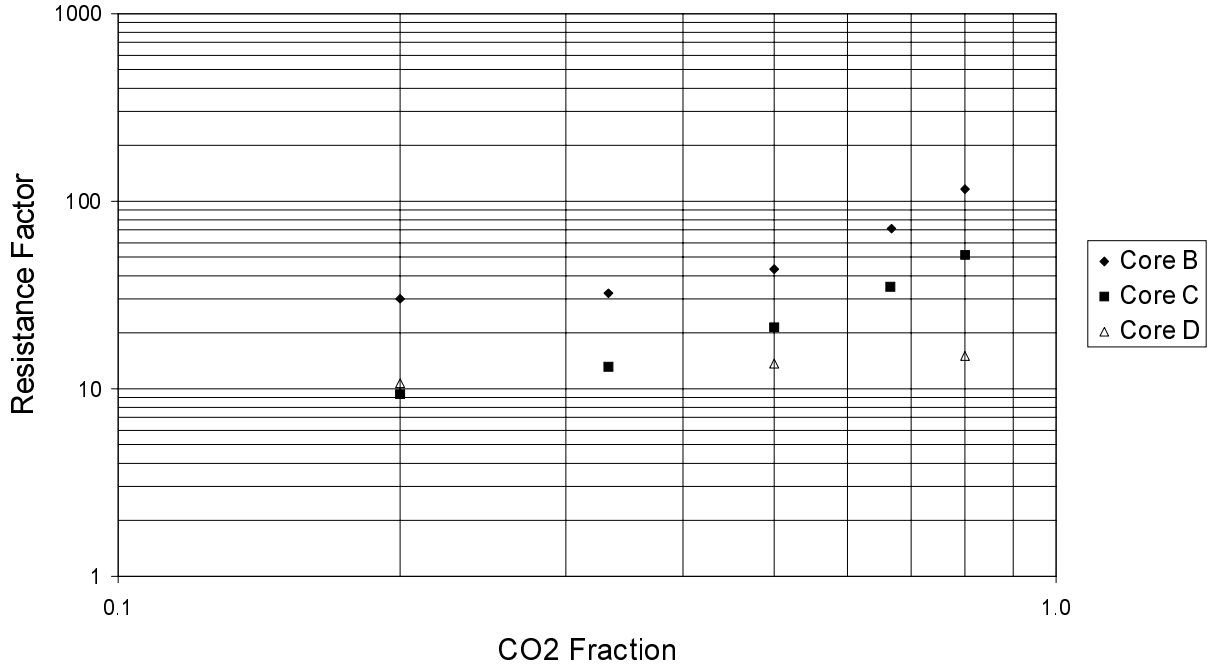

Fig. 79. Resistance factor versus CO_2 fraction at 4.2 cc/hr for cores B, C, and D.

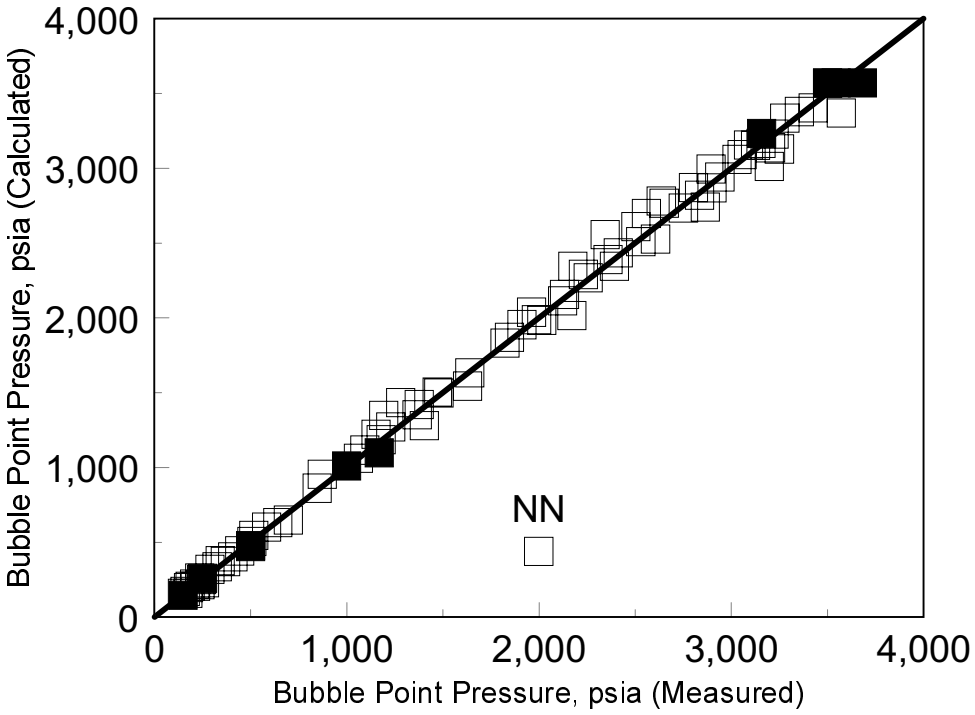

Fig. 80. Measured bubble points vs calculated (NN). Open squares are Mideast oils and solid squares are North Sea.

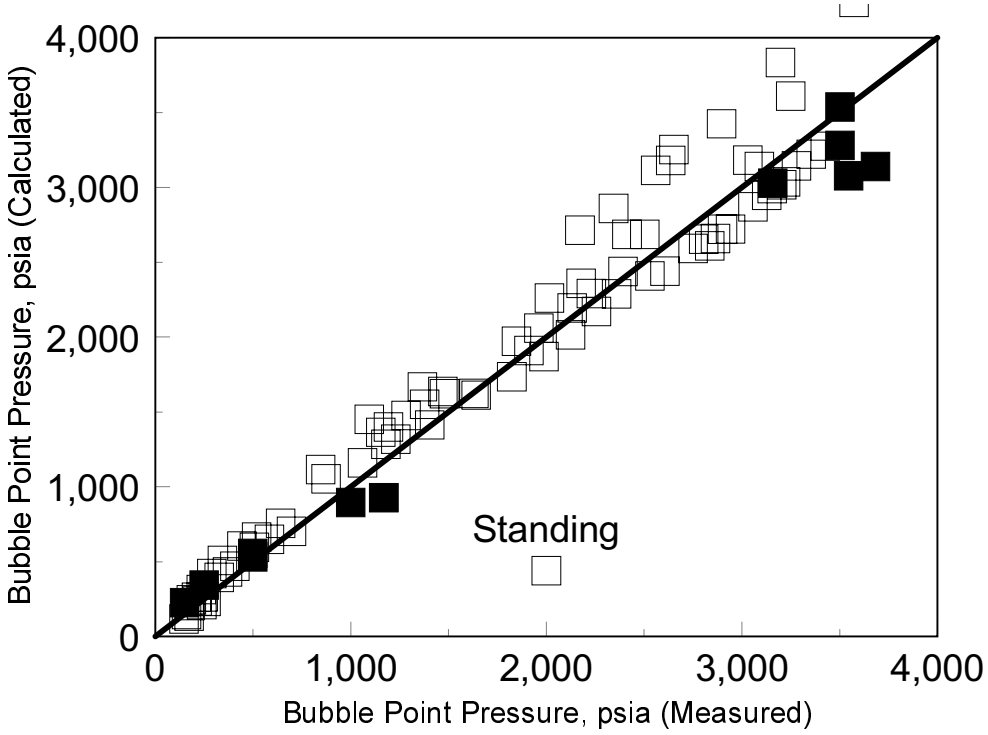

Fig. 81. Measured bubble points vs calculated (Standing). Open squares are Mideast oils and solid squares are North Sea.

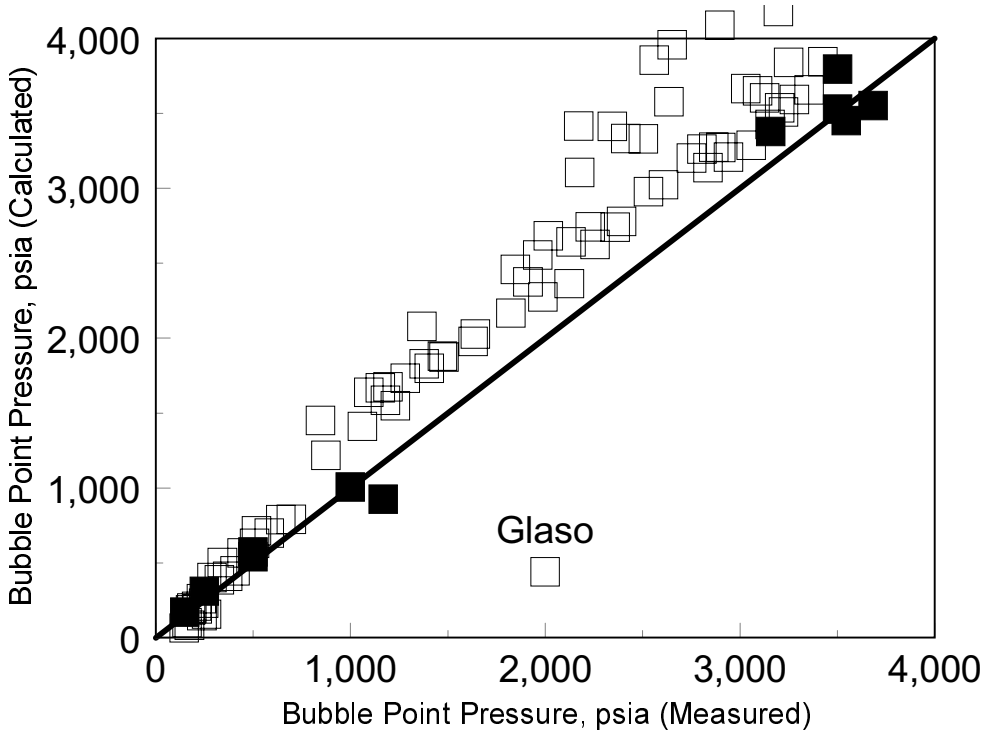

Fig. 82. Measured bubble points vs calculated (Glaso). Open squares are Mideast oils and solid squares are North Sea.

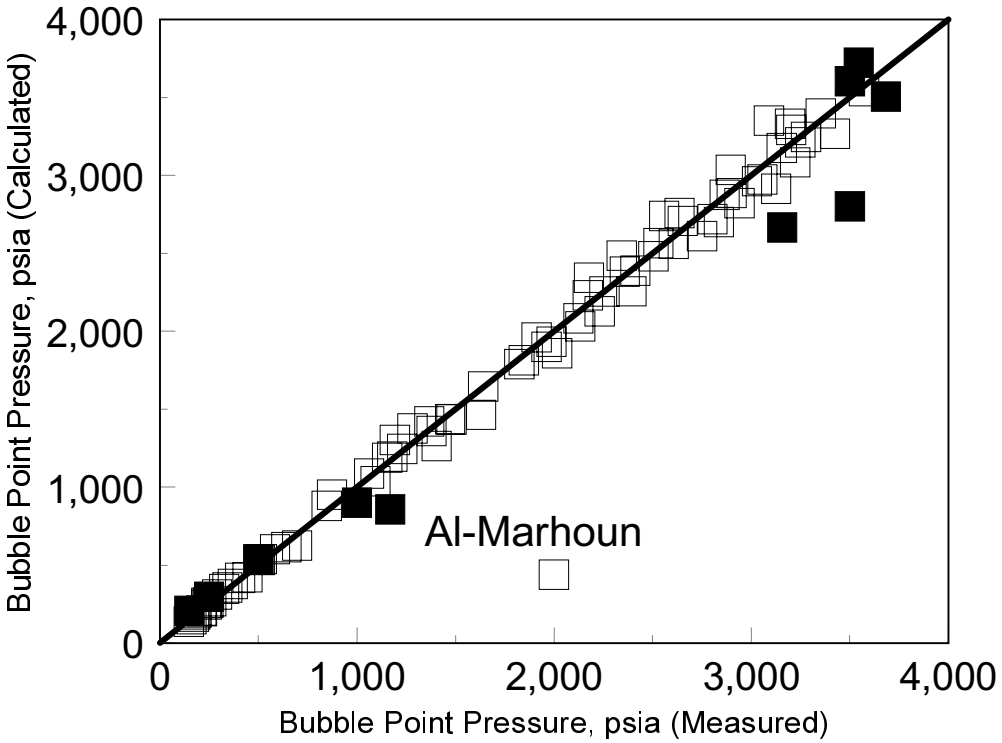

Fig. 83. Measured bubble points vs calculated (Al-Marhoun). Open squares are Mideast oils and solid squares are North Sea.

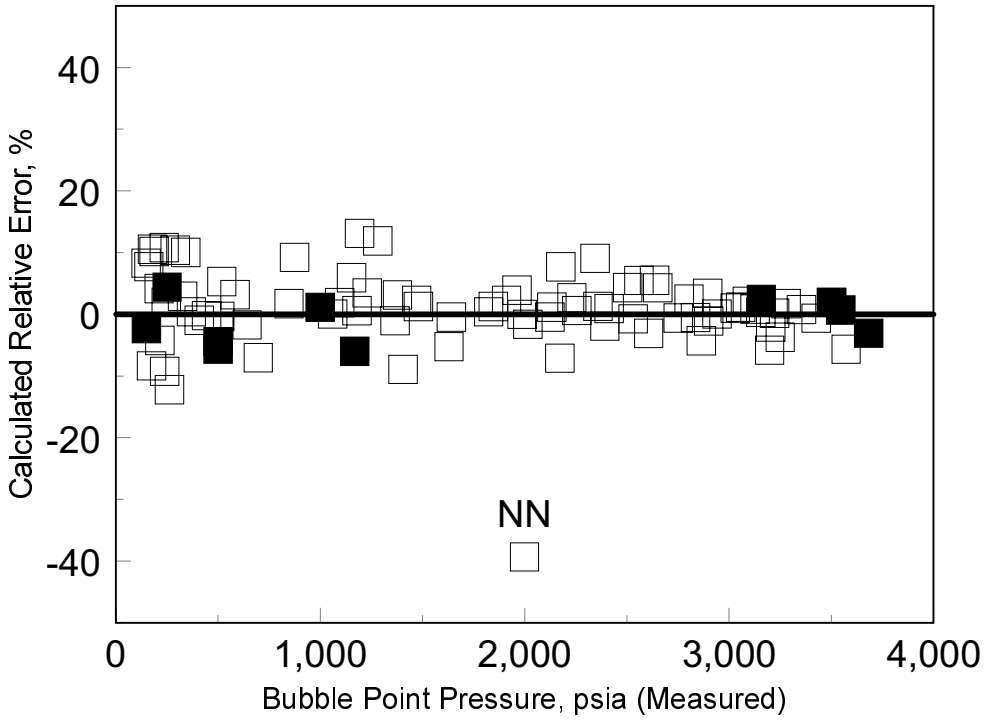

Fig. 84. Relative error of calculated bubble points (NN). Open squares are Mideast oils and solid squares are North Sea.

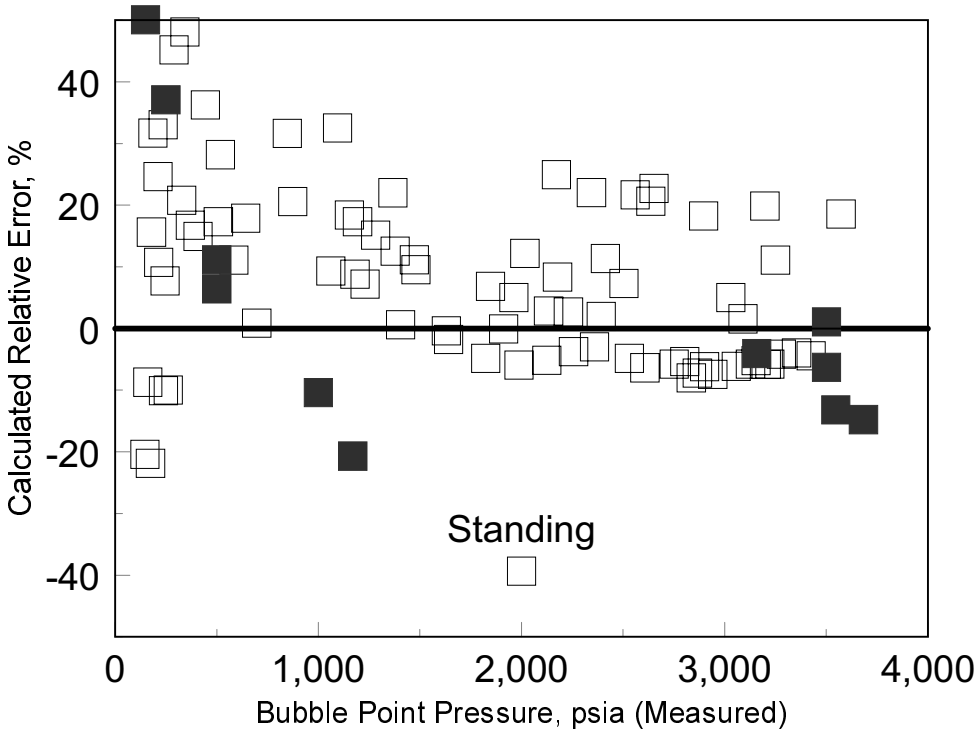

Fig. 85. Relative error of calculated bubble points (Standing). Open squares are Mideast oils and solid squares are North Sea.

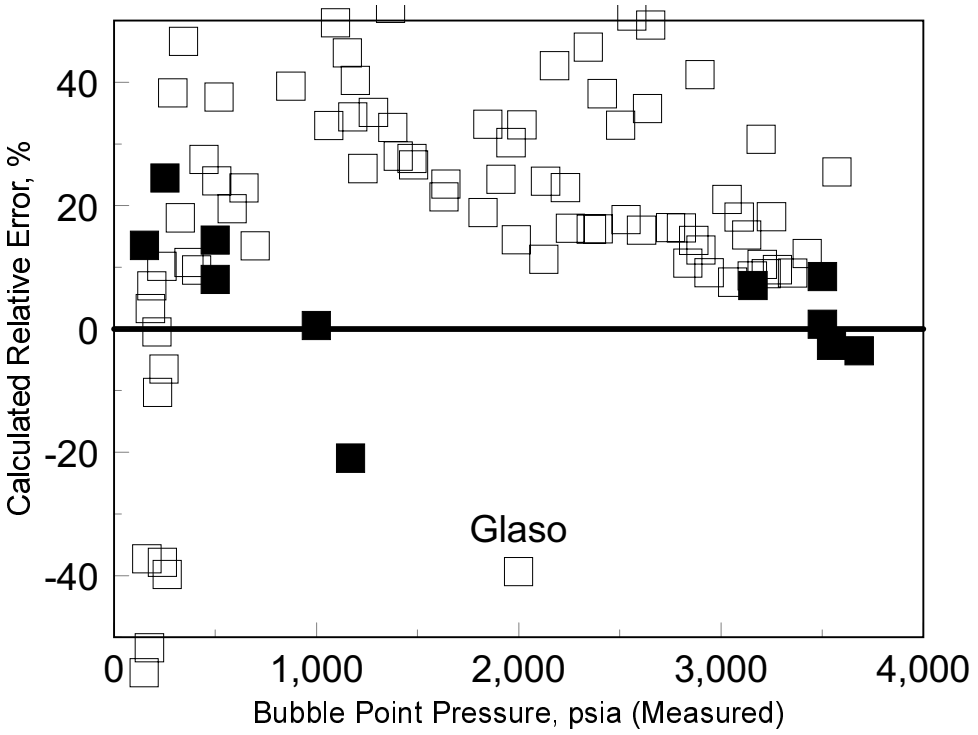

Fig. 86. Relative error of calculated bubble points (Glaso). Open squares are Mideast oils and solid squares are North Sea.

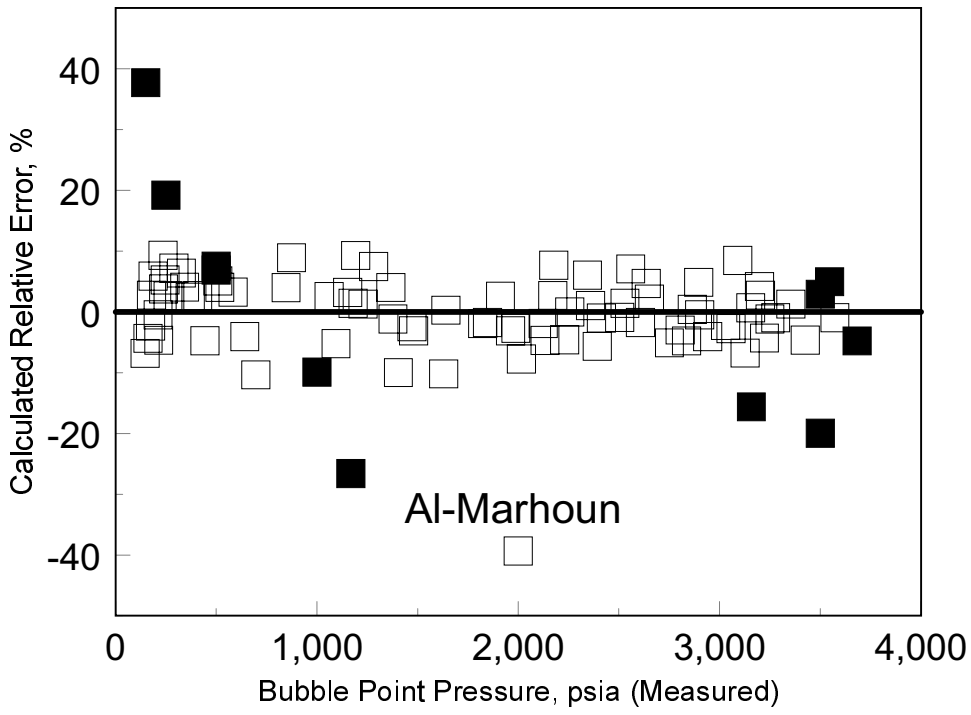

Fig. 87. Relative error of calculated bubble points (Al-Marhoun). Open squares are Mideast oils and solid squares are North Sea.

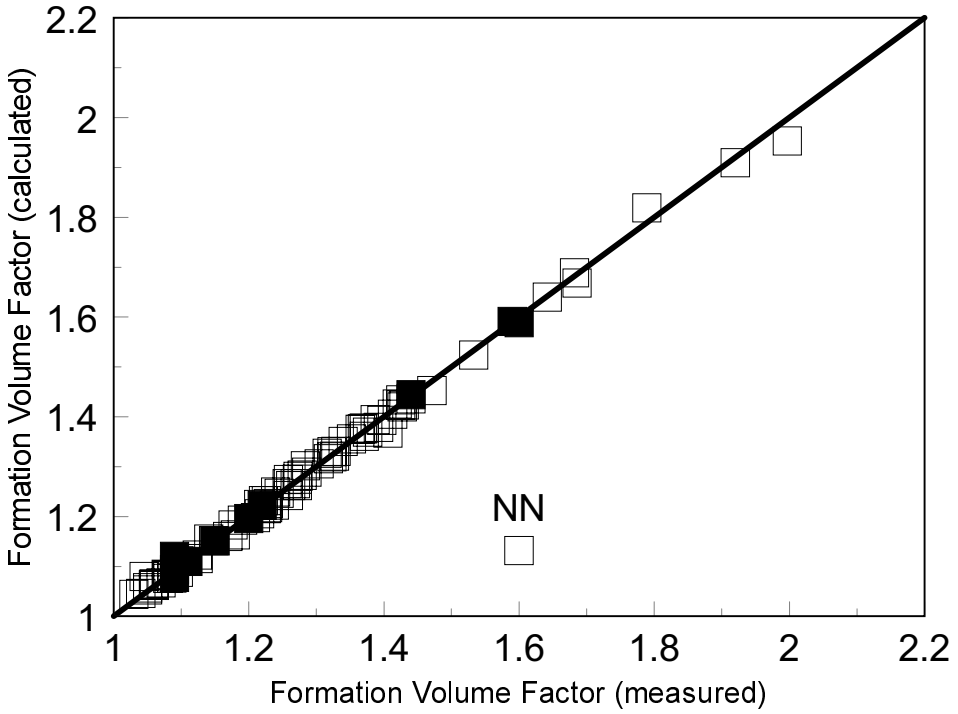

Fig. 88. Formation volume factor: measured vs calculated (NN). Open squares are Mideast oils and solid squares are North Sea.

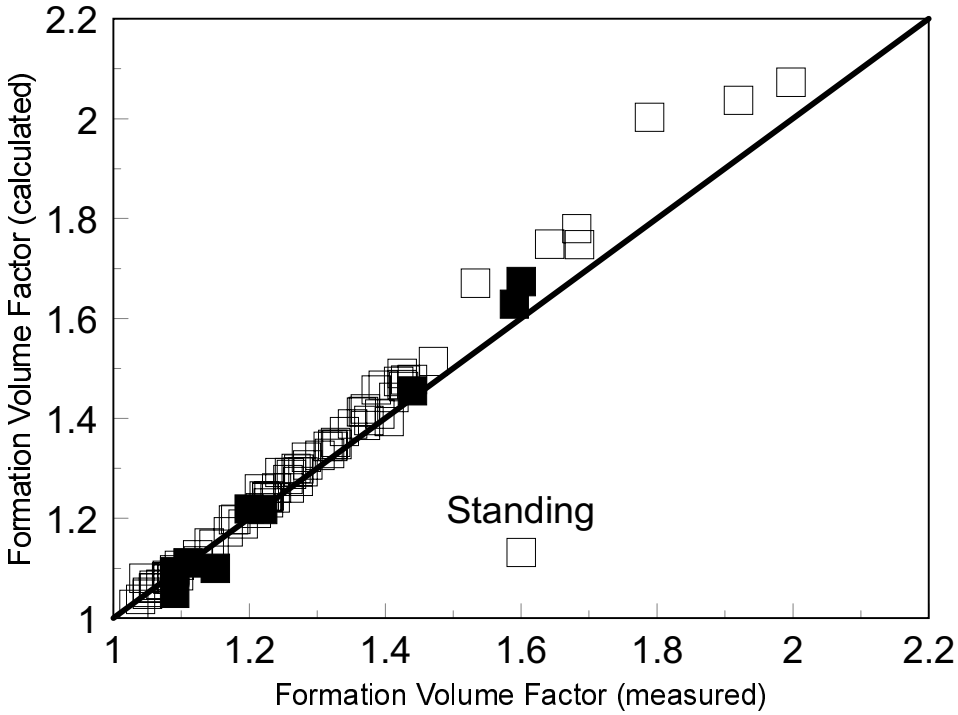

Fig. 89. Formation volume factor: measured vs calculated (Standing). Open squares are Mideast oils and solid squares are North Sea.

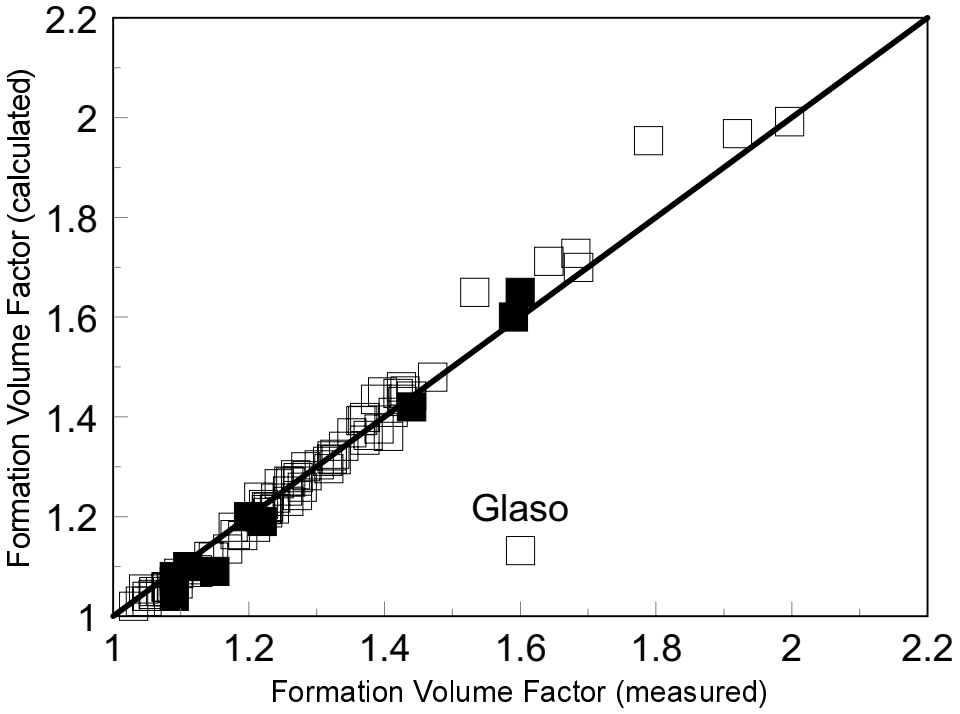

Fig. 90. Formation volume factor: measured vs calculated (Glaso). Open squares are Mideast oils and solid squares are North Sea.

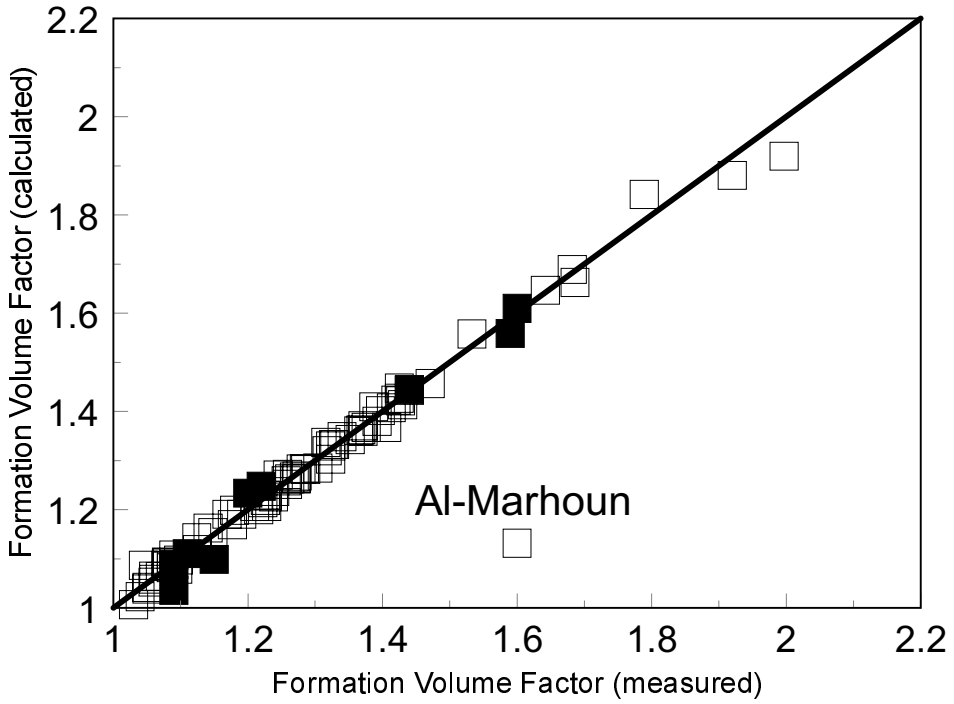

Fig. 91. Formation volume factor: measured vs calculated (Al-Marhoun). Open squares are Mideast oils and solid squares are North Sea.

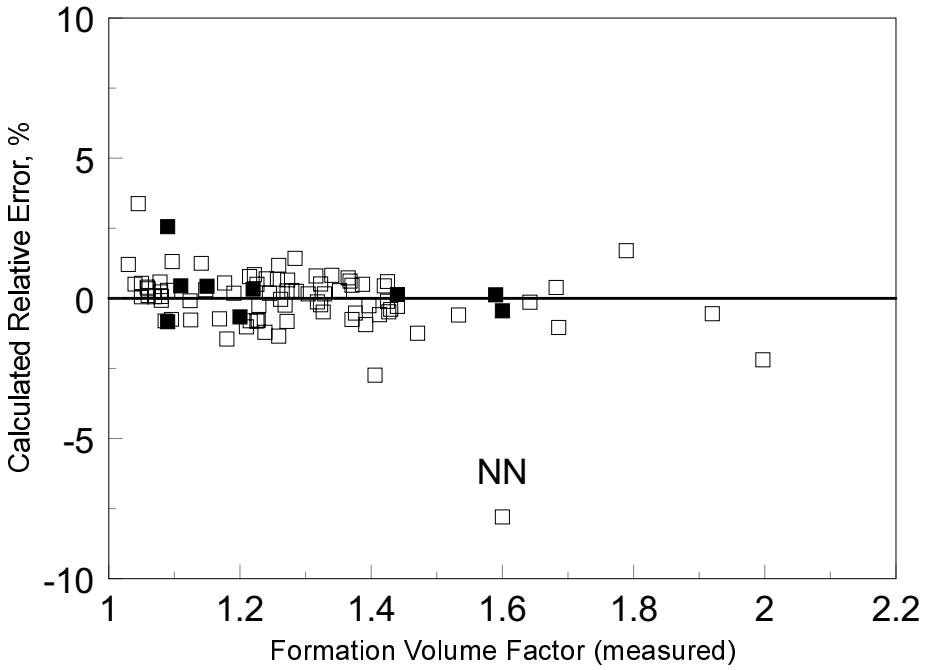

Fig. 92. Relative error % of formation volume factor (NN). Open squares are Mideast oils and solid squares are North Sea.

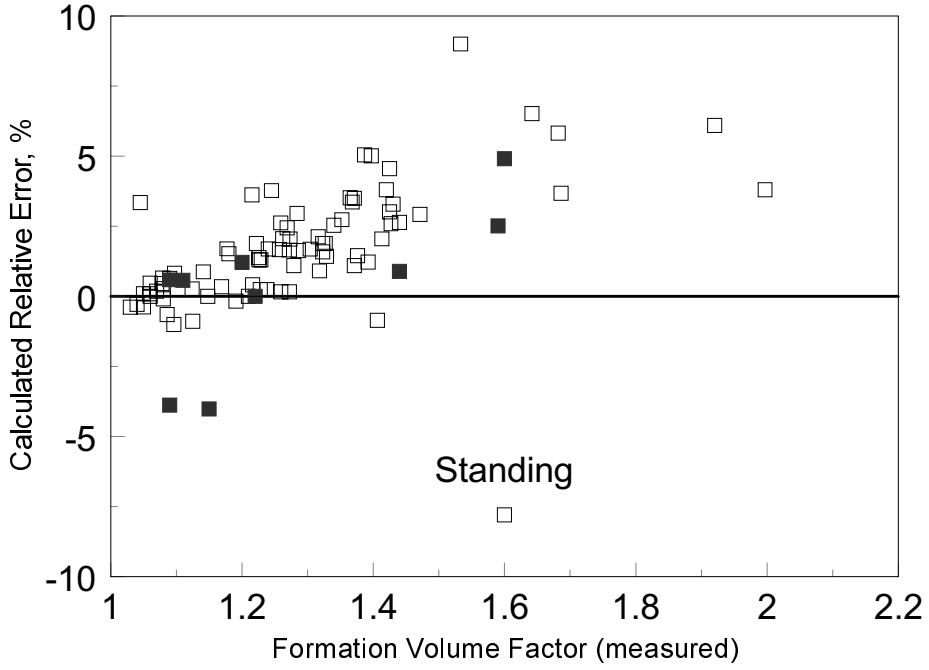

Fig. 93. Relative error % of formation volume factor (Standing). Open squares are Mideast oils and solid squares are North Sea.

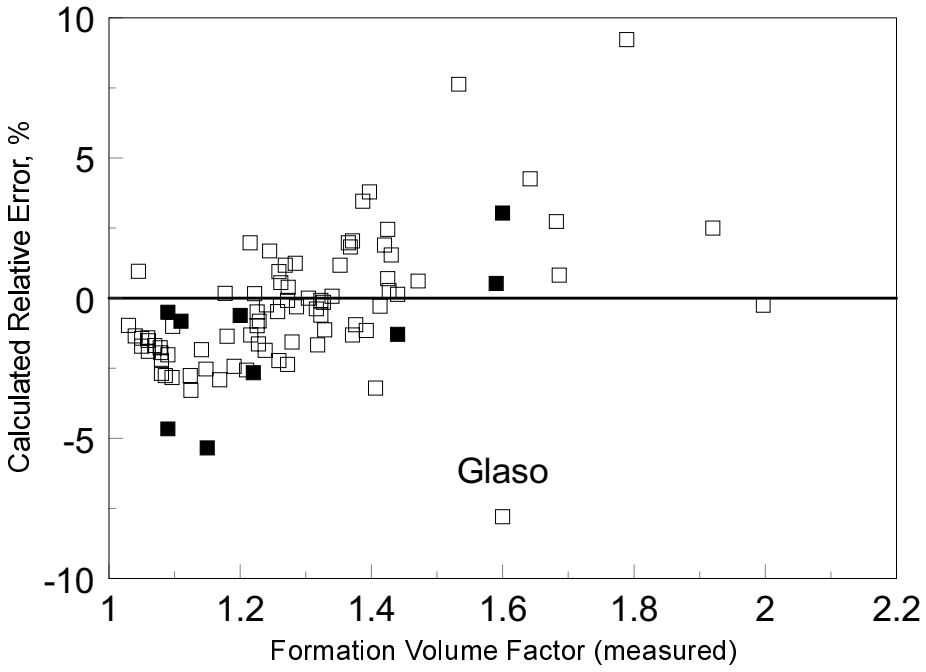

Fig. 94. Relative error % of formation volume factor (Glaso). Open squares are Mideast oils and solid squares are North Sea.

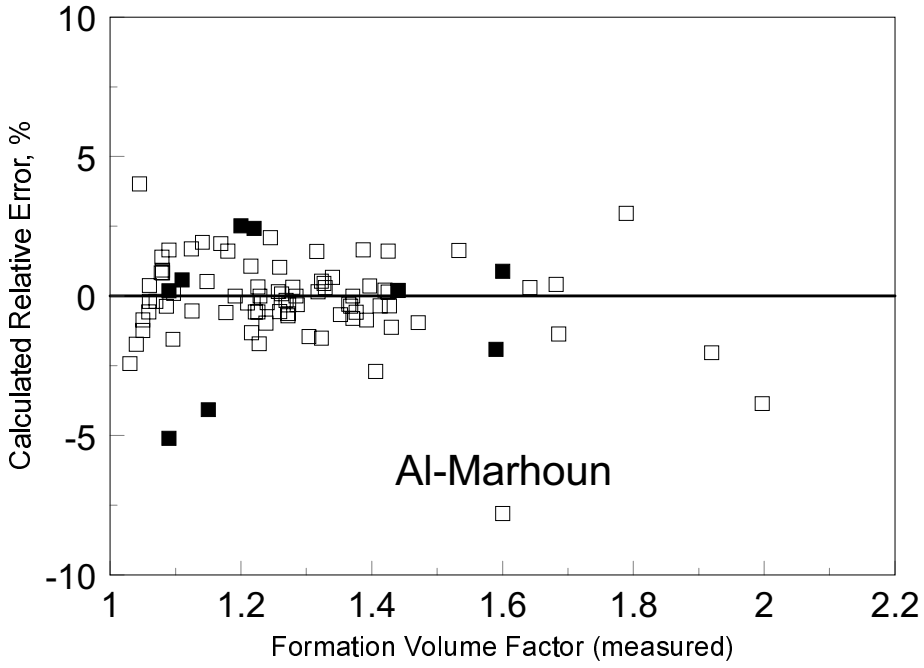

Fig. 95. Relative error % of formation volume factor (Al-Marhoun). Open squares are Mideast oils and solid squares are North Sea.

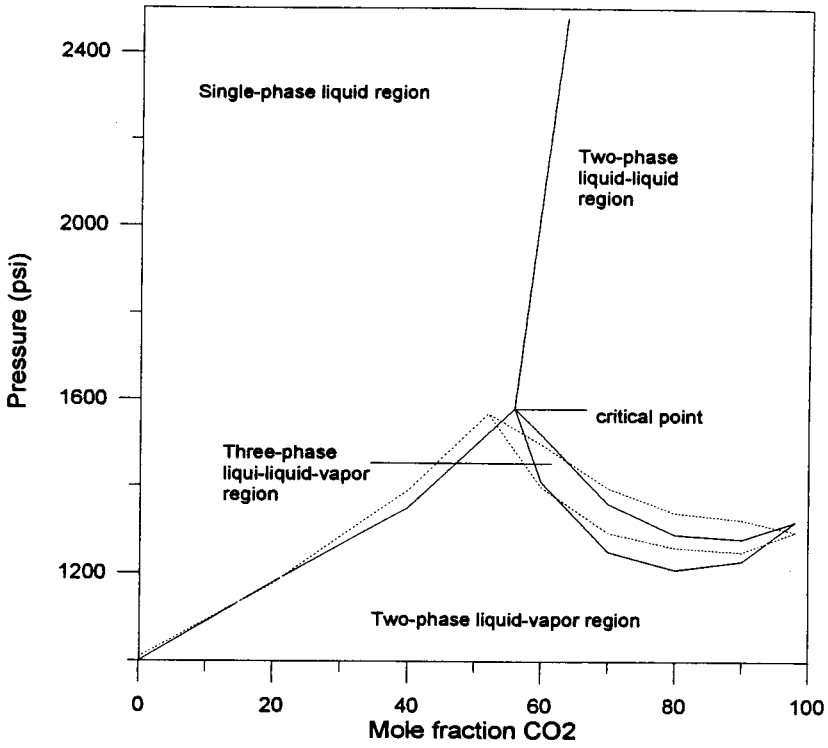

Fig. 96. Experimental (solid line) and predicted (dashed line) phase diagram for oil F.

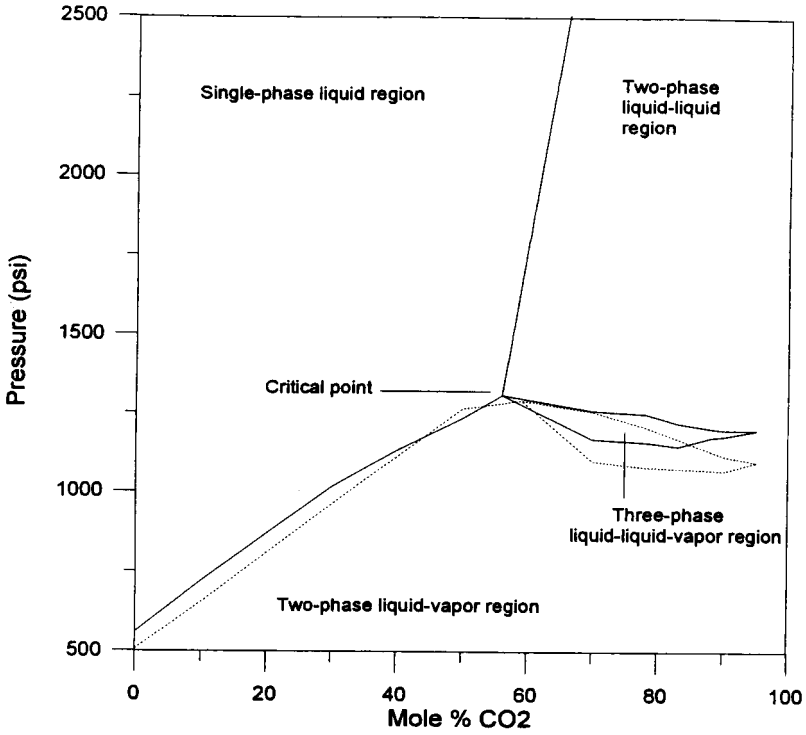

Fig. 97. Experimental (solid line) and predicted (dashed line) phase diagram for oil BSB.

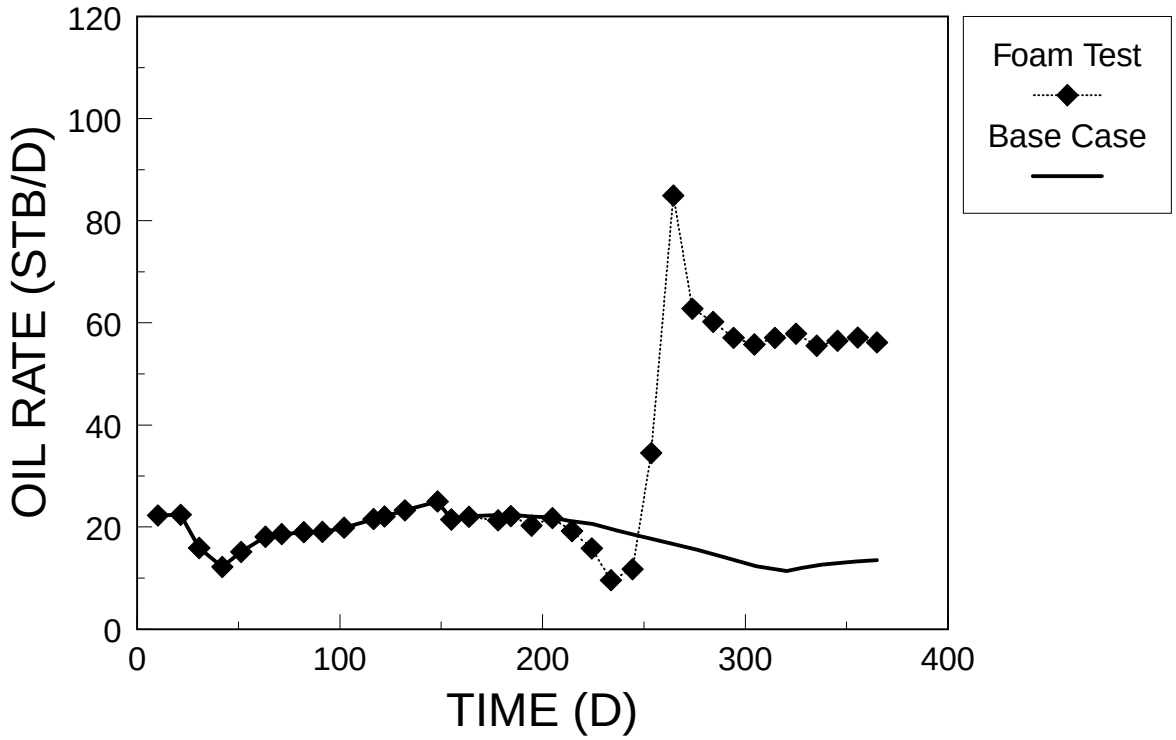

Fig. 98. Comparison of oil rate history for problem I.

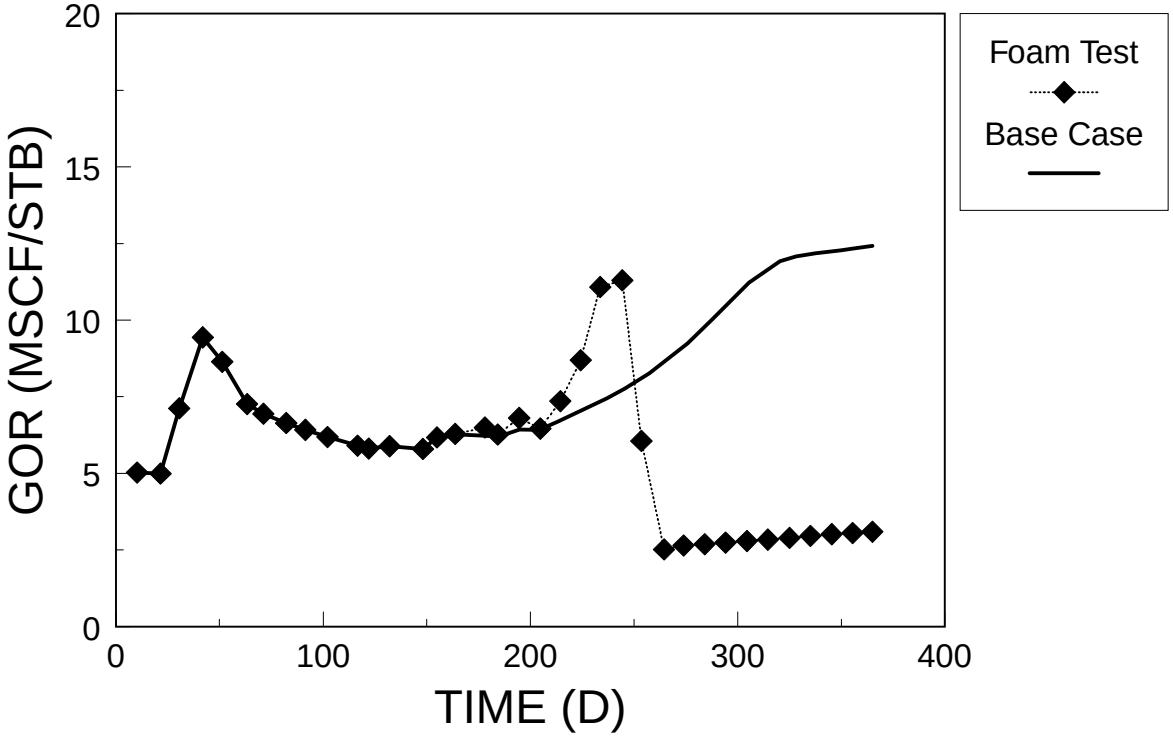

Fig. 99. Comparison of gas-oil ratio for problem I.

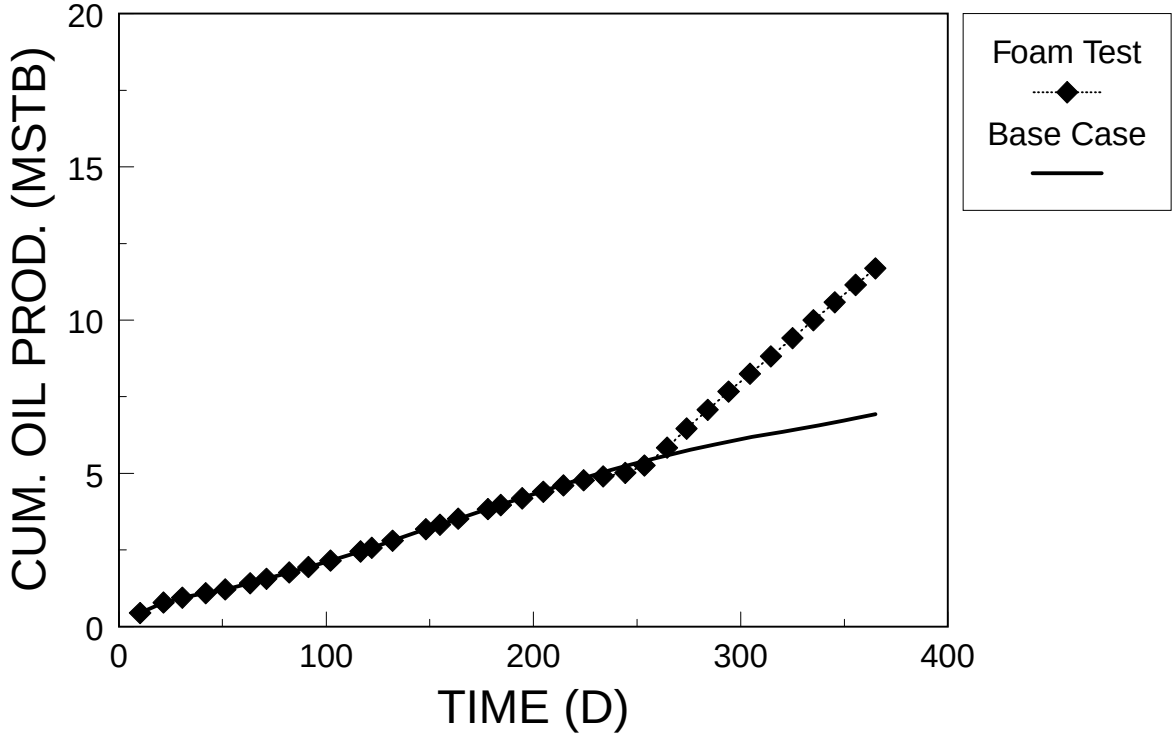

Fig. 100. Comparison of cumulative oil production for problem I.

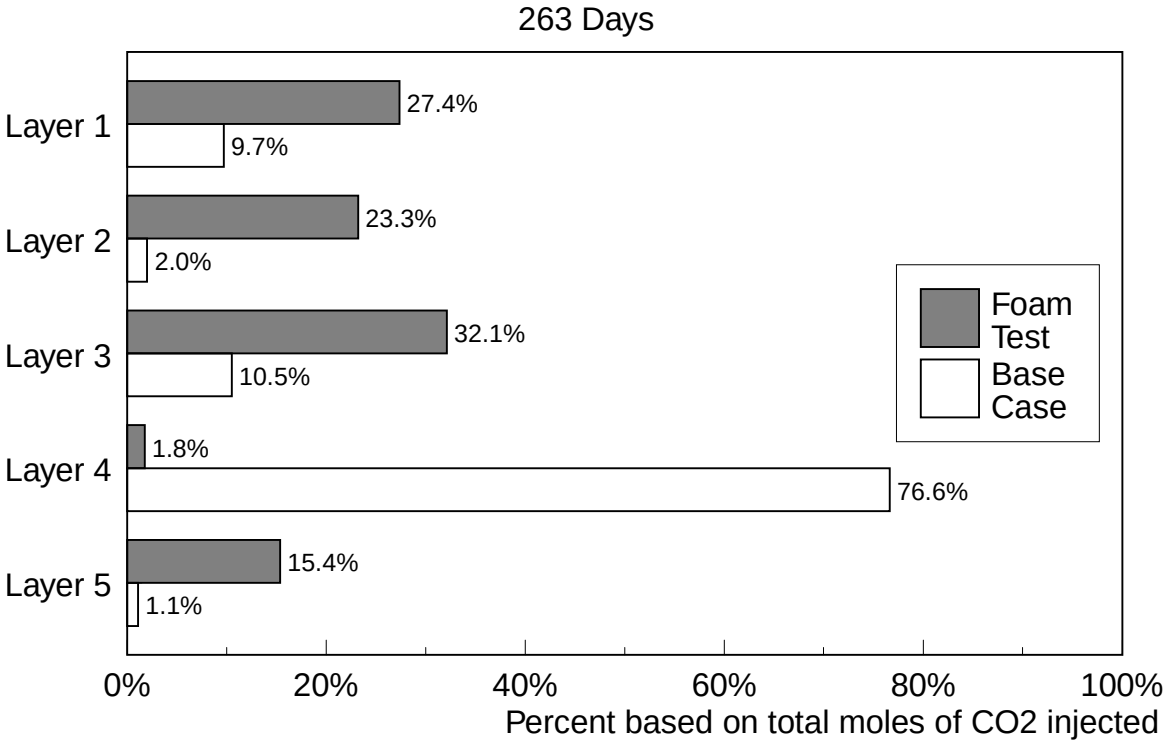

Fig. 101. Comparison of CO_2 injection profile at 263 days for problem I.

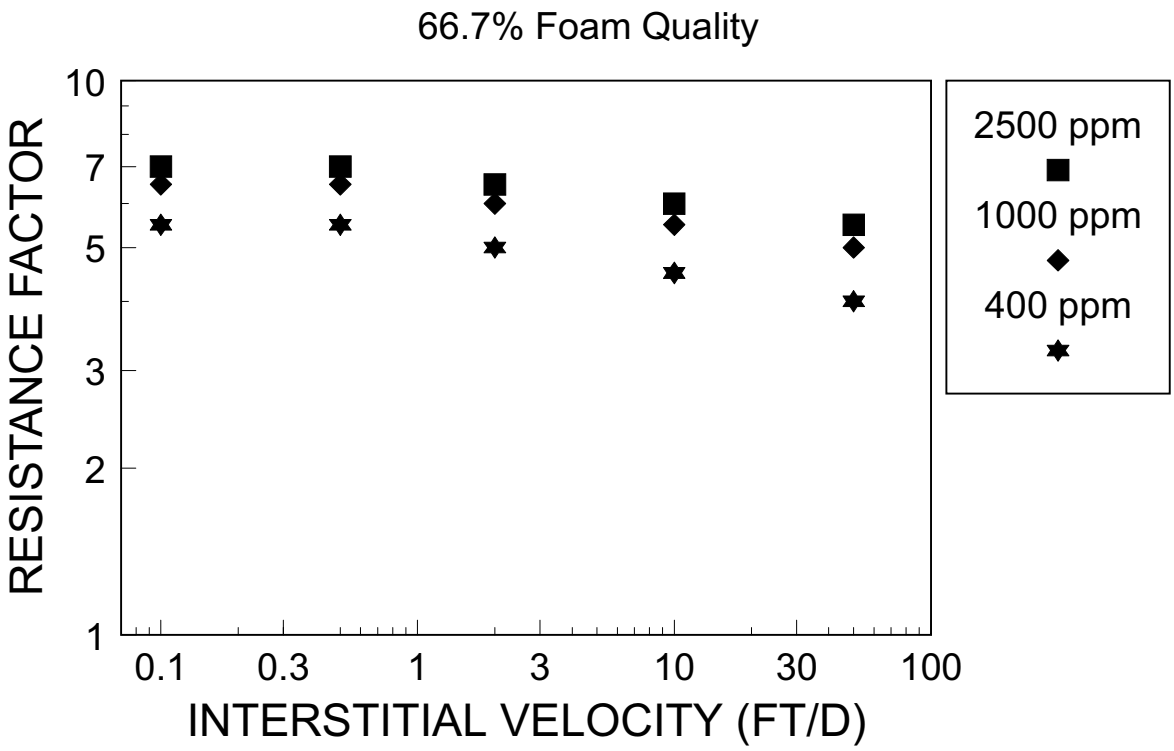

Fig. 102. Foam resistance factor vs interstitial velocity at 66.7% foam quality and different surfactant concentrations.

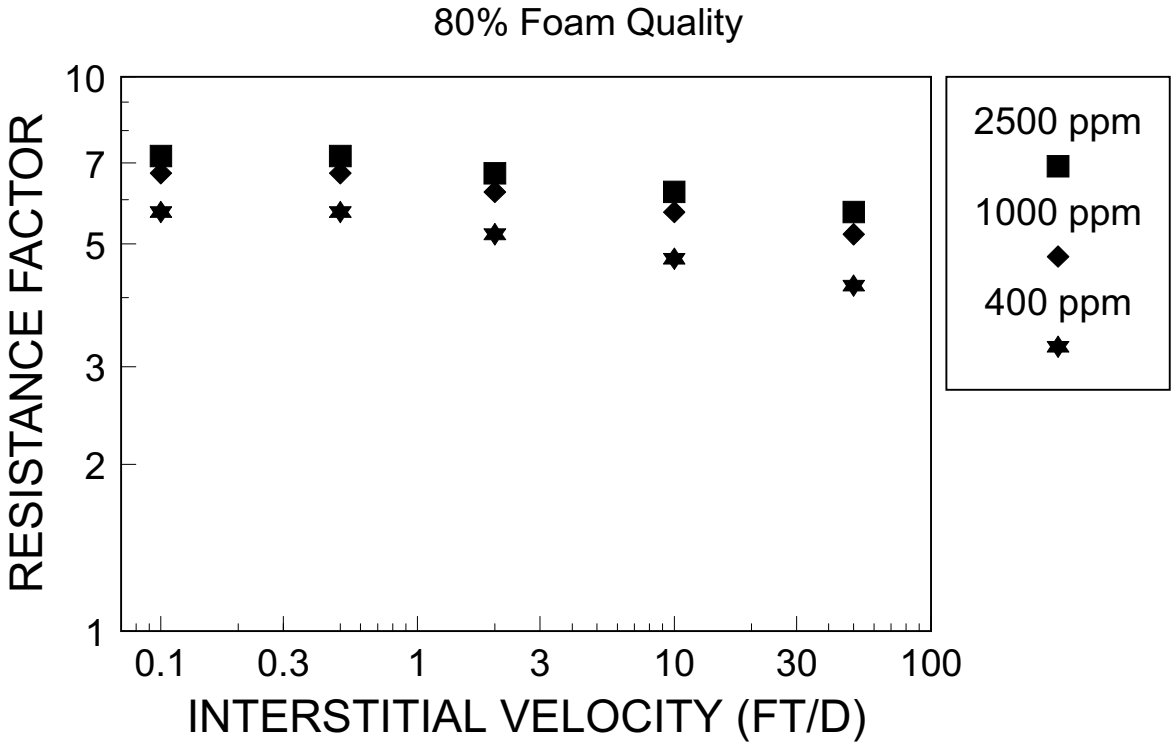

Fig. 103. Foam resistance factor vs interstitial velocity at 80% foam quality and different surfactant concentrations.

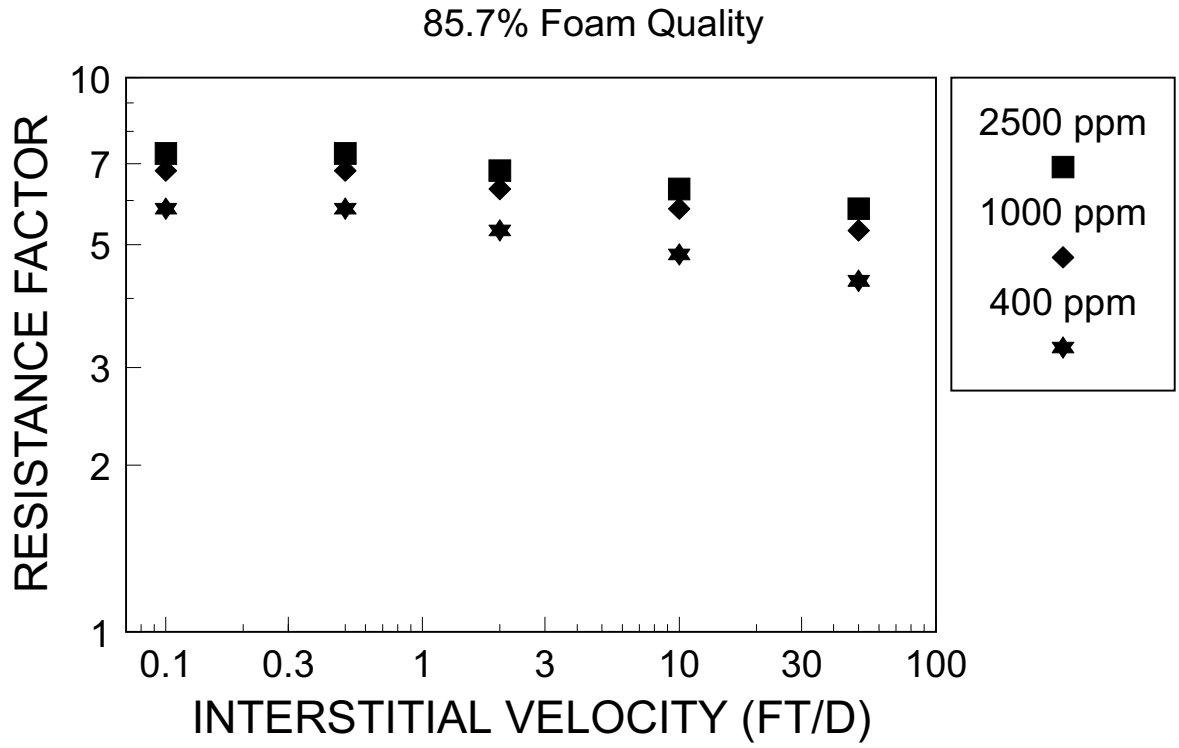

Fig. 104. Foam resistance factor vs interstitial velocity at 85.7% foam quality and different surfactant concentrations.

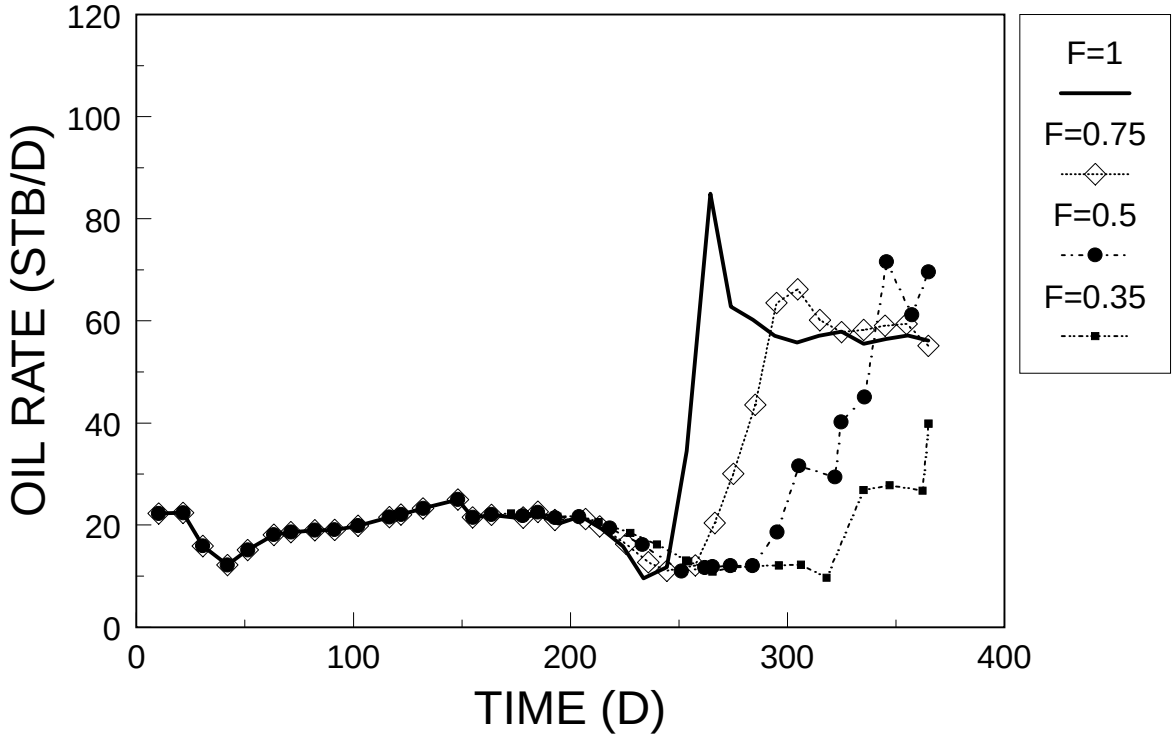

Fig. 105. Effect of scaling parameter F on oil rate response for problem I.

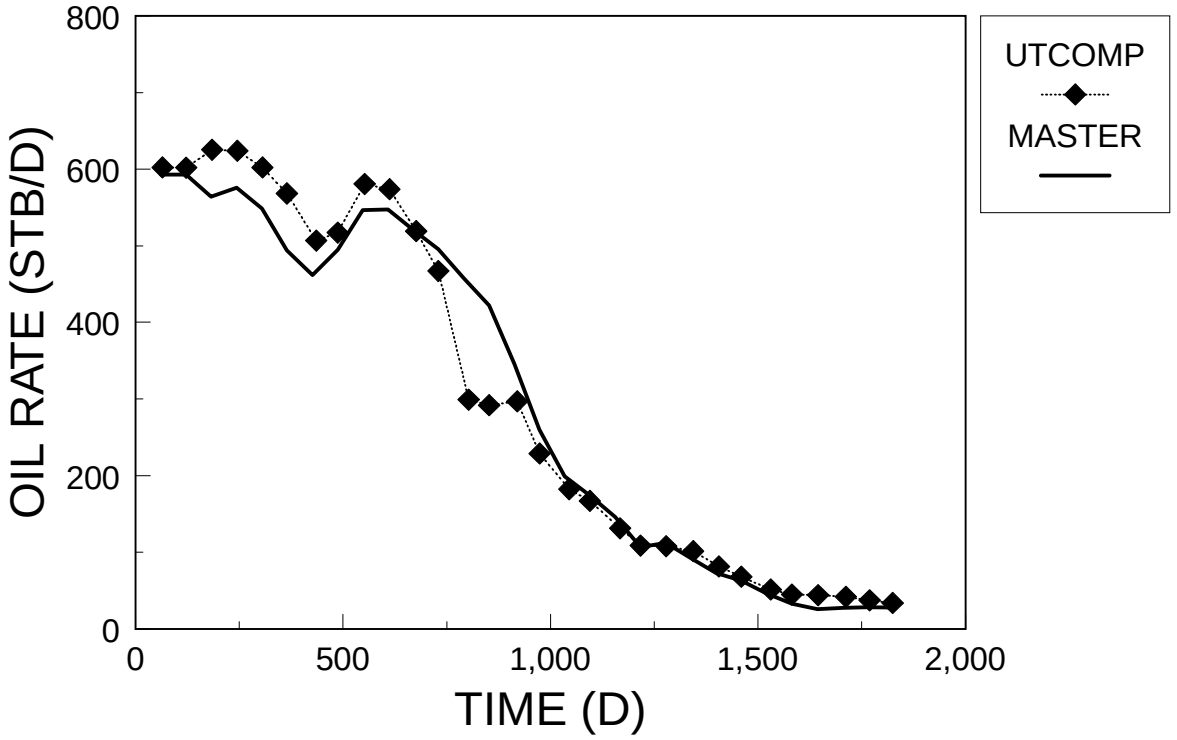

Fig. 106. Comparison of oil rate history between UTCOMP and MASTER for problem II.

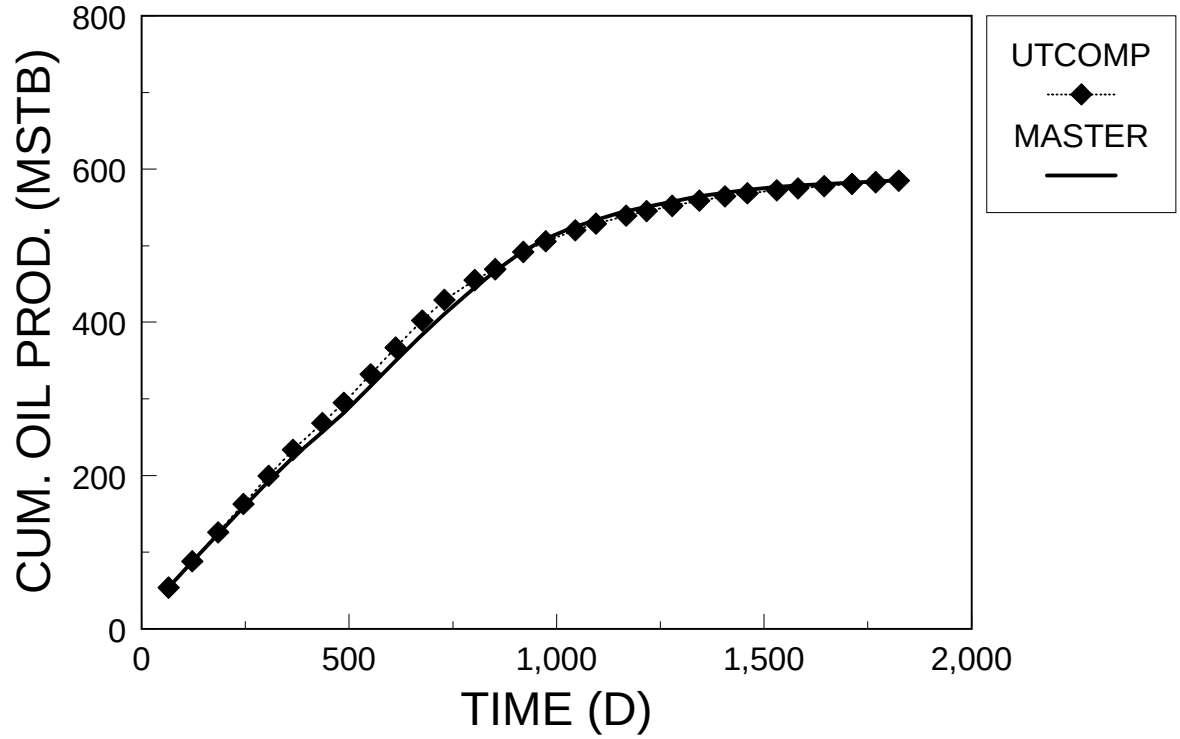

Fig. 107. Comparison of cumulative oil production between UTCOMP and MASTER for problem II.

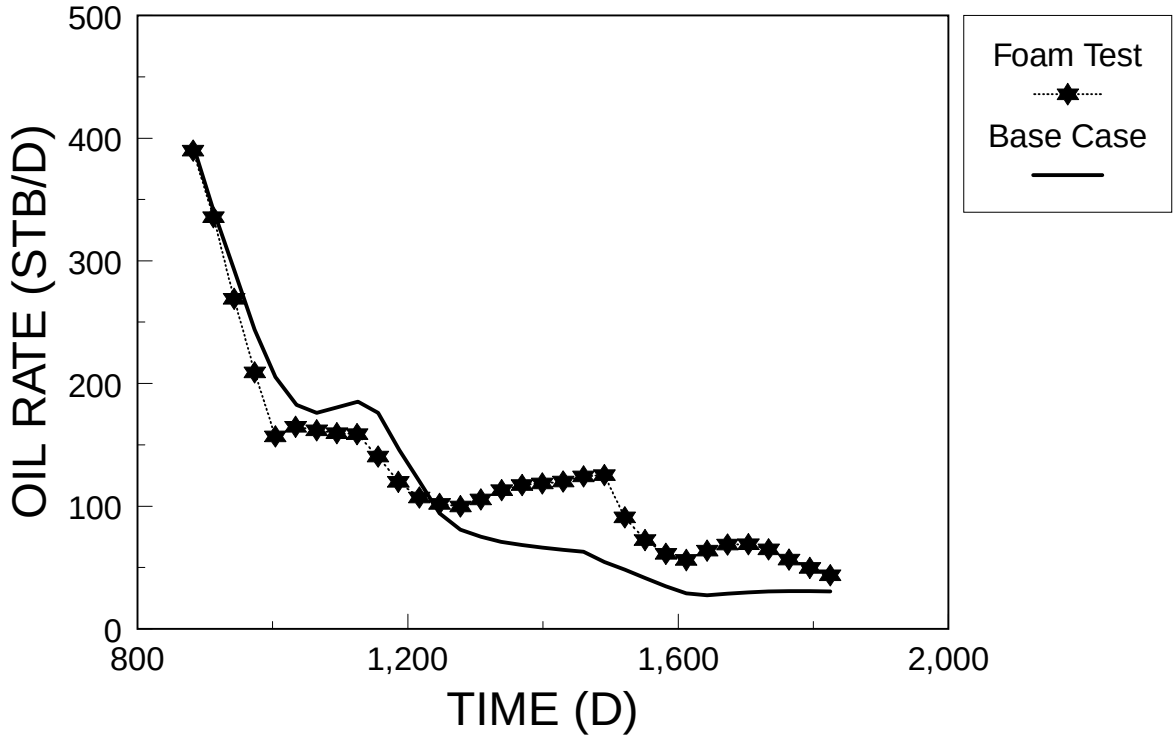

Fig. 108. Comparison of oil rate history for problem III.

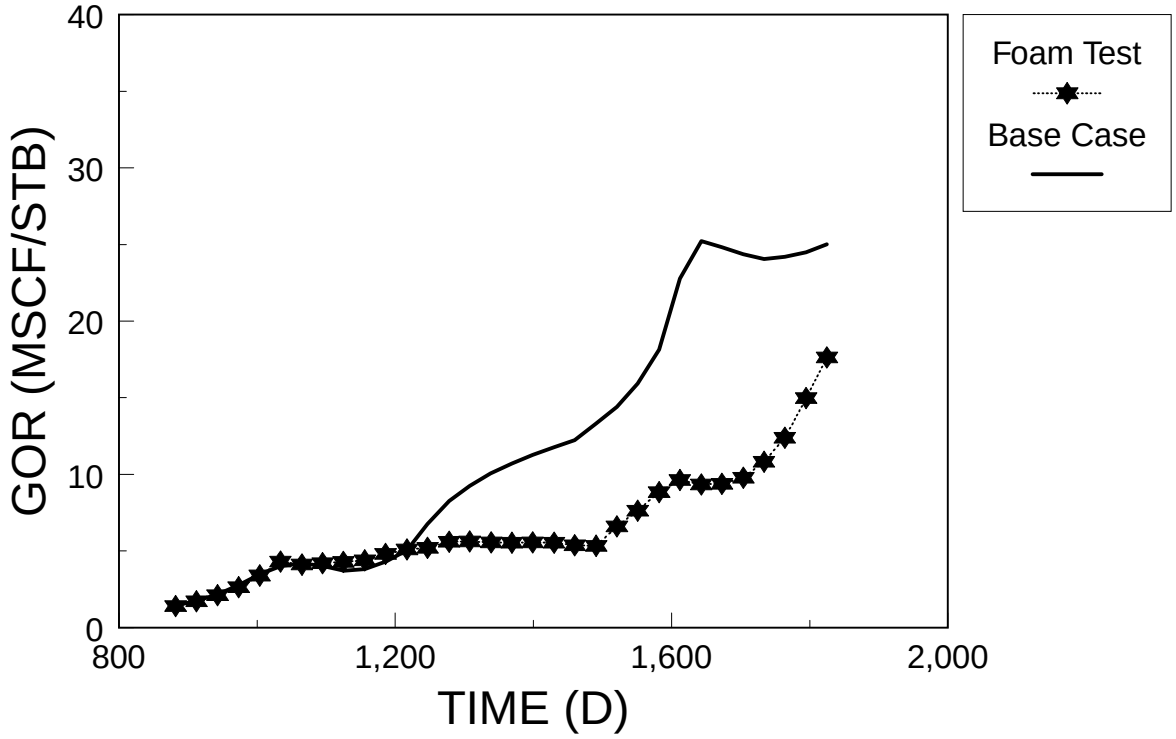

Fig. 109. Comparison of gas-oil ratio for problem III.

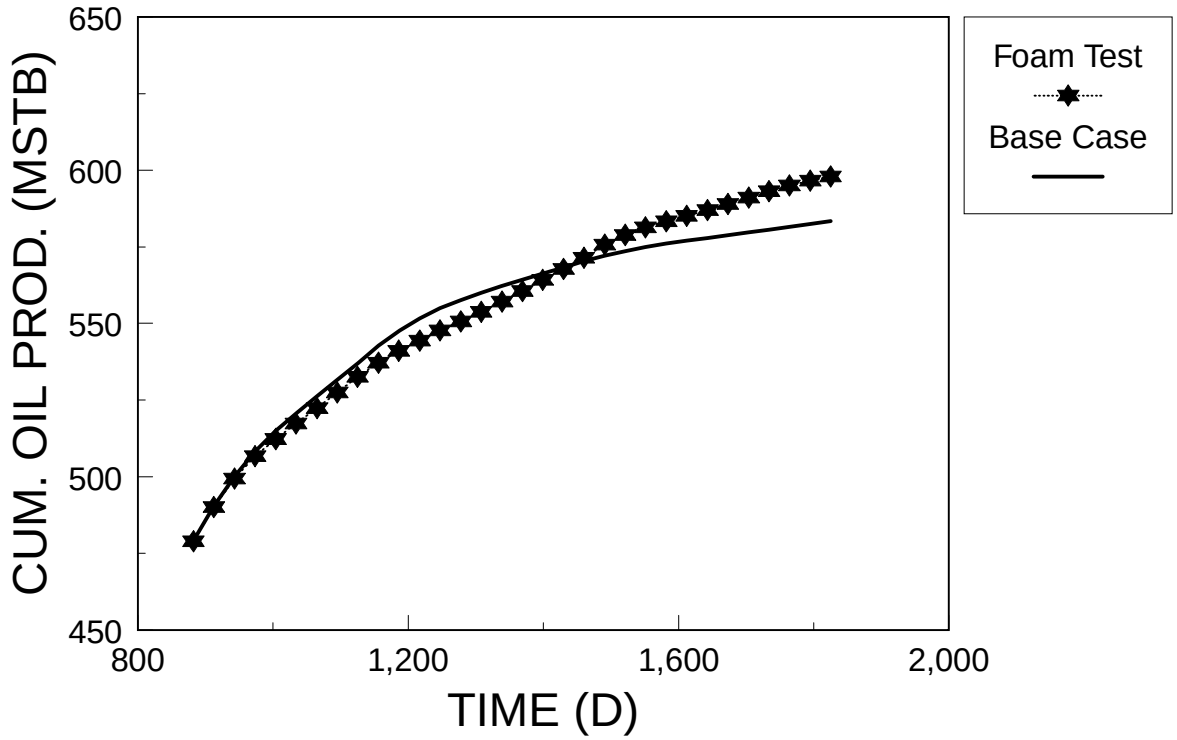

Fig. 110. Comparison of cumulative oil production for problem III.

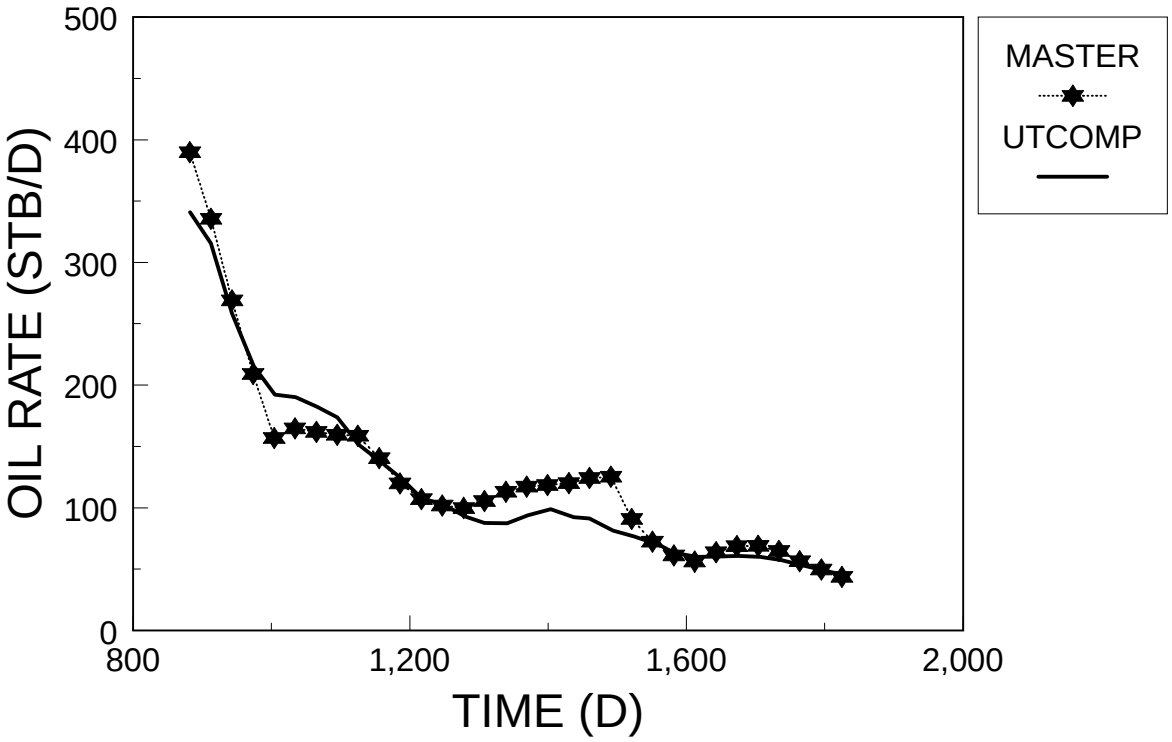

Fig. 111. Comparison of oil rate recovery between MASTER and UTCOMP for problem III.

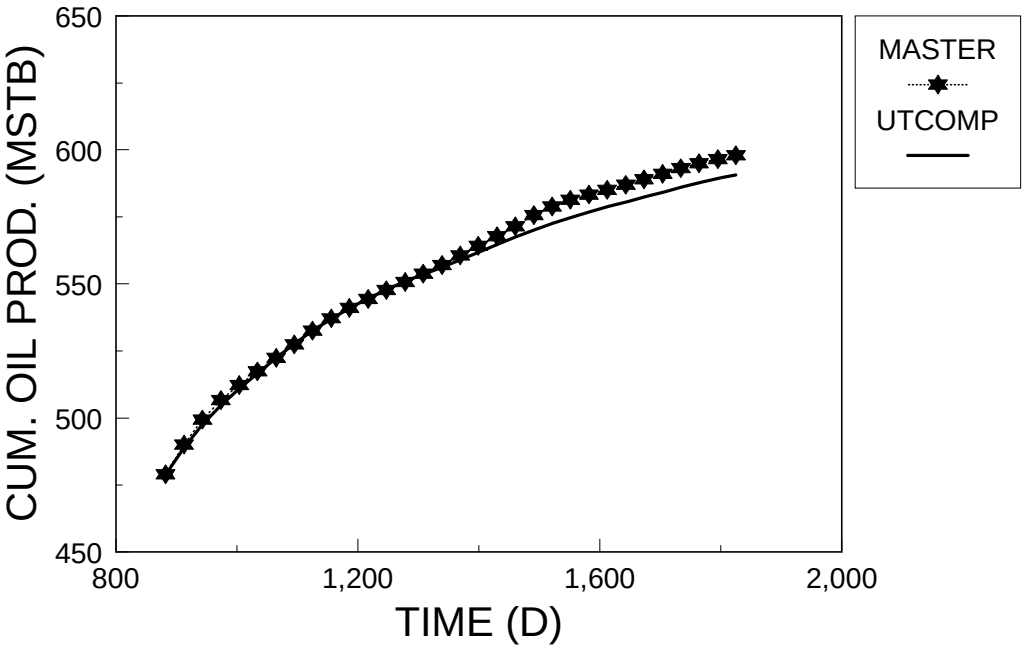

Fig. 112. Comparison of cumulative oil production between MASTER and UTCOMP for problem III.

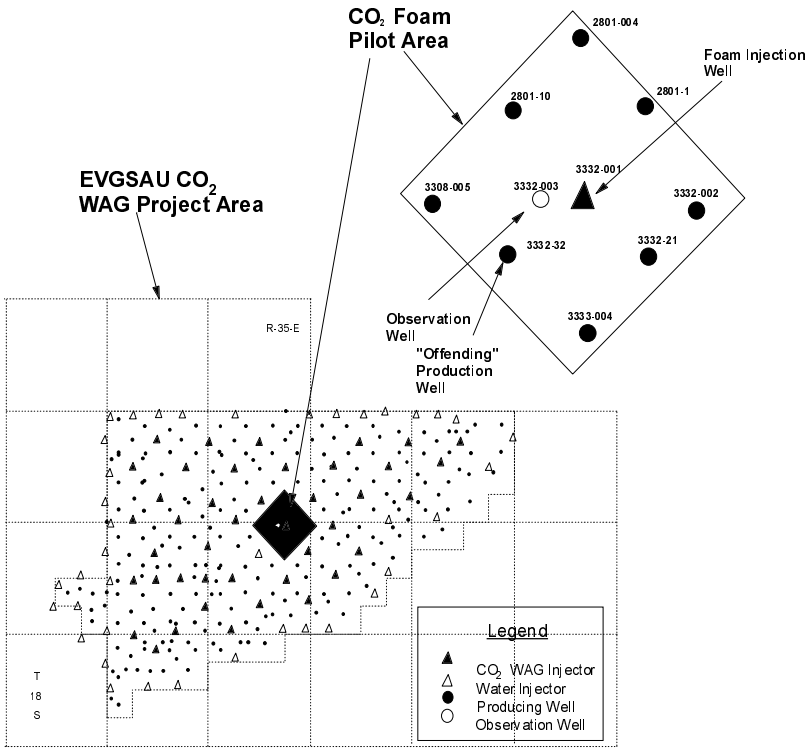

Fig. 113. East Vacuum Grayburg-San Andreas Unit (EVGSAU) CO_2-foam pilot area.

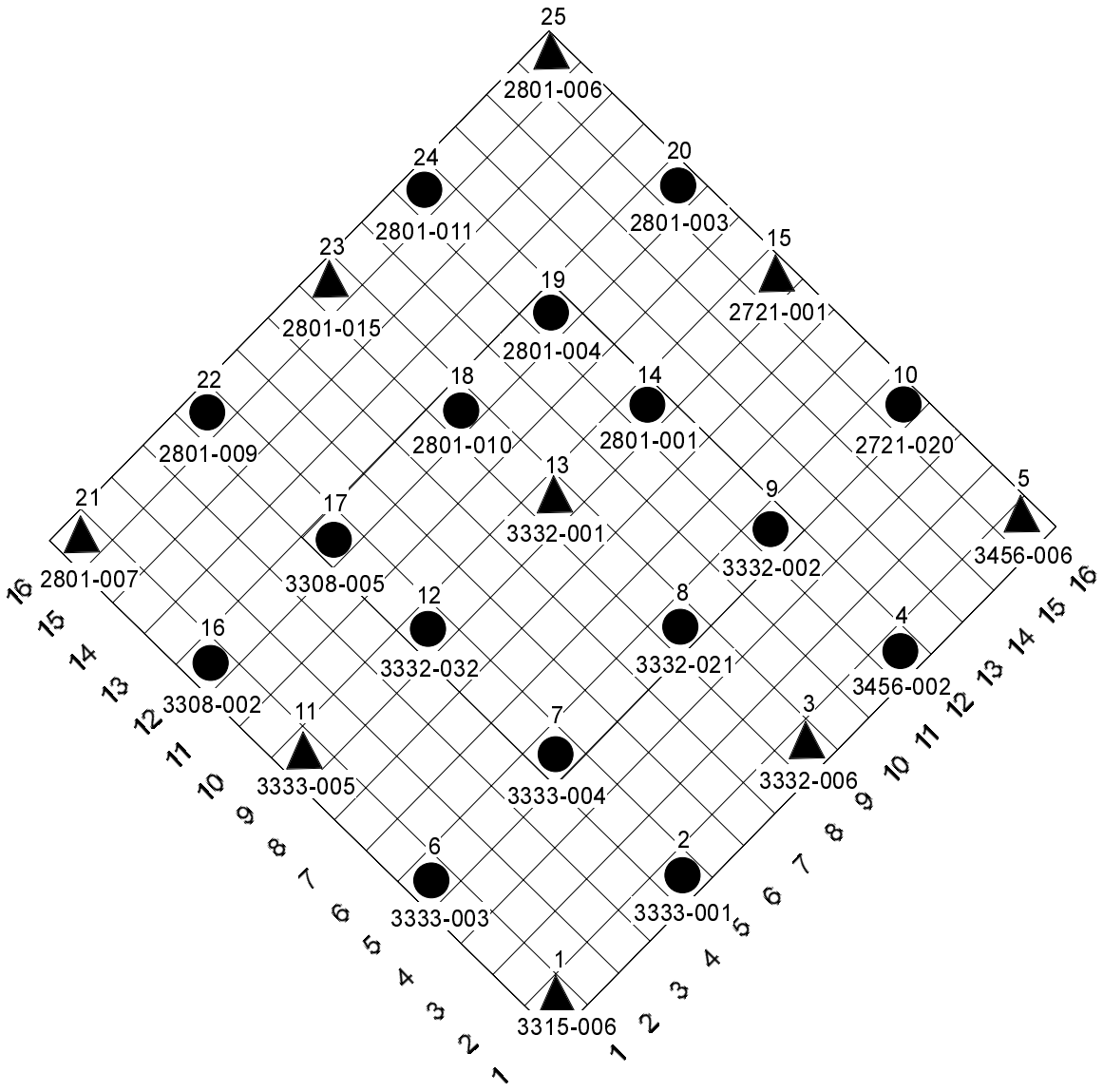

Fig. 114. The history match model, consisting of a 16 x 16 grid in seven separate layers for a total of 1792 grid blocks.

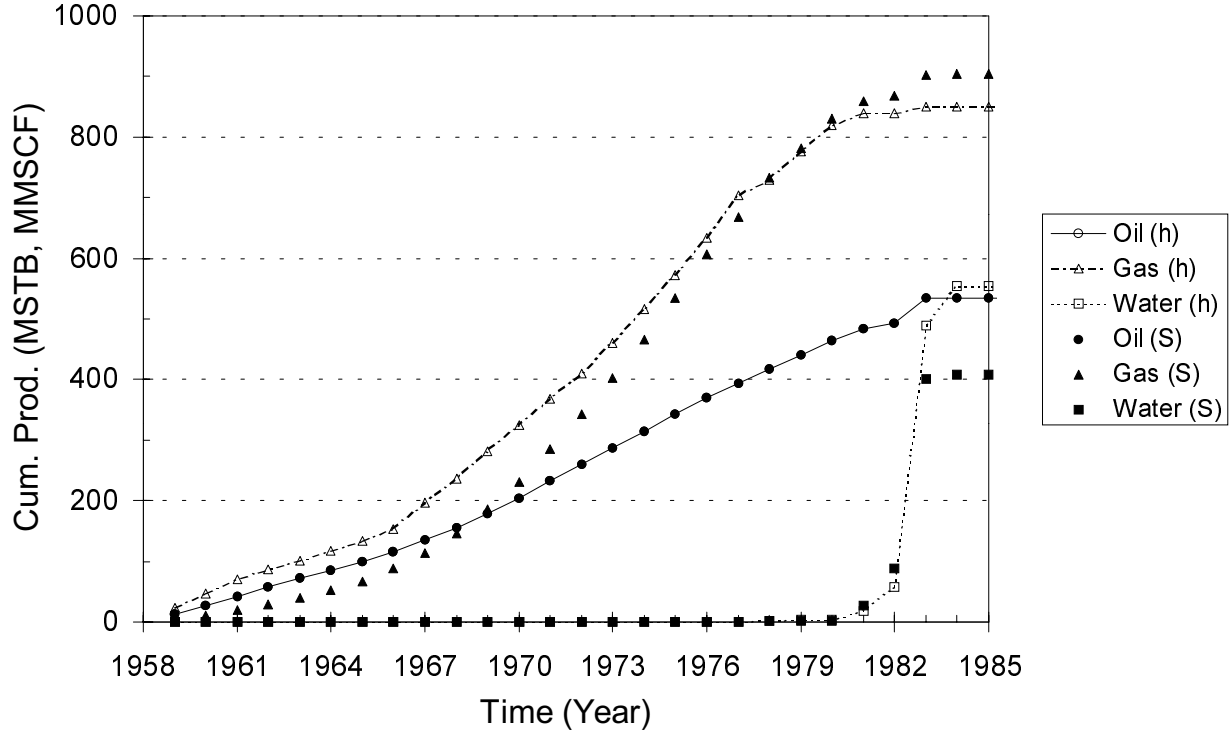

Fig. 115. Comparison of historical and simulated cumulative production for the offending well 3332-032 of the pilot area.

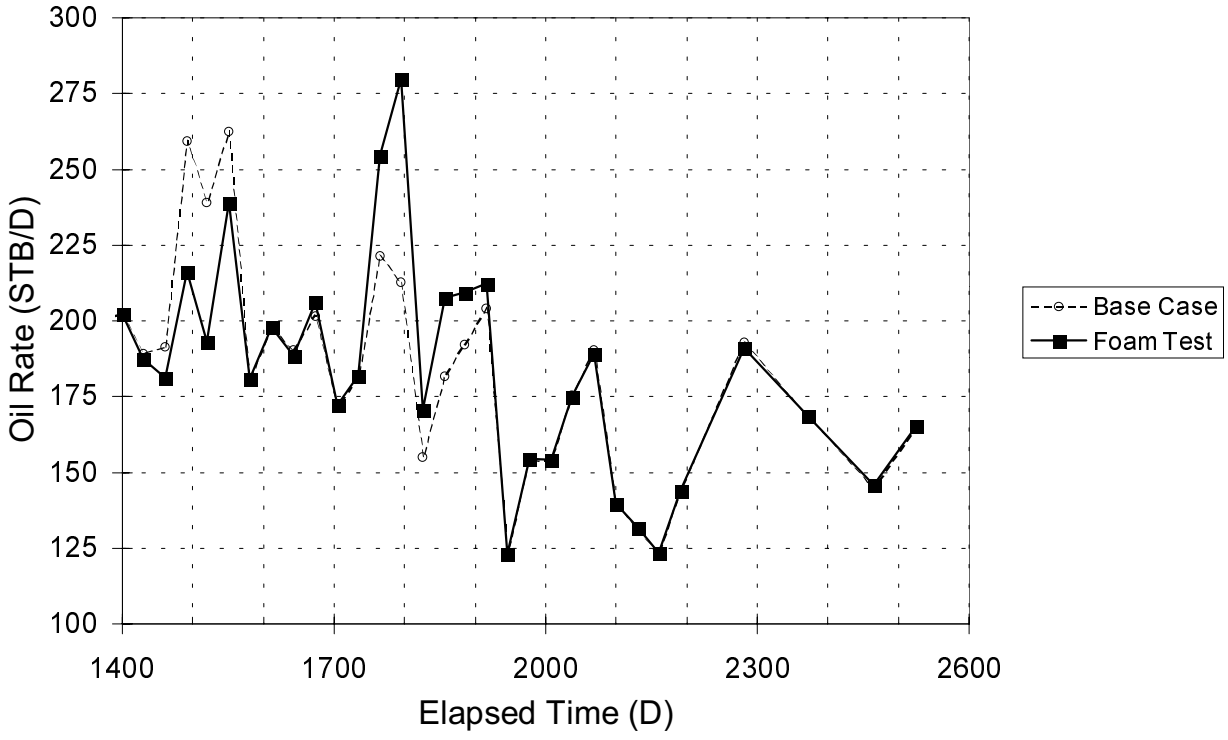

Fig. 116. Comparison of oil rate history between the foam test and the base case for the offending well.

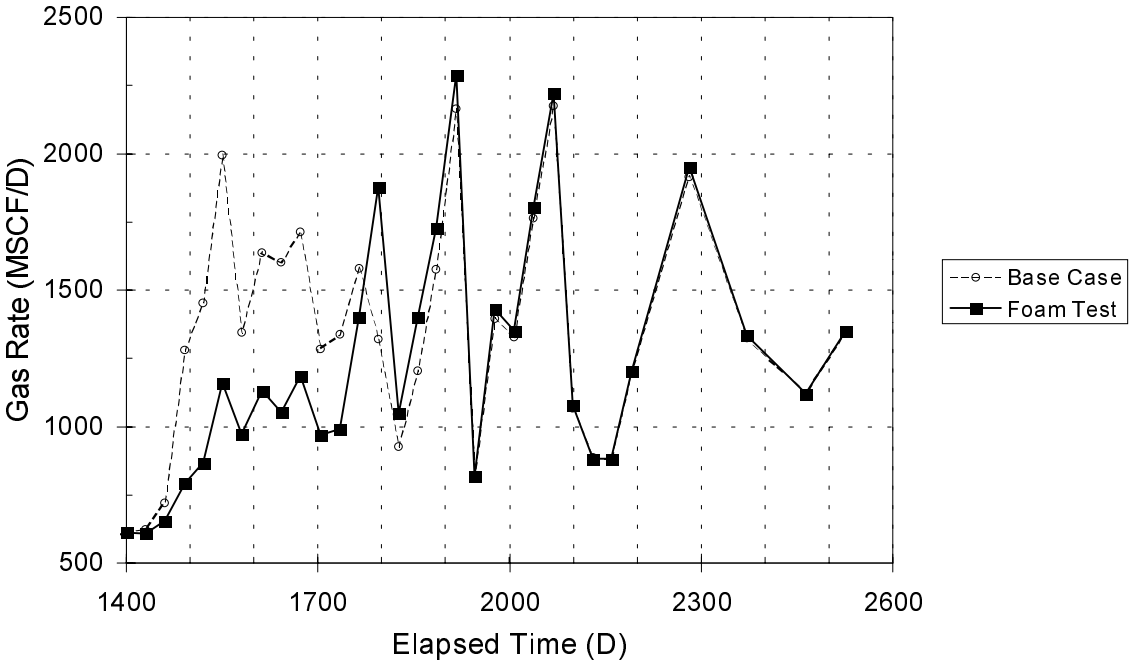

Fig. 117. Comparison of gas rate history between the foam test and the base case for the offending well.

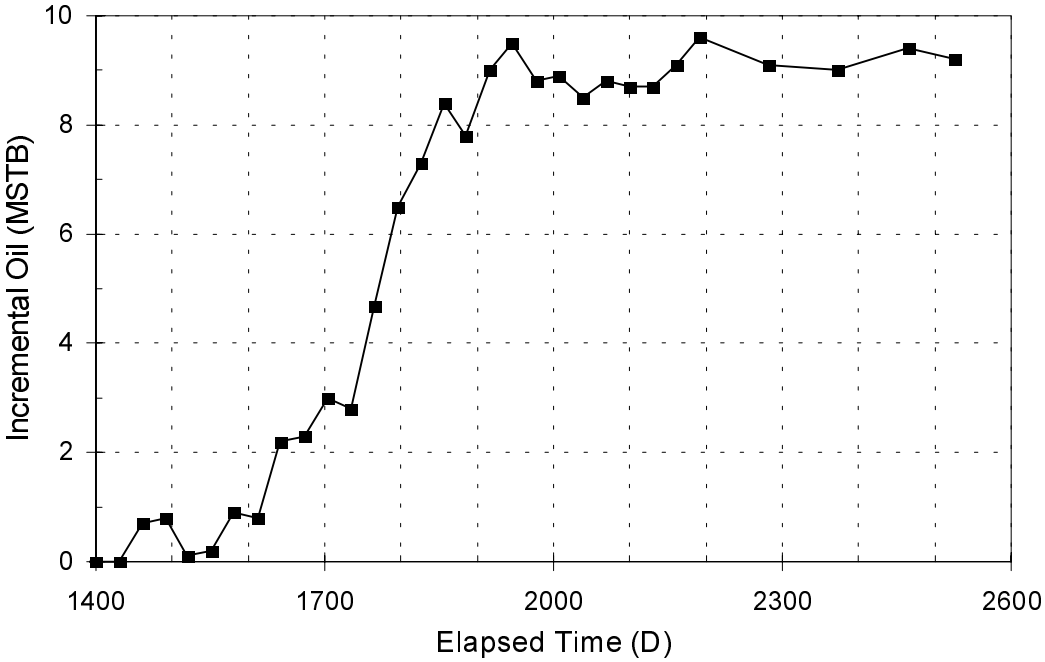

Fig. 118. Incremental oil for the foam test for the whole pilot area.

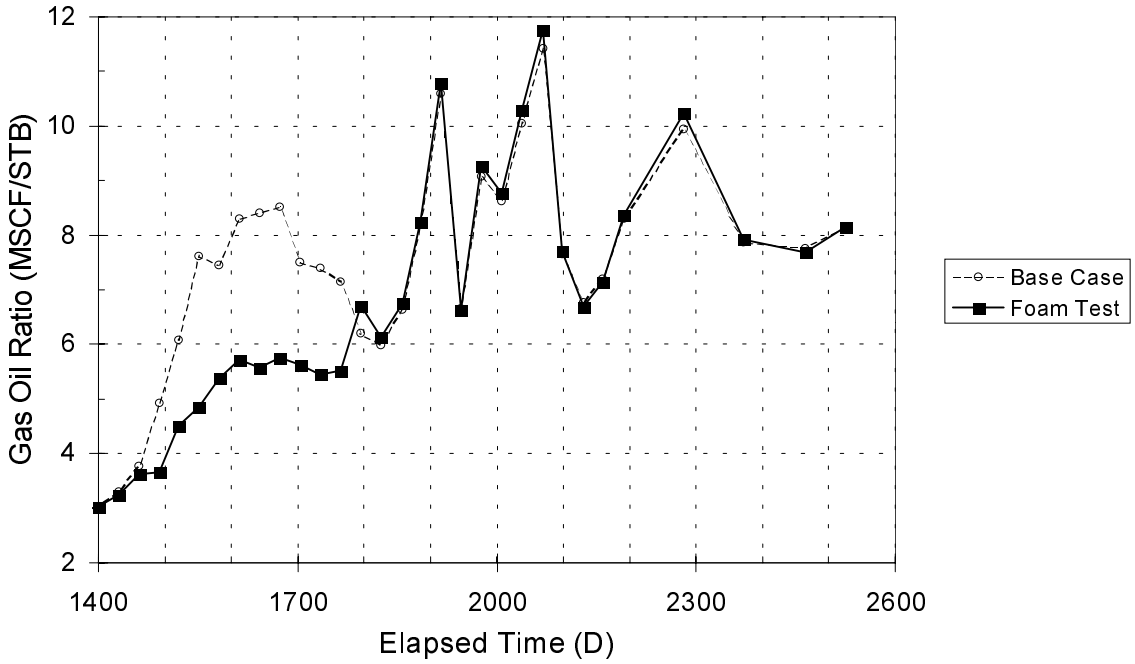

Fig. 119. Comparison of gas oil ratio between the foam test and the base case for the offending well.

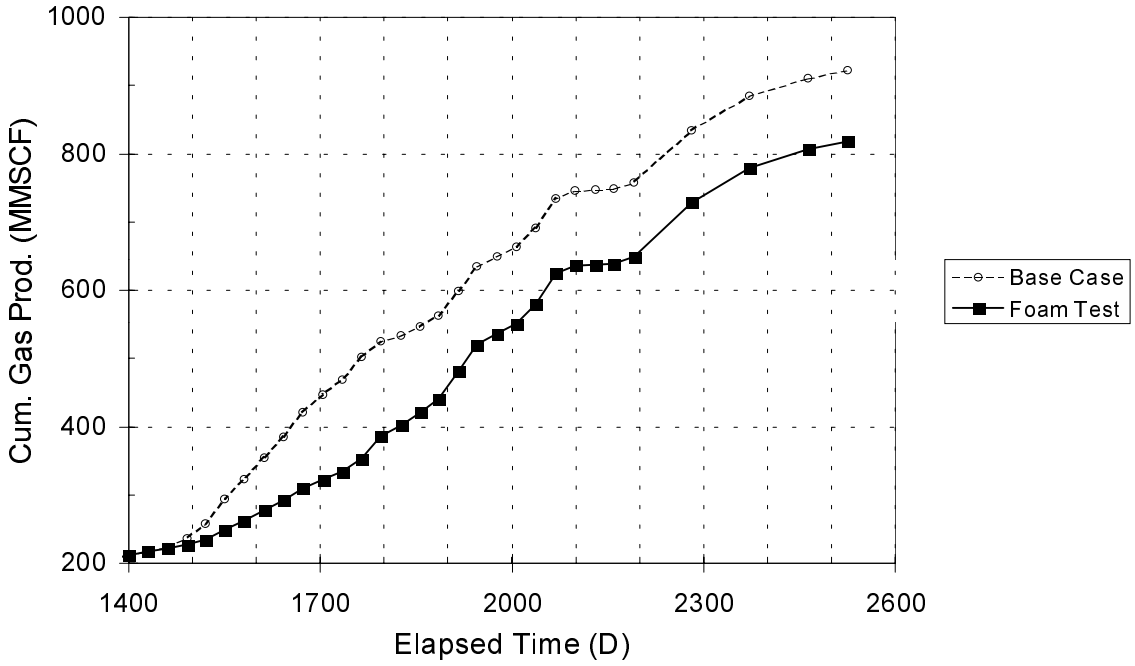

Fig. 120. Comparison of cumulative gas production between the foam test and the base case for the offending well.

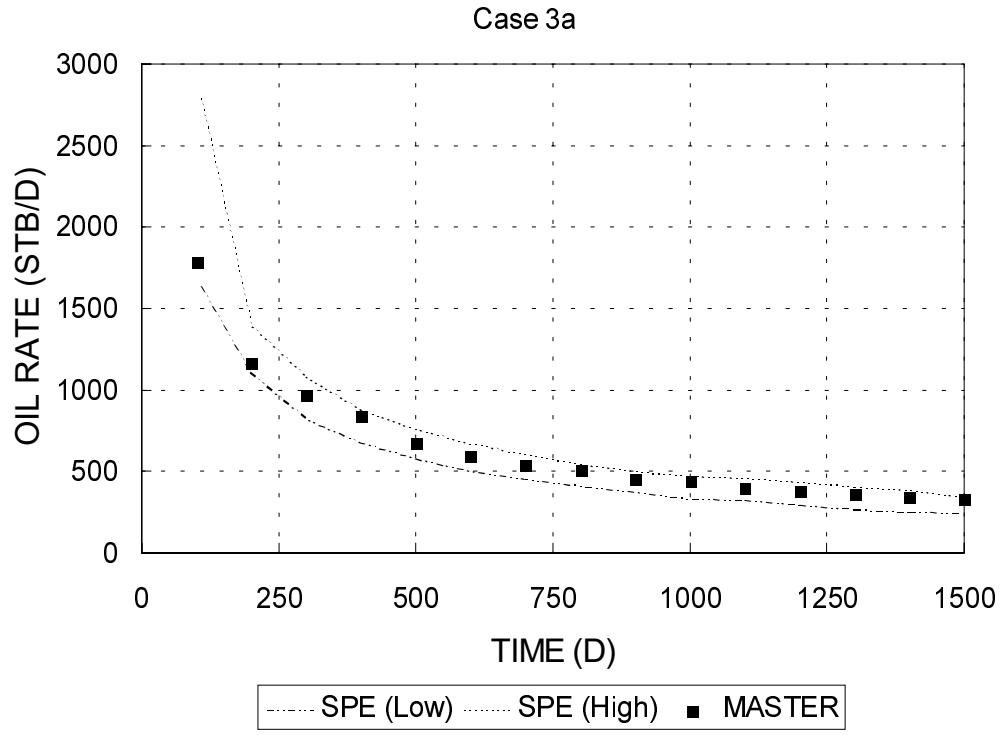

Fig. 121. Comparison of oil rate history for case 3a of seventh SPE comparative solution project.

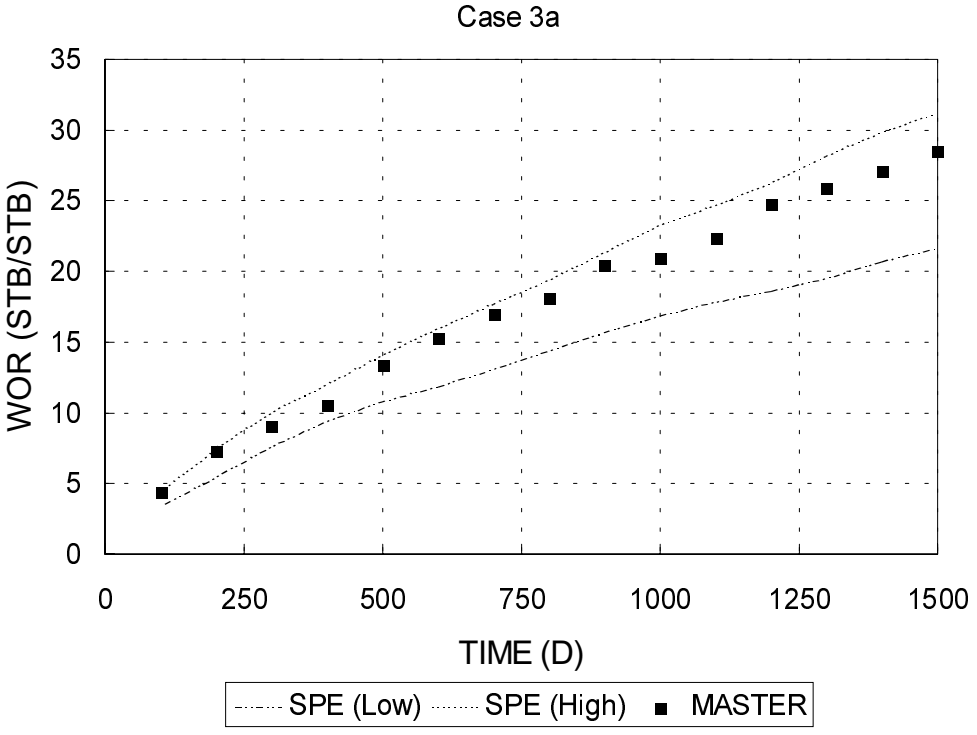

Fig. 122. Comparison of water-oil ratio for case 3a of seventh SPE comparative solution project

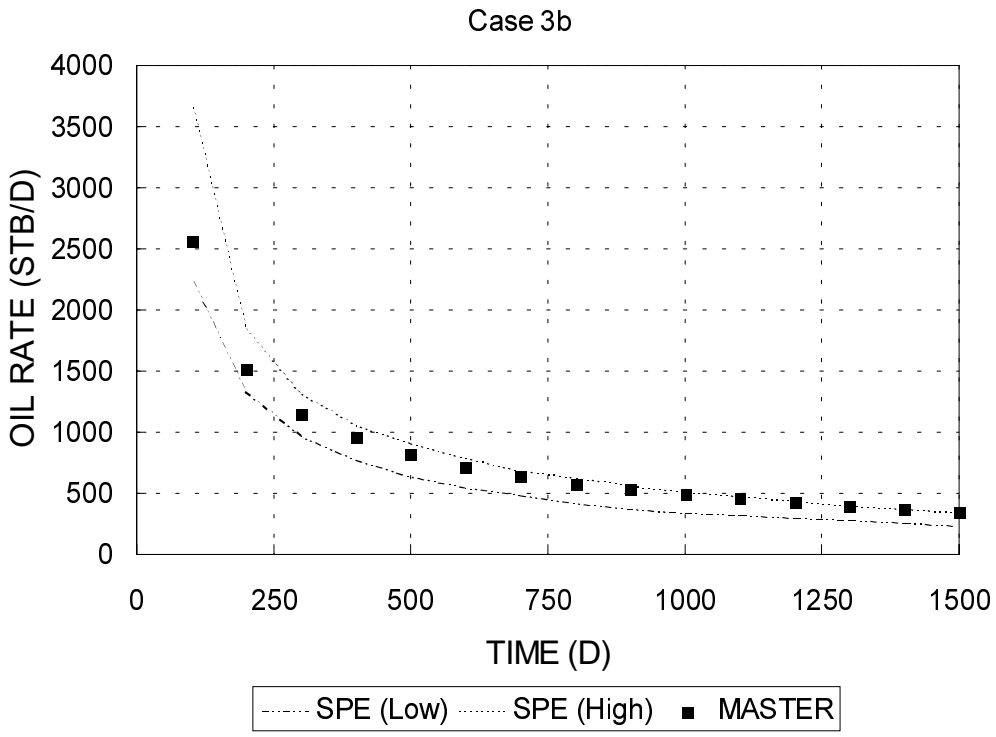

Fig. 123. Comparison of oil rate history for case 3b of seventh SPE comparative solution project.

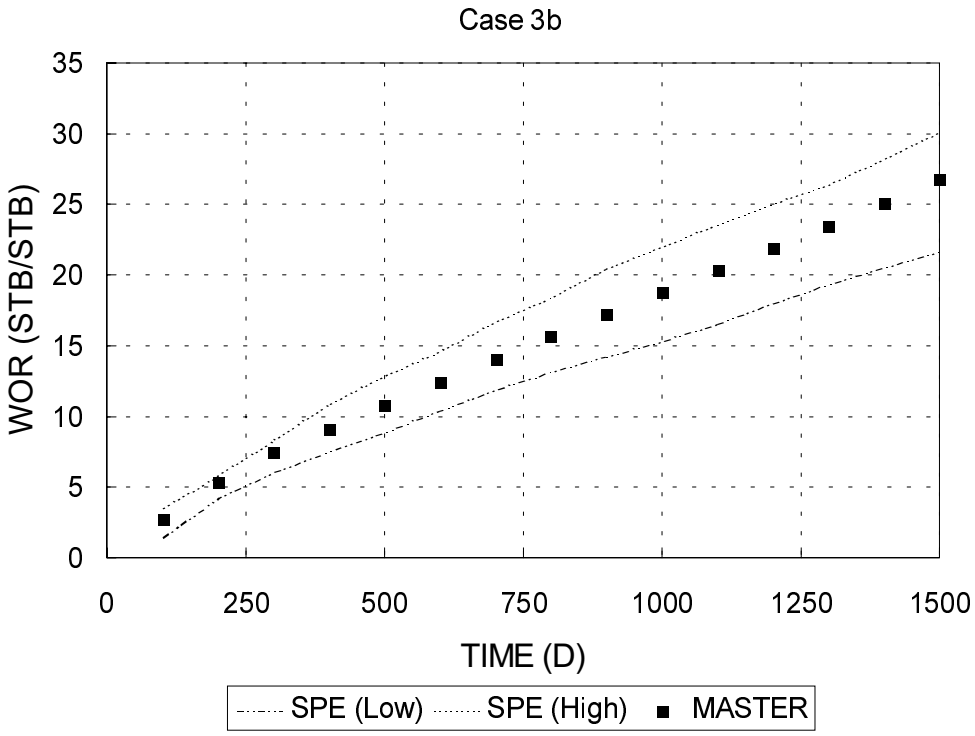

Fig. 124. Comparison of water-oil ratio for case 3b of seventh SPE comparative solution project.

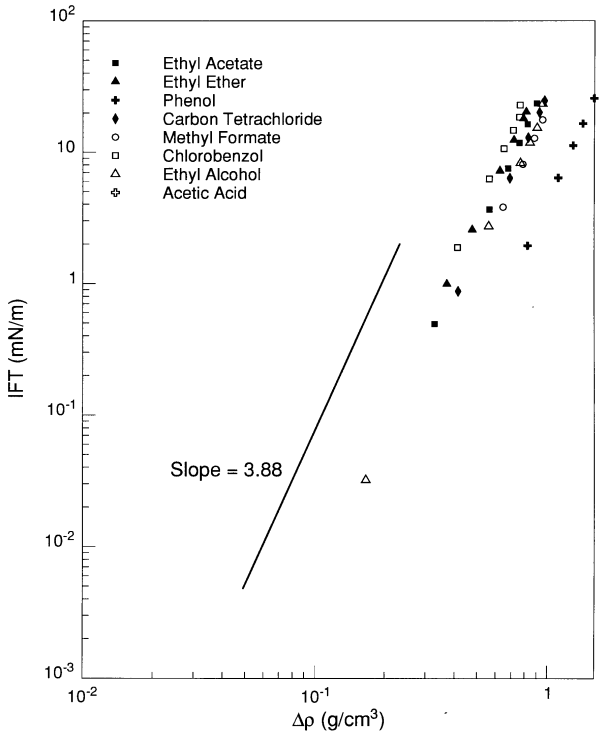

Fig. 125. Interfacial tension vs density difference measurements by Macleod (also shown in Table 24). Theoretical slope of 3.88 is shown for comparison.

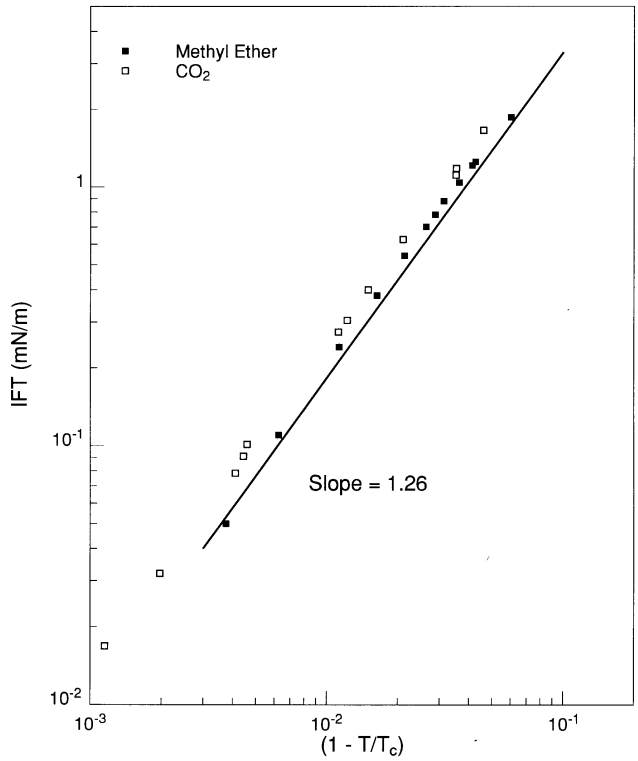

Fig. 126. Interfacial tension vs reduced temperature for methyl ether and CO_2. Theoretical slope of 1.26 is shown for comparison.

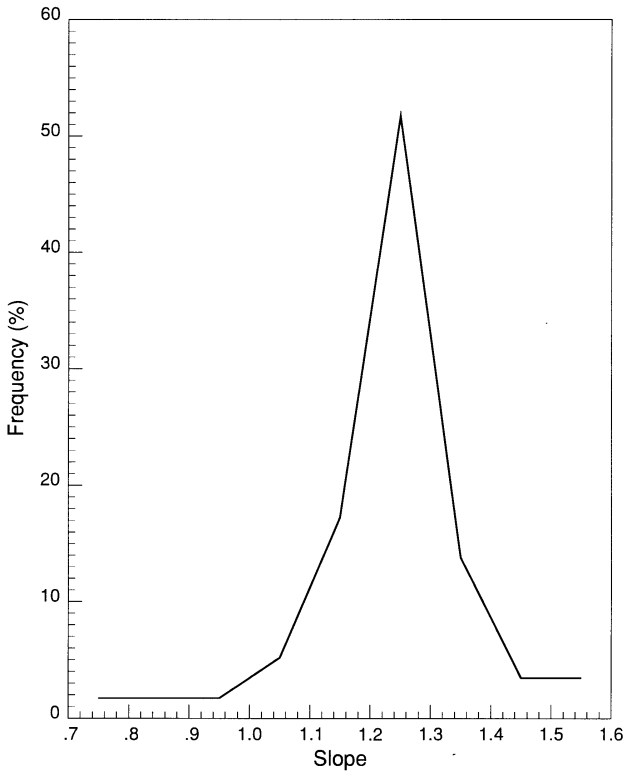

Fig. 127. Slope (γ in Eq. 6) distribution of IFT vs $(1-T/T_c)$ plots for 57 pure components.

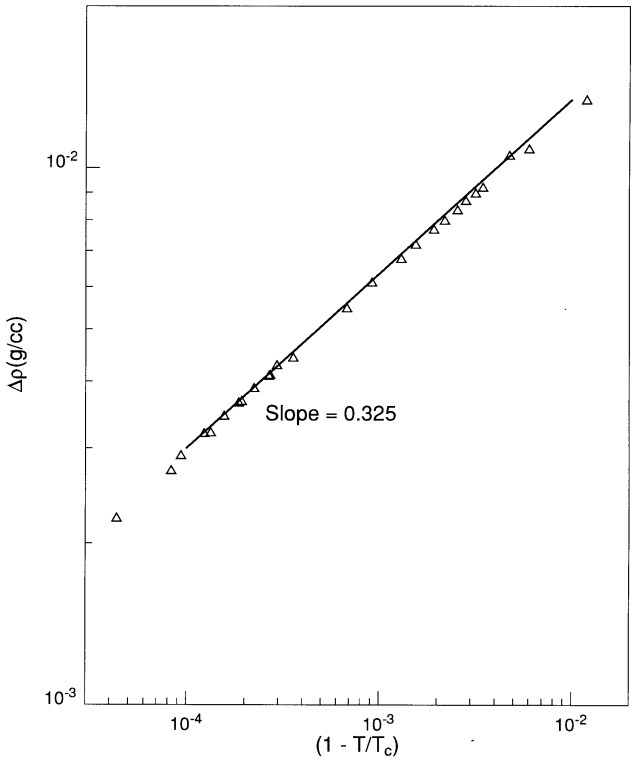

Fig. 128. Density difference vs reduced temperature for iso-butyric acid/water. Theoretical slope of 0.325 is shown for comparison.

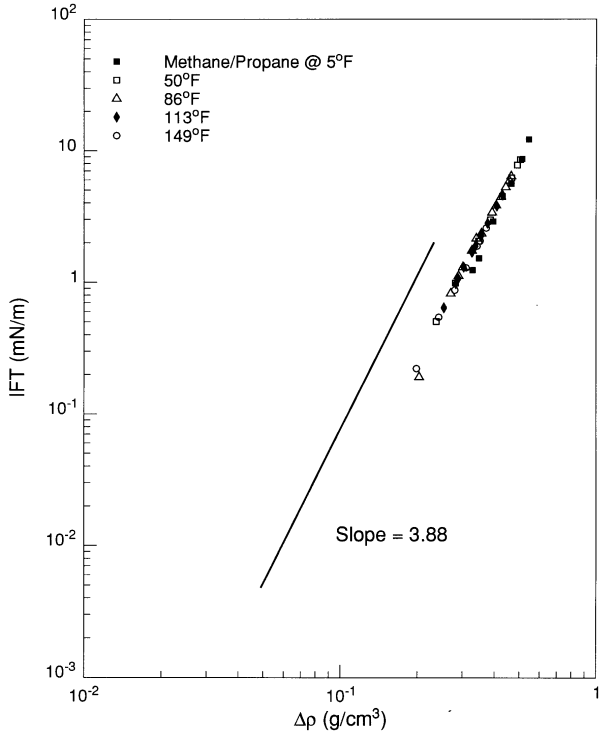

Fig. 129. Interfacial tension vs density difference for methane-propane mixtures. Theoretical slope of 3.88 is shown for comparison.

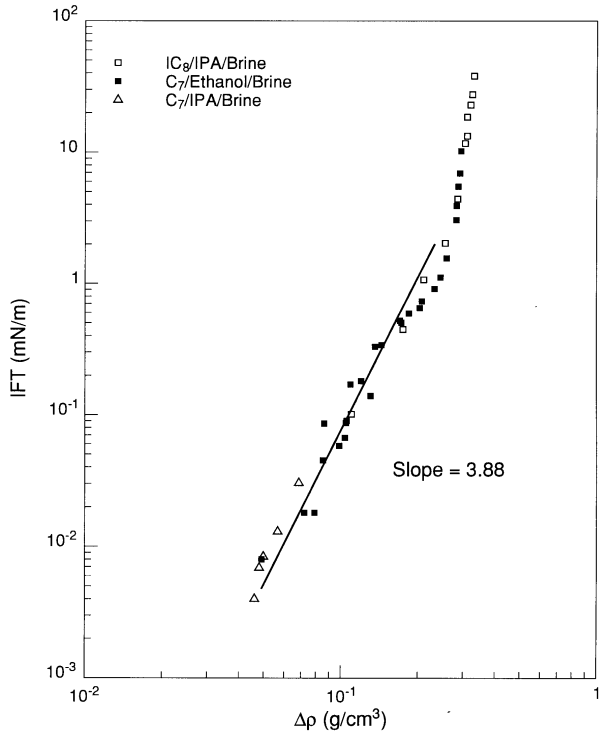

Fig. 130. Interfacial tension vs density difference for water/alcohol/oil systems. Theoretical slope of 3.88 is shown for comparison.

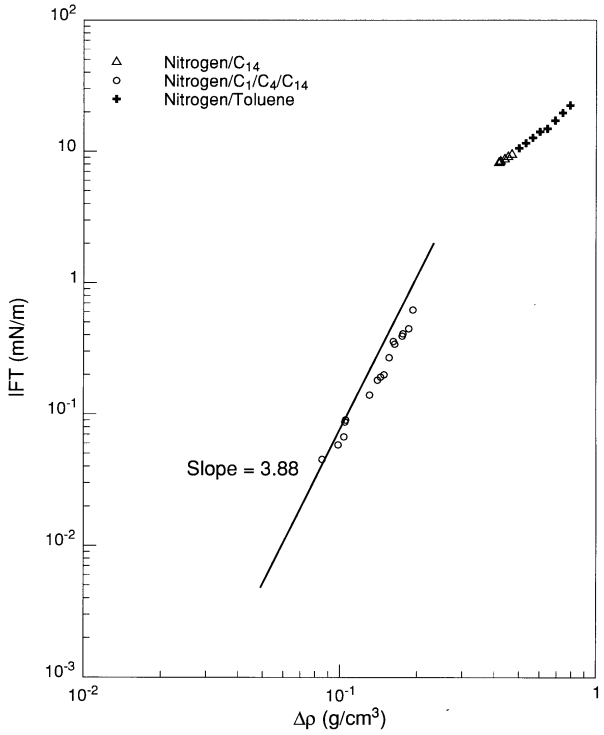

Fig. 131. Interfacial tension vs density difference for N_2/oil systems. Theoretical slope of 3.88 is shown for comparison.

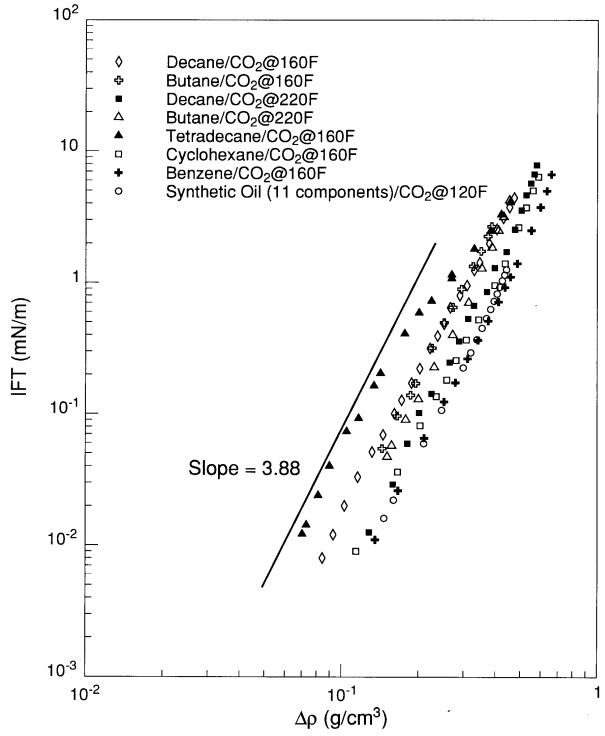

Fig. 132. Interfacial tension vs density difference for oil/CO_2 systems. Theoretical slope of 3.88 is shown for comparison.

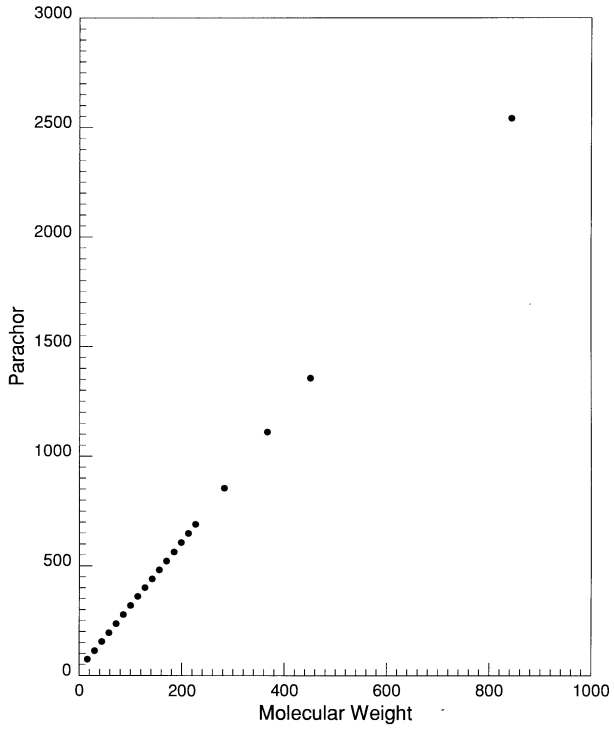

Fig. 133. Parachor vs molecular weight for 20 normal paraffins.

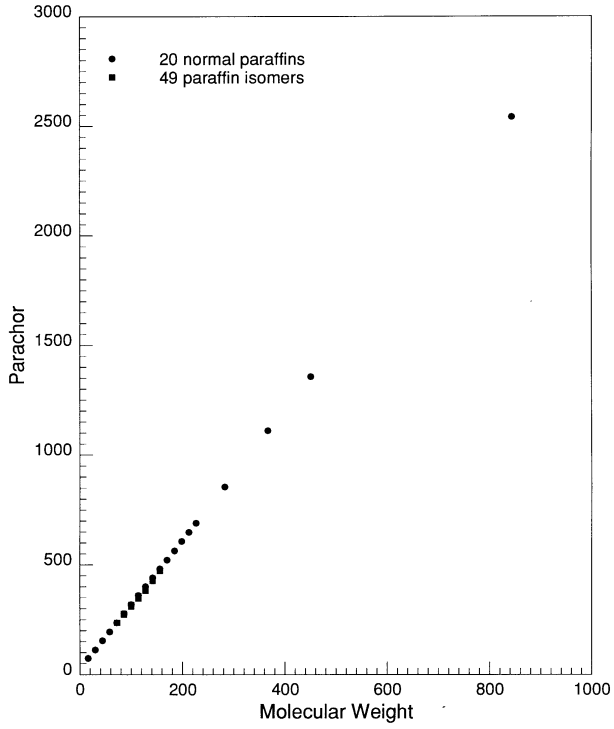

Fig. 134. Parachor vs molecular weight for 69 hydrocarbons.

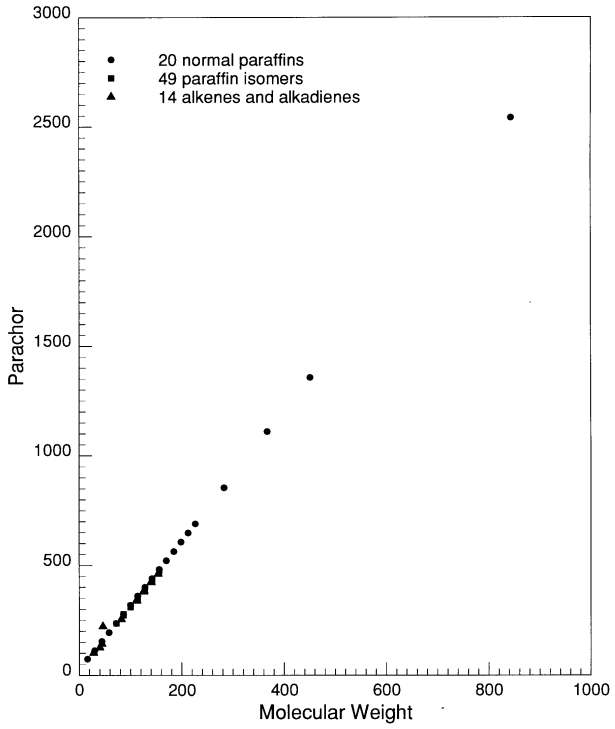

Fig. 135. Parachor vs molecular weight for 83 hydrocarbons.

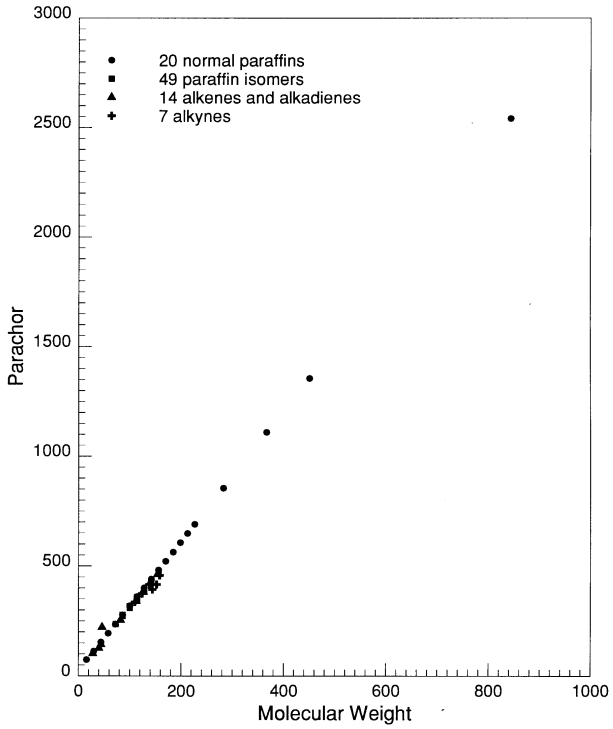

Fig. 136. Parachor vs molecular weight for 90 hydrocarbons.

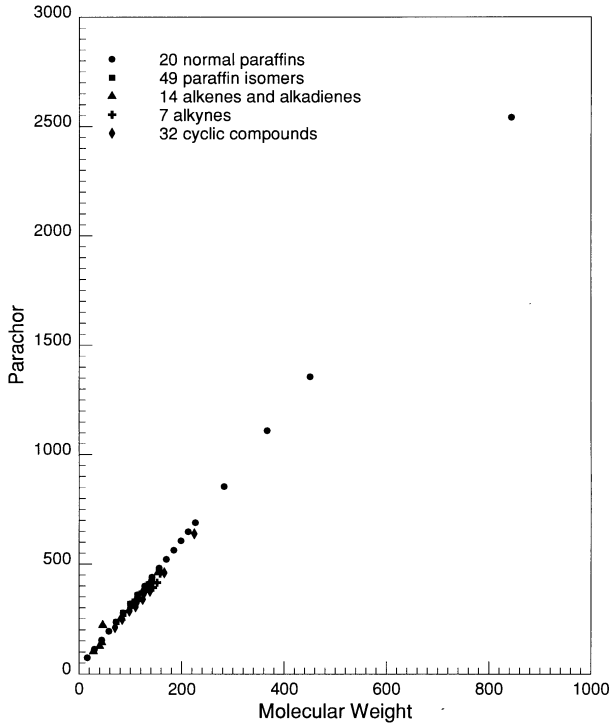

Fig. 137. Parachor vs molecular weight for 122 hydrocarbons.

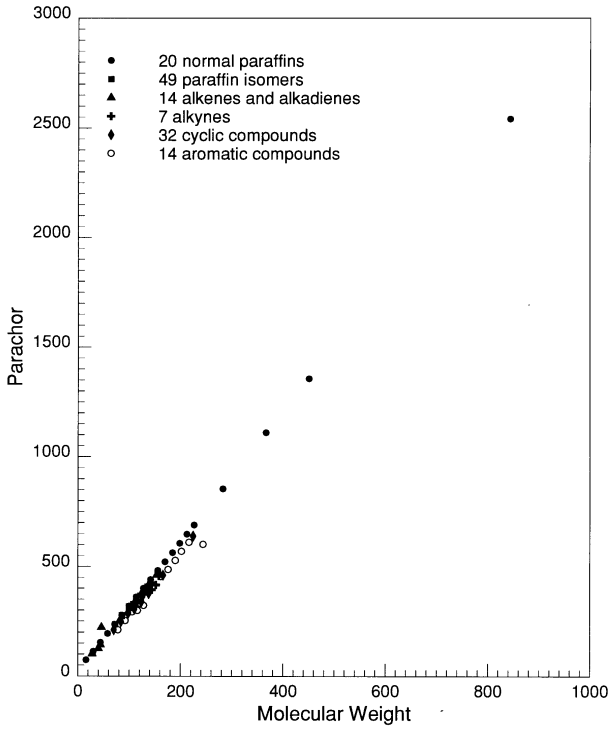

Fig. 138. Parachor vs molecular weight for 136 hydrocarbons.

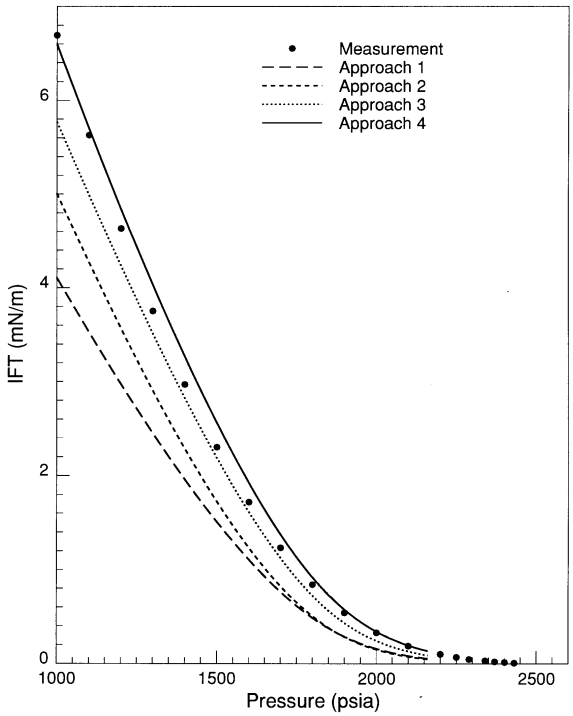

Fig. 139. Measured and PREOS-predicted IFTs of system VI.

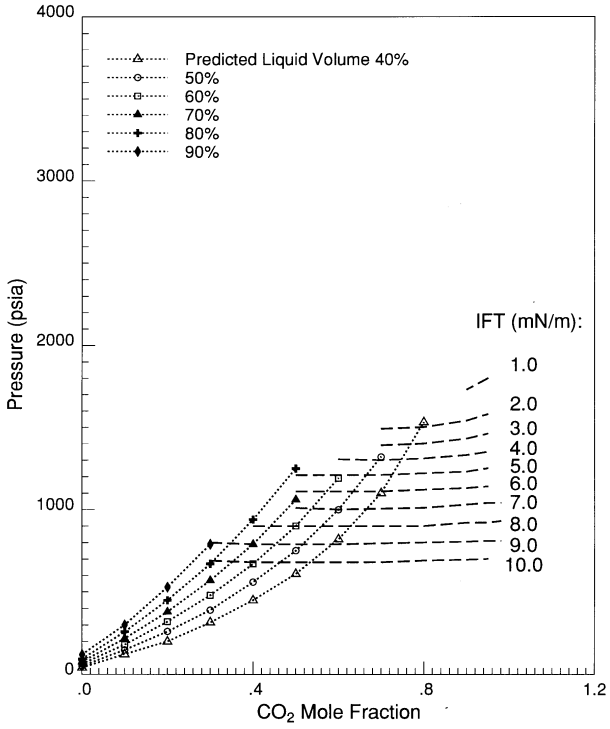

Fig. 140. PREOS-predicted IFTs of Spraberry separator oil.

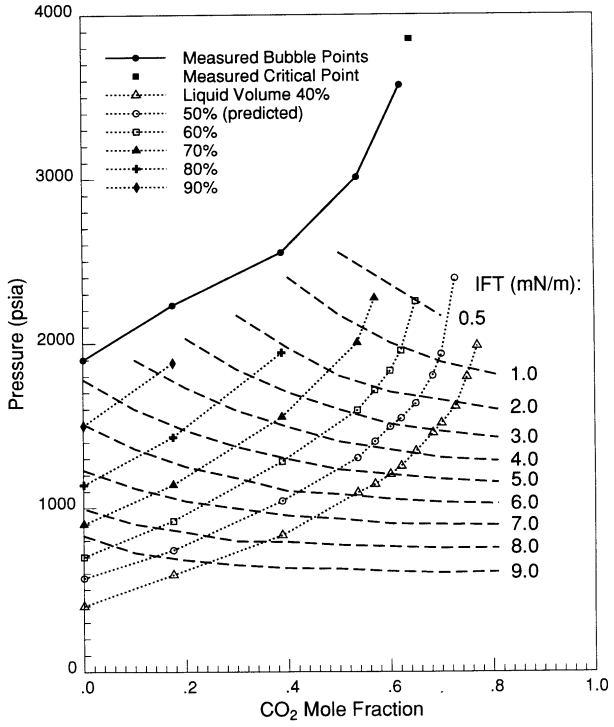

Fig. 141. PREOS-predicted IFTs of CO_2/Spraberry reservoir oil.

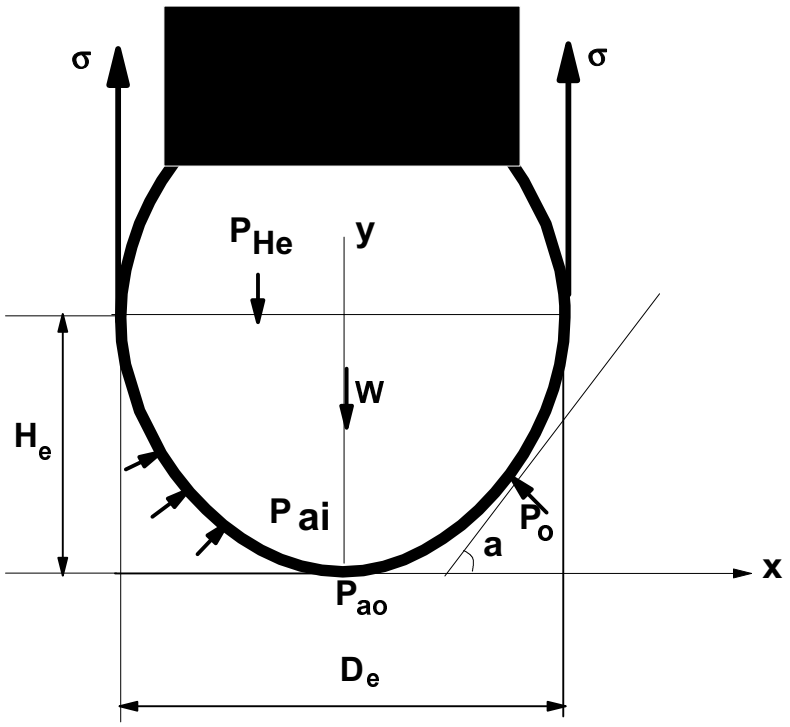

Fig. 142. Geometry of a pendant drop.

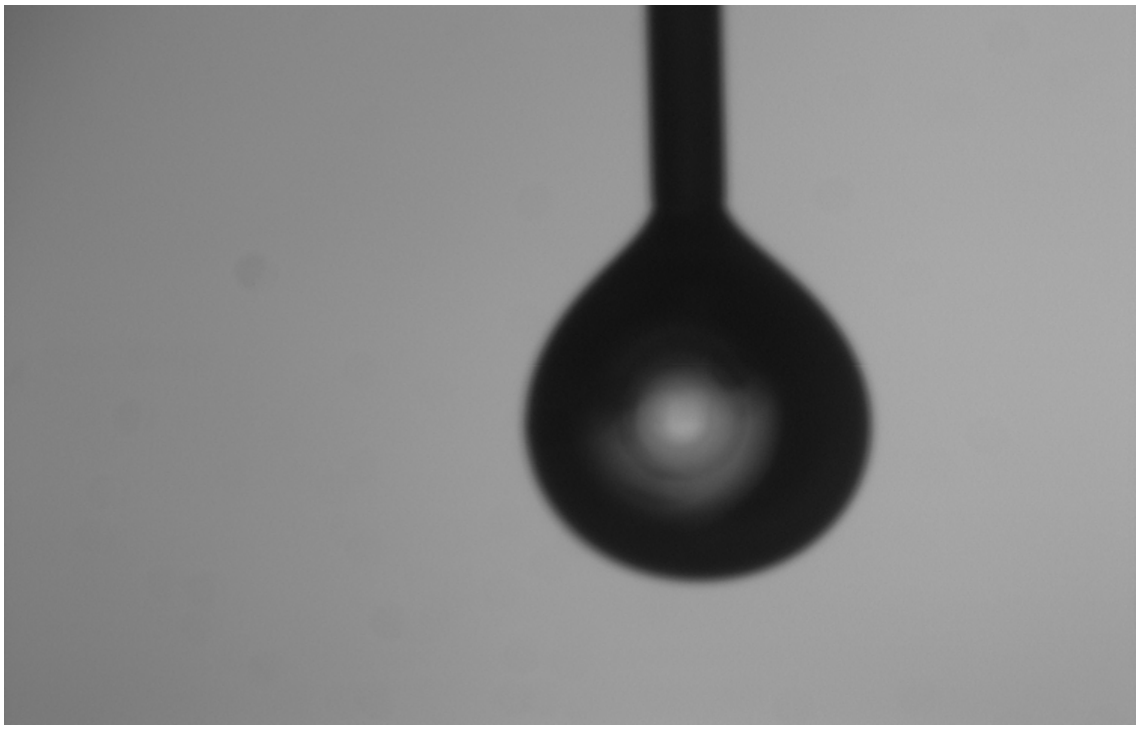

Fig. 143. Pendant drop for nitrogen/water system.

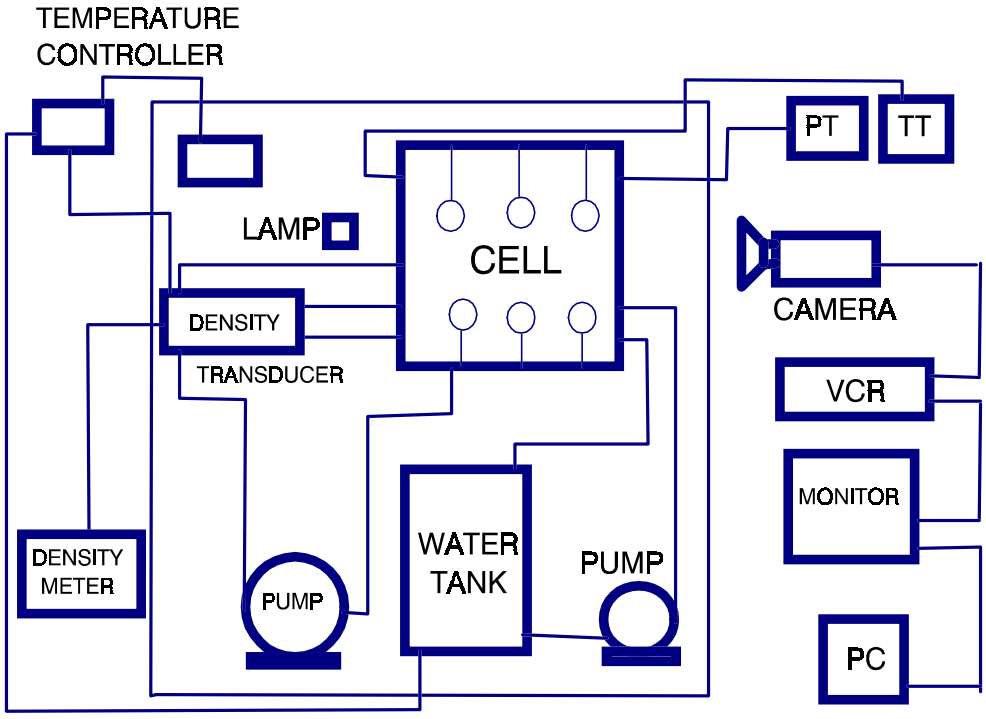

Fig. 144. Sketch of pendant drop experimental setup.

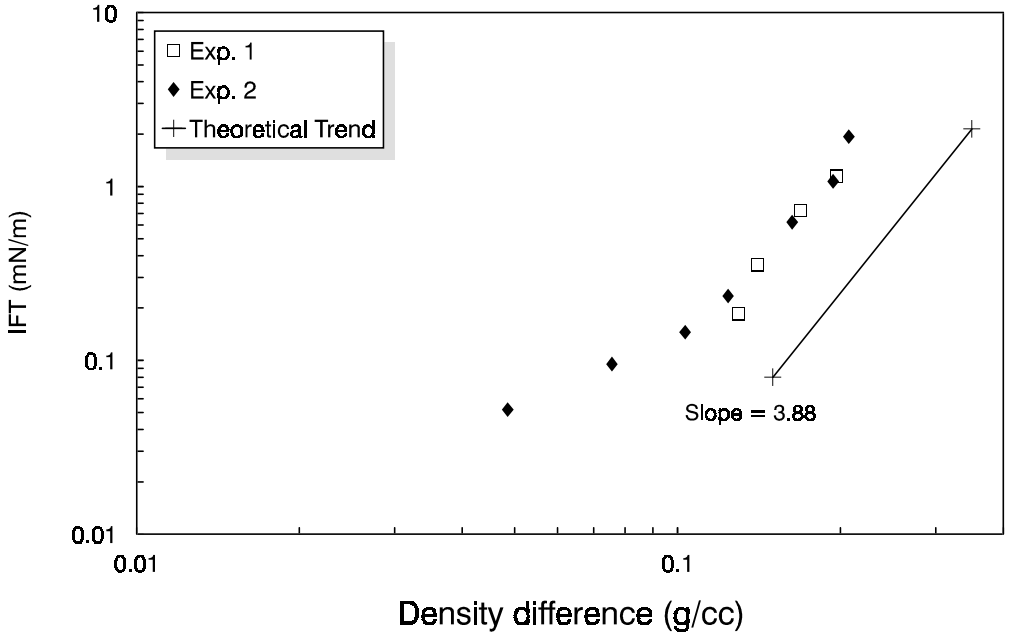

Fig. 145. Measured IFT for brine/heptane/alcohol system.

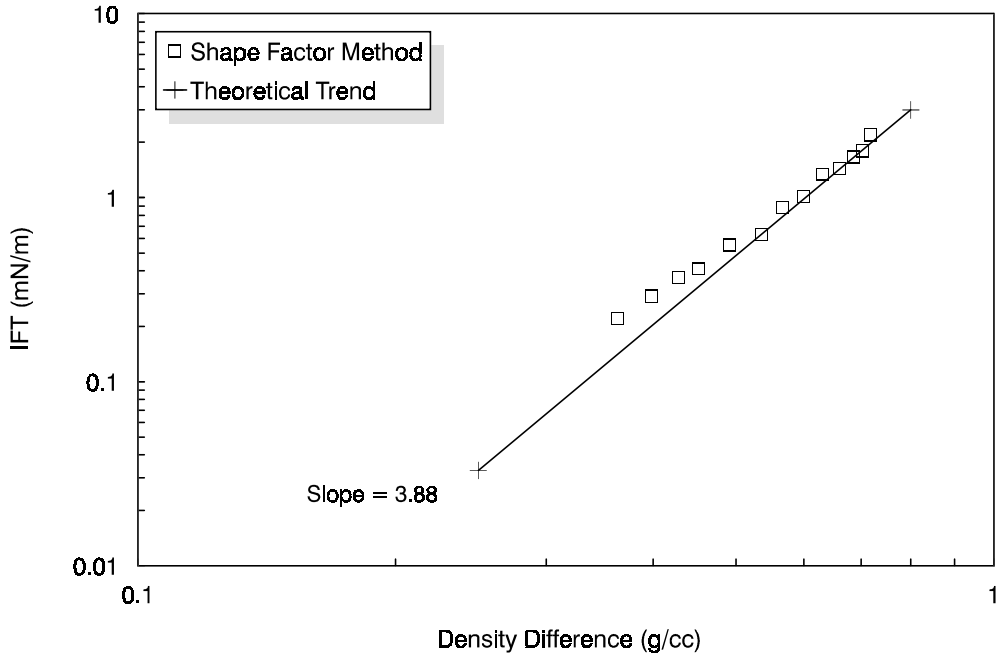

Fig. 146. IFT versus density difference for pure CO_2.

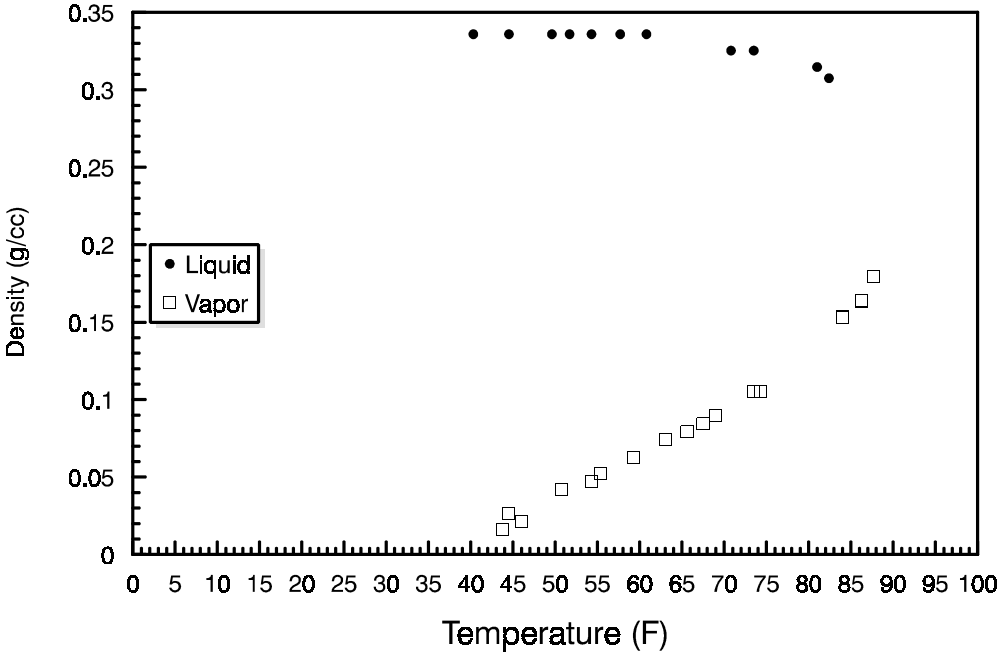

Fig. 147. Measured ethane densities.

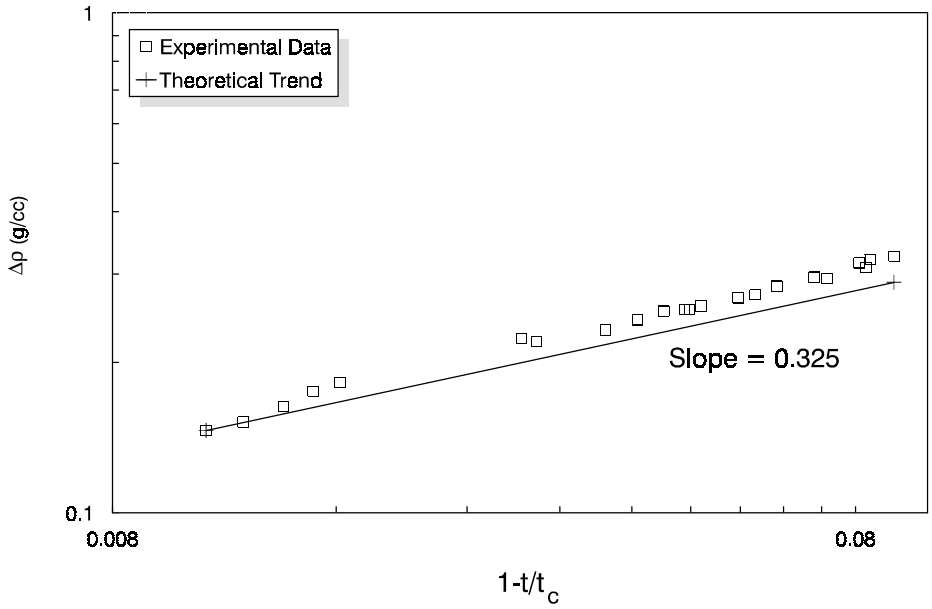

Fig. 148. Surface tension versus reduced temperature for ethane.

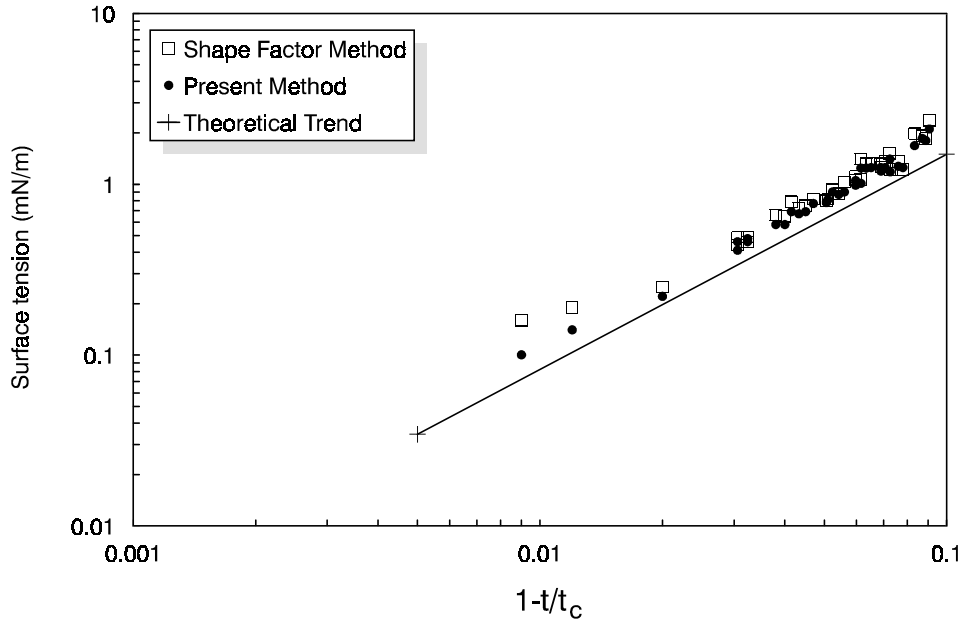

Fig. 149. Surface tension of ethane versus reduced temperature.

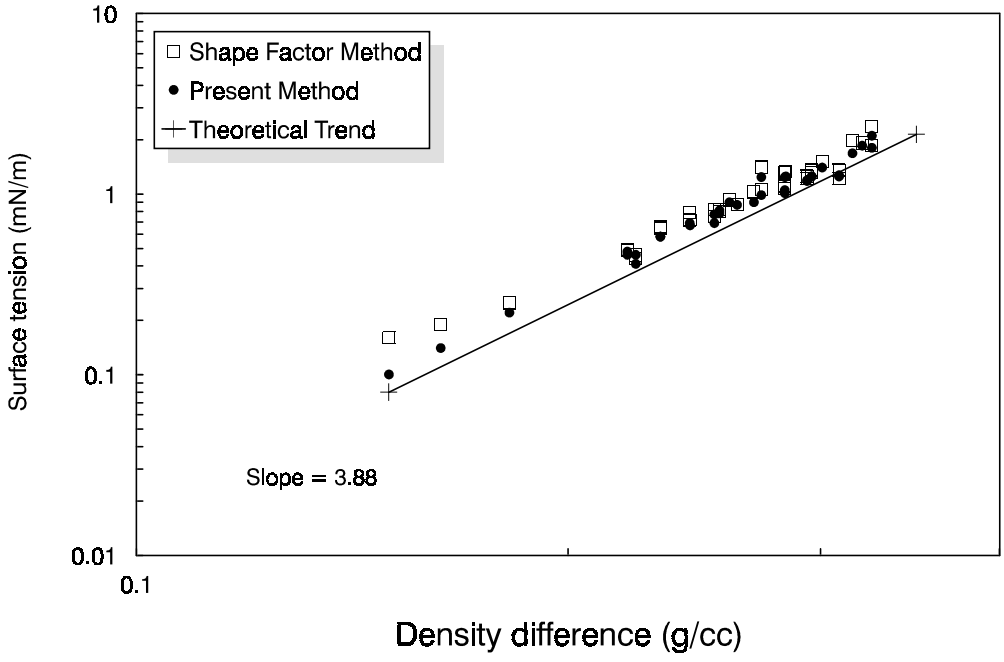

Fig. 150. Surface tension versus density difference for ethane.

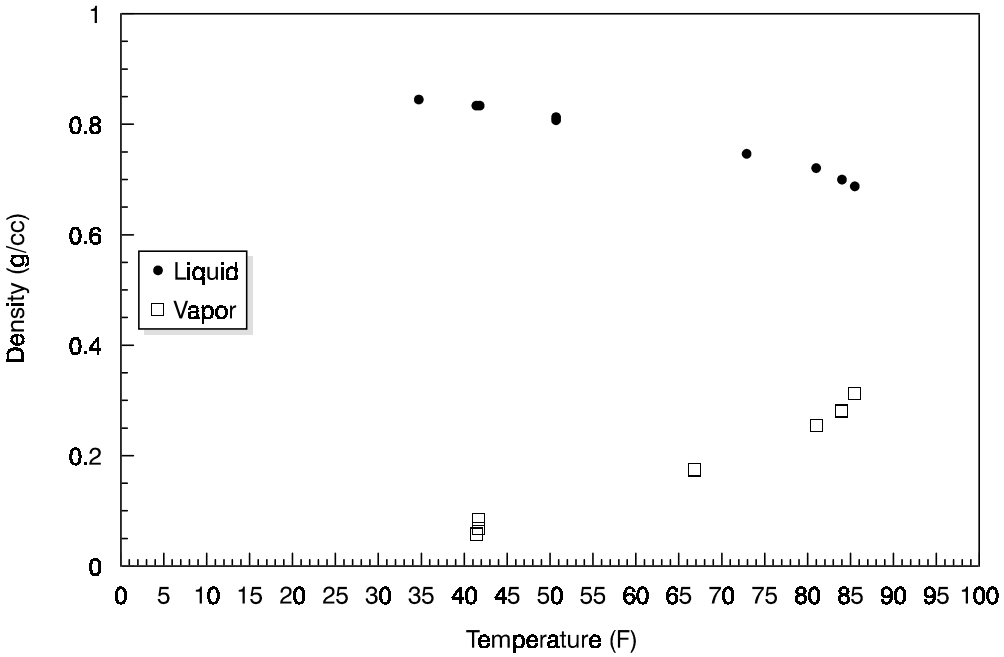

Fig. 151. Measured phase densities for CO_2.

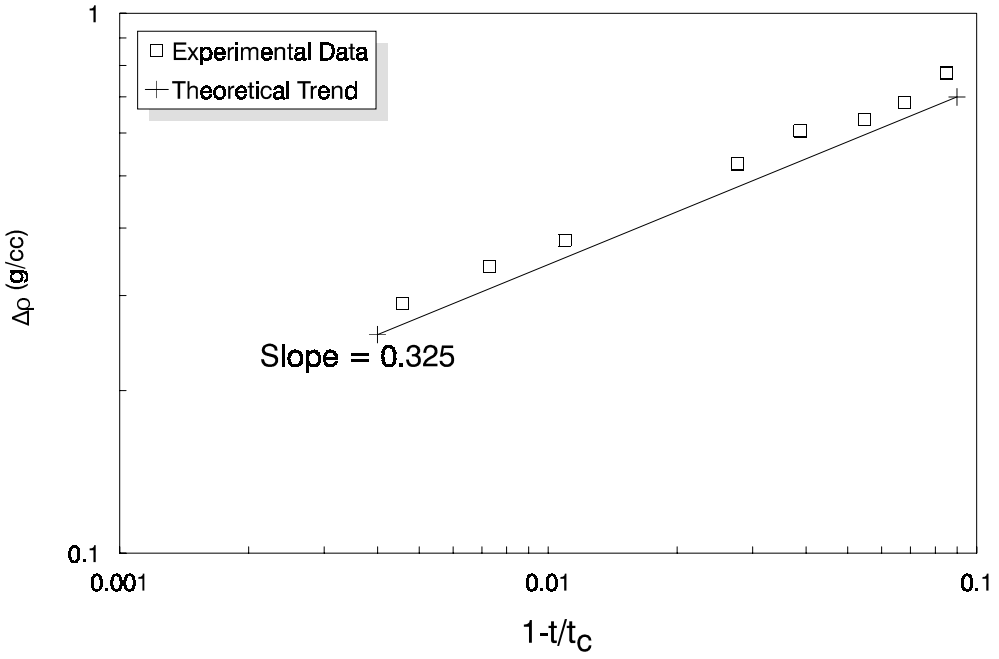

Fig. 152. Density differences for CO_2 versus reduced temperature.

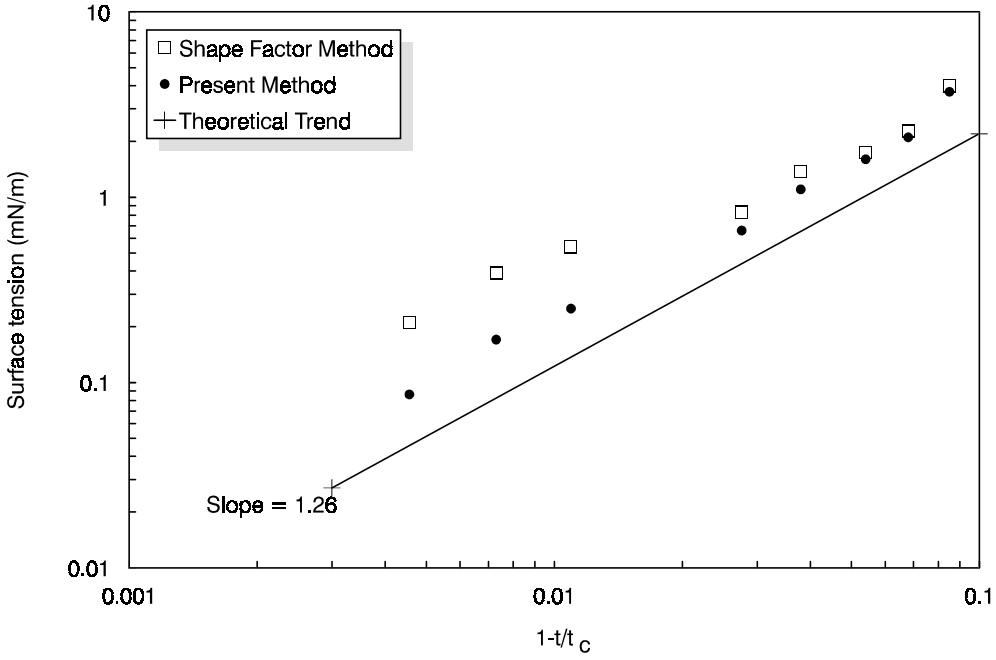

Fig. 153. Surface tension versus reduced temperature for CO_2.

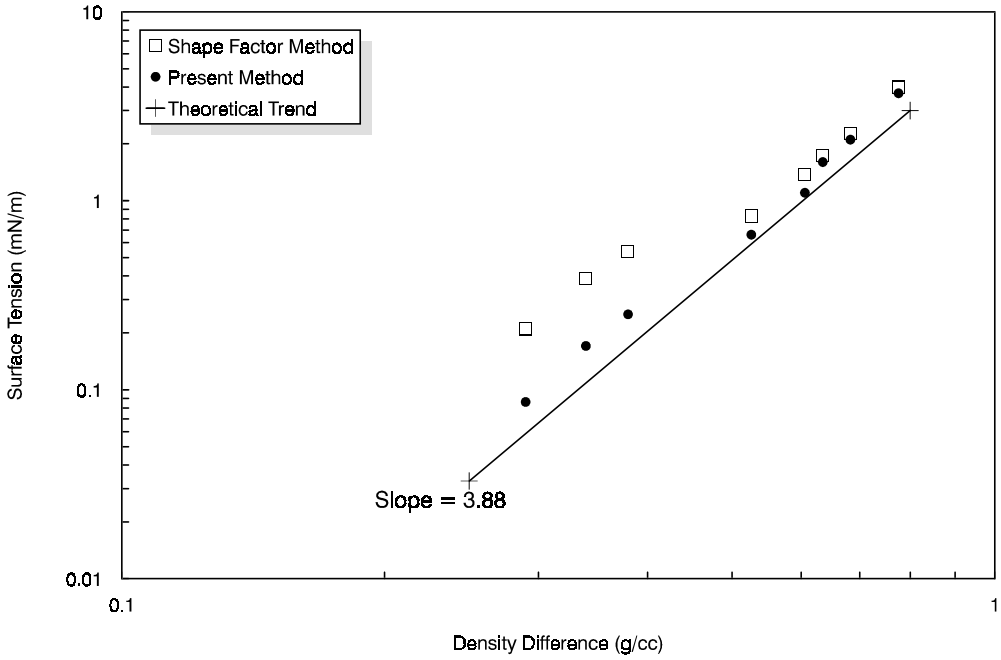

Fig. 154. Surface tension versus density difference for CO_2.

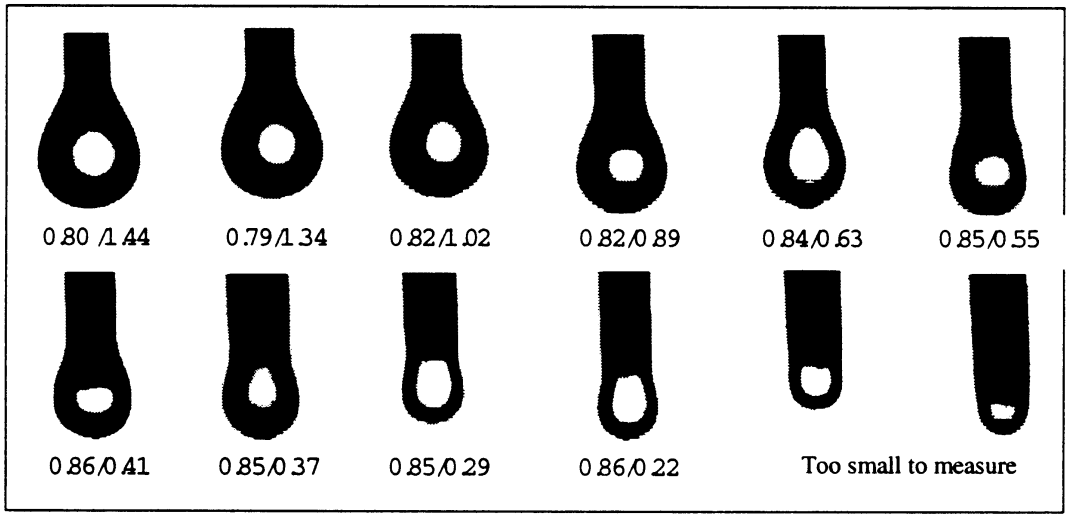

Fig. 155. Shape factor/surface tension of pure CO_2 drops. Note change in shape as low IFT is attained.

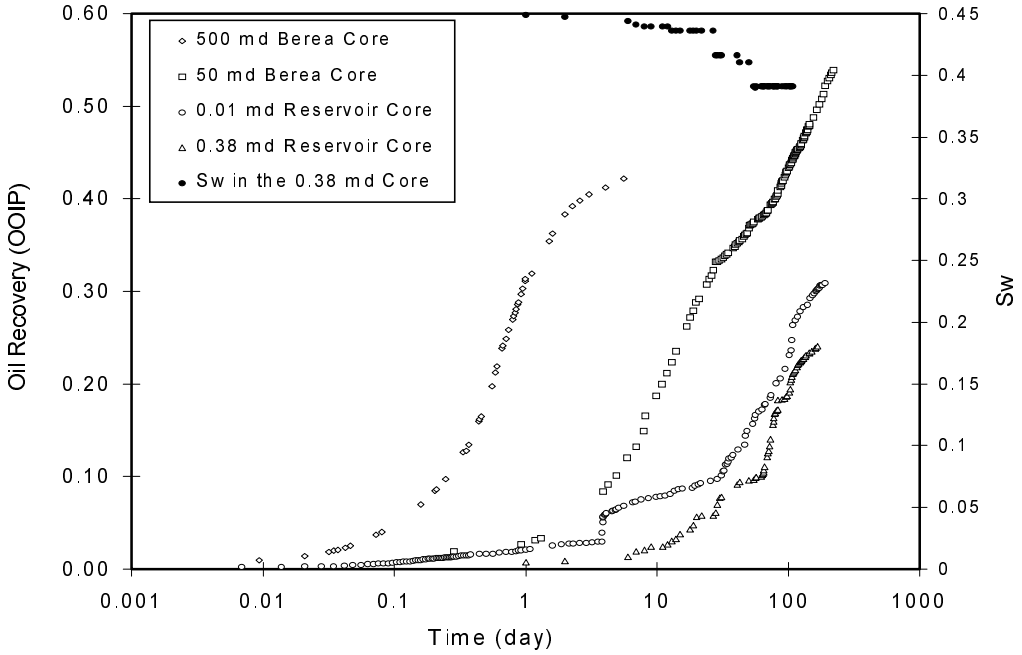

Fig. 156. Pressure history for low permeability core experiment.

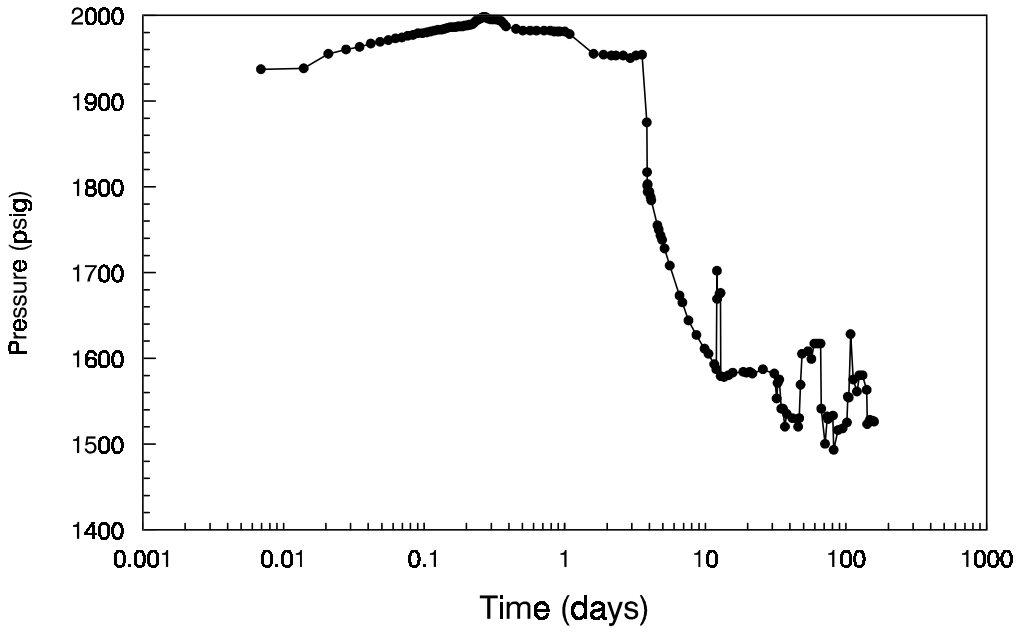

Fig. 157. Pressure history for low permeability core experiment.

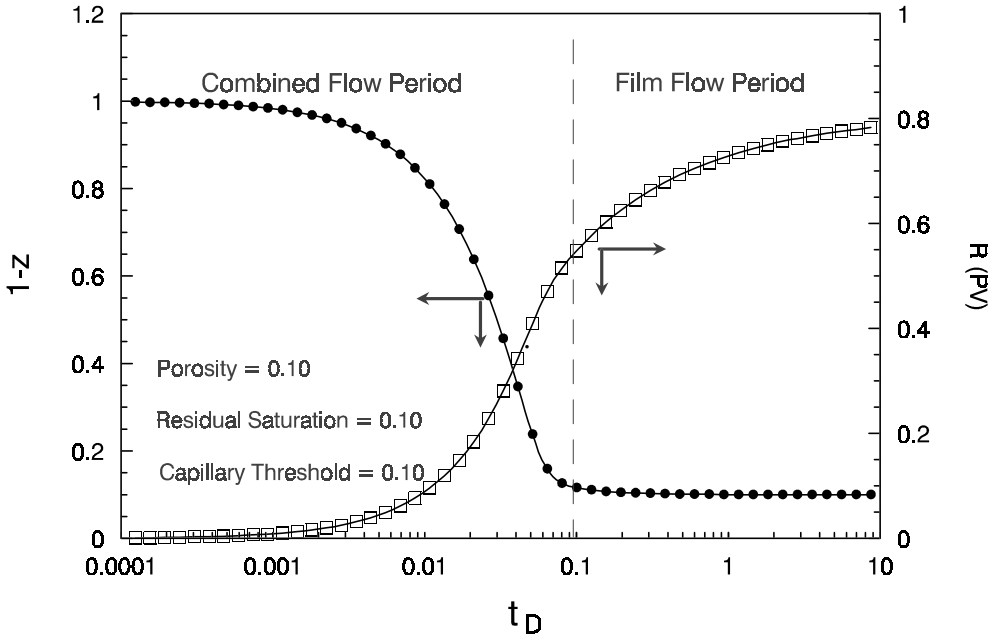

Fig. 158. Solution to demarcator and recovery for Fs = 1.0.

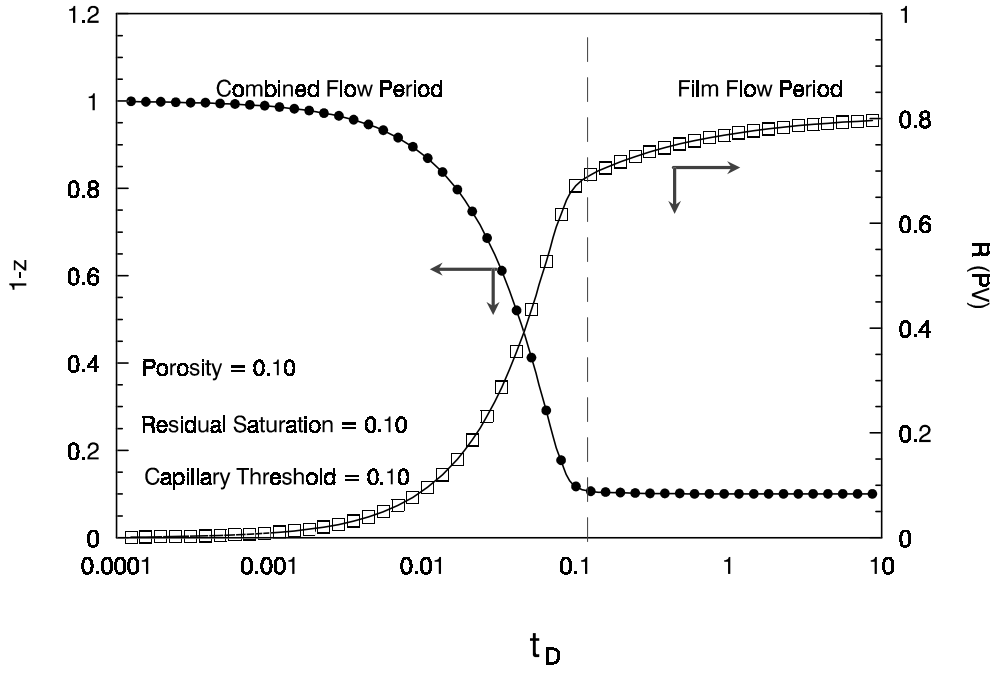

Fig. 159. Solution to demarcator and recovery for Fs = 0.5.

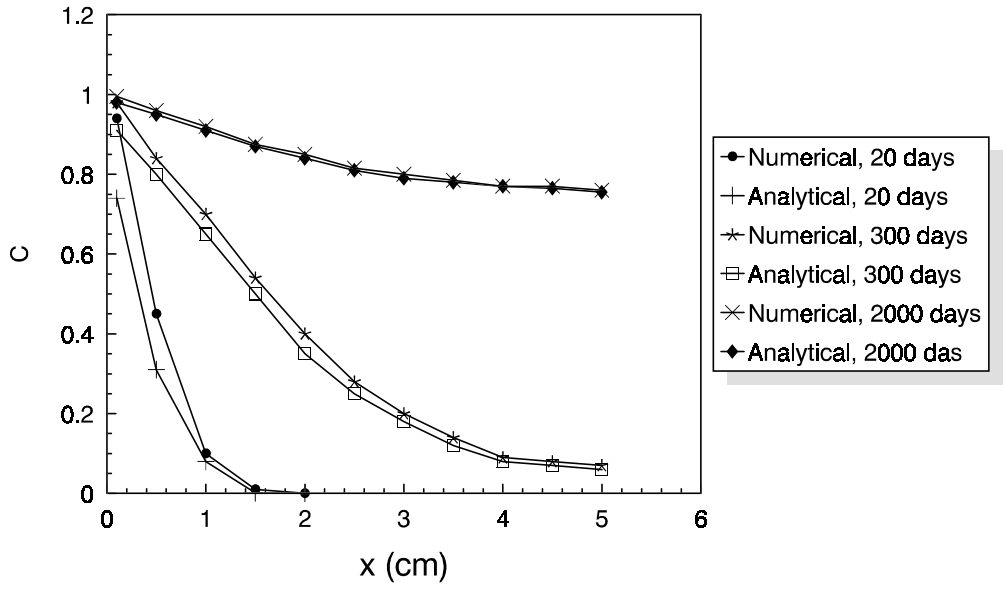

.

Fig. 160. Model calculated dimensionless concentration.

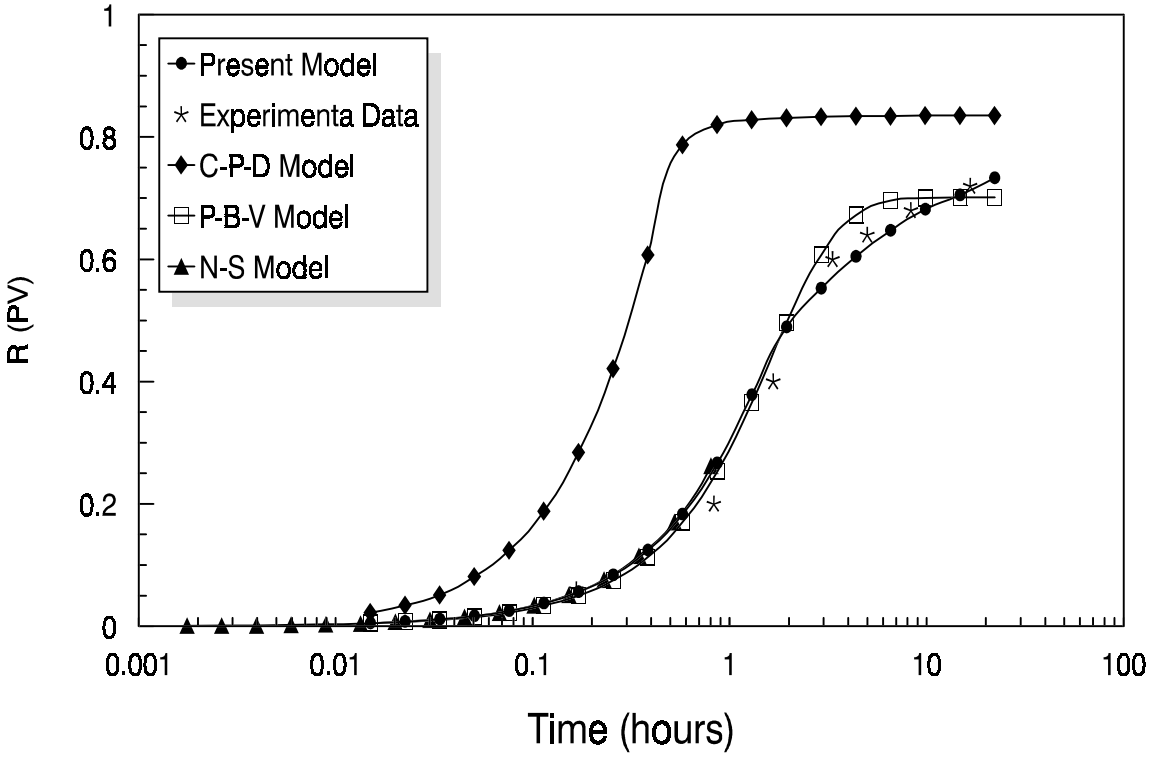

Fig. 161. Comparison of calculated and observed oil recoveries.

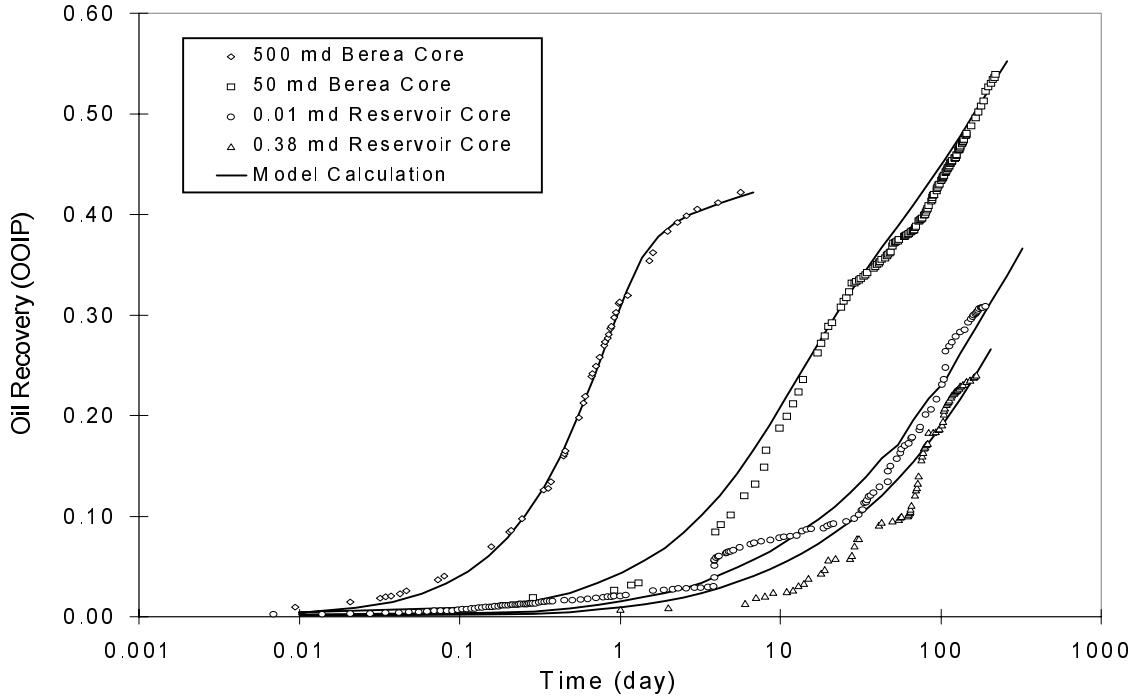

Fig. 162. Matched and observed oil recoveries from four cores.

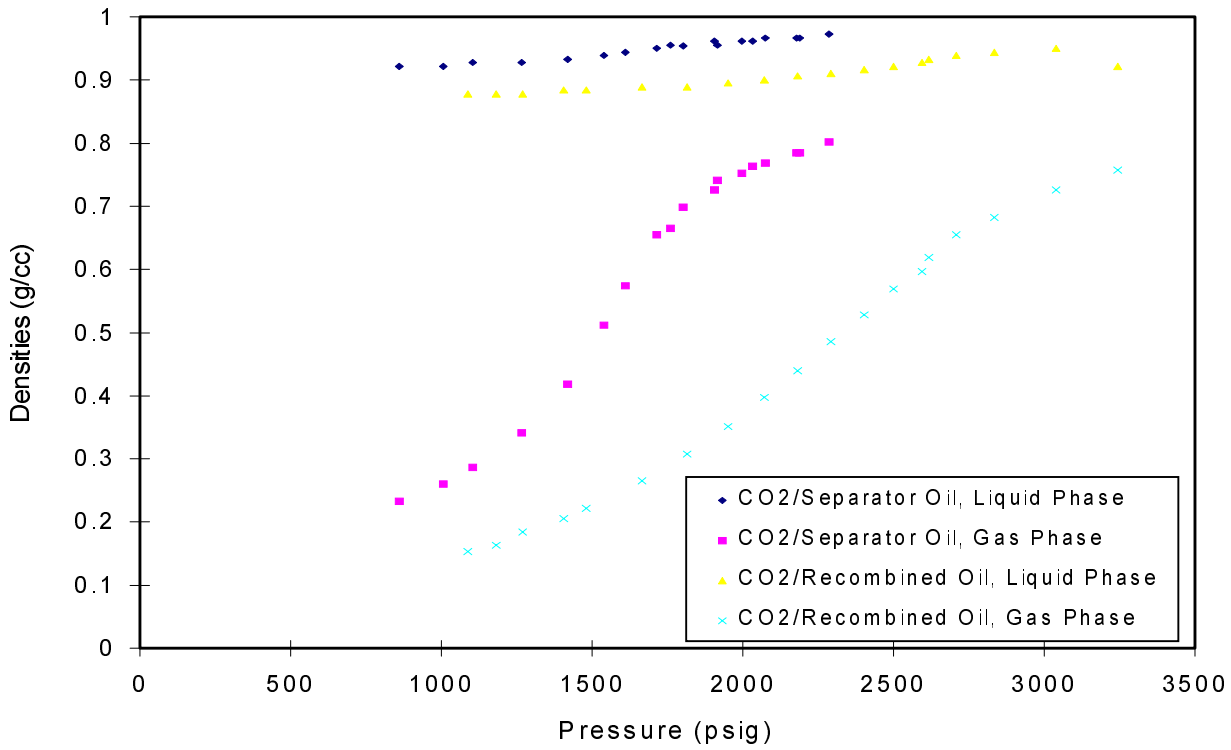

Fig. 163. Measured densities of two CO_2/crude oil systems.

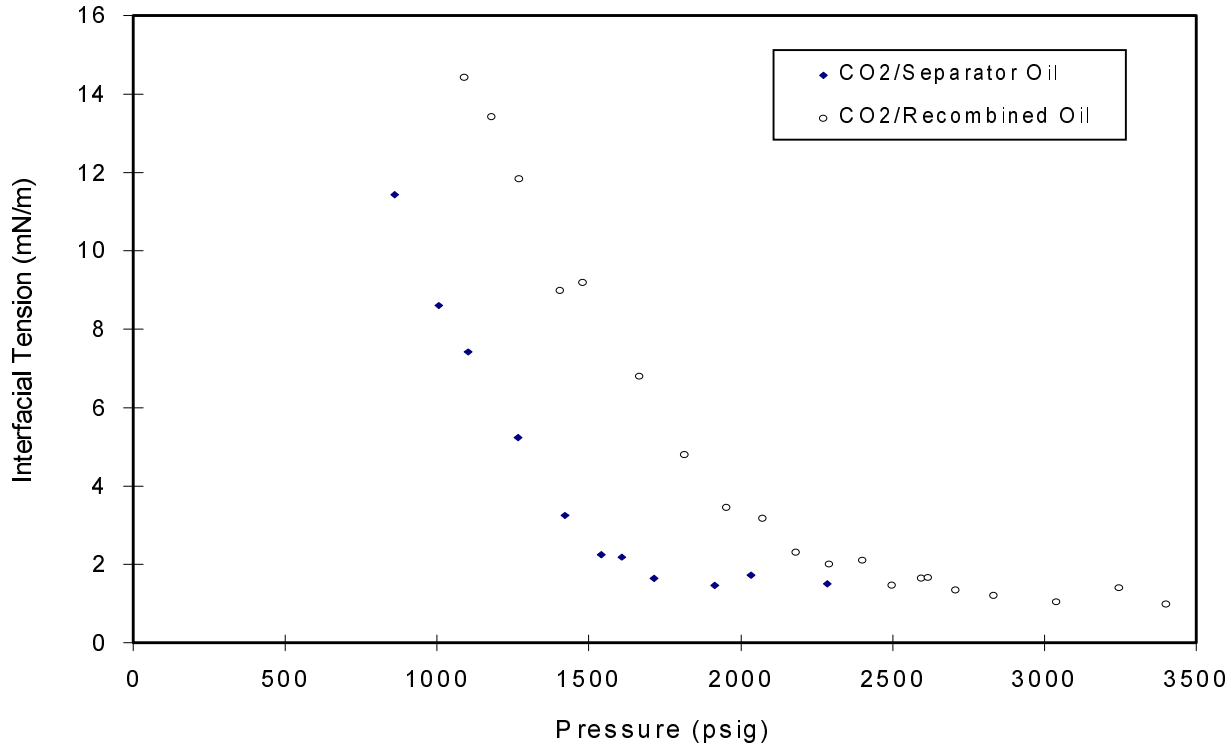

Fig. 164. Measured IFT of two CO_2/crude oil systems.

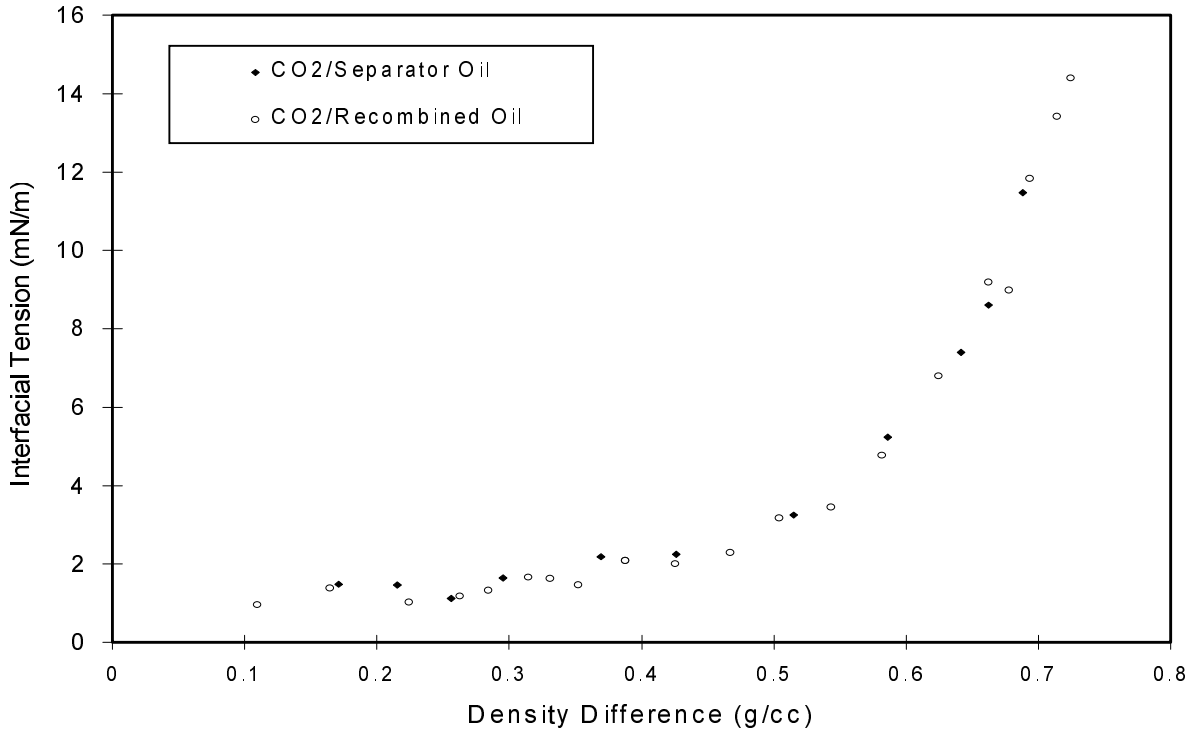

Fig. 165. Relationship between density difference and IFT of two CO_2/crude oil systems.

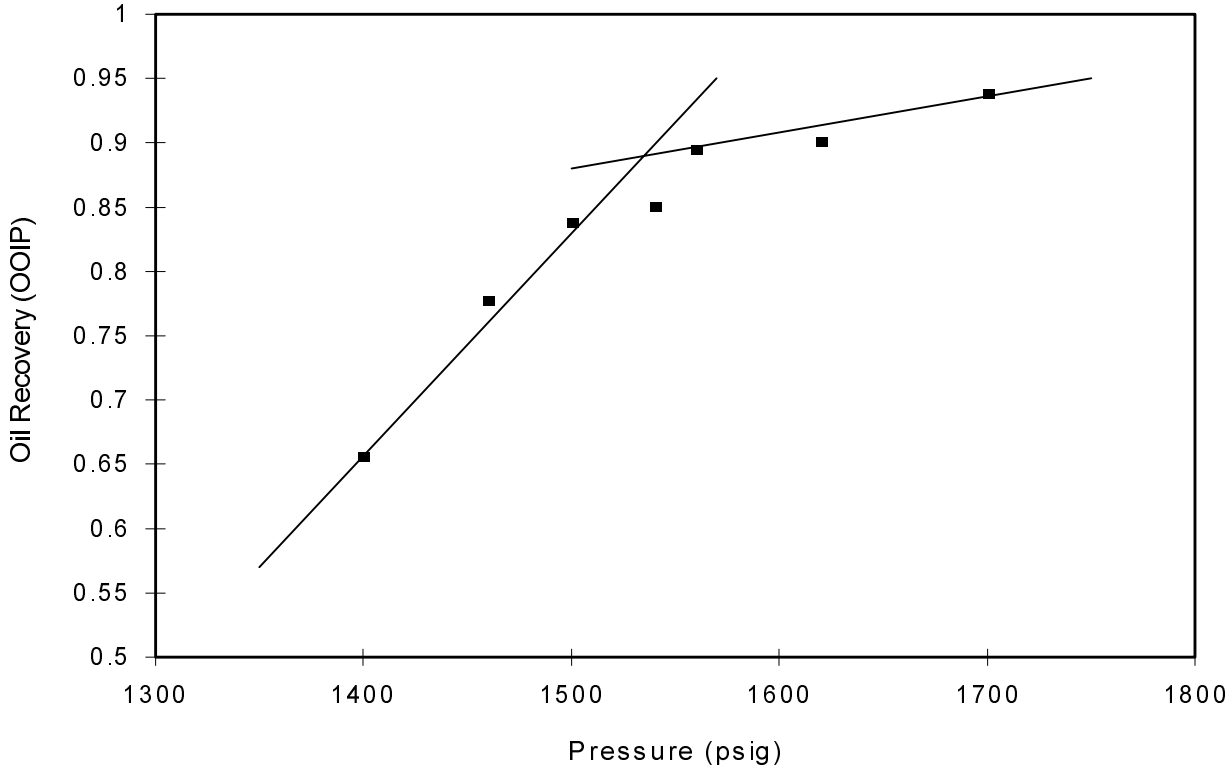

Fig. 166. Slim tube MMP for the separator oil is about 1550 psig.

CONCLUDING REMARKS

The final technical report on PRRC's current CO_2 project defines three specific tasks and describes the work that has been performed on them during the three-year project covering April 17, 1994 to May 31, 1997. Each of the three tasks is directed towards solving a particular problem encountered in CO_2 flooding, the solutions to which will make possible more efficient oil recovery from fields amenable to production enhancement by high-pressure CO_2 injection, especially heterogeneous reservoirs.

The report is divided into three sections, each of which covers in detail the work performed on the corresponding task. In each case vital introductory material is covered, as well as technical descriptions of progress important to the domestic oil industry. The results of this project will be directly implemented into ongoing and planned field work.

ACKNOWLEDGMENTS

It is a pleasure to acknowledge financial assistance from the U.S. Department of Energy and the State of New Mexico. Support has also come from several oil companies—although as is well known that they themselves are operating under greatly reduced research budgets. The following companies are supporting the PRRC's research into CO_2 applications: AMOCO Production Company, the Chevron Chemical Company, Marathon Oil Company, Mobil E&P USA, Mobil Research and Development Corporation, Parker & Parsley Development Company, and Texaco E&P Technology Department.

In addition to the Principal Investigators, mention must be made of the numerous other individuals who have participated actively in the research work. These include Senior Research Associates Dr. Jyun-Syung Tsau, Dr. S-H. (Eric) Chang, and Dr. Boyun (Gordon) Guo, as well as laboratory technicians Charles Durbin, David Fritchman, John Kernodle, James McLemore, Cletus Scharle and Robert Svec, and graduate students Amulya Dixit, T-C. Huang, Chao Li, Hujun Li, Hsi Lin, Ucok Siagian, and Hossein Yaghoobi. Also, thanks to Liz Bustamante, technical editor of this document. Finally, a special thanks to John P. Heller and F. David Martin, who retired during the second year of this project.